

**AFRL-AFOSR-UK-TR-2013-0021**



## **TURBULENCE CONTROL THROUGH SELECTIVE SURFACE HEATING USING MICROWAVE RADIATION**

**Professor Nina F. Yurchenko**

**Institute of Hydromechanics  
National Academy of Science of Ukraine  
Laboratory for Advanced Aerodynamics  
8/4 Zheliabov Street  
Kiev, 04380 Ukraine**

**EOARD CRDF 07-9002**

**Report Date: May 2013**

**Final Report from 27 November 2007 to 26 November 2012**

**Distribution Statement A: Approved for public release distribution is unlimited.**

**Air Force Research Laboratory  
Air Force Office of Scientific Research  
European Office of Aerospace Research and Development  
Unit 4515 Box 14, APO AE 09421**

<b>REPORT DOCUMENTATION PAGE</b>				Form Approved OMB No. 0704-0188	
<small>Public reporting burden for this collection of information is estimated to average 1 hour per response, including the time for reviewing instructions, searching existing data sources, gathering and maintaining the data needed, and completing and reviewing the collection of information. Send comments regarding this burden estimate or any other aspect of this collection of information, including suggestions for reducing the burden, to Department of Defense, Washington Headquarters Services, Directorate for Information Operations and Reports (0704-0188), 1215 Jefferson Davis Highway, Suite 1204, Arlington, VA 22202-4302. Respondents should be aware that notwithstanding any other provision of law, no person shall be subject to any penalty for failing to comply with a collection of information if it does not display a currently valid OMB control number.</small> <b>PLEASE DO NOT RETURN YOUR FORM TO THE ABOVE ADDRESS.</b>					
<b>1. REPORT DATE (DD-MM-YYYY)</b> 07-05-2013		<b>2. REPORT TYPE</b> Final Report		<b>3. DATES COVERED (From – To)</b> 27 November 2007 – 26 November 2012	
<b>4. TITLE AND SUBTITLE</b>  TURBULENCE CONTROL THROUGH SELECTIVE SURFACE HEATING USING MICROWAVE RADIATION				<b>5a. CONTRACT NUMBER</b> FA8655-03-D-00010035	
				<b>5b. GRANT NUMBER</b> CRDF 07-9002	
				<b>5c. PROGRAM ELEMENT NUMBER</b> 61102F	
				<b>5d. PROJECT NUMBER</b>	
<b>6. AUTHOR(S)</b>  Professor Nina F. Yurchenko				<b>5d. TASK NUMBER</b>	
				<b>5e. WORK UNIT NUMBER</b>	
<b>7. PERFORMING ORGANIZATION NAME(S) AND ADDRESS(ES)</b> Institute of Hydromechanics National Academy of Science of Ukraine Laboratory for Advanced Aerodynamics 8/4 Zheliabov Street Kiev, 04380 Ukraine				<b>8. PERFORMING ORGANIZATION REPORT NUMBER</b>  N/A	
<b>9. SPONSORING/MONITORING AGENCY NAME(S) AND ADDRESS(ES)</b>  EOARD Unit 4515 APO AE 09421				<b>10. SPONSOR/MONITOR'S ACRONYM(S)</b> AFRL/AFOSR/IOE (EOARD)	
				<b>11. SPONSOR/MONITOR'S REPORT NUMBER(S)</b> AFRL-AFOSR-UK-TR-2013-0021	
<b>12. DISTRIBUTION/AVAILABILITY STATEMENT</b>  Distribution A: Approved for public release; distribution is unlimited.					
<b>13. SUPPLEMENTARY NOTES</b>					
<b>14. ABSTRACT</b> The project aims at a search and development of innovative engineering solutions in the framework of the formulated flow-control concept based on thermal initiation of given-scale streamwise vortices. The objective of the implemented interdisciplinary research is the development of operation flexible and energy advantageous control of turbulent flows using microwave (MW) methods to generate a spanwise-regular temperature boundary condition. Two mutually complementing parts of the project were implemented in the fields of aerodynamics and electrodynamics. PART 1 (Hydromechanics Institute, National Academy of Sciences of Ukraine, IHM NASU, in collaboration with National Aviation University of Ukraine, NAU) - Fundamental aerodynamic investigations consist of matched experimental and numerical studies of boundary-layer characteristics under the condition of remote heating of local flow areas with dosated MW irradiation. PART 2 (Moscow Radiotechnical Institute, MRTI, RAS, Russian Federation) - Electrodynamic investigations are focused on a search of flexible, inertialess and reliable engineering tools for active and remote flow control based on the specified spanwise-regular heating of a near-wall flow.					
<b>15. SUBJECT TERMS</b>  EOARD, microwave discharge, plasma aerodynamics, weak ionized gas					
<b>16. SECURITY CLASSIFICATION OF:</b>			<b>17. LIMITATION OF ABSTRACT</b>  SAR	<b>18. NUMBER OF PAGES</b>  153	<b>19a. NAME OF RESPONSIBLE PERSON</b> Gregg Abate
<b>a. REPORT</b> UNCLAS	<b>b. ABSTRACT</b> UNCLAS	<b>c. THIS PAGE</b> UNCLAS			<b>19b. TELEPHONE NUMBER</b> (Include area code) +44 (0)1895 616021

# **FINAL REPORT**

**Project № UKE2-1518A-KV-07**

## **TURBULENCE CONTROL THROUGH SELECTIVE SURFACE HEATING USING MICROWAVE RADIATION**

**November 2007 – November 2012**

### **Recipients:**

Institute of Hydromechanics,  
National Academy of Sciences of Ukraine

Federal State Unitary Enterprise “Moscow Radio-Technical  
Institute, Russian Academy of Sciences”

### **Authorized Secondary Collaborator:**

National Aviation University of Ukraine

### **Partner:**

European Office of Aerospace Research and Development

# CONTENT

## Summary

## Chapter I. INTRODUCTION

- Interdisciplinary research: formulation of problems and basic tasks
- Part 1, aerodynamic RESEARCH: matched numerical and experimental investigations of a flow-field response to temperature boundary conditions
- Part 2, ELECTRO-DYNAMIC RESEARCH: development of microwave-based tools for the localized near-wall flow heating
- References

## Chapter II. AERODYNAMIC COMPLEX FOR INTERDISCIPLINARY RESEARCH (ACIR), *IHM, Kiev*

### *2.1. Purpose, design, and development*

- Initial configuration
- ACIR upgrade and present configuration
- Laboratory for Advanced AIR

### *2.2. Flow field investigations*

- ACIR characteristics

### *2.3. Data acquisition and control system (DAS)*

### *2.4. Experimental procedure and data reduction*

### *2.5. Summary*

## Chapter III. DEVELOPMENT OF MW-BASED FLOW CONTROL SYSTEMS: LOCALIZED HEATING OF THE SURFACE, *MRTI, Moscow*

### *3.1. Introduction*

### *3.2 Experimental installation*

- 3.2.1. Electrodynamic system optimization. Numerical experiment
- 3.2.2. MW generator and its high-voltage pulse modulator

### *3.3. System of microwave-heated elements of air-foil model*

- 3.3.1. System of EM linear high-Q metallic vibrators
- 3.3.2. System of EM linear Low-Q vibrators:
  - Vibrator array based on low Q-factor resistive elements: Experimental investigations and determination of a range of EM radiation parameters.
  - Calculations of thermal modes of MW-heated elements in the aerodynamic experiment.
  - Design of a resistive vibrator array for the airfoil model to be tested in a wind tunnel

- Systems of vibrators on the basis of graphitic compound heated up in the field of MW radiation
- Numerical simulation and optimization of the developed MW-heated multi-vibrator system based on thin graphite strips
- Q-low linear vibrators

### **3.4. *Experimental problems and their solutions. Summary.***

## **Chapter IV. DEVELOPMENT OF MW-BASED FLOW CONTROL SYSTEMS: MW-INITIATED ARRAYS OF PLASMA DISCHARGES, *MRTI, Moscow***

### **4.1. *Various designs of electromagnetic vibrators-initiators of MW discharges***

#### **4.2 *New-type EM vibrators located close to a metal screen-reflector***

- 4.2.1. Results of 3D numerical simulation
- 4.2.2. Results of experimental investigations

### **4.3. *New “poker-type” efficient initiator of MW discharges***

- 4.3.1 Numerical simulation of the problem of MW-discharge location
- 4.3.2 Complete aerodynamic model as an assembly

### **4.4. *Ring MW plasma actuators***

#### ***Summary***

## **Chapter V. AERODYNAMIC DESIGN AND FABRICATION OF MW-CONTROLLED MODELS, *IHM, Kiev***

### **5.1. *Models with arrays of microwave-heated elements:***

- MW-heated elements made of metal foil
- MW-heated TVO resistors
- Dispersed graphite MW-heated elements
- Thin graphite lines ("pencil system")
- R800 airfoil with heated elements

### **5.2 *Models with arrays of plasma actuators***

- Linear plasma initiators
- Ring-type plasma initiators
- R800 Model with plasma initiators

#### **5.2.3 *Circular cylinder models***

- Prototype cylindrical models with mechanical vortex-generators
- Cylindrical model with linear plasma initiators

#### **5.2.4 *Streamlined airfoil profile, SAP***

### **5.3. *Summary***

## **Chapter VI. NUMERICAL SIMULATION OF THERMALLY CONTROLLED FLOWS, IHM, Kiev**

### ***6.1. Introduction: goals, problem formulation, numerical instruments***

### ***6.2. Localized heating of the surface (distributed temperature boundary condition)***

6.2.1. Definitions, formulation of the numerical approach

6.2.2. Results and discussion: 2D and 3D modeling, effects of a finite length and a downstream location of the controlled section, free-stream velocity, model's angle of attack

6.2.3. Conclusions, physical phenomena, and recommendations

### ***6.3. Arrays of mechanical vortex-generators (Pprototype problem)***

6.3.1. Formulation and numerical procedure

6.3.2. Calculation results

### ***6.4. Arrays of plasma discharges (Localized temperature sources)***

6.4.1. Pre-crisis flow regime around a circular cylinder

6.4.2. Thermally controlled flow around a cylinder

6.4.3. Conclusions and prospects

## **Chapter VII. AERODYNAMIC EXPERIMENTS WITH THERMALLY CONTROLLED MODELS: IHM, Kiev**

### ***7.1. Localized MW heating of the surface***

7.1.1. Flow visualization

7.1.2. Hot-wire measurements of a boundary-layer flow structure modified with spanwise-regular surface heating

7.1.3. Variations in the designed models with localized MW-heating. Other types of heaters

7.1.4. Comparative analysis of different types of MW-heated strips for flow control (nichrome foil, vitrified bulk carbon resistors, fine-dispersed bulk graphite heated elements, graphite lead lines)

7.1.5. Conclusions

### ***7.2. Localized flow excitation with arrays of mechanical vortex-generators (prototype problem)***

7.2.1. Symmetric excitation using spherical vortex-generators

7.2.2. Asymmetric excitation using O-ring mechanical vortex-generators

### ***7.3. Localized MW heating of flow with arrays of plasma discharges***

7.3.1. Plasma-controlled experiments with a circular cylinder

7.3.2. EM mode:  $t=500\ \mu\text{s}$  at the repetition rate,  $F=50\ \text{Hz}$

7.3.3. EM mode:  $t=60\ \mu\text{s}$  at the repetition rate,  $F=500\ \text{Hz}$

### ***7.4. Preliminary wind-tunnel testing of the Streamlined Aerodynamic Profile, "SAP", controlled with an array of plasma discharges***

## **Chapter VIII. ACHIEVEMENTS, PUBLICATIONS, PROSPECTS.**

### **8.1. *Achievements***

Verified proof of the developed flow-control concept based on minimal energy outlay  
Engineering feasibility of the concept realization within a spectrum of possible solutions  
Innovative Aerodynamic Complex for Interdisciplinary Research (ACIR)

### **8.2. *Publications***

### **8.3. *Prospects***

MW potential as an engineering basis of the flow-control strategy  
TEMs' potential to generate the given temperature boundary condition for flow control

## I. INTRODUCTION

The project aims at a search and development of innovative engineering solutions in the framework of the formulated flow-control concept based on thermal initiation of given-scale streamwise vortices.

### Thermal riblets for active flow control. Engineering realizations

The developed flow-control concept is based on generation of streamwise vortices intrinsic to the variety of flows and thus requiring minimal energy for such flow structure maintenance. Main issues are the correlation between parameters of generated vortices and basic flow characteristics as well as optimal locations of the vortex generation over a body. Detailed background of this concept and relevant results are described in earlier project reports (P-053, 2001-2003; UKE2-1508-KV-05, 2006-2009) and in published papers, e.g. [1, 2, 5, 6, 7, 9, 11, 14, 17-21].

The concept supposes a number of various engineering solutions for its realization. Those providing active methods of flow control were developed using “thermal riblets” in a form of a spanwise-regular temperature boundary condition. Basic advantages of such thermal flow control are as follows.

The controlled surface stays smooth while the controlling temperature is turned on and off as necessary. Its value can be varied according to an operation mode and locations of controlled sections over a body. Flow control can be optimized due to independently controlled sections over a surface.

In its turn, engineering approaches to generation of the thermal riblets can be based on resistive or microwave heating of embedded elements, and on spanwise arrays of plasma discharges. Each of these engineering solutions has its specific advantages and disadvantages while the second and the third ones can provide a remote mode of flow control due to the MW energy delivered remotely to the test surface. This additional strong advantage defined the circle of interdisciplinary flow-control investigations which included the development of appropriate MW-based tools.

Two solutions outlined in Fig. 1.1 are studied in the framework of the MW-based approach: (1) localized heating of the surface and (2) direct localized heating of the boundary-layer flow, the second having realized another advantage of the thermal methods as an almost inertialess impact on the flow and thus quick expected response in terms of modified aerodynamic performance. Quite different values of local temperature in these 2 cases imply different possibilities for potential applications (plasma is considered as a thermal source with  $T \sim 1000^\circ\text{C}$ ). That is why both approaches are thoroughly investigated within the project, arising difficulties and obtained results are analyzed from the viewpoint of expediency of further investigations.

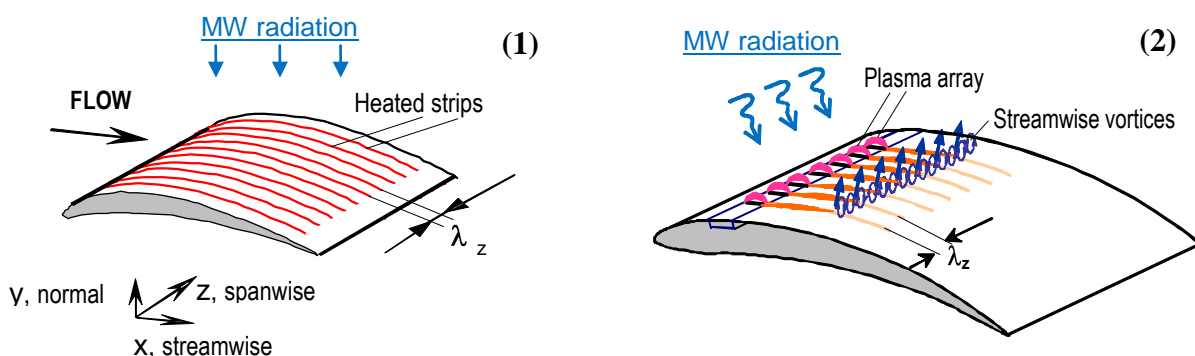


Fig. 1.1. MW-generated thermal riblets: (1) heated strips embedded into the model surface and (2) arrays of plasma discharges over a test model initiating vortices with a given  $\lambda_z$  scale

**OBJECTIVE of the implemented interdisciplinary research is the development of operation flexible and energy advantageous control of turbulent flows using microwave (MW) methods to generate a spanwise-regular temperature boundary condition.**

Two mutually complementing parts of the project were implemented in the fields of aerodynamics and electrodynamics.

**PART 1** (Hydromechanics Institute, National Academy of Sciences of Ukraine, IHM NASU, in collaboration with National Aviation University of Ukraine, NAU)

Fundamental aerodynamic investigations consist of matched experimental and numerical studies of boundary-layer characteristics under the condition of remote heating of local flow areas with dosated MW irradiation. The research efforts are focused on a thorough insight into the turbulent boundary layer response to the MW-generated thermal boundary conditions. This numerically found response in a form of a modified flow structure is analyzed together with measured integral aerodynamic characteristics like lift, drag, pitch moment coefficients and pressure distributions around the models. Thus the effectiveness of the applied flow control techniques is determined depending on flow and control parameters.

The initially supported 3-year research was extended to the 5-year term with a correspondingly extended and enriched the working plan. Due to the project extension, numerical and aerodynamic experimental potential (licensed software, more powerful wind-tunnel engine and optimization of its all systems) was enhanced and the new Laboratory for Advanced Aerodynamics and Interdisciplinary Research (Advanced AIR) was built and launched into operation at the IHM, NASU. It enables logistically supported measurements (owing to the equipped workshop) in a wider range of basic flow parameters for various models and provides better correlation between experimental and numerical results.

**PART 2** (Moscow Radiotechnical Institute, MRTI, RAS, Russian Federation)

Electrodynamic investigations are focused on a search of flexible, inertialess and reliable engineering tools for active and remote flow control based on the specified spanwise-regular heating of a near-wall flow.

For that, systems of electromagnetic (EM) vibrators are designed to provide high efficiency of their interaction with the MW beam under conditions of low energy consumption. Maintenance of the required z-regular temperature distribution is achieved using pulse EM radiation with properly chosen pulse duration  $\tau_{\text{pul}}$  and pulse repetition rate  $f_{\text{pul}}$ . A basic nature of the electrodynamic research and its complexity related to the connected wind-tunnel facility are illustrated by the case of linear EM vibrators. Rotating in a plane perpendicular to a propagation direction of linearly polarized EM radiation, angles between axes of these vibrators and the  $E_0$  vector of EM field will vary harmonically. Thus it is always to be taken into account that the energy transmitted for their heating (or for plasma ignition) will also vary harmonically together with the variation of the model angle of attack in the wind-tunnel test section.

High professional level of the research is reached due to close interaction and coordination of the aerodynamic and electrodynamic parts of this genuinely interdisciplinary project. Concluding stages of wind-tunnel measurements were implemented jointly in the Laboratory for Advanced AIR to make experiments efficient and exhaustive in a wide range of both aero- and electrodynamic parameters.

To show prospects of the guiding flow-control concept and a broad spectrum of related engineering solutions, the feasibility of one more engineering approach is considered in cooperation with the Institute of Semiconductor Physics, NASU. It is based on application of thermoelectric modules for generation of the necessary temperature boundary condition on the wall.

## Chapter II. ACIR – AERODYNAMIC COMPLEX FOR INTERDISCIPLINARY RESEARCH

### 2.1. Purpose, design, and development

#### 2.1.1. Initial configuration

Aerodynamic Complex for Interdisciplinary Researches (ACIR) was created in the framework of the UKE2-1508-KV-05 project implementation, "Advanced method of boundary-layer control based on localized plasma generation" to combine a multi-purpose wind tunnel with microwave radiation and protection systems. Initially it was built at the National Aviation University as the project partner.

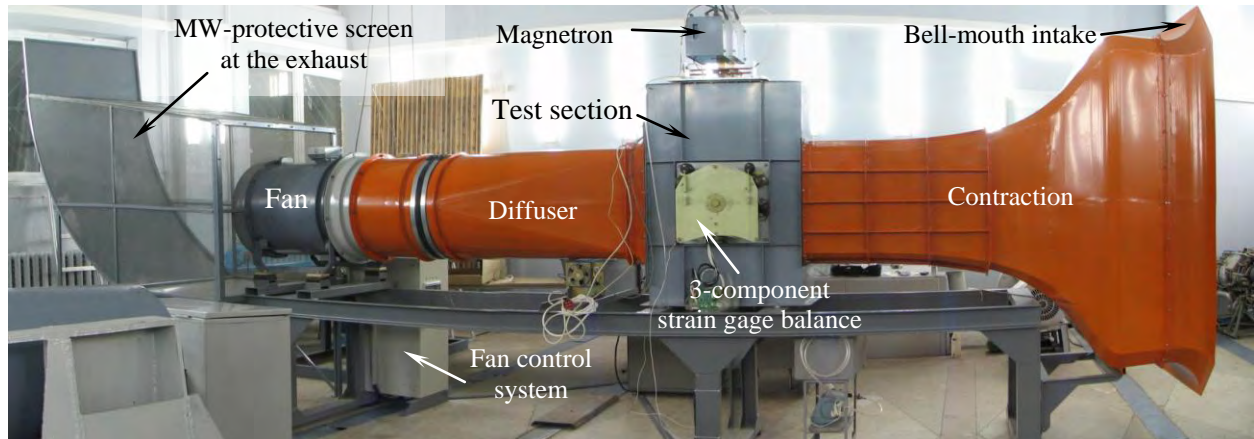


Figure 2.1. Initially designed ACIR

ACIR included atmospheric low-speed wind tunnel (WT) of open-return type, which was equipped with a dynamic pressure measurement and control system, 3-component strain gage balance, multipoint surface pressure measurement system, 2-channel constant temperature anemometer, the microwave radiation system operating in continuous and pulse modes. Metal wind-tunnel (WT) frame together with special shields at the intake and exhaust provided personnel and equipment protection from harmful MW radiation. WT control and measurements during experiments were performed using the affiliated data acquisition and control system through the specially created software.

#### 2.1.2. ACIR upgrade and present configuration

Regular control of WT characteristics in a process of ACIR operation showed its certain shortcomings like low flow stability, insufficient value of free-stream velocity, excessive noise. In addition, it did not enable to provide the required spanwise-regular temperature boundary condition over the controlled model because of the insufficient intensity of electromagnetic (EM) field and its strong nonuniformity because of multiple reflections in the test section.

Detailed numerical and experimental investigations in MRTI in the electrodynamic analogue of the WT test section resulted in the recommendation to change the ACIR geometry narrowing its test section from 31 cm to 28 cm that was expected to improve the EM situation around the model and to stay with the same low energy consumption for MW control purposes. Such a significant redesign of the test section inevitably involved the corresponding reconstruction of other ACIR parts.

As a result, the new test section was designed according to typical wind-tunnel requirements accounting for those related to the electrodynamic part. It is made of 20 mm thick steel sheets bolted together without welding, has slotted upper and lower walls, a larger access door and opening for the MW horn antenna connected to magnetron. The used technology better maintains the given precise geometry preventing from hogging and provides better flow quality.

An old intake was substituted by the new streamlined one (Fig. 2.2), which eliminated harmful vortex generation on sharp edges of the bell-mouth. The 400-mm long settling chamber with the inbuilt 160-mm long 40x40 mm cell honeycomb was added upstream the contraction (Fig. 2.3).



Figure 2.2. New intake

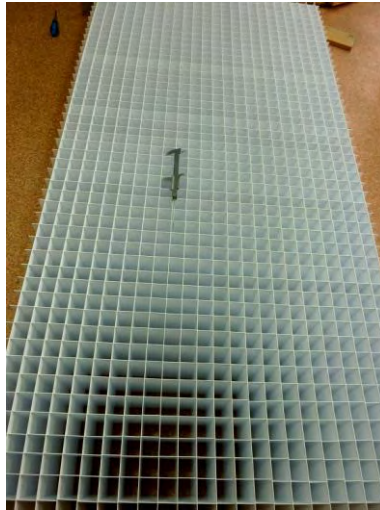


Figure 2.3. Honeycomb assembly



Figure 2.4. Wind-tunnel test section with the MW radiation system on its top

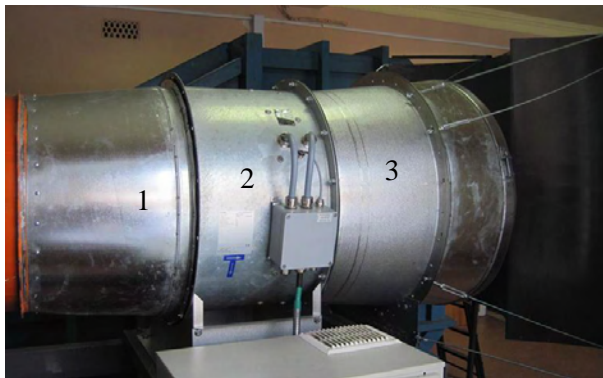


Figure 2.5. New fan/diffuser assembly:  
1 – front diffuser; 2 – fan; 3 – exhaust diffuser

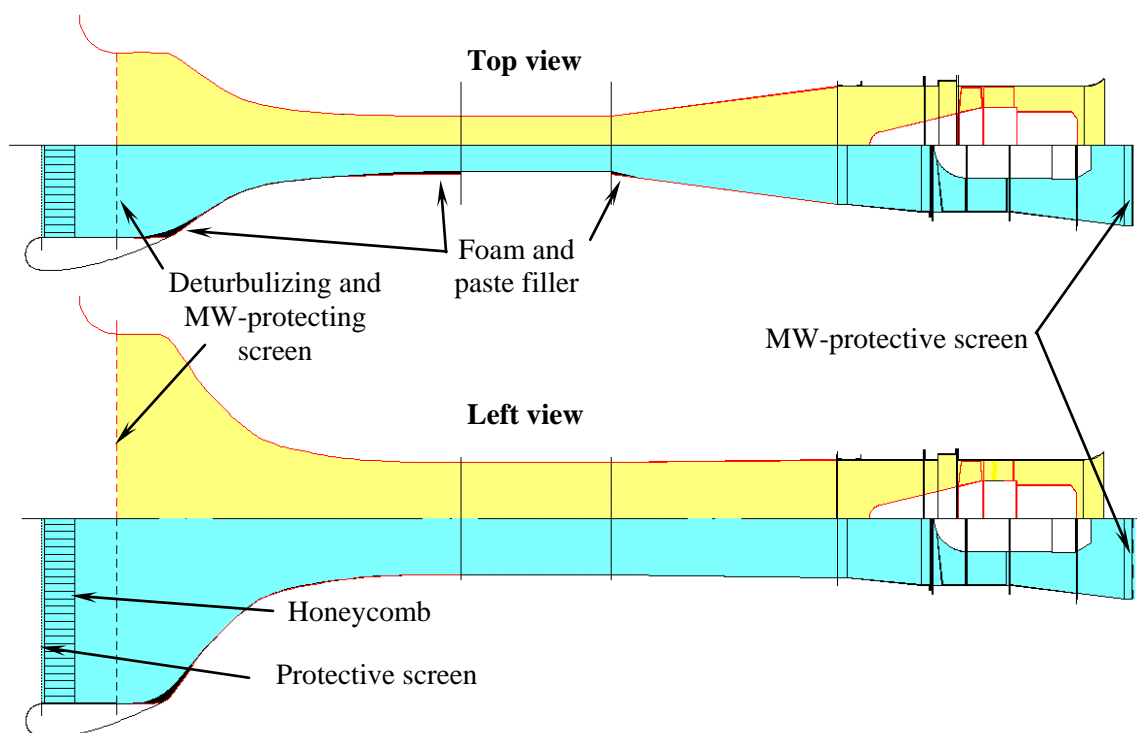


Figure 2.6. Comparison of internal contours of old (yellow/red) and new (blue/black) ACIR configurations

The new developed 25-point pressure measurement system and of the relevant software raised the experiment efficiency and reduced its cost. Random errors of aerodynamic force measurements were diminished, the raised EM field uniformity provided similar influence on separate elements of the embedded thermal array that improved the spanwise-regular  $T(z)$  boundary condition over models.

This cycle of the ACIR optimization was accompanied with its transfer to the IHM and ended up with

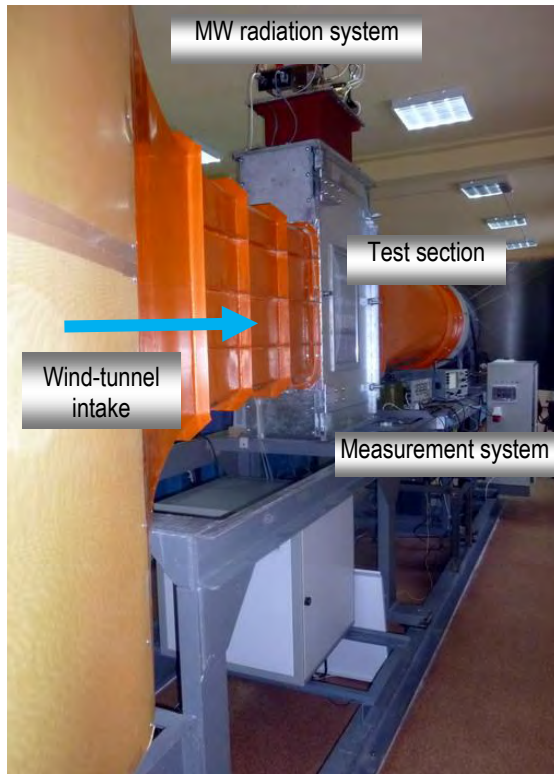


Fig. 2.7. Optimized ACIR

its integration into the systems of the created **Laboratory for Advanced Aerodynamic and Interdisciplinary Research (Advanced AIR)**.

During the concluding stage of the project, a more efficient fan with supplementary diffuser sections was purchased and installed (Fig. 2.5). Accordingly, the contraction internal contour was adjusted and considerably smoothed to eliminate high-curvature couplings in the very upstream section to avoid extraneous vortex generation inside the tunnel (Fig. 2.6). Under the condition of the same power consumption, these modifications resulted in significantly raised free-stream velocities (from 40 to more than 65 m/s) and reduced noise levels. The improved flow quality is illustrated by Fig. 2.7, where two time series of measured dynamic pressure variations are shown for similar regimes in the old and new WT. From the grown critical Reynolds number for the cylinder  $\sim 5 \times 10^4$ , it is assumed that the free-stream turbulence also decreased.

Technical characteristics of the ACIR are given in the Table 2.1.

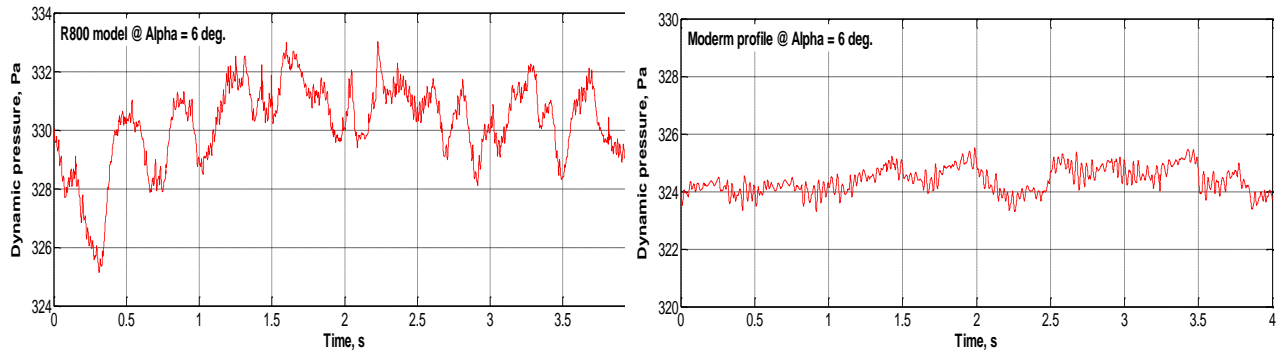


Figure 2.7. Comparison of dynamic pressure variations in the ACIR with old (top) and new (bottom) configurations

## 2.2. Flow field investigations

The basically comparative type of tests reduced a number of flow parameters to be monitored in the experiments. They are dynamic pressure  $q_{ts}$ , static pressure  $P_{S,ts}$ , static temperature  $T_{S,ts}$ , specific humidity  $SH_{ts}$ , air density  $\rho_{ts}$ , air cinematic viscosity  $\nu_{ts}$ , free-stream velocity  $U_{ts}$ , and Reynolds number of the model,  $Re$ . Only some of them are measured directly while the others are calculated using the ideal gas approximation assuming that pressure and temperature do not noticeably differ from the atmospheric values and the free-stream Mach number is small enough. Dynamic pressure is evaluated from the static pressure difference in settling chamber and the test section. The

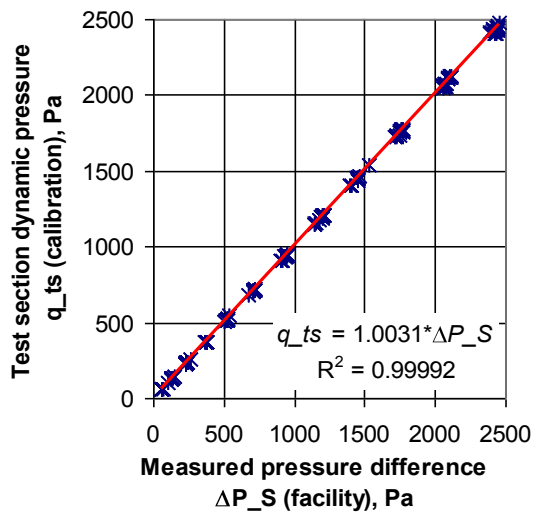


Figure 2.8. Dynamic pressure calibration curve: combined data for 5 locations of a reference pressure probe in the test section: asterisks refer to measured values (totally 368 points), solid lines are the liner approximation

correlation between a reference dynamic pressure in the test section and measured pressure difference is determined in calibration tests.

Here a reference pressure probe is placed in the test section and two parameters are measured simultaneously: pressure difference on pressure probe  $q_{ts, (calibration)} = \xi_{pp} P_{T,probe} - P_{S,probe}$  (where  $\xi_{pp}$  is calibration coefficient of the pressure probe) and static pressure difference in the two sections of air channel of wind tunnel  $\Delta P_{S, (facility)} = P_{S,sc} - P_{S,ts}$ . Calibration has been performed for five positions of reference pressure probe across test section: -100, -50, 0, +50, and +100 mm left and right from its longitudinal centerline in horizontal plane. Combined data are shown in Fig. 2.8.

Table 2.1. ACIR characteristics

Parameter	Units	Value	
		Old	New
Test section: rectangular with trimmed corners	–	Solid walls	Solid side walls, slotted upper and lower walls
Test section size (Width × Height × Length)	cm	31 × 60 × 80	28 × 60 × 80
Test section cross area	m <sup>2</sup>	0.185	0.167
Free-stream velocity range	m/s	5 – 40	5 – 65
Contraction ratio	–	10.6	11.8
Fan motor type	–	3-phase induction	3-phase induction
Fan motor rated power	kW	18	22
Fan control system	–	Danfoss VLT-6032 frequency converter	
Fan control system rated power	kW	22	
Strain gage balance:			
number of measured components	–	3 (lift, drag, pitch moment)	
measurement range	N	200 N for lift, 60 N for drag, pitch moment	
model position range	deg.	360	
Surface pressure measurement system			
number of sensors	–	25	
sensors type	–	Differential, amplified	
measurement range	kPa	0...4.0 (20 sensors); 0...6.0 (5 sensors)	
Continuous-radiation microwave system:			
power consumption	kW	up to 1.5, regulated	
magnetron cooling	–	water	
Pulse-radiation microwave system:			
power in pulse	kW	up to 7, regulated	
mean power consumption	kW	< 1	
magnetron cooling	–	air	

Static pressure  $P_{S,ts}$  and temperature  $T_{S,ts}$  are calculated from direct measurements of barometric pressure and temperature in the room and of dynamic pressure  $q_{ts}$ . Specific humidity  $SH_{ts}$  is

calculated from a measured value of relative humidity in the WT room. Air density  $\rho_{ts}$ , air kinematic viscosity  $\nu_{ts}$ , are calculated using the ideal gas law and measured values of dynamic pressure. Free-stream velocity  $U_{ts}$  is calculated from dynamic pressure values and the calculated air density.

### 2.3. Data acquisition and control system (DAS)

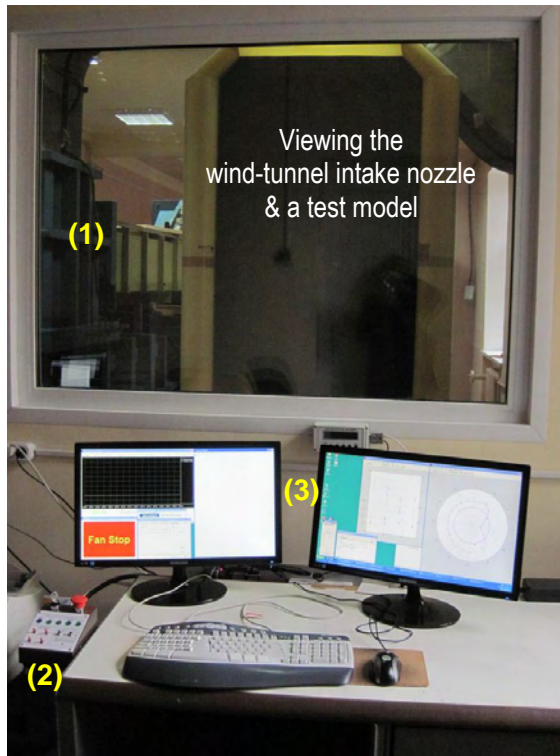


Fig. 2.9. ACIR operator's workplace:

(1) viewing window to watch ACIR operation,  
(2) control panel to manage experiments remotely:

- On-Off buttons for separate systems,
- continuous or pulse mode of MW radiation,
- Alpha-mechanism (model position) control,
- individual lighting

(3) monitors displaying data acquisition and processing

The developed data DAS aims at control of wind tunnel operation and model pitch, measurements of a number of parameters, calculation of necessary values and their presentation in a graphical and text forms in the course of experiments.

DAS includes a PC with two data acquisition boards: i) Advantech PCI-1710 universal board with 16 analog input channels, 2 analog output channels, 16 digital input-output channels and ii) Advantech PCI-1713 with 32 analog input channels. PCI-1710 provide digital control of WT fan, microwave system switching, and control and measurement of model pitch mechanism, as well as for measurements of analog signals from constant temperature anemometer. PCI-1713 is used for simultaneous measurement of dynamic pressure, model loads and surface pressure distribution during the experiment. DAS is powered from the proper UPS.

Wind tunnel control consists of setting a necessary free-stream velocity and its stabilization using feedback in VLT-6032 frequency converter. Desired parameters of fan operation are displayed on the monitor (Fig. 2.9).

In the course of experiments, information about the dynamic pressure, loadings from a strain gage balance and up to 25 signals of surface pressure is registered; lift, drag and pitch moment coefficients are calculated and plotted.

### 2.4. Experimental procedure and data reduction

Typical experimental procedure includes simultaneous measurements of aerodynamic forces and pressure distributions following the developed program.

1. A software subroutine "Testing task" is created, which is a set of necessary parameters defined using graphic user interface. They are current angular position of the model, initial and final angles of attack, and angle step; voltage of MW-system power supply, pulse repetition rate and pulse duration; barometric pressure, temperature, and relative humidity in the WT room measured with "Troposphere-G" air monitoring system. All the characteristic parameters of measurements are registered like a measurement time, model description, etc.

2. After the testing task file is created, weight testing software program is started. It reads program initialization file and loads coefficients of calibration functions of all measuring channels. The process is controlled on monitors.

3. All three force components are measured in the still air for the initially defined angles of attack. Results of zero-velocity measurements are approximated using 3rd power polynomial. Approximation

errors typically do not exceed 0.02-0.03 N.

4. Operator starts the WT at an automatically or manually set free-stream velocity. Measured values of dynamic pressure together with values of atmospheric parameters are used to calculate free-stream velocity and Reynolds number.

5. Model is set at a predefined angle of attack to start the following sequence of measurements.

- a) **The MW radiating system remained switched OFF in a reference case without flow control.**
  - b) Atmospheric parameters are read from "Troposphere-G" air monitoring system.
  - c) During "measuring time" with "sample rate" and within "measuring range" set in Testing task subroutine, measurements are performed of output signals of dynamic pressure transducers, load sensors of strain gage balance, and pressure transducers of surface pressure measuring system.
  - d) Physical parameters are calculated for each set of instantaneous values of output signals using calibration functions of corresponding measurement channels. These parameters are lift, drag, and pitch moment, static pressures in tap points, free-stream velocity, and Reynolds number for a current angle of attack.
  - e) Instantaneous values of lift, drag and pitch moment coefficients, pressure coefficients, free-stream velocity and Reynolds number are calculated using conventional ways.
  - f) Sample means and standard deviations of named parameters are calculated. Obtained sample means are output to load coefficient plot and vector pressure distribution plot.
  - g) **In the controlled cases, the MW system is ON** and procedures b) through g) are repeated.
  - h) **MW radiation is switched OFF** and the model is left cooling during 10-15 s.
6. Procedures listed in clause 5 are repeated as many times as it is defined by parameter in the Testing task subroutine.
7. After a cycle of measurements is over, the next ones are carried out in the described manner.
8. WT is stopped and obtained data together with plots are saved to hard disk in a binary format.

## 2.5. Summary

1. The unique aerodynamic complex is developed and launched into operation. It enables multidisciplinary investigations related to advanced flow-control methods using microwave-based techniques like localized heating and plasma generation. The whole operation including the MW system goes with low energy consumption and is safe for personnel and equipment.

2. The ACIR provides a broad spectrum of experimental studies both of single models, their tandems, and low-lift compressor-type cascades.

3. Aerodynamic complex is equipped with relevant instrumentation including a 3-component strain gage, pressure distribution measurement system and others, it can operate in manual or remote automatic modes, performs sophisticated analysis of various types of data in the course of experiment and after its completion.

4. A number of the complex optimizations resulted in a considerable improvement of flow quality and increased free-stream velocity up to 65 m/s, which corresponds to  $Re_{ts} = 4.2 \times 10^6 \text{ m}^{-1}$  of typical models.

### III. DEVELOPMENT OF MW-BASED FLOW CONTROL SYSTEMS (MRTI).

#### Microwave selective surface heating approach

##### 3.1. Introduction

Last decade new methods of control of aerodynamic factors and boundary-layer characteristics on the surfaces of a streamline body based on creation near a body or on its surface of localized zones of energy release are more and more actively developed.

Energetically effective control method based on creation on a surface of a streamline body of regular system of localized discharge [3.1] has been offered. Besides, the new approach to realization of idea in the conditions of aerodynamic experiment – application of a remote, contactless supply of energy to multisystem of initiators of MW discharges (or heated up elements) – is represented more convenient for engineering.

Thus, despite obvious advantages of methods of plasma aerodynamics, realization of this method using a regular system of similar extended elements heated up by remote source of microwave (MW) energy is of great scientific interest. First, these problems are in many respects similar from the point of view of electrodynamics, and investigations in this direction will allow understanding general laws of electromagnetic interactions and dissipation of energy in a system of various passive resistive vibrators in the EM wave field. Secondly, for MW heating of vibrators application of powerful pulse sources of MW energy is not required.

##### 3.2 Experimental installation

###### 3.2.1. Electrodynamic system optimization. Numerical experiment

In conditions of aerodynamic experiment it was necessary to provide uniform heating of located on a model surface multisystem of parallel vibrators with an extent in the spanwise direction (along axis “Z”) about 200 mm. Wavelength of external magnetron type source of MW radiation  $\lambda = 12.24$  cm, and stabilized output power – no more than 1000 W. Minimum possible distance from the irradiating antenna to model is equal 300 mm.

Results of the numerical simulation of the electrodynamic “situation” in the working section of the wind tunnel in Kiev fulfilled in frames of the parallel project CRDF #UKE2-1508 completely confirmed results of experimental investigations. Analysis of obtained earlier results says that in this design of the working chamber it is necessary to realize separate adjustment of the microwave radiation incident field: (i) transversally to the flow in the spanwise direction of the model, i.e. over the axis “Z”, and (ii) along the flow over the axis “X” of the chamber.

The walls of the chamber (at given  $E$  vector polarization parallel to them) create some open overdimensioned waveguide system. The distance between walls about 310 mm is comparable with the radiation wavelength  $\lambda = 122$  mm. Therefore a diverging wave irradiated by the horn is transformed by the chamber walls in the chamber center (in model location place) into typical double-peak wave structure. In other words, in our case the walls of the working chamber “themselves” determine the field pattern  $E(z)$  at sufficient distance from the horn.

In order to form an even “shelf” on the  $E(z)$  distribution  $\sim 200$ mm in thickness (width of the model and of the multivibrator array) it is necessary only to



Fig.3.1. Initial experimental chamber created and used in MRTI during works on the Project CRDF UKE2-1508A-KV-05

somewhat “compress” MW radiation in Z-direction. This task can be solved by location of additional walls inside the chamber with a distance of 270-290mm between them and with small slopes in their upper part.

At the same time, in order to increase  $E$ -field amplitude it is necessary to realize as sharp as possible focusing of the incident radiation in the flow direction, along axis “X” of the chamber, because sizes of the vibrator system are small in this direction:  $2L < 100$  mm.

Two versions of the electrodynamic system forming the electromagnetic radiation in the central zone of the working chamber were proposed and calculated.

#### First version.

The simplest way to deliver a radiation to vibrators array with minimal losses would be using common waveguide. However this way is impossible at experiments in the wind tunnel. The idea consists in changing of this waveguide by a structure of thin vertical plates parallel to the flow with a break  $\sim 100$ mm directly over the model. The structure represents the beyond-cutoff waveguide at the distance between the plates  $\Delta z < \lambda/2$  (practically at  $\Delta z < 40$ mm) and if the plates are parallel to MW vector  $\mathbf{E}$ , it forces the radiation to propagate only in Y-direction toward to the vibrators array.

However, in spite of the idea’s fruitfulness, good field amplification in the working zone and comparably low cost, this design is very sensitive to manufacturing tolerances and, what is most important, it encumbers the working space of the testing chamber. After long discussions with colleagues from Kiev it was decided to temporary refuse this version.

#### Second version

The second version is “classical” means of EM radiation beam forming with a help of a dielectric focusing lens, see Fig. 3.2. The problem here consists in the fact that at commensurability of the lens sizes and the radiation wavelength it is difficult to get a good focusing: the geometrical optics approximation works at the lens aperture starting from  $A = (6 \div 10) \cdot \lambda$ .

The aperture of the horn was enlarged from 200×200mm to 392×210mm after numerical modeling and tests of several tens versions of the radiating system. Partly this fact also helped in better focusing and increase of a field in the working zone. However, one has to remember that it is impossible in principle to reach an ideal “point” focusing at the given geometrical sizes of the chamber and the wavelength, and so called diffraction limit of a focal spot size decrease is  $\sim \lambda$  by the level  $e^{-1}$ .

From the viewpoint of represented above requirements numerical optimization of electrodynamic system as a whole has allowed to determine its main parameters. The cylindrical lenses should be made of polyethylene ( $\epsilon = 2.26$ ,  $\tan \delta \sim 4 \cdot 10^{-4}$ ). Their curvature radius is equal 270mm (while calculations by the “thin lens” formula gives 180 mm), and their total height is 176 mm. The distance between additional walls in the chamber is 280 mm, height and depth of walls slopes in their upper part is 100mm and 35 mm, respectively.

The results of numerical simulation of a field distribution in the working chamber are shown in Fig. III.3. Width of both chambers in IHM and in MRTI is equal 310 mm. Boundaries of additional internal walls are conditionally shown by dashed lines in Fig.3.5 in the left picture. One can see that the field distribution obtained in the result of the system optimization in the area of the model location represents a relatively even “table” (curve “3”); and the field amplitude at the chamber axis approximately by two times exceeds its initial value (curve 2). The last one is equal to fourfold increase of MW generator power.

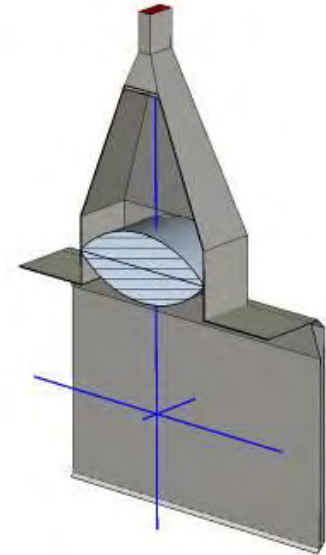


Fig.3.2. New electrodynamic system

For a comparison, in the same picture the  $E$ -field distribution in the anechoic Chamber N2 is also shown (curve “1”). One can see that a difference in these field patterns is essential.

The right picture in Fig.3.3 illustrates radiation focusing capabilities in the longitudinal direction along the flow with a help of double cylindrical lens.

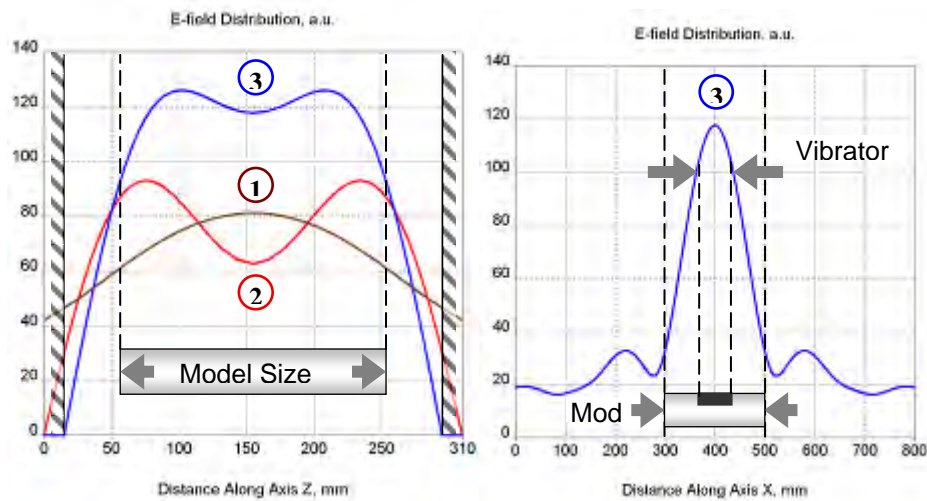


Fig.3.3. Electric field  $E$  amplitude distribution transversally and along the flow: along axis  $Z$  (at the left) and axis  $X$  (at the right) of the vibrator system. 1 – anechoic Chamber, 2 – new Chamber (analogue of the working chamber in IHM), 3 – the developed design with focusing lenses (see Fig.2.5)

Fig.3.4 illustrates  $E$ -field distribution diagram in the chamber central plane (top view from the side of the input waveguide with the horn). One can see that the field is maximal just in the area of the vibrators array on the model, i.e. the radiation energy is used most effectively.

However, in spite of the promising results of the electrodynamic system developed model, only experiments can give the final answer. Besides, former recommendations on application of cylindrical focusing mirror located at the bottom of working chamber in IHM stay in force, because at the given (limited) power of available MW generator it is necessary to use all the possibilities of the MW field increase. An appearance of the new chamber in two projections is shown in Fig. 2.5. A form and geometrical sizes of the chamber including wall bevels in its corners duplicate those in the test chamber of the wind tunnel. The chamber is manufactured of foiled fiber-glass plastic (textolite) and is fixed in rigid framework of steel angles.

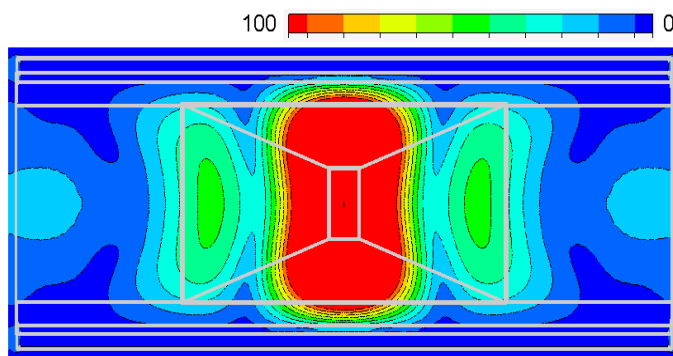


Fig.3.4.  $E$ -field distribution diagram in the plane  $X0Z$  of the model.

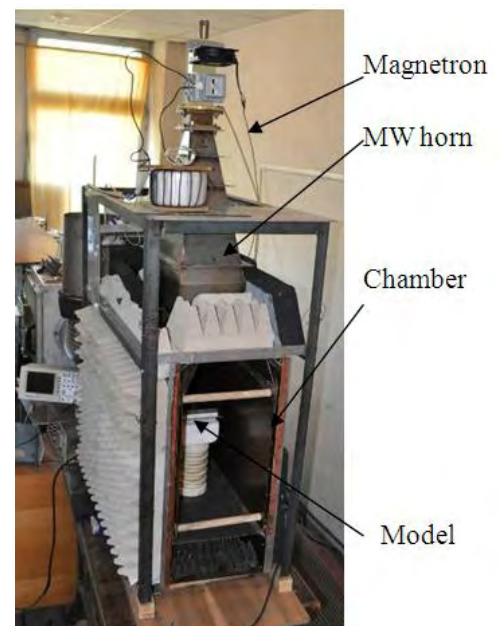


Fig.3.5. New optimized experimental chamber in MRTI – the full electrodynamic analogue of new wind-tunnel test section in IHM, Kiev

### 3.2.2. MW generator and its high-voltage pulse modulator

For maintenance of reliable ignition of discharges multi-system on a model surface the higher level of EM field is required in the model location in the chamber, and the required amplitude of electric field increases in the system with growth of vibrators number. At the limited average power of used magnetron type generators (1-2 kW, 2.45 GHz) the way forward consists in transition to “packet” pulse-periodic operating mode of MW radiation source that allows at short MW pulse duration and at

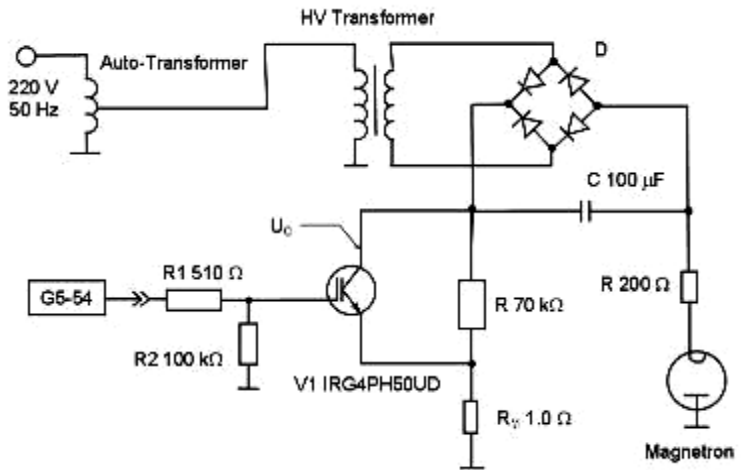


Fig.3.6. Circuit diagram of the modulator and power supply

conservation of average power of the supply to substantially raise amplitude of the pulsed MW field. However producing by the industry domestic magnetrons is not designed for work in such a mode, and modulators of a high voltage for this purpose are not produced by the industry.

Therefore the original scheme of the pulse modulator for low-power magnetrons on the basis of high-voltage IGBT-type transistors IXGH32N250A has been developed. ( $U_{CM} = 2500$  V). The scheme of such a modulator is shown in Fig.3.6. The modulator application has allowed raising the pulse power of MW generator to 6-9 kW.

The modulator works in a mode with the partial discharge of storage capacity  $C$  and provides change of pulse temporary parameters (pulse duration and repetition rate) in a packet in very wide limits, which are limited only by a size of the energy reserved in the capacity and a power of a force power supply.

### 3.3. System of microwave-heated elements of air-foil model

#### 3.3.1. System of EM linear high-Q metallic vibrators

Physical grounds, main tasks of the mentioned above problem and ways of their solution were partially described in the previous report on the Project. Detailed investigations fulfilled during that quarter have shown that the given problem is much more difficult than initially expected.

Since average computation time of realistic multi-vibrator system with satisfactory accuracy exceeds 30-40 hours then for decrease of the computation time we earlier undertook investigations with a model with relatively small number of ED vibrators in the system – about 5, 8 strips, not more. Final goal of the given investigations consists in development of the vibrator system for a full scale model, i.e. placed on a surface of the model 200mm wide in spanwise direction and consisting of 39 elements (at optimal value  $\lambda_z = 5$ mm).

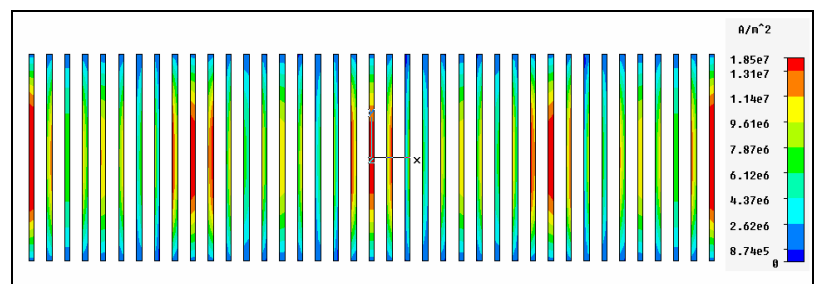


Fig.3.7. Current density distribution in the strip metallic system;  
 $2L = 54$  mm,  $\lambda_z = 5$  mm

Results of numerical modeling of such structure with strips length  $2L = 54$ mm at application of the code CST Microwave Studio (from the software package CST Studio Suite 2008, “Computer Simulation Technology” production) are presented in Figs. 3.7. Vibrators were made of NiCr

alloy; strip thickness was  $b = 8.5 \mu\text{m}$ , and their width was  $2a = 1.5\text{mm}$ . Here and further for definiteness we accept the amplitude of falling linearly polarized (vector  $\mathbf{E}_y$  is parallel to a long side of vibrators) flat electromagnetic wave to be  $10 \text{ V/cm}$ .  $\mathbf{H}_x$  vector of the incident wave is directed along the axis of the vibrator system that goes through their centers (it is necessary to note that this direction corresponds to the coordinate axis “Z” in aerodynamic experiment)). A wavelength of MW radiation is  $\lambda = 12.24 \text{ cm}$  ( $f = 2.45 \text{ GHz}$ ). The system is situated in a free space, i.e. there are absent any metallic walls, reflectors and focusing mirrors.

Thus, a structure of resulting electromagnetic field (that is a superposition of vectors of falling and reflected by the system radiation) is rather complex and very inhomogeneous with respect to position of different vibrators even in this idealized system. One can distinctly see that at least three transversal oscillation modes are excited in the system. In the result one can see in corresponding Fig.3.7 strongly inhomogeneous distribution of loss current density  $j_a$  in the system. In other words a value of absorbing MW power  $P_a$  is different in different elements of the system; in one accounts that a temperature of a heated element is  $T \sim P_a \sim j_a^2$ , then he gets that the temperature distribution in the spanwise direction will be even more inhomogeneous than in Fig.3.7.

Though a frequency of MW radiation is fixed in experiments and is  $2.45 \text{ GHz}$ , a frequency representation of electrodynamic system characteristics is very convenient for understanding of EM radiation interaction with objects of a complex form. Resonance characteristics of investigated vibrators represent separately smooth curves and optimal length of a signal vibrator is  $2L = 54\text{mm}$ . However, individual characteristics of the same vibrators being among similar ones and forming multi-vibrator system are sharply different. Resonance features of separate elements of a simplified system consisting of 5 and 8 vibrators were considered in the Report for the 3-d quarter of the Project.

At the same time this approach is not a deadlock. The right way consists not in tuning of the system “in resonance”, but in shifting of amplitude-frequency characteristics of the whole system to the side from the working frequency.

Simple increase of vibrator length from  $54\text{mm}$  to  $60\text{mm}$  leads to shifting of the indicated area to the region of working frequency  $f = 2.45 \text{ GHz}$ . Results of such shifting are shown in Fig.3.8.

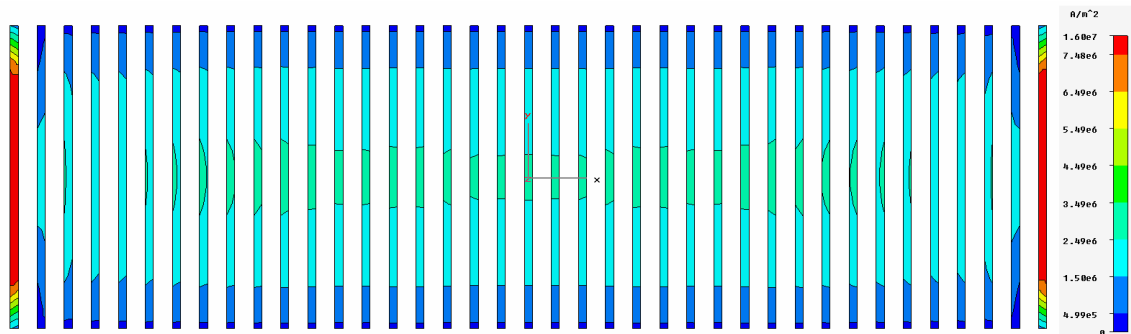


Fig.3.8. Current density distribution in the strip metallic system;  $2L = 60\text{mm}$ ,  $\lambda_z = 5\text{mm}$

Noticeable increase of the field amplitude and a value of absorbed energy in extreme vibrators does not have any problem, since a level of fields and currents in them can be easily decreased to required value by simple change of length / or width of these strips, location of a microwave absorbing material near them (for example making of face walls or side technological “cheeks” of airfoil model applied in aerodynamic experiments), etc. In any case this question one and will solve at finishing of a real model.

Practical and rather essential disadvantage of the considered solution means of the EM fields and currents uniformity problem in the strip multivibrator system in conditions of the experiment consists in necessity of considerable increase of MW generator’s out put energy – approximately by 20-25 times.

### 3.3.2. System of EM linear Low-Q vibrators

#### 3.3.2.1 Vibrator array based on low Q-factor resistive elements: Experimental investigations and determining of a range of EM radiation parameters

Thus, application of high quality elements (i.e. with some ohmic resistance) is undesirable from the point of view of uniform field realizing on a surface of the model with a system of MW-heated vibrators. At the same time there are no metals, steels and alloys, with required conductivity minimum by two – three orders of magnitude smaller then those of NiCr and similar alloys ( $\sigma \sim 10^6$  S/m). Also needed semi-conductor makes of necessary sizes are difficultly available and non-technological at processing in laboratory conditions. Besides their conductivity is usually sharply dependent on temperature, this is also a negative factor. Magnetic materials also possess similar disadvantage (Curie point).

An alternative way of the problem solving is application of low Q-factor elements made of composite materials. They can be divided in two classes from electrodynamic point of view:

- Materials with volumetric concentration of a conducting phase over a percolation threshold (usually in a range 0.30-0.45), i.e. having through conductivity. “Vibrators” manufactured of this material in some sense are low Q-factor analogues of those considered in the previous section. But their interaction with EM field is qualitatively different from the electrodynamic point of view: if the metallic strip vibrator may be considered as infinitely thin layer of a conductor with given width and length (and in calculation of the system to be limited to induced surface currents), vice-versa the radiation absorption in the composite material has a volumetric character.

- The second type is composite materials or, otherworld, microwave absorbing materials, which ohmic conductivity on a constant current is close to a conductivity of dielectrics. A concentration of an absorbing phase in them can be also sufficiently high, but “bridges” of the through conductivity are absent. Elements of a system made of such a material usually do not expose distinct resonant features.

A search of fitting materials of second type will be continued. But here we will consider features and prospects of the first type materials.

Developed system of MW-heated electromagnetic vibrators on a basis of resistors TVO type, results of its numerical modeling, technology of adjustment and design features are in details in the quarter reports for 4-6 stages of the Project.

#### 3.3.2.2 Calculations of thermal mode of MW-heated elements in an aerodynamic experiment

Thus we suppose to use a periodic system of heating elements in the aerodynamic experiment; they represent linear resonant vibrators loaded by the ohmic resistance. A part of the resistor surface (upper in Fig.3.9) is assembled flash with the model surface and is streamlined by the airflow. High temperature of the resistance surface locally heats the airflow moving along it.

Calculations of resistive element thermal mode in the realistic design with accounting for all the factors are the complicated problem. However, one can suppose that a heat removal due to cooling by the airflow and the contact with the model will not significantly influence during the time of MW field impact. Besides, the calculations have been carried out in two dimensional approaches, because a length of the element is much greater than its transversal sizes. Coordinate axes and resistor sizes arbitrary notations in the central cross section are represented in Fig.3.9. By grey color we show the Ohm component – a volumetric heat source, by yellow – a ceramic isolator, by blue – a cover of the model.

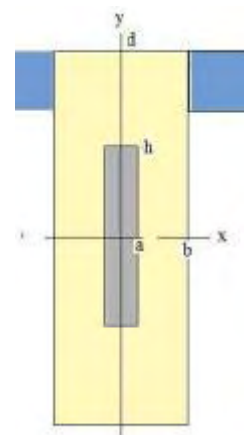


Fig.3.9. TVO element cross section

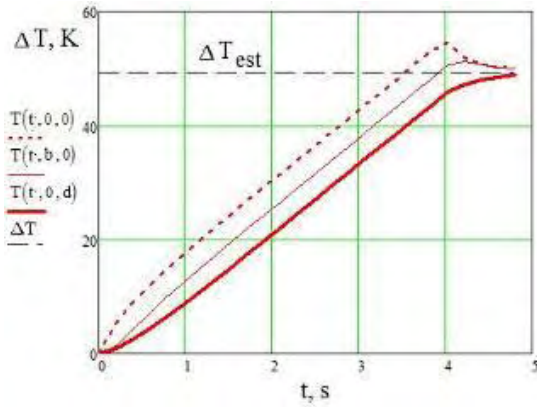


Fig.3.10. Temporary dependences of temperature increase in the resistor

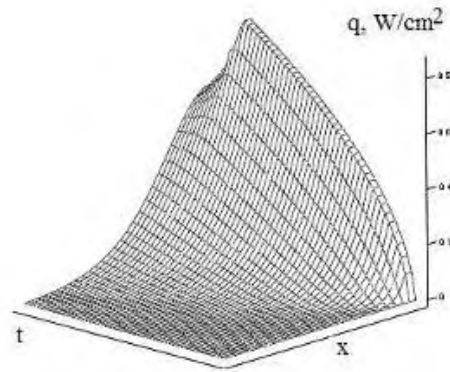


Fig.3.11. Spatial and temporary thermal energy flux density distribution in the plastic layer

One can see that the resistor is heated practically uniformly with temperature increase  $\Delta T \sim 50^\circ\text{K}$  at released MW power  $\sim 3\text{ W}$ . The heated surface of the model touches the plastic layer of the model. The spatial and temporary thermal energy flux density distribution in the plastic layer in the end of MW pulse is represented at Fig.3.11 at heat conductivity coefficient  $\eta_s = 8.15 \cdot 10^{-4} \text{ W/cm} \cdot \text{K}$ .

Integral energy flux into the plastic layer from the resistor over the whole area of the contact with the plastic is equal to  $Q = 2 \cdot L \cdot g \cdot q(t, 0)$  and is  $0.3\text{ W}$ ; that is by ten times smaller than the whole heating power of the resistor. Thus the initial supposition about smallness of losses into the plastic cover is justified. The temperature on the surface of the model has time to spread smaller than for  $1\text{ mm}$  during the heating pulse of  $\tau \sim 4\text{ s}$ .

#### Estimation of air heating in the boundary layer over heated resistance

Air flight time over a surface of the resistor of a length  $L$  is

$$t_{pass} = \frac{L}{V_0} = 1.84 \cdot 10^{-3} \text{ s},$$

where  $V_0$  is the flow velocity. This is much smaller than the heating pulse duration, so the problem can be considered as the quasi-stationary with the given temperature of the surface (the heat sink to airflow can be considered as small). The incident flow we consider as the laminar; and the surface is ideal. At these suppositions a solution of the problem about a temperature distribution in the boundary layer in the moment of MW pulse finish in the end of the resistor is represented in Fig.2.24 and 3.12.

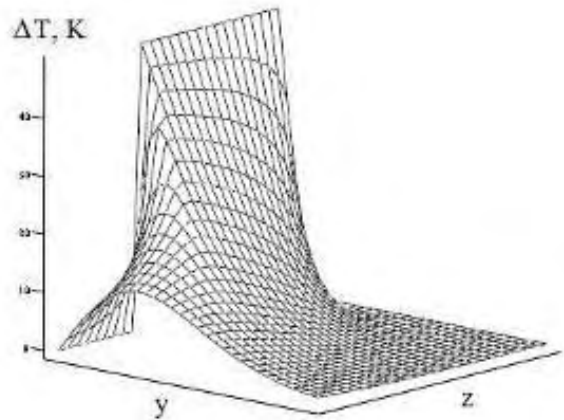


Fig.3.12. Spatial and temporary distribution of temperature in the boundary layer,  $t = \tau$

The solution of the problem on thermal energy flow density in the model boundary layer shows, that the integral of energy flow density over the surface of the resistor contacting to an air flow, that is air heating power by the resistor, is by 10 times less the power allocated in the resistor, and the heating efficiency of the airflow by the resistor is  $\sim 8\%$ .

In aerodynamic experiment the temperature of resistive elements surface was essentially higher by the end of MW pulse action than in the estimated calculation resulted here. However search of materials and working out of the new electrodynamic system of MW-heated elements with larger extent of a surface contacting to the boundary layer is expedient for continuing.

### 3.3.2.3 Design of airfoil model with resistive vibrator array for wind-tunnel experiments

The next joint task of this stage of the Project was a development and manufacturing of the model with resistive elements with following undertaking of experiments with it in IHM, Kiev. An appearance of the model, its upper part and the whole assembled model with 19 resistive vibrators with the resistance of 150 Ohm located on it is shown in Figs. 3.13 and 3.14. One can see an aluminum foil-reflector of EM radiation on the internal surface of the model.

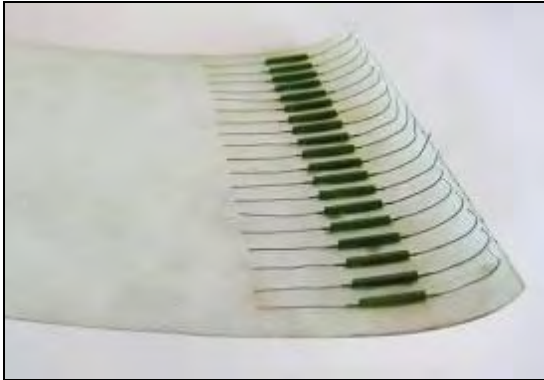


Fig.3.13. Upper part of the model. Internal appearance

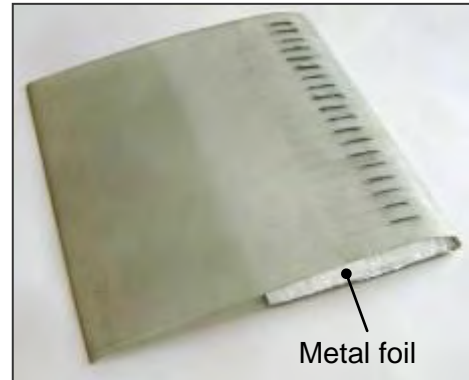


Fig.3.14. Assembled model

Temperature distributions in the set of resistors on the surface of the model before and after its adjustment are represented in Fig.3.15. The system adjustment can be carried out by two ways: bending resistor contact tips or cutting them. The second way provides to be more effective. Measurements have been carried out in the new chamber of the installation in the MRTI with a distance of 280mm between the side walls. The MW generator switching on time is  $\tau = 7$  s before the model adjustment at the given output power  $\sim 1000$ W.

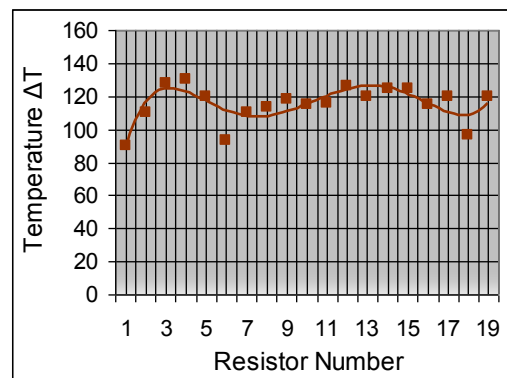


Fig.3.15. Temperature distributions in the set of 19 resistive elements after the adjustment

Experimental tests have completely confirmed conclusions of the theory and numerical experiment. On the basis of obtained data, technological and quite efficient (from the point of view of electrodynamics) multisystem of MW-heated elements based on industrial small-sized ceramic resistors has been developed. At the same time the developed system of MW-heated elements based on TVO-type ceramic resistors did not appear enough efficient at carrying out joint aerodynamic experiment in Kiev in august this year. The last numerical investigations executed by experts from IHM, Kiev, have indicated that for reliable manifestation of effect of the developed method of boundary layer control more extended heated up elements with smaller spatial step between them in spanwise direction are necessary.

### 3.3.2.4 Systems heated up in the field of MW radiations of vibrators on the basis of graphitic compound

The system of vibrators is executed on the basis of glutinous resistive compound by "Contaktol radio» on the basis of micro powders of graphite and various metals. Appearance of the top part of the model prepared for tests in IHM is shown on Fig. 3.16.

Vibrators are made on the following technology. On the top part of model parallel slots in length of 78 mm, width 0.5mm and depth of 1mm have been made. Distance between slots – 8 mm. These slots were filled specified compound (resistance of one vibrator nearby 5 kOhm). Then

all system became covered by a heat-resistant lacquer. According to the specification the maximum working temperature of a lacquer is 650<sup>0</sup>C.

On the bottom part of a wing the screen-reflector representing an aluminum foil in the thickness about 0.05mm from the inside is pasted. Thanks to it efficiency of absorption of MW energy by vibrators increases. The same technology has been applied at manufacturing of model with the heating elements located on its bottom surface. Form of model (top view) is presented on a photo in Fig.3.17. Joint experiments in IHM with the developed models have been performed.



Fig.3.16. Top part of the airfoil model with array of flush mounted MW-heated vibrators

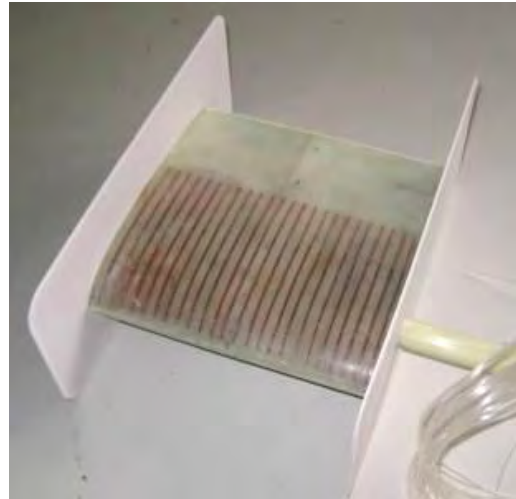


Fig.3.17. Ready to test airfoil model

### 3.3.2.5 Numerical simulation and optimization of the developed MW-heated multi-vibrator system based on thin graphite strips

The next MW-heated low-Q multi-element system based on thin “pencil” strips has been developed, tested in MRTI and its several samples were prepared to the planned wind-tunnel experiment in IHM. Because of very complicated character of such electrodynamic problem, unobvious pattern of resulting electromagnetic and temperature fields in such system the best approach to clear up the problem is the use of modern 3D simulation technologies, see annual reports on the Project for the 1st and 2d years.

Main parameters of the low-Q strip-like graphite vibrators used in described arrays of MW-heated elements are: Vibrator length  $2L=80\text{mm}$ , width  $2a=0.8\text{mm}$ , thickness  $2b\sim 10\mu\text{m}$ , resistance  $R=30\text{ Ohm}$  (conductivity  $\sigma=333\text{ S/m}$ ), distance to metal  $h=18\text{mm}$ , spanwise spacing  $\Delta=10.0, 7.5$  and  $5.0\text{mm}$  at number of strips  $N=19, 27$  and  $39$ , respectively. Distributions of density of power losses along the axis of a single vibrator at different values  $h$  are resulted in Fig.3.18

At  $h = \lambda/4 \approx 31\text{mm}$ , i.e. in the crest of a standing-wave,  $E$ -field magnitude and density of MW losses increase by two and four times correspondently. Similar coefficients in the intermediate case of  $h = 18\text{mm}$  (which corresponds to the real distance between upper and lower parts of the tested aerodynamic model) are equal 1.6 and 2.57 accordingly. All these experimental data are in good agreement with the well known law  $P \sim E^2$ .

Main results of numerical simulation being of practical interest are summarized below:

- full absence of any resonant phenomena and, thus, absence of the problem of multi-mode non-uniform excitation of electromagnetic and temperature fields in low-Q high-resistive vibrator systems, see Fig.3.19;
- EM field fully penetrates into thin-film ( $\sim 10$  microns in thick) resistive strips with low

conductivity that makes possible and sharply simplifies analytic calculations and estimations;

- there is not any influence of the vibrator width  $2a$ , spanwise spacing  $\Delta$  and number of elements  $N$  in system on the power release density and, thus, dynamics of forming of temperature fields on a model surface;
- the comparative analysis of numerical and experimental results indicates that all the remaining problems are of purely technological character and lie out of frames of basic research program of the Project.

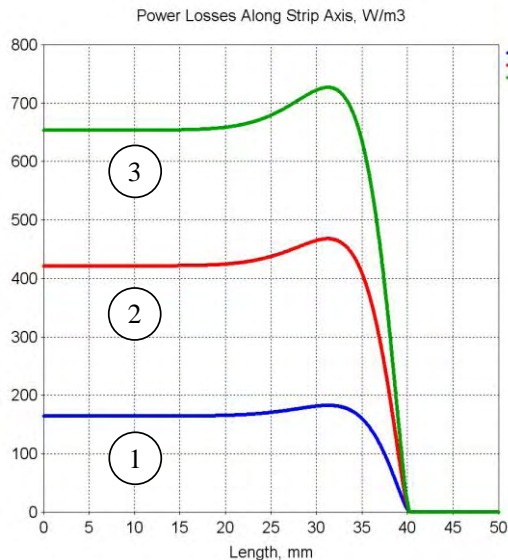


Fig.3.18. Distributions MW power losses along vibrator's half-axis ( $L = 40$  mm). 1 –  $h \gg \lambda$ , 2 –  $h = 18$  mm, and 3 –  $h = \lambda/4 \approx 31$  mm

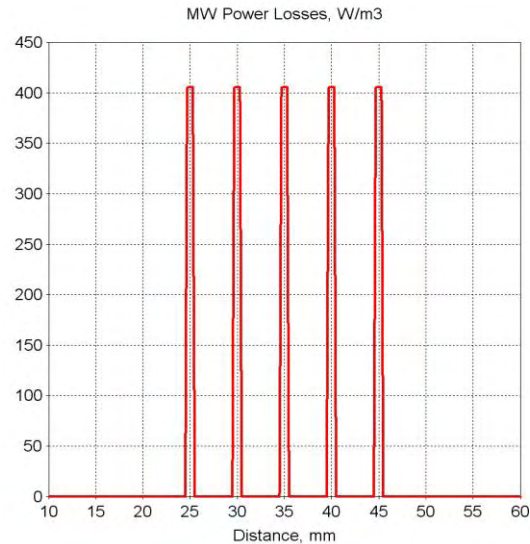


Fig.3.19. Uniform distributions of MW power losses in system of 5 graphite strips in span-wise direction at spacing  $\Delta = 5$  mm and  $h = 18$  mm

### ***Q-low linear vibrators***

The reasons on which we have been compelled to refuse application energetically more effective Q-high vibrators are in detail stated in the previous reports under the project (10<sup>th</sup> Quarterly Progress Report). At the same time it is necessary to recognize the received results quite satisfactory as the main electrodynamic problem is solved: *homogeneous* heating of a multisystem of vibrators to the set temperature from *remote low-power* source of MW radiation was provided.

Described in previous reports results of scrupulous numerical simulation and experimental tests have indicate that final choice of low-Q system of MW-heated strip-like graphite non-resonant vibrators is right choice. Several variants of airfoil models with different systems of such vibrators were manufactured, tested in Moscow and prepared to joint aerodynamic experiment in Kiev, see Fig.3.20.



Fig.2.20. Airfoil model with MW-absorbing strip graphite elements on its surface (one can see system of thin parallel dark lines)

### 3.4. Experimental problems and their solutions. Summary of Chapter III.

#### *Microwave-heated system embedded in the aerodynamic model*

The developed system of localized surface heating using MW radiation was thoroughly investigated. The details are given in relevant Quarterly and Annual project reports; the variety of engineering solutions and a scope of the work can be summarized as follows.

- ✧ High-quality-factor systems made of thin conducting strips and metallic wires.
- ✧ Bulk (3D) resistive elements with different values of Q-factor based on industrial ceramic high-frequency resistors.
- ✧ Various elements based on different industrial conducting compounds.
- ✧ Hybrid versions of high-Q and low-Q vibrators in a form of thin wires covered with conducting compounds.
- ✧ Systems based on volumetric microwave-absorbing composite materials.
- ✧ Structures in a form of thin graphite belts and rods, etc.

In such systems, no excitation of multimode structures of an electromagnetic field is observed at all that provides most uniform microwave heating of separate elements. Any spanwise regularity  $\lambda_z$  can be realized in this system, it is least labourious and rather cheap in manufacturing. It is especially true for the system of “pencil” graphite elements (see 11 Qrt Report) which showed itself operationally easy in laboratory conditions to prove the approach feasibility.

However despite of certain advantages, all the listed above engineering solutions had to be rejected either at a stage of numerical modeling and initial testing in MRTI or at a later stage of wind-tunnel experiments after initiators were mounted in aerodynamic models in IHM. It deals with the system inability to generate and maintain the spanwise-regular temperature boundary condition required for flow control.

In this connection, further research efforts were focused on another MW-based control of temperature variation in the vicinity of the model surface. This is the method of spanwise arrays of MW plasma discharges that was tested earlier and showed a good potential in terms of generation of necessary temperature gradients near the surface in the flow. Thus the second stage of the electrodynamic part of the project aims at optimization of the MW plasma generation system to provide active and remote flow control.

#### References to Chapter 3

3.1 Esakov I., Grachev L., Khodataev K., Ravaev A., Yurchenko N., Vinogradsky P., Zhdanov A. Initiated Surface Microwave Discharge as an Efficient Active Boundary-Layer Control Method. AIAA Paper 2009-0889.

## IV. DEVELOPMENT OF MW-BASED FLOW CONTROL SYSTEMS (MRTI):

### W-initiated arrays of plasma discharges

#### 4.1 Various designs of electromagnetic vibrators-initiators of MW discharges

In order to understand why we needed to investigate and develop for a long time a lot of new various designs and systems of initiators of microwave discharges, it is necessary to specify two electrodynamic problems which solution is not only of applied but also of basic significance.

1. The first problem is creation of only one microwave discharge on a surface of object in low electric field of a remote source of microwave energy of the limited power. In the considered project in conditions of aerodynamic experiment, microwave discharges had to be ignited in the MW electric field with magnitude no more than 100 V/cm whereas the threshold field magnitude

of air breakdown at atmospheric pressure equals 30'000 V/cm. In other words, the factor of multiplication of  $E$ -field on the tip or in the gap of an electromagnetic vibrator-initiator should not be less than three hundred:  $\eta > 300$ .

2. Secondly, at creation of a large number of close located microwave discharges because of mutual influence of electromagnetic vibrators, multiplication factor of a single initiator should be even higher:  $\eta > 1000$ . But the main problem caused by strong electromagnetic interaction of vibrators in system consists in excitation in real system (with limited geometrical sizes) of so-called multi-mode structures induced EM fields. This results in formation of strongly non-uniform spatial structure of the induced fields and, accordingly, complexity of generation of regular *homogeneous* system of plasma formations.

It is obvious that achievement of so high values of strengthening factor is possible only by means of resonator-type designs, namely – high-Q resonant electromagnetic vibrators. During works on projects CRDF #UKE2-1508-KV-05 and UKE2-1518-KV-07 various designs of EM vibrators have been offered and investigated, Ref.[4.1]. The most interesting of them are presented as schematic examples in Fig.4.1.

To reveal typical lacks and advantages of different types of initiators, new results of their 3D numerical simulation in identical (as it is possible) conditions are presented below. All initiators are “manufactured” of a perfect electric conductor (PEC) of a wire 1mm in diameter. Their ends are rounded, and all gaps, if they exist, are equal 1mm too. Besides, any dielectric materials in all considered in this section designs are absent (influence of real materials on properties of vibrators will be considered below).

First two types of electromagnetic vibrators, “a” and “b” in Fig.3.1, have been investigated in detail at execution of the previous project #UKE2-1508-KV-05. At that time it seemed that the best solution of a problem in the form of system of ring or loop-shaped “magnetic” vibrators with a gap is found; the first important results in aerodynamic experiment have been obtained with model supplied just with these initiators. However it was soon found out that it is not enough, and both above mentioned electrodynamic problems are still present in full measure.

Next two types of EM vibrators have been offered, investigated and applied as a part of new cylindrical model already during works on the present project in 2011. Without dwelling on physical backgrounds and ideas put in new designs of initiators of MW discharges. Let us carry

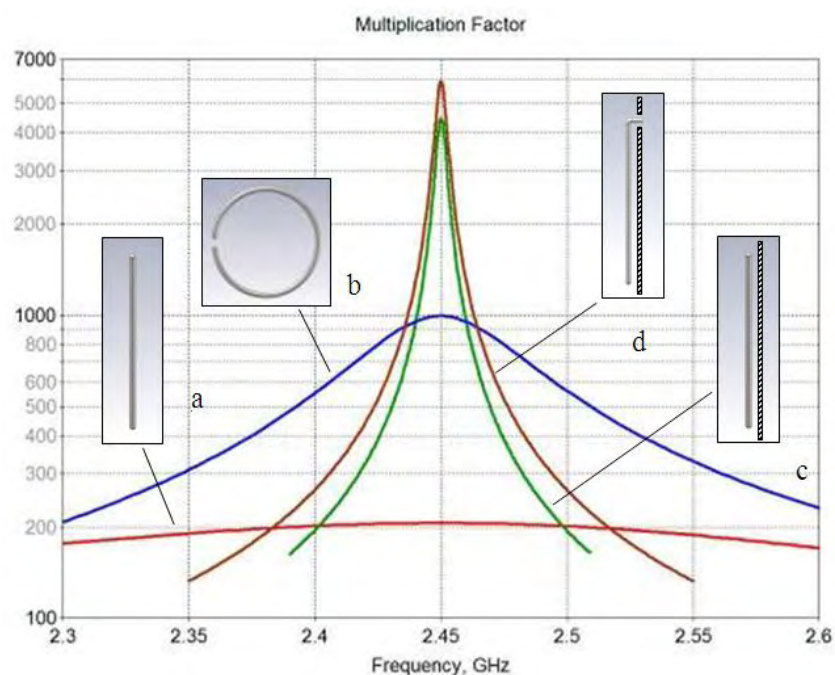


Fig.4.1. Frequency dependences of gain factors of different electromagnetic vibratos all adjusted to the operating frequency 2.45 GHz at fixed resonant lengths.

out the comparative analysis of main properties of the vibrators depicted in Fig.4.1.

From comparison of graphs in Fig.4.1 it follows that the maximum multiplication factor of the “simple” linear vibrator 1mm in diameter reaches values  $\eta \approx 200$  at the quality-factor of its equivalent resonant circuit  $Q \approx 2.7$ . Multiplication factor of the ring magnetic vibrator is higher:  $\eta \approx 1000$  at  $Q \approx 21$ . At last gain factors of new vibrators (“c” and “d”) are close and already reach values  $\eta \approx 5000 \dots 7000$  at their quality factor  $Q \approx 310-320$ . Thus, any of the considered vibrators is suitable for initiation of a *single* microwave discharge in external MW field  $E = 100$  V/cm, including the simple linear vibrator if one make it of thinner wire and/or point its working end.

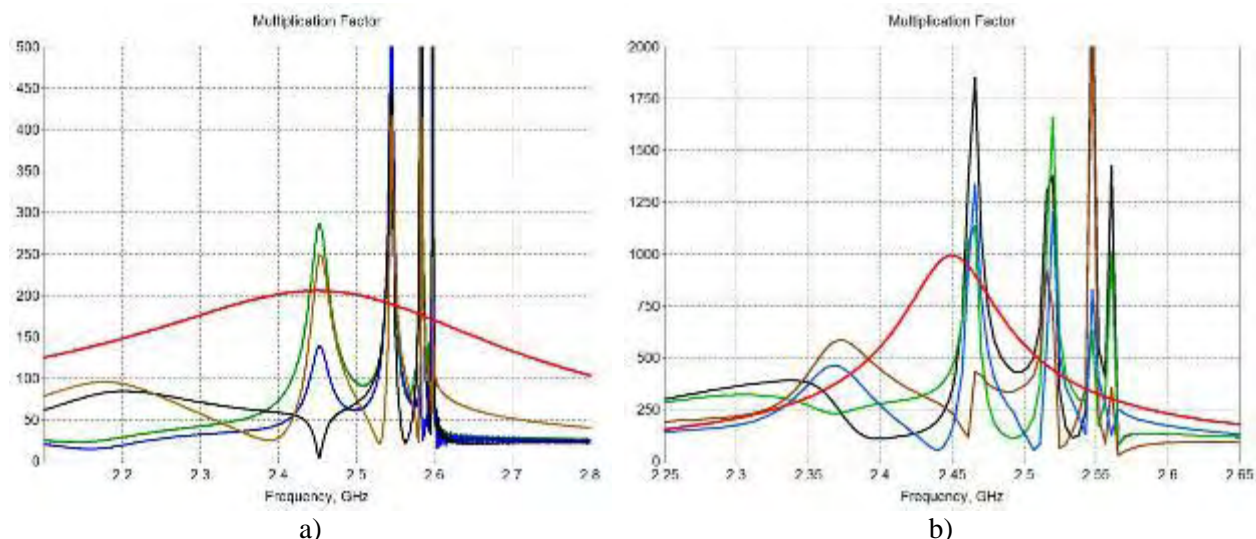


Fig.4.2. Frequency dependences of several elements in multi-vibrator system as compared with graphs of single vibrators (red curves): a) linear EM vibrator, b) ring magnetic vibrator

The simple linear vibrator in system cannot initiate the microwave discharge in an external field of incident electromagnetic wave about 100 V/cm. Its multiplication factor is  $\eta \approx 40$ . Corresponding coefficient of the loop-shaped vibrator  $\eta > 200$ , and if one point its ends in the discharged gap these vibrators could be applied in aerodynamic experiments. Final joint experiments at the end of the previous project confirmed this very well.

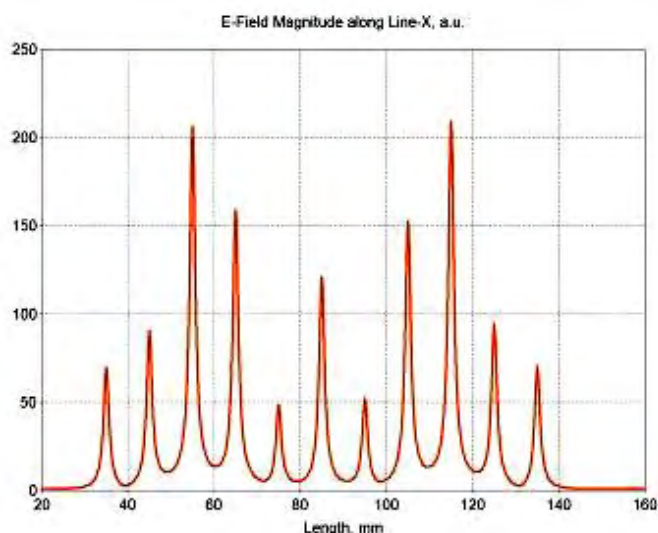


Fig. 4.3. Distribution of MW-field magnitude in the gaps of various ring vibrators in system of 11 elements

excitation of a multi-mode structure of electromagnetic fields in system is very difficult for intuitive understanding and forecasting.

The frequency dependences of multiplication factors of the several arbitrarily chosen initiators in the system consisting of 11 identical elements and located with spacing step of 10mm for linear and ring vibrators are resulted in Fig. 4.2.

One can see how dramatically varies the picture of excitation of EM vibrators in real system) and how much difficult to adjust such system *in vitro*. Actually there no places in these graphs where the amplitude of an induced microwave field would exceed a threshold of air breakdown simultaneously for all elements in system. Besides, the problem of

More visually this effect is shown in Fig.4.3 where external appearance of 3D computational model and corresponding distribution of induced  $E$ -field in such system at working frequency of 2.45 GHz are presented. Heights of peaks of MW field multiplication in the gaps of different elements differ from each other very much.

It is easy to see that in contrast to graphs depicted in Fig.4.2 on the graphs in Fig.4.4, a at the left there is comparatively wide frequency area where gain factors of all elements are sufficient for initiation of MW discharges. In picture on the right this area is shown in the increased scale. It is essentially important and absolutely unequivocal conclusion: it is necessary to adjust a multisystem of vibrators not on very sharp resonant peaks with the highest magnitude (it is practically impossible) and on the common for all elements flat enough frequency region being aside of initial adjustment of the single elements.

## 4.2 New-type EM vibrators located close to a metal screen-reflector

Previous investigations of various MW-heated resistive electromagnetic vibrators showed certain advantages of the high-Q systems made of linear conducting strips or pieces of thin metallic wires mounted along the flow near to the metal screen-reflector (see 6<sup>th</sup> Quarter report on the Project). Sure, due to high multiplication factors of  $E$ -field, such vibrators can be also used as effective initiators of plasma discharges. Physical features of such vibrators (initiators) and their unique properties are considered in detail in Ref. [4.2].

The most significant basic results are as follows. First, properties of the linear EM vibrator which is placed in the “unbounded space” or in front of a metal screen in crest of a standing wave (at distance  $h=\lambda/4\approx 31\text{mm}$  from its surface) radically differ from the properties of the same vibrator which is in immediate proximity to the screen ( $h\ll\lambda/4$ ). According to a recently prevailing opinion, such a vibrator would not work at all. But this erroneous opinion was completely refuted in referenced above works.

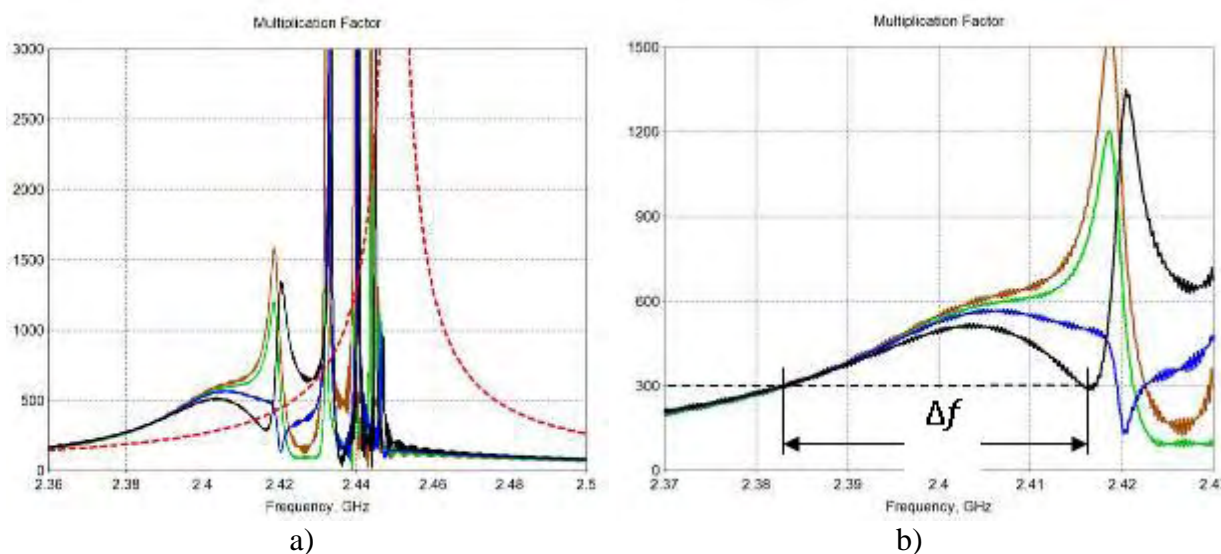


Fig.4.4. Frequency dependences of several elements in the “poker-type” multi-vibrator system as compared with graph of such single vibrator (red dashed): a) general graphs, b) adjustment region

Secondly, new-type vibrators allow creating plasma discharges in essentially lower microwave fields, i.e. using low-power sources of MW radiation. Third, solution of the well-known above stated problem of prevention of excitation in multi-vibrator system of a multimode pattern of induced EM fields, i.e. the problem of formation of non-uniform resulting fields on a model surface, is considerably facilitated.

At the same time, the earlier investigations had an exclusively qualitative, fundamental character. In particular, it has been proven that in absence of any dielectric substrate (if

permittivity  $\varepsilon = 1$ ) or in case of “ideal” dielectric (if  $\varepsilon \neq 1$  but loss tangent  $\text{tg}\delta=0$ ) the factor of amplification  $\eta$  of the  $E$ -field on a tip of infinitely thin resonant piece of a conductor with distance  $h$  decrease tends to infinity. Real materials have dielectric permeability  $\varepsilon > 1$  and MW losses ( $\text{tg}\delta \neq 0$ ). Therefore determining the influence of dielectric properties (as a material of aerodynamic model) on parameters of EM vibrators and induced fields is a paramount task.

The second problem to be solved is an influence of radius of curvature of a model surface on properties of considered initiators. It is important for aerodynamic experiments with cylinder models having a large surface curvature. Finally, developing an optimum design of the MW

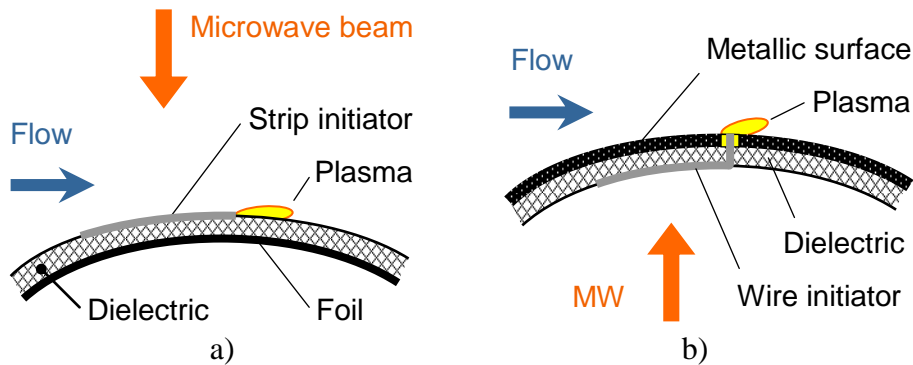


Fig.4.5. Two designs of new-type electromagnetic vibrators.

initiator system for aerodynamic purposes, its practicality should be taken into account, i.e. fabrication technology in laboratory conditions, repeatability and reliability of experimental results.

According to the mentioned above, research efforts in project was focused on

the two types of design of EM vibrators to be mounted on cylindrical airfoil model (Fig.4.5).

The first type of the initiator (Fig.4.5,a) being analogue of the wire vibrator in Fig.4.1,c was studied earlier and is the *basic design* in the framework of the project Extension in 2011. Investigation of characteristics of these vibrators with a focus on properties of real dielectric materials which can be used for fabrication of test models were carried out. Another modification of this vibrator is shown in Fig.4.5b (and also in Fig.4.1d). Interest to it is caused by a number of prospective advantages. First, such design promises to be more technological and easy in adjustment as dielectric in this case plays only a role of the initiator holder and consequently it can consist of separate small moved parts. Secondly, exact trimming and polishing of all vibrators flush with a model surface is not required. Thirdly, in the given design it is possible to apply any materials including materials with low dielectric losses and, thereby, to vary quality factor  $Q$  and coefficient of multiplication  $\eta$  of the MW electric field induced at the ends of such vibrators.

There is also one more advantage of the considered design, namely: modeling of conditions of a noncontact (what is very important) supply of electromagnetic energy to initiator system *from inside* of aerodynamic model. However, development of a compact and effective MW irradiator which provides uniform “illuminating” of all system of initiators on the area at least about  $70 \times 200 \text{ mm}^2$  and which is possible to be inserted inside small model is a very difficult problem and it can be solved only within the frames of the separate big project. Here it is simply supposed that the bottom part of model (it is not shown in Fig.4.5b) is made of a radiotransparent dielectric.

#### 4.2.1. Results of 3D numerical simulation

Results of numerical simulation have confirmed the assumption that properties of a dielectric substrate in designs of considered here new-type high-Q electromagnetic vibrators play very important role.

Considering that fact that forthcoming experiments are supposed to be carry out with a cylindrical aerodynamic profile with rather small radius of curvature ( $2R = 90 \dots 120 \text{ mm}$ ), the degree of shortening of geometrical length of the linear half-wave vibrator at use of a real material (foil-laminated textolite with permittivity  $\varepsilon = 5.5$  and microwave loss tangent  $\text{tg}\delta \approx 0.04$ ) is of great interest.

In the numerical model, the EM vibrator represents a rectilinear piece of wire with a varied length  $2L$  and the fixed diameter  $2a = 0.35$  mm, “made” of Ni-Cr alloy with conductivity  $\sigma = 1 \cdot 10^6$  S/m. The vibrator is completely immersed into the dielectric substrate; its axis is at a distance  $h$  from the substrate foil. The MW electric probe is located at one of the vibrator ends.

The resonant curve of the vibrator at  $h = 1.9$  mm is shown in Fig.4.6. One can see that in comparison with similar vibrators without dielectric, Ref.[4.2], the quality factor  $Q$  and coefficient of amplification  $\eta$  of MW field at very small distances  $h$  are relatively small; and factor  $\eta \approx 200$  is obviously insufficient for reliable initiation of the multiple MW discharges in conditions of experiments in MRTI and IHM.

The most important result is that contortion of the linear vibrator on the cylinder surface of radius  $R = 45$  mm is comparatively small. Therefore there is no doubt that considered new-type vibrators will fully keep their unique properties being mounted on cylindrical model with  $2R = 90$  mm in diameter. Only small correction of dimensions of a final design will be required.

The curves have the expressed non-monotonic character, and their maxima do not coincide. The curves presented in Fig.4.7 are even more indicative. Here influence of MW losses in real dielectric on an efficiency of work of such initiator is clearly visible: in absence of losses but at terminal conductivity of a vibrator material (in our case of Ni-Cr alloy) the amplification factor maximum is displaced toward the reflector. Herewith quality factor of an equivalent contour and factor  $\eta$  on the ends of the initiator significantly increase. Let us also remind that in full absence of losses in system (loss tangent is equal zero and conductivity  $\sigma = \infty$ ) the function  $\eta(h)$  has monotonic and expressed exponential character, and at  $h \rightarrow 0$ ,  $\eta \rightarrow \infty$ , Ref.[4.2].

In need of application of glass-fiber laminate (textolite) with comparatively high MW losses the optimum thickness of a dielectric substrate increases to 7-8 mm. With this the amplification factor of a MW field can be insufficient for reliable ignition of a multi-system of close-located discharges. Mutual influence of EM vibrators at the bigger distances  $h$  also increases. Last factor negatively affects on uniformity of distribution of induced electromagnetic and resulting temperature fields on a model surface.

#### 4.2.2. Results of experimental investigations

For qualitative check of presented above results and conclusions a series of experiments has been executed. Key feature of described below experiments is that for determining of resonant characteristics of vibrators  $\eta = \eta(2L)$  the original techniques described in the reports on the Project EOARD CRDF UKE2-1508-KV-05 was applied. The point is that the problem of measuring of a MW field in a vicinity of initiator of the MW discharge is very complicated task, especially considering the limited power dynamic range of available MW generators.

The technique essence is that in the course of experiment instead of direct measurements of a

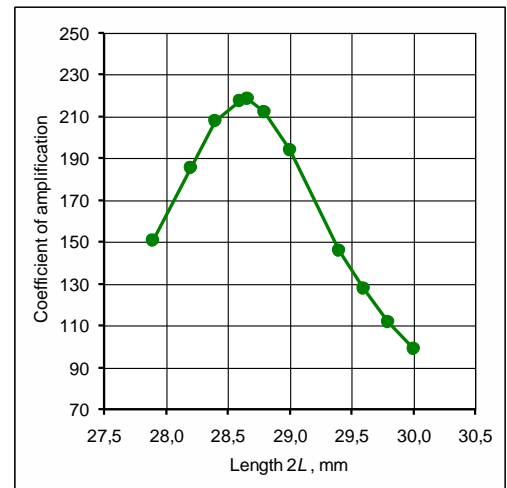


Fig.4.6. Resonant curve of the EM vibrator on foil laminated textolite substrate at  $h = 1.9$  mm

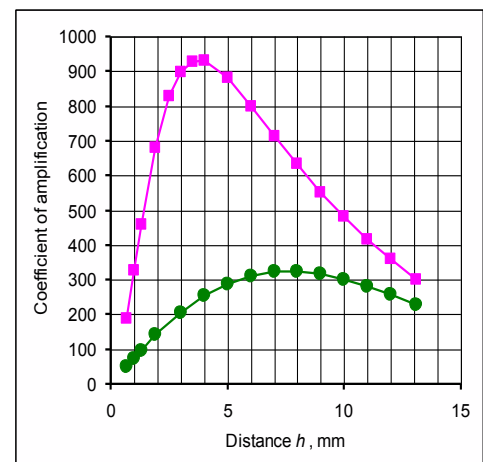


Fig.4.7. Dependences of amplification factor on distance  $h$  for dielectric substrates with MW losses (green line)

MW field magnitude one measures pressure of breakdown of gas at the initiator tip. Unlike level of power of the MW generator, it is much easier to vary in wide limits the pressure in the chamber. And there is the well-known direct dependence between pressure of breakdown and amplitude of electric field. In more details about this technique it was said in mentioned reports on the theme UKE2-1508

The base model of the vibrator which is flat analogue of the version in Fig.4.5a was tested in the experiments.

Results of measurements of resonant characteristics of initiators are presented in Fig.4.8. Hereinafter power of the MW generator was 1.6kW; the mode of operation – quasicontinuous with a pulse duration of 0.5s.

The average resonant geometrical length of the vibrator obtained in experiments, at the same length of wave of the MW generator  $\lambda=122.4\text{mm}$ , was  $2L_0\approx 37\text{mm}$  and differs from that received as a result of numerical simulation ( $2L_0\approx 28.7\text{mm}$ ). It is due to the difference of the specified above form and the geometrical sizes of the tested vibrator and, obviously, smaller dielectric permeability of a real material (textolite). Estimations carried out on the basis of comparison of the received results gives value of dielectric permittivity of the used in experiment material  $\epsilon\approx 3.3\text{-}4.0$ .

However in this case all these differences are not essential. The general laws of behavior of such class of initiators of MW discharges on the real material possessing microwave dielectric losses are indeed important. Experimental and numerical results are in a good agreement:

1. The resonant length of the linear electromagnetic vibrator weakly depends on a thickness of the substrate  $h$  and decreases with  $h$  increasing;
2. Growth of  $h$  within a certain range results in widening of the resonant curve, i.e. in increased coefficients of amplification of E-field  $\eta(h)$  at the vibrator ends. In other words, the optimum thickness the foil-laminated dielectric substrate at the given wavelength of MW radiation is about a few millimeters rather than zero.

As one would expect, incomplete filling of space with dielectric material in the considered design corresponds to smaller values of so-called effective permeability.

$$\epsilon^* \approx \epsilon_s \frac{h_s + h_{\text{var}}}{h_s + h_{\text{var}} \cdot \epsilon_s} < \epsilon_s,$$

where  $\epsilon_s$  is permittivity of dielectric substrate. This results in increase of resonant geometrical length of initiators of MW discharges. Such solution allows not only to reduce weight of a substrate (and of the model shell), but also to carry out adjustment of the multiinitiator system changing parameter  $h_{\text{var}}$ , i.e. simply moving the screen-reflector inside model.

### 4.3. New “poker-type” efficient initiator of MW discharges

Three models with 4 initiators mounted on textolite of different thickness  $h$  have been prepared, namely:  $h=1\text{mm}$ ,  $2\text{mm}$ , and  $3\text{mm}$ . Diameter of apertures in the metal cover of model equaled  $4\text{mm}$ . In order to fasten initiators in the place where their ends leave on an external surface of model, special rapid-hardening ceramics was applied. Other ends of vibrators were fastened with the foam holder. As earlier, the developed technique of measuring of breakdown air pressure  $p_{\text{br}}$  was applied to determine resonant characteristics of vibrators. Obtained dependences  $p_{\text{br}}(2L)$  presented in Fig.4.9 allow estimating with high accuracy main characteristics of EM vibrators, including their optimum distance from metal  $h$  and resonant length  $2L$ . And from the graphs presented in Fig.4.9 one can conclude that the optimum thickness of the textolite holder is about  $h=2\text{mm}$ .

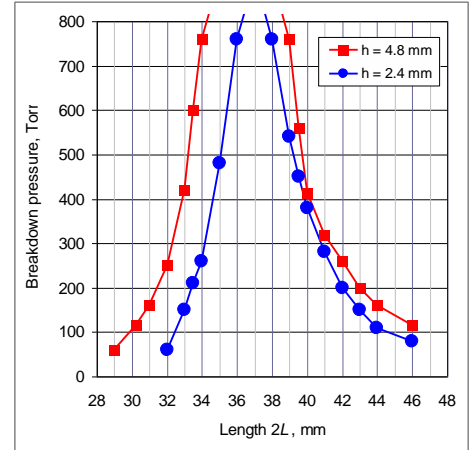


Fig.4.8. Breakdown pressure vs. vibrator length at different thickness of dielectric substrate  $h$

Then the model consisting already of 10 vibrators has been simulated and manufactured. As the material of model in the area of MW discharges is heated up, first, the integral holder made of ceramics 2mm in the thickness was used for fastening of initiators. In the given model distance between vibrators was of 10mm, and diameter of a wire – 1mm. Appearance of the model and system of generated MW discharges on its bottom (opposite to MW irradiating antenna) surface are shown in Fig.4.10. The ceramic material has demonstrated good thermal stability but in aerodynamic model where initiators should be mounted on a curvilinear surface (cylinder cover) its application is inconvenient. Therefore

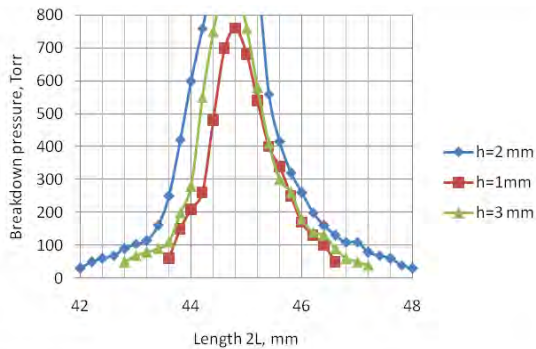


Fig.4.9. Dependence of breakdown pressure on vibrator length at various thickness of substrate



Fig.4.10. External appearance of the vibrator design and system of generated MW discharges

in all the following experiments textolite and rapid-hardening ceramics were used.

Experiments have shown that during work wire initiators heat up, and after some time of work the polyfoam holder melts, see Fig.2.62. Therefore further the holder of initiators was made of heat-resistant material TZMK-10. This material represents amorphous quartz fibers and keeps working capacity up to temperatures 1000°C and above. It is important that its dielectric permeability is close to unity, i.e. it practically does not affect on characteristics of EM vibrators. Density of this material is 140-150 kg/m³.

#### 4.3.1 Numerical simulation of the problem of MW-discharge location

New investigations directed on the further perfection of system of initiators generating microwave discharges on a surface of aerodynamic model have been carried out.

The point is that already at execution of the first tests of new initiators possibility of initiation of MW discharges on both ends of EM vibrators, that is not only in the proper point on a model surface but also inside the model cover became one of the unexpected problems. Numerical calculations confirm and explained this possibility well. The field magnitude at the internal (bottom in picture) end of the vibrator is fairly high and can even exceed that at its working end (in the hole of a metallic cover).

Different approaches to solution of this problem have been studied. One of possible way consists in placement of a small asymmetrical metal ball on the internal end of the vibrator. The result of 3D numerical simulation of an electromagnetic field induced by such vibrator is presented in Fig.4.11. Unfortunately, application of this solution on the model is failed because such ball should be small, less than 1mm in diameter, and simultaneously very smooth with low surface roughness. In laboratory conditions it was not executable task.

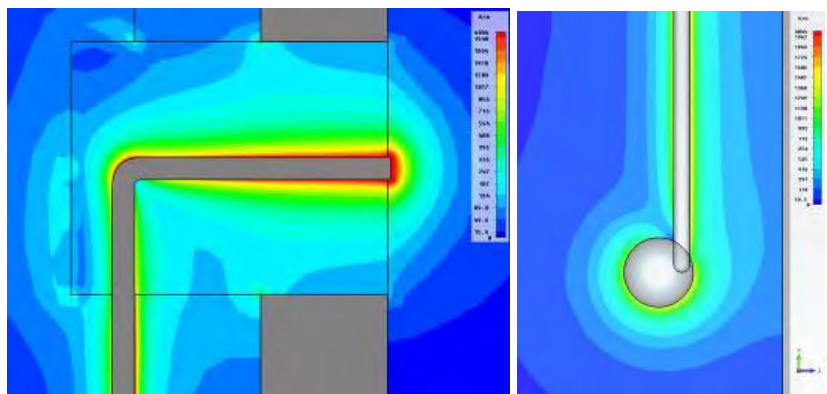


Fig.4.11. MW field patterns around vibrator tips, one been ended with a small metallic ball

### 4.3.2 Complete aerodynamic model as an assembly

During preparation for final experiment two aerodynamic models with 18 initiators have been made. Model with 18 initiators have been used at carrying out of joint aerodynamic experiment. During tests some part of initiators has burnt out. Completely, before burning out all system of initiators has worked about 40s.

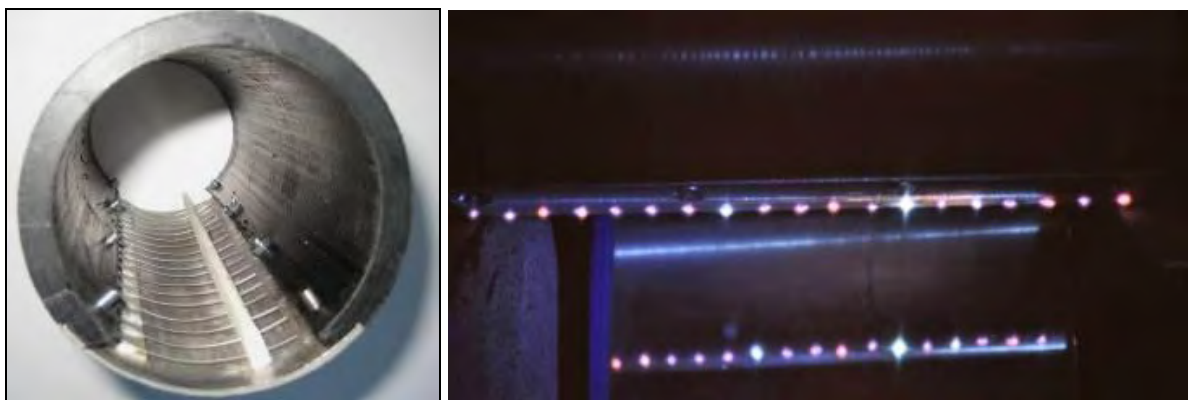


Fig.4.12. External views of aerodynamic model and views of model located in working chamber with initiated MW discharges

External view of cylindrical model and systems of initiated microwave discharges on the model surface at execution of tests in the wind-tunnel in IHM, Kiev, is presented in Fig.4.12.

Carried out tests have highlighted strong influence of some constructive parts of the model, working chamber and used materials on electromagnetic properties of vibrators. New efforts on perfection of system of initiators on model as an assembly should be continued. First of all one has to pay paramount attention to the joint, strictly co-ordinated approach as to a choice of a model design and materials of which it is made.

Besides, during future project taking into account strictly limited power of the used MW generator based on domestic magnetron and also remote external supply of MW energy one should change scheme of experiment and focus further efforts on development of new feeding electrodynamic system with more efficient MW energy supply from inside of airfoil model.

### 4.4. Ring MW plasma actuators

The newly designed linear initiators described above in paragraphs #2.4.3 are energetically more effective and provide the noncontact delivery of electromagnetic energy to the initiator system from inside of an aerodynamic model (the airfoil). However under conditions of the wind-tunnel measurements in IHM, the system appeared to lose its efficiency because of the fixed location of the MW radiating system on the top of the wind-tunnel test section. In a number of tests the model had to be turned upside down in the test section to face the horn antenna if initiators were



Fig.4.13. New aerodynamic models with ring-type plasma initiators

mounted on an opposite side of the model that changed the electromagnetic situation. Similarly, it was changed for the plasma array when models were tested at varied angles of attack. It was this mismatch of aerodynamic and electrodynamic requirements and peculiarities that resulted in a search of a mutually acceptable solution of the formulated flow-control problem. Therefore the earlier developed and tested idea of ring-type initiators (Project #UKE2-1508-KV-05) was reconsidered, the inserts with ring-type initiators were fabricated for airfoil models which were jointly tested in the Aerodynamic Facility for Interdisciplinary Research, IHM (see Fig.4.13). Only such a flexible multi-faceted coordinated research could result in successful implementation of the multidisciplinary project.

## Summary

1. The «microwave-plasma» approach to generation of a system of regular pointwise energy release around the aerodynamic models is more efficient compared to the localized “microwave-heating”. In addition, it affects the flow inertialessly due to the direct generation of thermal sources in fluid.
2. Various types of MW plasma actuators are investigated. Properties of (1) linear and (2) ring-type EM vibrators are studied in detail, the first having been placed near a metallic-reflector (metalized airfoil surface). An impact of dielectric permittivity and microwave losses of real model materials on characteristics and applicability of MW actuators is investigated. As an outcome, recommendations are developed on the design and choice of materials.
3. Thorough analysis of high-Q linear  $\Gamma$ -shaped electromagnetic vibrators showed their high values of multiplication factor of EM fields. It implies a possibility of low energy consumption for flow control due to very small levels of an initiating electromagnetic field propagating from a remote low-power MW radiation source.
4. The developed  $\Gamma$ -shaped vibrators were applied in test models with high curvature including circular cylinder models as well as with a metal surface shell; for the first time it enabled MW energy supply to the electromagnetic vibrator system from the interior of aerodynamic models. This type of plasma actuators needs further development to follow aerodynamic requirements of wind-tunnel experiments.
5. Ring-type plasma actuators offered in the Project #UKE2-1508-KV-05 proved to better fit aerodynamic experiments. Therefore they were used in airfoil models for the concluding stage of joint flow-control experiments.
6. The developed insight into matched aero- and electrodynamic problems guarantees a higher efficiency and scientific level of prospective multidisciplinary researches aimed at improvement of aerodynamic performance in the framework of the developed flow-control concept.

## References to Chapter 4

- 4.1. Kirill Khodataev. Various types of initiators for attached undercritical MW discharge ignition. AIAA Paper 2007-0431
- 4.2. A. A. Ravaev, I. I. Esakov, L. P. Grachev, P. B. Lavrov: Main features and application of electromagnetic vibrators located near to a metal wall. AIAA Paper 2011-1078.

## Chapter V. AERODYNAMIC DESIGN AND FABRICATION OF MW-CONTROLLED MODELS

Two aerodynamic shapes were tested with various realizations of the developed flow control strategy. They are the "R800" airfoil and a circular cylinder. A perspective profile of a supercritical airfoil called here "streamlined airfoil profile" (SAP) was considered for detailed future investigations. All models have span (length of generatrix for cylinders) of 200 mm with end plates installed from both ends.

### Flow-control approaches

A number of engineering solutions was applied to the models in the framework of the flow-control concept based on a spanwise-regular flow excitation. One of the most advantageous is that using thermal excitation applied either to the model (localized surface heating) or to the flow (arrays of plasma discharges). Both of them can be realized in an active and remote mode using microwave radiation.

### 5.1 Models with arrays of microwave-heated elements

All streamwise heated elements are combined in the array with spanwise steps between the elements,  $\Delta z = 5$  or 10 mm. Being flush-mounted or attached to the surface, they keep it smooth.

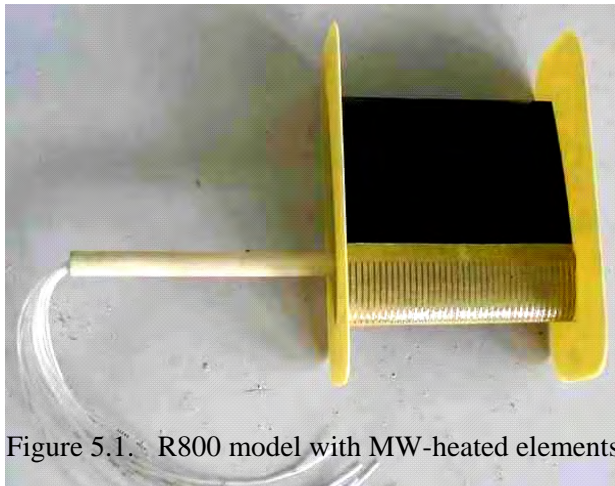


Figure 5.1. R800 model with MW-heated elements

*MW-heated elements made of metal foil* were fabricated using chemical etching of 8.4  $\mu\text{m}$  thick nichrome foil glued to the paper drenched with thermosetting resin so that a total thickness of the package was 45  $\mu\text{m}$ . Photographic masks enable very accurate and uniform sets of heated elements. Foil strips were 1.5 mm wide and 55 mm long. The sheet of heated elements was glued to the model surface (Fig. 5.1).

Initial version of this idea in a form of *resistively heated elements* embedded into the R800 model was investigated earlier and showed good results. For the present project, the model holder was modified to match the side-wall-mounted 3-component strain gage balance. The resistively heated model was used in prototype tests to investigate the flow field using a constant temperature anemometer.

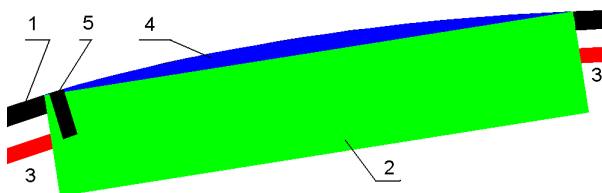


Figure 5.2. Fabrication technology for a model with TVO resistors: 1 – model shell; 2 – resistor; 3 – resistor terminals; 4 - epoxy resin filler; 5 – tap port

The next version in a form of *MW-heated TVO resistors* were vitrified parallelepiped-shaped graphite resistors of 18 x 3.0 x 1.3 mm (length x height x thickness). To flush-mount such elements into the curved surface of the model, the following approach was used (Fig. 5.2). Nineteen slots were sawed through the model shell at a chosen chordwise position with a spanwise step of 10 mm. Resistors were inserted into the slots and glued to the shell. The segment-shaped caves were filled with thermostable epoxy resin, and the model surface was grinded with sandpaper to form a

smooth shape. Maximal thickness of the resin did not exceed 0.6 mm; the thermal conductivity of the layer was raised using metal extender in the filler.

*Dispersed graphite MW-heated elements* were made of fine-dispersed graphite mixed with heat-resistant lacquer. To accommodate them, twenty-four 0.5 mm wide 115 mm long through slots were made in model shells, one set in the convex surface of model #11 and another set in the concave surface of model #12. The slots were covered inside with paper and one layer of glass-fiber soaked with epoxy resin. After compound curing, slots were filled with graphite-lacquer mixture and left for dryout. Finally, the surface was smoothed with sandpaper (Fig 5.3). Metal foil was glued to the internal surface of opposite shell of the model, and the whole model was assembled. Detailed layouts of models with this type of heated elements are shown in the Appendix to Chapter V.

*Thin graphite lines ("pencil system")* are simple patterns of thin pencil lines with integrated ohmic resistance in a range of  $10^4$ - $10^5$  Ohm, drawn on a sheet of usual paper (see Fig. 5.4). After lines were drawn, both sides of the paper were covered with temperature-resistant lacquer and the sheet was glued to the model surface. The main advantage of this approach is the simplicity of fabrication of any array configuration. Some of them were made with spanwise steps of 5 and 7.5 mm and streamwise length of 80 mm and glued to concave and convex surfaces of R800 models. Photos and sketches of the models with glued "pencil systems" are given in the Appendix to Chapter V.

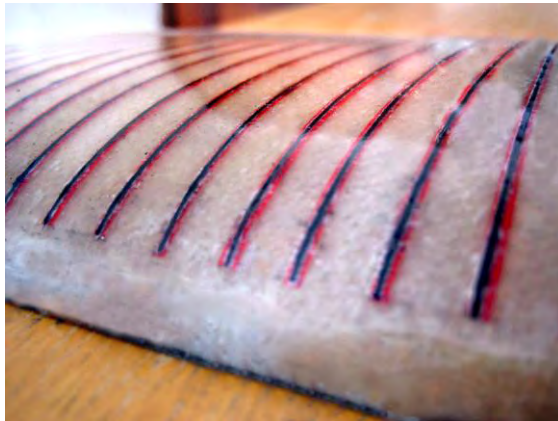


Fig. 5.3. Upper surface of the R800 model with an array of flush mounted MW-heated bulk-graphite EM vibrators

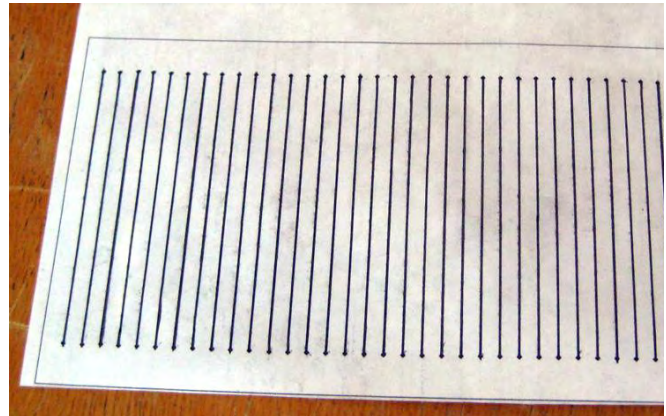


Figure 5.4. "Pencil system" on a paper: spanwise spacing  $\lambda_z = 5$  mm; strip width  $2a = 0.8$  mm; length  $2L = 80$  mm; ohmic resistance  $R = 20$  KOhm

However the easiness of fabrication was accompanied with a short life time of the system before the model burnout that enable only a limited number of test runs. The main drawback of the MW heating resulted from the non-uniformity of energy absorption along a separate heated element and by different elements in the system. It is in agreement with the MRTI assessment that the energy absorbed in the places where it was high by itself that decreased the fraction of energy absorbed by the rest part of the array. So when for some reason a burnout occurred in a certain point, organic substances in model burnt out and were blown away but some of them consisting mainly of carbon remained in the model. Since carbon is a good absorber of microwave radiation, a considerable amount of radiated power was absorbed by the burnt portion of model leading to its further overheating while the rest of the heated elements remained almost cold.

### 5.1.1 R800 airfoil with heated elements

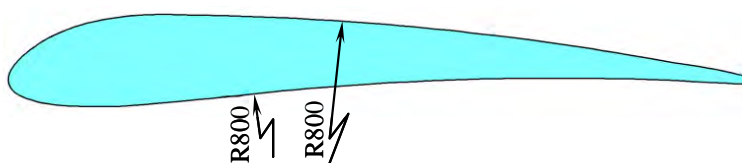


Figure 5.5. R800 airfoil-type model

R800 airfoil was developed in as relatively simple aerodynamic shape consisted of two cylindrical shells coupled aerodynamically to form a profile shown in Fig. 5.5. Its relative thickness is 12.4%.

Totally, over ten R800 models

were manufactured during the project implementation. All of them have the same basic design. Each model consists of two thin shells for convex and concave surfaces with internal structural elements – ribs and a spar as a holder extension. All structural units are glued together with epoxy. Pressure taps are drilled in central sections of the shells. Extension pipes are attached to tap ports, brought out through the holder and connected to pressure transducers of the **surface pressure measurement system (SUPREMESY)**.

The model design and fabrication is subject both to aerodynamic and electrodynamic requirements. The aerodynamics requires the model to be rigid and strong to withstand aerodynamic loads. Electrodynamics requires high EM transparency and low value of dielectric loss tangent at a given MW frequency in order not to distort the MW field. That is why only plastic models with relatively thin shells and absence of metal structural elements were found to be acceptable.

Before the final assemblage, polyethylene pipes were glued to drain ports drilled in the shells in determined locations. Following MRTI recommendations, vitrified parallelepiped TVO resistors were chosen as heated elements with dimensions of 18 x 3.0 x 1.3 mm (length x height x thickness).

The model layout is shown in Fig. 5.6.

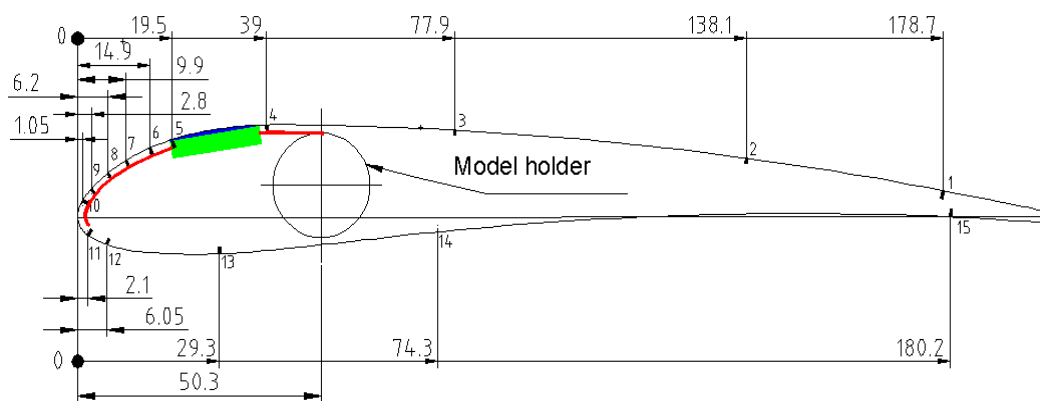


Fig. 5.6. R800 Model layout, dimensions in mm:

numbers 1 - 15 near dimension lines designate drain port numbers; heated elements (TVO resistors) are shown in green with their terminals shown in red

## 5.2 Models with arrays of plasma actuators

### 5.2.1 Actuators of plasma discharges

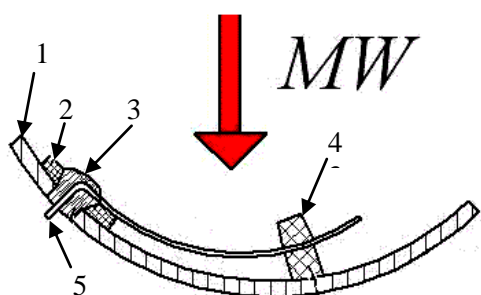


Figure 5.7. Linear plasma initiator:  
1 – cylindrical metal segment; 2 – glass-fiber material; 3 – cement; 4 – quartz fiber foam; 5 – linear initiator tip

*Linear plasma initiators* developed in MRTI for the cylindrical model were supposed to be less sensitive to the non-uniformity of electromagnetic field and consume less MW energy. The initiator is made of thin nichrome wire, its tip is bent and brought to the outer surface of the cylinder through the hole in the metal segment. The wire is fixed in the hole with high-temperature cement. The "tail" of the wire is located inside the cylinder approximately parallel to cylinder internal surface and is fixed in this position by a strip of low-density sintered quartz fiber. The metal segment works as an electromagnetic mirror for the initiator (Fig. 5.7). The lengths of "tails" are tuned to obtain

reliable and stable discharges in the multiple- initiator system.

It was found during the experiment preparation that this type of initiators was sensitive to EM field variations caused by dielectric structural elements of the model and requires precise tuning of the model as a whole as well as an accurate positioning of the radiating horn antenna. No decrease of required MW energy was found for this type of initiators. Another problem was a narrow range of permissible angular cylinder positions relative to flow direction where discharges were reliably ignited. Finally, discharges in this system often traveled from outside to inside of the model thus blocking any energy release in the flow. In this connection, only a limited number of tests was possible with this type of initiators.

*Ring-type plasma initiators* were developed earlier and showed themselves quite operable despite of certain application inconveniences. The plasma array consists of a set of ~17 mm diameter split rings made of 1 mm thick nichrome wire which are flush-mounted into the model using high-temperature cement so that the gap is situated on the surface (Figs. 5.8, Fig. 5.9).

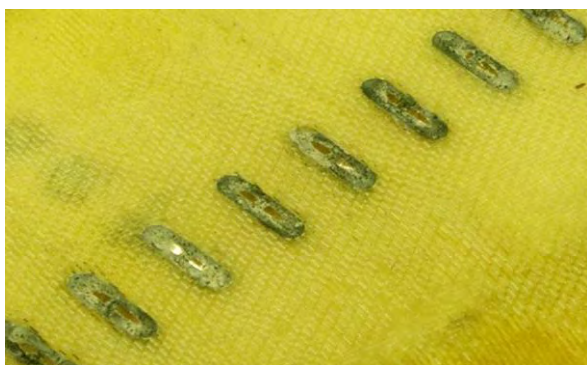


Figure 5.8. Exterior of the R800 model with an array of ring-type plasma initiators installed

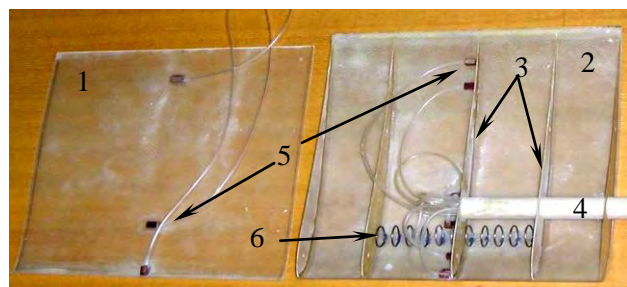


Figure 5.9. Interior of the R800 model:

1 – concave shell; 2 – convex shell; 3 – rigidity ribs;  
4 – holder; 5 – tap ports with pressure pipes; 6 – ring-type plasma initiators

This is a sharp EM resonant system, which requires precise sizes of rings and accurate positioning of the horn antenna. This engineering solution is also sensitive to variations of model electrodynamic properties but after appropriate adjustments of the model and MW-generation system, it demonstrated sufficiently reliable plasma ignition in the determined range of angles of attack of the model. The durability of initiators was satisfactory for several tests in the series and easy model renewal if necessary.

### 5.2.2 R800 Model with plasma initiators

Model shells were formed in the mold made of glass-reinforced epoxy resin using master-model. Two main technologies were used: (a) vacuum molding of shells from glass-fiber cloth soaked with epoxy resin and thermal curing and (b) application of gelcoat to the mold. Gelcoat shells had smoother surface, which was good from the aerodynamic point of view. However, the technology of shell forming led to increase of shell thickness that deteriorated electromagnetic properties of the model. That is why only one model was made using this technology. Ribs and spar/holder were made of industrial glass-fiber-reinforced plastic: 1-mm thick sheet for ribs and Ø20 mm tube (Ø28 mm for new pitch mechanism). Fig. 5.9 gives a general view of the glass-fiber R800 model before its final assemblage. This is a type of the model that was basically used for flow-control experiments based on MW formation of spanwise-regular thermal fields.

### 5.2.3 Circular cylinder models

#### *Prototype cylindrical models with mechanical vortex-generators*

To guide more expensive and sophisticated MW-based experiments, the prototype models were tested with spanwise arrays of mechanical vortex-generators. For that, two circular cylinder

models were designed and manufactured,  $\varnothing 106.6$  mm and  $\varnothing 128$  mm. Both models were made of 200 mm long polyvinylchloride tubes with wall thickness of 2 mm and had four internal circular ribs made of 3-mm thick glass-fiber plastic to provide sufficient stiffness to the structure. The 28 mm holder was mounted coaxially to model surface and all the structural elements were glued to each other. Each model had 24 tap ports located with  $15^\circ$  circular pitch and the endplates on the both sides.

Two types of excitation was used: (a) asymmetric excitation using spherical turbulizers 4.2 mm in diameter located along the cylinder generatrix with a variable step and (b) symmetric excitation using O-ring turbulizers with a circular cross-section of  $d=2.5$  and  $d=4.6$  mm in diameter. Cylinders with spherical and O-ring turbulizers are shown in Figs. 5.10 and 5.11.

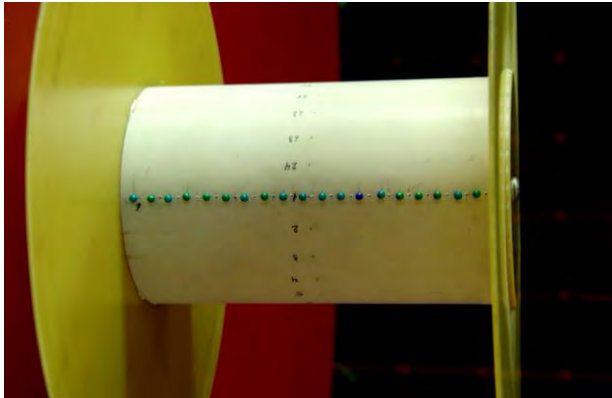


Figure 5.10. Cylindrical model  $\varnothing 128$  mm with an array of spherical turbulizers,  $\Delta z=10$  mm



Figure 5.11. Cylindrical model  $\varnothing 106.6$  mm with O-rings,  $\varnothing 2.5$  mm cross-section,  $\Delta z=10$  mm

### *Cylindrical model with linear plasma initiators*

The model of Fig. 5.10 type was used as a direct prototype for the plasma-controlled model shown in Figs. 5.12, 5.13 where the array of mechanical vortex-generators was replaced with an array of thermal sources, or plasma discharges.

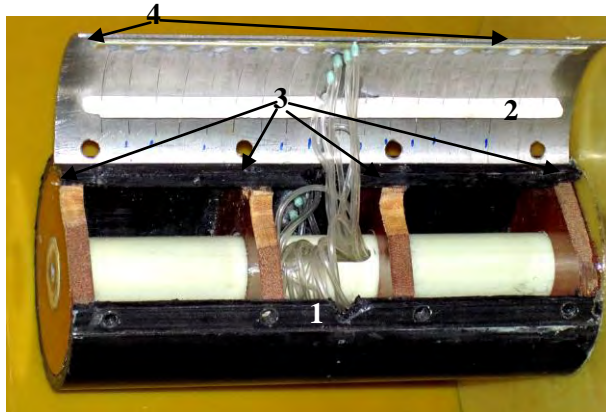


Figure 5.12. Internal design of cylindrical model with linear plasma initiators:

- 1 – PVC cylinder; 2 – metal segment; 3 – cloth laminate ribs; 4 - initiators; 5 – model holder;
- 6 - pressure tap pipes

This plasma-controlled cylinder is a complex structure combining plastic and metal elements. The polyvinylchloride tube with 6 mm thick walls is used to make the model contour. Its  $105^\circ$  segment is cut out and substituted with the 2 mm thick metal segment fixed by 8 countersunk screws. Inside the model, 4 cloth laminate 10 mm thick ribs are mounted and glued to provide sufficient rigidity of the assembled model with a holder. In the middle section of the model, 24 pressure taps are made with  $15^\circ$  circular pitch.

Nineteen 5-mm holes with a 10 mm spanwise step are made along the generatrix of the metal cylinder segment

to nest plasma initiators. After the model parts were fabricated and assembled, the model was grinded as a single whole to smooth the surface. The aerodynamically required 3-mm thick, 270 mm diameter endplates are mounted to the both ends of the cylinder; they are made from glass-bonded dielectric plastic to satisfy electrodynamic requirements for plasma generation.

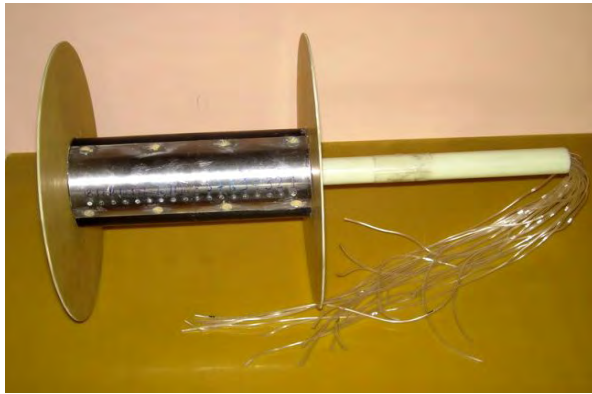


Figure 5.13. Circular cylinder model with linear plasma initiators and side plates to mount in the wind-tunnel test section

obtained improvement of aerodynamic performance. It has a profile similar to modern supercritical wings of modern transport jet airplanes (Fig. 5.14). The model is designed like the

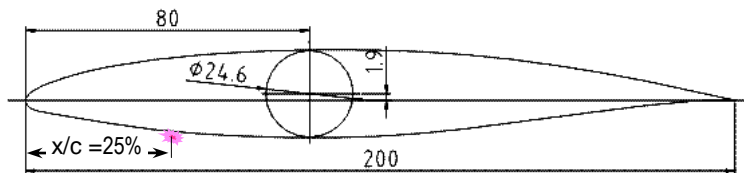


Figure 5.14. Geometry of the “SAP” with shown locations of a tube holder and plasma initiators at 0.25c

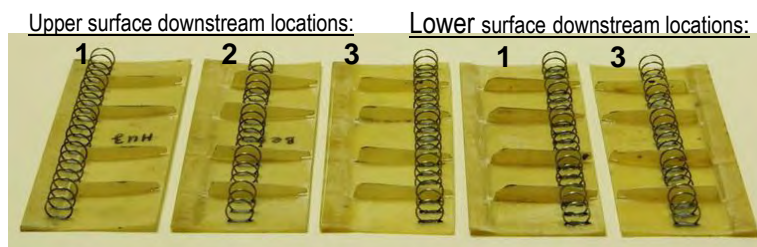


Figure 5.15. “SAP” model (top) with the left endplate removed. Five inserts (bottom) providing different chordwise locations of plasma arrays on the both model surfaces.

Four airfoil and cylinder types of test models are developed, fabricated, and tested with a number of flow-control versions within each type based on microwave and mechanical spanwise-regular flow excitation. All models enable simultaneous measurements of three components of full aerodynamic load and surface pressure distribution.

To install initiators and adjust them for stable generation of a number of plasma discharges, the assembled model is typically sent to MRTI. After the electrodynamic part of the work is done, the completed and tuned model is sent back to IHM and tested in the ACIR. General view of the model is shown in Fig. 5.13. Detailed engineering drawings and description are given in the Appendix to Chapter V.

#### 5.2.4 Streamlined airfoil profile, SAP

A streamlined airfoil model aims at the prospective investigations which will give an insight into physical mechanisms of the R800 models with thin shells, internal ribs, and spar, with the same overall dimension: constant chord  $c = 200$  mm and span  $l = 200$  mm. SAP material is thermally cured fiberglass-reinforced epoxy resin. Two elliptical endplates  $400 \times 300$  mm are mounted at the model side edges. Each model has 29 pressure taps with pipes for connection to SUPREMESY.

An essential design difference between SAP and R800 models is that instead of separate models for each chordwise location of initiators, a 30% opening is made in upper or lower surfaces of respective SAP models (one in each model). For them, the inserts mimicking a surface fragment are designed with initiator arrays mounted at different chordwise locations (Fig. 5.15). Total 6 inserts are to be tested for upper and lower surfaces with ring initiators mounted at 20, 25, and 30% of chord.

### 5.3. Summary

## Chapter VI. NUMERICAL SIMULATION OF THERMALLY CONTROLLED FLOWS, *IHM, Kiev*

### 6.1. Introduction: goals, problem formulation, numerical instruments

Numerical simulation of the formulated flow-control problem aimed firstly at general diagnostics of the boundary-layer flows affected by spanwise-regular thermal sources. It enabled to reveal optimal values of space scales of the thermal arrays, of their location over a model, and of energy input levels. Secondly, the modeling enables to obtain not only integral characteristics like forces or pressure for certain sets of basic flow parameters but also continuous distributions of various flow characteristics that is necessary to analyze flow structure and behavior.

The fluid dynamic modeling tools included in the ANSYS software were basically used. In the beginning of the project it was CFX, then Fluent of the later ANSYS version. The calculation domains and meshes were built using initially Design Modeler and ICEM CFD, and later Pointwise.

In all studied tasks, a reference case was modeled first, i. e. a flow around the investigated body at a give range of free-stream velocities and a constant temperature in the entire calculation domain. The obtained data were used as initial conditions for a case with a higher temperature value applied by the thermal sources; thus an impact of the thermal sources on a flow structure could be found from the analysis of the two cases.

### 6.2. LOCALIZED HEATING OF THE SURFACE (Distributed temperature boundary condition)

#### 6.2.1. Definitions, formulation of the numerical approach

Localized heating of a body surface was modeled by specifying the surface boundary condition in a form of surface temperature varying regularly in a spanwise direction,  $T(z)$ . This variation space scale,  $\lambda_z$ , defines a scale of vortical disturbances introduced in boundary layers.

A simplified numerical approach – modeling of the flow over surfaces with constant curvature radius - was used to get an idea about the influence of the heated elements (their width ( $d_{\text{element}}$ ), spacing ( $\lambda_z$ ), temperature gradient ( $\Delta T$ )) onto the boundary-layer characteristics at certain free-stream velocity, and to reduce a range of parameters which should be analyzed in the full-scale numerical simulations.

Thus the studied flow developed over a convex solid surface with 0.8 m curvature radius; the calculation domain was 0.5 m long (streamwisely), 4 cm wide (spanwisely), and 2 cm high (normally to the wall). The flow entered the domain tangentially to the wall and stayed fully attached throughout the entire domain. The uniform flow velocity  $U_0$  was specified at the inlet, no-slip boundary conditions were taken on the bottom boundary (wall), the free-slipping surface was assumed on the top boundary, and periodicity conditions were given on the side boundaries of the calculation domain. Longitudinal strips of variable temperature in the bottom wall modeled the embedded microwave-heated elements.

#### 6.2.2. Results and discussion: 2D and 3D modeling, effects of a finite extension and a downstream location of the controlled section, free-stream velocity, model's angle of attack

The reference turbulent flows over a surface (uniform temperature) did not contain any detectable vortical structures. After the heated strips were applied, longitudinal vortices emerged with a size and intensity correlated with a temperature gradient, width and spacing of the strips. Figs. 6.1, 6.2 show a typical vortical pattern with the applied temperature boundary condition.

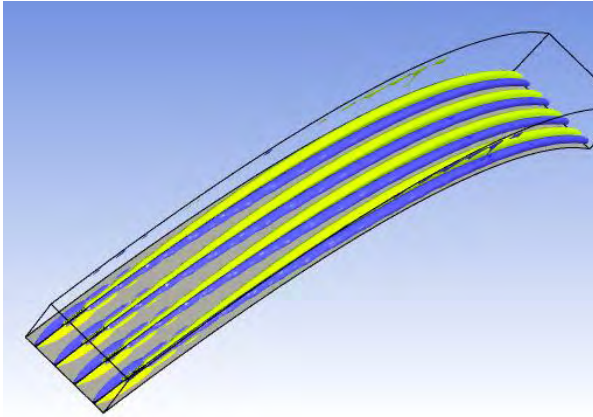


Fig. 6.1. Isosurfaces of longitudinal vorticity ( $\pm 1 \text{ s}^{-1}$ ):  
 $\Delta T = 100^\circ\text{C}$ ,  $\lambda_z = 10 \text{ mm}$ ,  $d_{\text{element}} = 1 \text{ mm}$

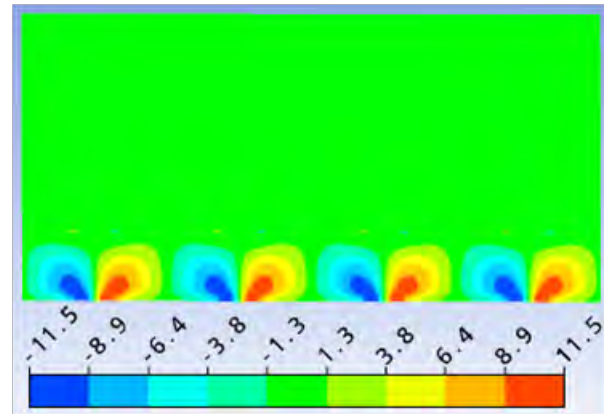


Fig. 6.2. Contours of longitudinal vorticity in the  
 $x = 0.26 \text{ m}$  downstream section;  
 $\Delta T = 300^\circ\text{C}$ ,  $\lambda_z = 10 \text{ mm}$ ,  $d_{\text{element}} = 1 \text{ mm}$

Parametric analysis of the model problem of the flow over a convex surface with finite-width longitudinal thermal sources showed that for a given free-stream velocity, a set of optimal values of control parameters can be determined: width and spanwise spacing of the heated elements, spanwise temperature gradient. These are conditions for reliable generation and maintenance of a system of intense streamwise vortices modifying flow characteristics in a favorable way. It results in recommendations to wind-tunnel experiments to make flush-mounted heated strips  $\sim 1 \text{ mm}$  wide with their spanwise spacing of about  $1 \text{ cm}$  for free-stream velocities within  $14 \text{ m/s}$  to  $30 \text{ m/s}$ , and a temperature gradient of up to  $300^\circ$ .

At the next stage of 3D modeling, the found parameters were used to analyze the thermally controlled flow around the airfoil (Fig. 6.3) with the chord length  $c = 20 \text{ cm}$ , at similar parameters of the flow and heated elements.

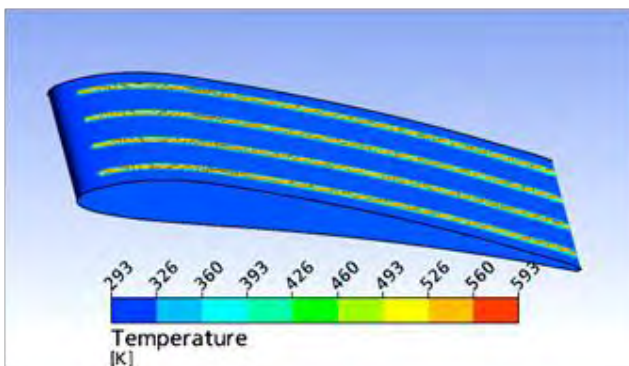


Fig. 6.3. An array of spanwise-regular heated elements over the airfoil surface:  
 $\Delta z = 9 \text{ mm}$ ,  $d_{\text{element}} = 1 \text{ mm}$

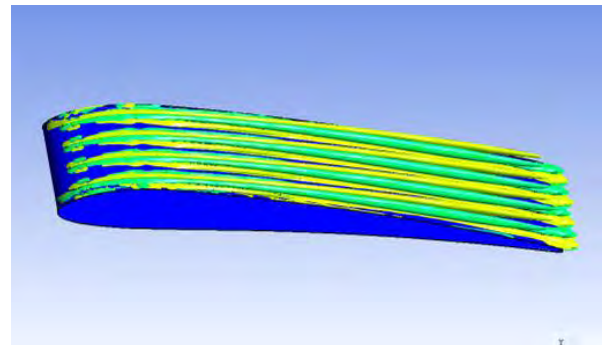


Fig. 6.4. Longitudinal vortices developing  
over the thermal array.

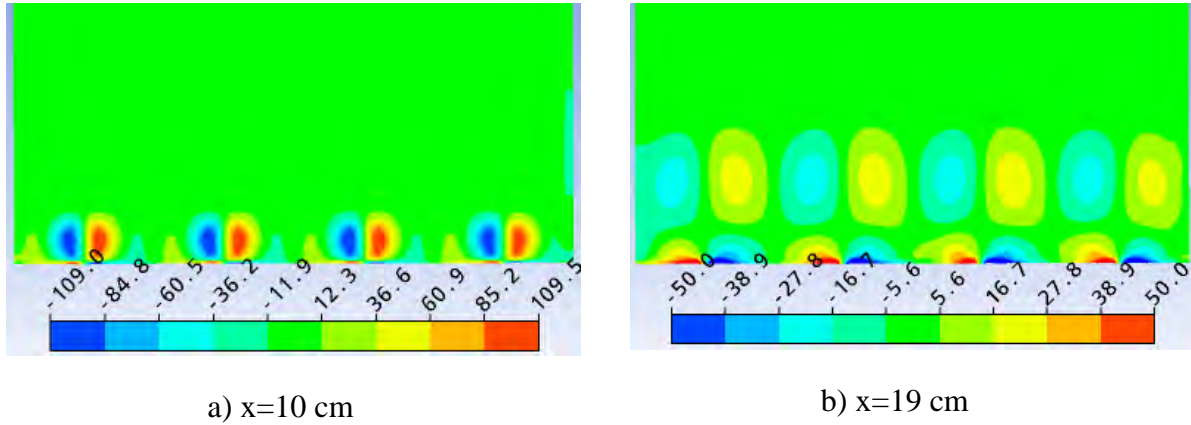


Fig. 6.5. Longitudinal vorticity contours in cross-sections of the flow over the upper airfoil side at  $\Delta T=300^\circ\text{C}$ ,  $\Delta z=9\text{mm}$ ,  $d_{\text{element}}=1\text{mm}$

Similar to the impact on flow topology in the model problem of the cylindrical convex surface, the vorticity intensity over the airfoil at moderate angles of attack was found to vary with the temperature gradient  $\Delta T_z$ . However the vorticity magnitude appeared to be higher than that in the 2D model problem at the same  $\Delta T_z$  (Fig. 6.5). It happens because of the essentially different pressure gradient along the airfoil surface compared to that over the 2D convex wall. The leading edges of heated elements over the airfoil are located in the zone of lower pressure and higher velocities; therefore the velocity disturbances induced by the spanwise-regular heating generate stronger vorticity. The maximum value of vorticity in the vortex cores rapidly decreases downstream, but further its level as well as the vortex size stay almost constant to the airfoil trailing edge.

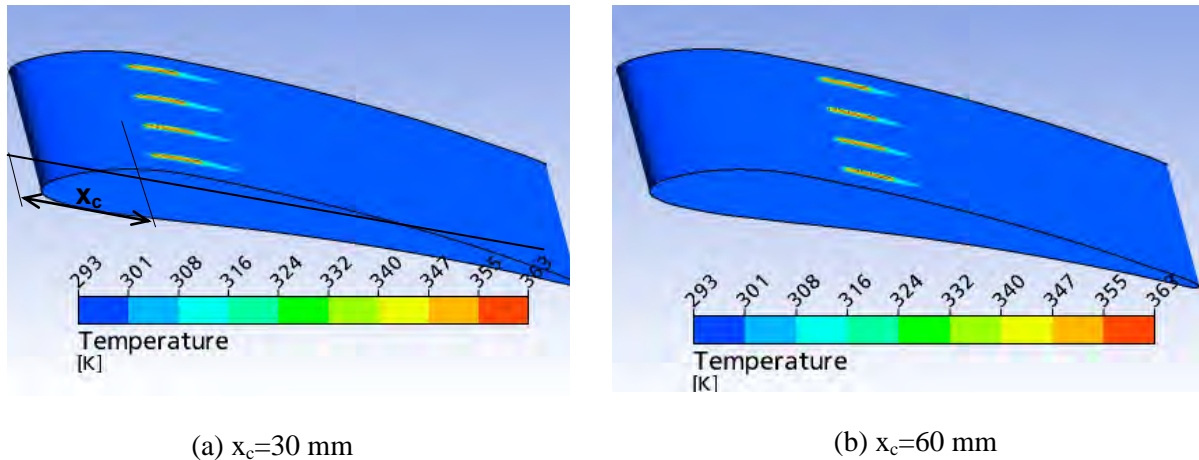
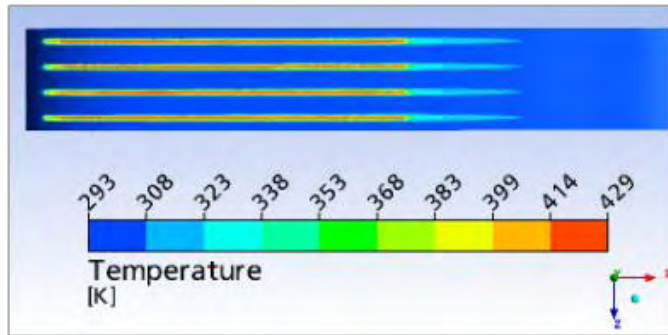


Fig. 6.6. Temperature contours on the airfoil surface with finite heated elements ( $U_0=15\text{ m/s}$ ,  $\alpha=8^\circ$ )

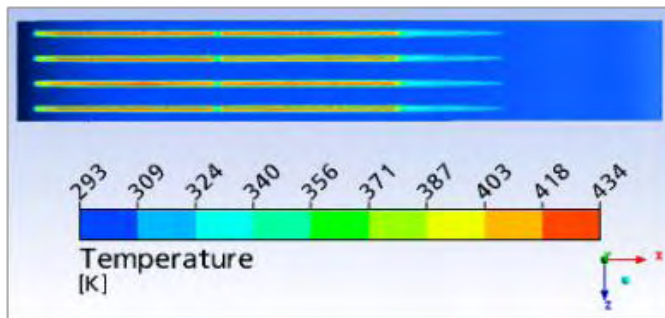
Another difference between 2D (cylindrical surface) and 3D (airfoil surface) types of flow is that the vortices over the airfoil move upward from the surface near the trailing edge.

The obtained results bring to the conclusion that in case of flow over the airfoil, the spacing between the heated surface elements can be increased or a temperature gradient can be reduced to get the same effect as in the 2D case under all other equal conditions. It is an important issue for planning both electro- and aerodynamic experiments that provides greater flexibility for relevant engineering solutions.

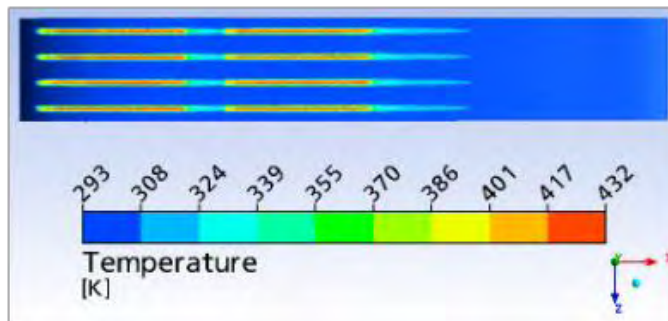
The influence of a finite length and a chordwise location ( $x_c$ ) of the heated elements (Fig. 6.6) on a flow structure over the airfoil was the task of the next stage of investigations.



a) Case 1,  $\alpha=0^\circ$



c) Case 2,  $\alpha=0^\circ$



d) Case 3,  $\alpha=0^\circ$

Fig. 6.7. Temperature contours on the profile surface for different sizes of heated elements ( $U_0=15\text{m/s}$ ,  $\Delta T=150^\circ\text{C}$ .)

Shorter elements and longitudinal discontinuity in the array (the downstream gap up to  $\sim 2\text{ cm}$  or about 30% of the section length) produce similar global topology of the flow as continuous elements do. However the total shorter heated part release less energy into the flow and, correspondingly, generates weaker vorticity. The fulfilled parametric analysis provides the knowledge and flexibility to make decisions on optimal designed of thermally controlled models.

It was found that the flow excitation with short heated elements at their temperatures achievable with the microwave heating was not sufficient to modify the boundary-layer structure. The limited streamwise extent of the controlled section shows a spatially local flow response; moreover, the effect decays with growing angle of attack. Thus the expected contribution to integral flow characteristics or to the airfoil performance improvement appeared to be negligible.

Taking into account this estimate as well as the need to further guide experiments, the case was numerically simulated of two sections of thermal arrays successively located in the downstream direction (Fig. 6.7). For that, the actual geometry of the experimental airfoil model was taken with such an arrangement of heated elements that could be realized in practice following both aero- and electrodynamic requirements to the control system fabrication. Varied parameters were the heated element length, location along the chord and longitudinal spacing of the arrays. The elements were placed on the upper or lower surface of the airfoil, the angle of attack varied within  $0^\circ - 12^\circ$ .

It was found that longitudinal vortices generated over the heated elements of finite length do not disappear immediately at their downstream propagation but are sustained in the flow along a certain distance. Shorter elements and longitudinal discontinuity in the array (the downstream gap up to  $\sim 2\text{ cm}$  or about 30% of the

### 6.2.3. Conclusions and recommendations

The general recommendation deals with possible ways to compensate the decaying intensity of developing vortices. Generated by shortened heated elements, the favorable vorticity can be maintained due to increased temperature gradient approximately inversely to the decrease of the total heated area. Secondly, it is recommended to locate heated sections in the vicinity of minimum pressure over a body that initiates more intense vortical pairs. Thirdly, the method works better at higher free-stream velocities which support the development of stronger vortices.

Growing angles of attack change pressure distribution over a model and a boundary layer thickness. It moves the longitudinal vortices up from the airfoil surface that makes the near-wall region less susceptible to their presence.

The numerical modeling showed that longitudinal vortices thermally generated in the boundary layer over the airfoil surface noticeably changed the structure of velocity and turbulence components in the area of  $y^+ < 200$  ( $y^+ = y u_\tau / \nu$ , where  $u_\tau = \tau_w / \rho$ ,  $\tau_w$  is local shear stress on the wall).

An insight into **physical phenomena** related to thermal boundary-layer control with the spanwise-regular temperature of the surface can be described as follows.

A heated surface results in the growth of the air-flow temperature in its vicinity. It cause two opposite effects to come into action. On the one hand, the molecular viscosity of gas grows with temperature growing that would result in growing shear stresses (friction drag). On the other hand, local velocities change too. A decrease in the normal velocity gradient causes the friction drag decrease.

A lower velocity gradient is observed in the area where a pair of longitudinal vortices generates an upward secondary flow, i.e. over a heating element. In the place where the secondary flow is directed towards the airfoil surface, the velocity gradient grows.

Therefore the total effect of the distributed localized surface heating is the superposition of these spanwise local effects and depends on a relative contribution of each of them.

Summarizing the results on flow control with the temperature boundary condition applied to the wall, the key issue should be taken into consideration: if the temperature gradient is formed on the surface, its maximum always stays on the wall. But the near-wall region in the affected flow is, by definition, the low-momentum fluid. Therefore the additional energy transferred to the flow from the surface through this low-momentum layer cannot be used efficiently for the flow restructuring. Besides, the longitudinal vortices are shown to lift up from the surface especially in the areas close to separation. Under the applied thermal control, they start developing at a certain downstream distance from a leading edge of the heated section; as a result, an overall effect appears to be weaker at a given  $\Delta T(z)$  temperature gradient and the effectively shorter extent of the controlled section.

This numerically driven argumentation motivates application of engineering solutions where additional energy for the vortical structure maintenance can be released directly in the flow at the locations of vortex cores. It is a section with maximum influence of vortices on turbulence parameters, i.e. the section of maximum values of turbulent stresses.

An evident solution of this type is based on application of plasma discharges in the framework of the same flow-control strategy. Initiated with microwave radiation, they arise at a certain distance from the wall; the maximum local temperature is generated in the flow and its value is much higher. Besides, it minimizes the involvement of low-momentum fluid as well as the thermal inertia of the whole control system.

More details on the discussed numerical results are presented in the Appendix Ch.VI.

## 6.3. ARRAYS OF MECHANICAL VORTEX-GENERATORS (PROTOTYPE PROBLEM)

### 6.3.1. Formulation and numerical procedure

The multi-aspect analysis of boundary layers interacting with systems of local disturbance sources like plasma discharges is a very complicated problem taking into account variety of flow conditions over a surface including longitudinal pressure gradient, varying boundary layer thickness, unsteady behavior and separation, etc. In this connection, investigations started from a problem of a circular cylinder in a crossflow, which was extensively studied for a wide range of Reynolds numbers. It ensures a convenient model for the boundary-layer analysis over a curved surface for any of the above-mentioned regimes in the framework of one geometrical formulation.

To test the numerical approach and verify the obtained results with the experimental data, a prototype problem was considered of the flow around a cylinder disturbed locally by mechanical vortex generators. Model sizes, scale and location of the vortex-generators corresponded to those manufactured for the laboratory tests.

Since the whole analysis aims at generation of a streamwise vortical motion due to the imposed flow three-dimensionality, the problem was formulated in the 3D statement.

General numerical procedure was similar to that described in the previous chapter. First, a flow was modeled in the calculation domain in absence of any control factors, then it was used as an initial condition for the controlled flow.

Flow parameters and geometry were taken to match the experimental tasks and conditions in the available wind tunnels; circular cylinder models with diameters of  $D=86\text{--}128\text{ mm}$  were studied at free-stream velocities,  $U_0=5\text{--}15\text{ m/s}$  that corresponded to Reynolds numbers  $Re_D=3.5\times 10^4\text{--}1.05\times 10^5$ .

### 6.3.2. Calculation results

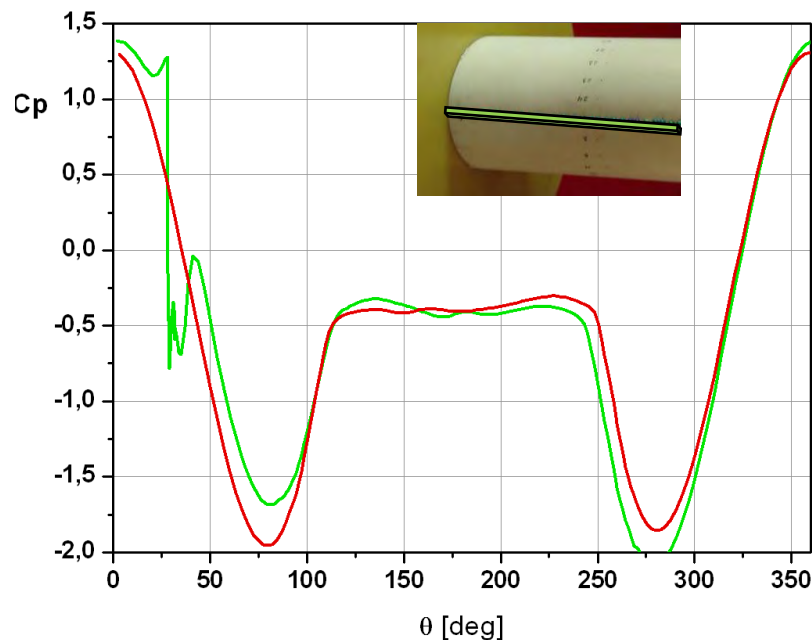


Fig. 6.8. Calculated pressure coefficients around the cylinder at  $U_\infty=15\text{m/s}$ : red – reference circular cylinder, green – cylinder model with an asymmetric rib-turbulizer.

The integral parameters such as lift and drag coefficients, pressure distribution and the separation area location along the cylinder surface were found to be in a good agreement with typical time-averaged values of these parameters obtained in similar studies for a cylinder flow in the drag crisis regime. However, the measurement results at similar free-stream velocities and Reynolds numbers showed rather the pre-crisis situation with a less pronounced pressure drop and, correspondingly, with a higher total drag. It is known, that the Reynolds number at which the drag crisis takes place can vary depending on flow conditions in

a wind tunnel, as well as on the numerical modeling technique. Therefore since physical mechanisms were a key issue in this research, matched numerical and experimental results were analyzed taking into account not only Reynolds number values but the whole flow situation.

To model the experimental situation with closely spaced spherical turbulizers, the numerical formulation was based on a spanwise rib placed along a cylinder generatrix at  $\theta=30^\circ$  (Fig. 6.8, top). The rib with a square cross-section of 2x4.2mm was chosen comparable by size to an array of spherical turbulizers in experiments.

This rib-turbulizer was shown to introduce asymmetry into the fields of all parameters relative to the flow direction. Upstream of the rib, an area of higher pressure was formed. The flow reversed downstream with a corresponding pressure drop. On the whole, 2% reduction of a drag coefficient was obtained; in addition, lift appeared due to the flow asymmetry with the lift coefficient of 0.2. It was in a good agreement with the measurement results for  $Re_D \sim 1.25 \times 10^5$ .

For the higher Reynolds number (free-stream velocity of  $U_0=15$  m/s), relative pressure drop behind the rib turbulizer diminished, influence on drag was negligible, while the flow asymmetry over upper and lower cylinder parts resulted in the same lift coefficient about 0.2.

It revealed an importance of a flow regime for a resultant impact of the turbulizer. The pre-crisis flow showed itself more sensitive that explains the essential favorable effect of turbulizers obtained in tests at flow regimes characterized by pre-crisis distributions of parameters.

The analyzed turbulizer can be considered as 2D by its influence on the flow at a sufficient distance from its sidewalls. Analysis of more refined effects of 3D spanwise arrays of “local” turbulizers mimicking those in experiments required finer grids, and correspondingly, enhanced computational resources compared to those available at the moment.

The performed numerical analysis of the prototype problem guided experiments in terms of a reduced range of parameters to be considered and a clue about an area for detail studies; besides, it enabled to develop and to test the numerical modeling procedure for the formulated 3D problem.

## **6.4. ARRAYS OF PLASMA DISCHARGES (LOCALIZED TEMPERATURE SOURCES)**

### **6.4.1. Pre-crisis flow regime around a circular cylinder**

The numerical approach developed for the prototype problem of modeling a 3D flow around a circular cylinder was used for the next stage of modeling of plasma discharges in a form of localized high-temperature sources distributed along a cylinder generatrix.

An impact of such sources on the cylinder flow was studied for the flow around the  $D=90$  mm cylinder at free-stream velocities varied within 20 to 60 m/s, which corresponded to the laboratory test conditions. The Reynolds number based on the cylinder diameter and a free-stream velocity was  $Re_D \approx 1.1 \times 10^5 \div 3.4 \times 10^5$ . Such conditions characterize the drag crisis when the drag coefficient drops abruptly from its pre-crisis values at a slight  $Re_D$  variation and the separation point moves to a higher angular position along the cylinder surface; correspondingly, a wake behind the cylinder becomes narrower, a vortex street is hardly observed due to strong mixing in a shadow zone.

In reference cases of the numerical modeling at uniform temperature in the entire domain, the drag coefficient varied from 1.1 at  $U_0=20$  m/s to 0.58 at  $U_0=60$  m/s, the separation point shifted along the cylinder span from  $\theta \sim 85^\circ$  to  $105^\circ$ , correspondingly.

In all cases, a transient regime of calculations with an adoptive time step was utilized. At a lower velocity, regular vortex shedding was obtained from the upper and lower surfaces together with a

well-resolved vortex street in the cylinder wake, while at higher velocities the flow reached almost a steady state. An unsteady regime was obtained after reducing the time step and fixing it to the value of  $10^{-5}$ s, and essential refinement of the mesh, which has become possible due to the essentially upgraded computer memory and performance.

At the same time, the flow acquired features resembling the very beginning of the drag crisis. For  $U_0=40$  m/s ( $Re \sim 2.2 \times 10^5$ ), the drag coefficient varied within 0.95 - 1.04, with the averaged value  $\cong 1$ . The separation point oscillated around the location of  $\theta \sim 96$ - $101^\circ$  and a periodical vortex shedding was observed (Fig. 6.9) with the Strouhal number  $\sim 0.53$ . The distribution of pressure coefficient on the cylinder in the reference case is shown in Fig. 6.10.

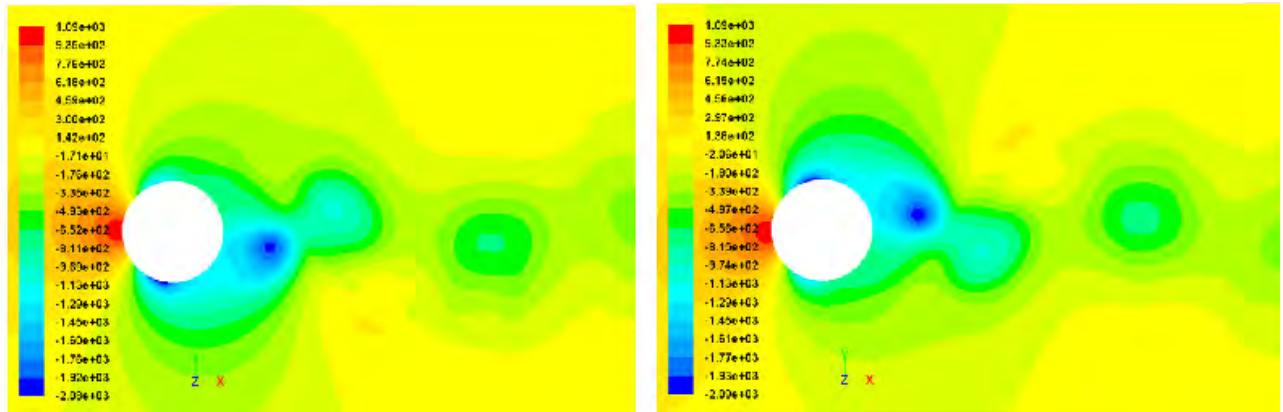


Fig. 6.9. Pressure distributions in the middle cross-section at moments of minimum and maximum lift, reference case.

#### 6.4.2. Thermally controlled flow around a cylinder

The plasma generated thermal sources were modeled with an array of fluid spheres of 2 mm in diameter with a high temperature prescribed inside the mesh cells limited by these spheres. A spanwise array of such spheres was placed over the cylinder surface at the angular locations of  $\theta = 60^\circ, 75^\circ, 85$  and  $95^\circ$  to the velocity vector, the spanwise spacing between the sources was  $\Delta z = 1$  cm and 2 cm. The temperature gradient of  $\Delta T = 1000^\circ$  is applied to the regularly oscillating flow obtained at a constant temperature of  $300^\circ\text{K}$ .

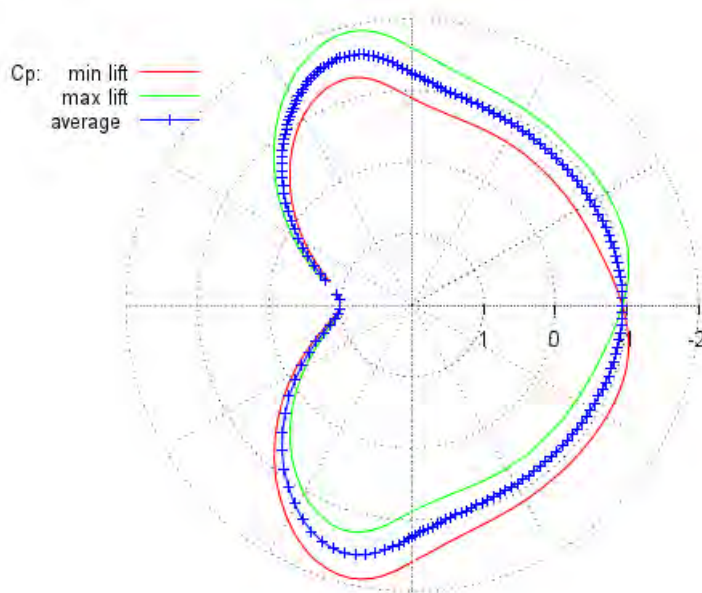


Fig. 6.10. Pressure coefficient along the cylinder surface at the moments of minimum, maximum lift and the average for the reference case.

The spanwise spacing,  $\Delta z \approx 1$ cm, between thermal vortex-generators providing the temperature gradient of  $1000^\circ$  is found to be optimal for sustainable vortex generation. Resultant longitudinal vortical pairs fill the span and are characterized with a regular cross-section geometry. A closer spacing can lead

to overlapping of neighboring vortices and a loss of their intensity, while wider spacing leaves too much space between the vortical pairs of given intensity and allows them oscillating in a spanwise direction thus causing additional flow instability.

The drag coefficient  $C_d$  increased at all angular positions of the thermal sources (Fig. 6.11). For the sources located at a greater angle  $\theta$ ,  $C_d$  grew slower and reached lesser values of its maximum. The dominant input into the total cylinder drag comes from the pressure drag. While skin friction is also affected by the thermal sources, its impact is incomparable with the drag due to pressure redistribution over the cylinder. Since pressure distribution depends on flow oscillations in the wake,  $C_d$  reaches similar values for all angular locations of the thermal sources and is less at the wider  $\Delta z$  spacing.

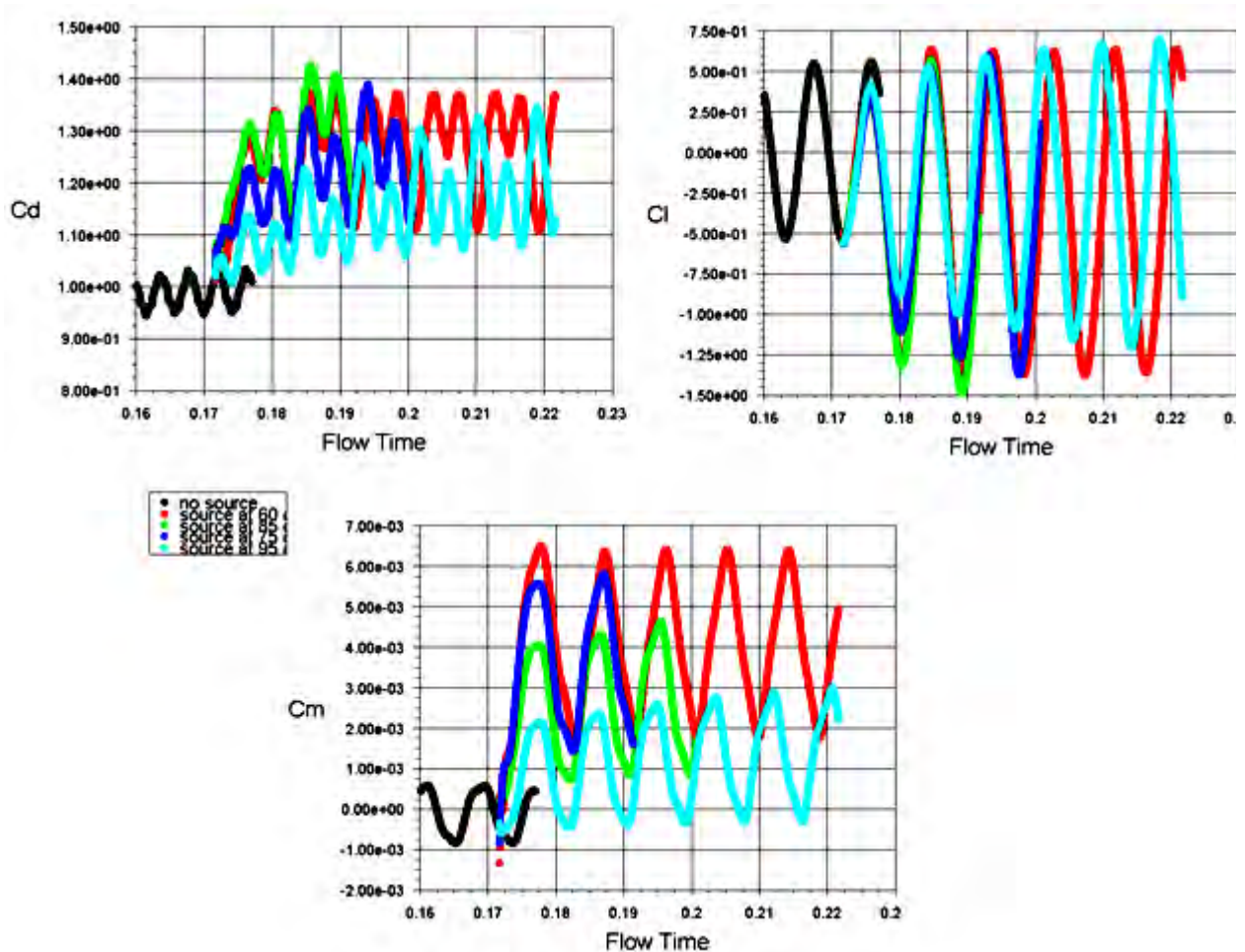
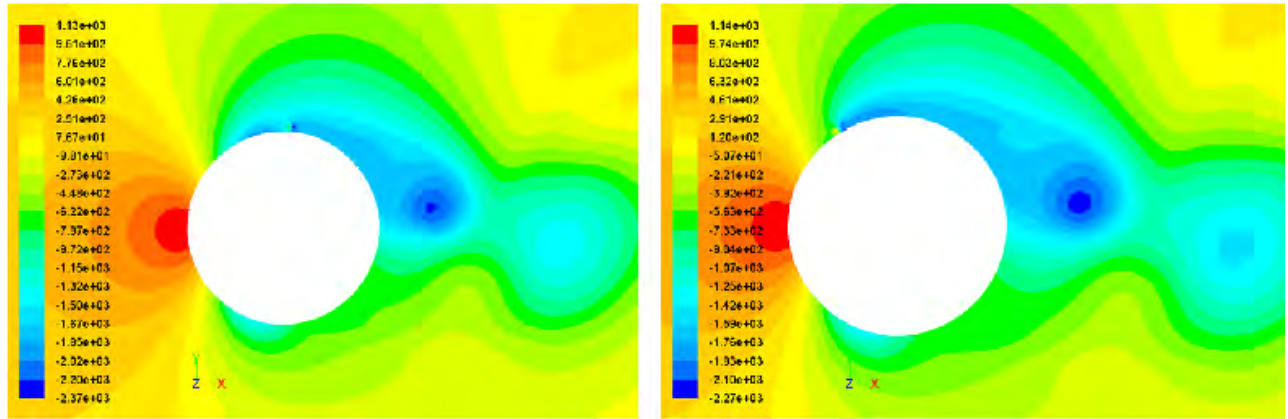


Fig. 6.11. Drag, lift and moment coefficients vs time in a reference (black curves) and controlled cases for different azimuthal locations of thermal sources along the cylinder:

$\alpha = 60^\circ$  (red),  $75^\circ$  (blue),  $85^\circ$  (green),  $95^\circ$  (turquoise);  $U_0=40$  m/s.

Plots of the lift and moment coefficients  $C_l$  and  $C_m$  reflects the asymmetry introduced in the flow by thermal sources: both parameters plots became asymmetrical relative to zero in the reference case. While maximum lift in the controlled case slightly exceeded its reference value, its minimum was less than a half of the reference (Fig. 6.11). The time-averaged value was negative in all cases. Thus positive lift value can be obtained by applying sources on the lower part of the cylinder. The average moment was also nonzero and growing for decreasing  $\theta$  (Fig. 6.11).



a)  $\alpha = 95^\circ$

b)  $\alpha = 60^\circ$

Fig. 6.12. Pressure in the middle cross-section at the moments of maximum lift

In the considered cases, thermal sources were located in the zone of decreased pressure (Fig. 6.12) but at a lower  $\theta$ , the sources were located in the area of thinner and attached boundary layer, thus at high velocities. Therefore the sources are relatively bigger compared to the boundary layer thickness and affect the flow more efficiently. In addition, due to a higher convective velocity, this impact propagates faster downstream.

### 6.4.3. Conclusions and prospects

Numerical modeling aimed at revealing physical mechanisms controlling the boundary layer characteristics with applied spanwise-regular thermal disturbances under various flow conditions including surface curvature, pressure gradient, Reynolds number, etc. The obtained results guided experiments in terms of the optimal choice of parameters and design of models.

The correlation was found between parameters of thermal sources, generated longitudinal vortices and variations of integral forces acting on the body.

#### *Distributed temperature boundary condition*

High surface temperature increases viscosity of gas thus local shear stresses grow and total friction drag increases. High temperature gradients over the surface are unacceptable because of technological considerations and longevity of laboratory models. Moderate  $\Delta T(z)$  temperature gradient along a certain downstream extent can release sufficient energy to maintain intensity and size of generated longitudinal vortices. That is flow conditions should not change drastically in the streamwise direction, e.g. the mean flow vector should not diverge much from the elements direction. This kind of flow control with an invariant boundary condition can be recommended for surfaces with rather “smooth” boundary layers over rather long streamwise sections.

#### *Spatially localized boundary condition (plasma arrays)*

Plasma discharges produce much greater energy locally thus creating high gradients of velocity. The generated disturbances reach high levels immediately near the thermal sources located in fluid and lose their intensity downstream growing in size and heating the surface. However mild changes in the flow direction are not critical in this case.

Both types of thermal sources become ineffective in the fast growing boundary layers and within separation zones.

The part of numerical simulation was performed on the basis of engineering software which is good for stable solutions of large-scale industrial problems. In the framework of the project, it was performed to match the laboratory tests, i.e. the numerical problem was formulated in accordance with the flow geometry and parameters in experiments. To mimic the experimental conditions, it requires a 3D formulation with a variety of space scales in boundary layers and in the far field. It means a large number of numerical mesh nodes and, correspondingly, high performance processors and large memory resources, and takes much computing time. In the course of the project, the numerical potential was upgraded to enable numerical solutions, which demonstrated good qualitative agreement with the measured data.

*Prospects for numerical simulation tasks*

The obtained results can serve as a basis for more detailed investigations of individual inputs of different physical mechanisms, including anisotropy of turbulence, variations of physical properties of real gases in presence of strong temperature gradients, etc. Better mesh resolution in the near-wall areas will also contribute significantly to the development of more advanced and complex turbulence models. The latter will require more sophisticated approaches to physical and numerical modeling and their realization.

Appendix Ch.VI gives more details on the discussed numerical approaches and results.

## Chapter VII. AERODYNAMIC EXPERIMENTS WITH THERMALLY CONTROLLED MODELS: *IHM, Kiev*

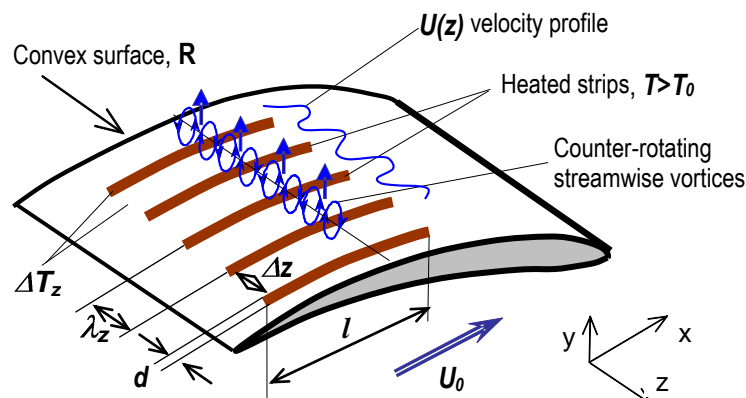


Fig. 7.1. A set of control parameters for the problem of MW-heated sections of streamwise strips:

$$\Delta T_z, \lambda_z (\Delta z), d, l$$

Fig. 7.1 illustrates the research problem of the aerodynamic performance improvement that can be achieved using an embedded spanwise array of finite-length strips heated in the field of MW radiation thus realizing active and remote flow control. One of the engineering solutions proposed in MRTI was application of resistive TVO elements for the thermal array as described in Chapters III and V. based on real characteristics of such an array, both numerical and experimental aerodynamic modeling was performed.

In experiments, the models were used with the thermal array mounted either on a convex (upper) or on a concave (lower) side of the model, the models have been marked correspondingly, e.g. model #09 and model #10.

### 7.1. Localized MW heating of the surface

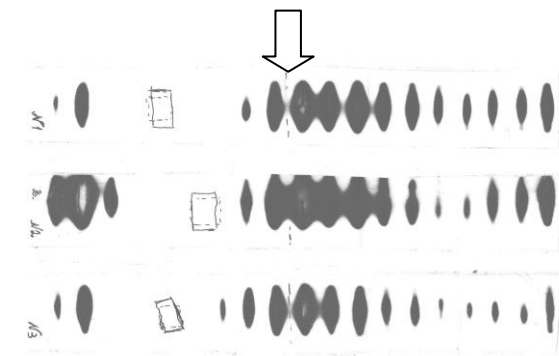


Fig. 7.2. Non-uniformity of MW heating indicated with thermosensitive paper: black arrow shows the model axis with pressure ports

The thermal field over a model surface was controlled with thermosensitive paper that is shown in Fig. 7.2 for the model #10. Similar results for the model #09 indicate strongly nonuniform MW field in the area of the thermal arrays. In spite of this unfavourable arrangement of the  $\Delta T(z)$  boundary condition, the wind-tunnel measurements were carried out to compare results in a reference and controlled case for a given range of angles of attack to post-stall values,  $\alpha = 12^\circ - 26^\circ$ . For lift, drag and pitch moment coefficients, all the data were combined into one sample and averaged for each angle of attack. Data for pressure coefficients were processed similarly.

Figs. 7.3 - 7.5 show variations of lift, drag, and pitch moment. No impact was found for the pre-stall region. At  $\alpha = 21^\circ$  lift coefficient in the controlled case was greater by 0.01 while drag coefficient was less by 0.008; pitch moment coefficient stayed almost the same.

Stall occurred at  $\alpha = 23^\circ$  in the reference case, and at  $\alpha = 22^\circ$  in the controlled case where the flow was unstable with a tendency to separate. This result is in a good agreement with that for the earlier studied resistively heated model.

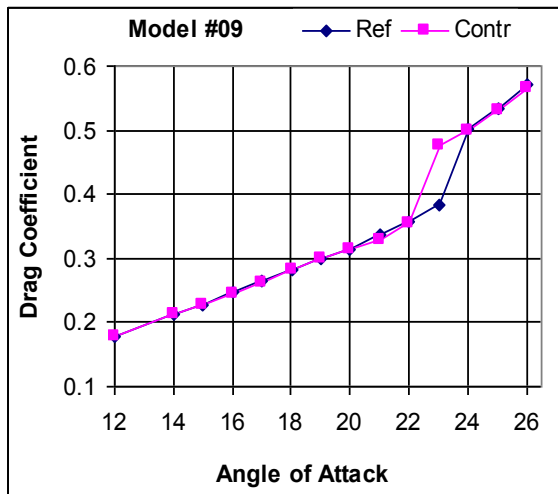


Fig. 7.3. Drag coefficient for model #09

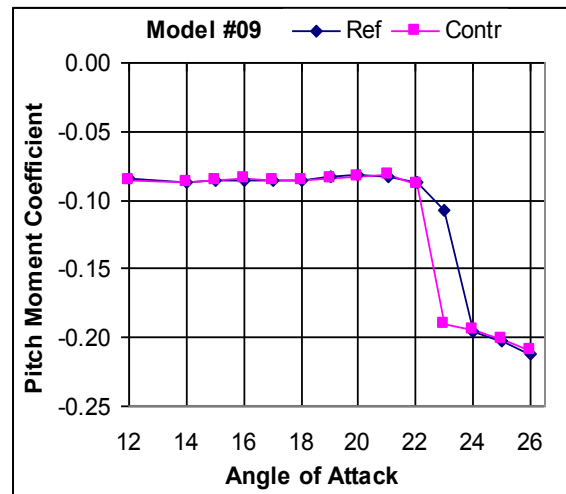


Fig. 7.5. Pitch moment coefficient for model #09

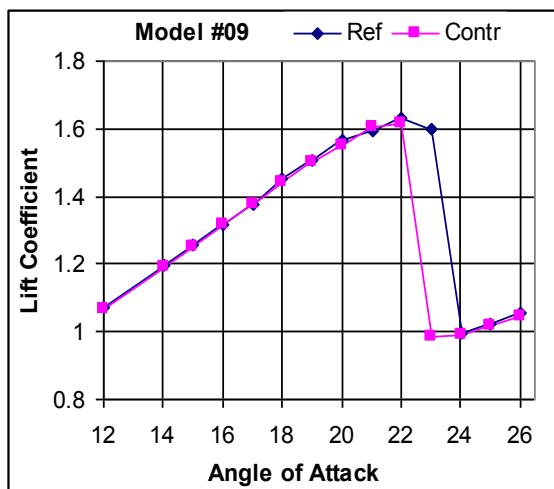


Fig. 7.4. Lift coefficient for model #09

The model #10 was tested at pre-stall to post-stall negative angles of attack,  $\alpha = -4^\circ$  to  $-14^\circ$ . The applied flow control showed just a little impact on aerodynamic coefficients within  $\alpha = -6^\circ$  to  $-10^\circ$ . It is typical for the R800 model when the control is applied to its concave surface.

Measured pressure distributions are in a good agreement with lift and drag. On a convex surface, suction grows with a growing angle of attack (pressure coefficients become more negative) up to the stall. When stall occurs, abrupt drop of suction is observed in a front part of the model where  $C_p < -1$ ; it increases in the aft part where  $C_p > -1$ . The stall is manifested with an abrupt change of pressure redistribution over the whole model surface; velocity over the convex surface drops and the critical point on a concave surface shifts towards the leading edge of the model.

**Flow visualization** revealed the peculiarity of the R800 test model profile and its extreme sensitivity to any geometry and other irregularities, especially in the vicinity of its leading edge. For the convex surface of the #09 model, it showed the separation bubble developing at  $\alpha = 12^\circ 06'$  at  $x_c \approx 20\%$  of a model chord near the rear edge of heated elements with flow reattachment at  $x_c \approx 30\%$ . At  $\alpha = 26^\circ 20'$  the bubble moves upstream starting at  $x_c \approx 8\%$  and the flow reattaches at  $x_c \approx 15\%$ . Flow visualization over a concave surface of the #10 model showed the separation bubble up to positive angles of attack with its location upstream of the thermally controlled section. Decreased angle of attack towards higher negative values results in a chordwisely shorter bubble that moves slightly upstream.

Since the separation bubble sits upstream or over a short TVO-resistor section, the thermal flow control is doomed to be least efficient. Only high positive angles of attack of the #09 model resulted in

the flow reattachment upstream of the control section that immediately showed a difference between reference and controlled cases. However this gain was small because of the upstream separation and intense downstream mixing of fluid that made the imposed temperature boundary condition insufficient to reorganize favourably the boundary-layer structure.

Thus comparatively low efficiency of the applied flow control deals both with the model and with the insufficient energy released in the boundary layer to suppress the arising separation bubble. It is a drawback of the given engineering solution of too short TVO resistors. Besides, a real  $\Delta T(z)$  value happened to be lower than the calculated one because the heated elements were deepened into the model body that resulted in heat dissipation inside the model. It is seen in Fig. 7.2 from diffused and overlapped heated spots in the thermal pattern. In its turn, it smoothed the  $\Delta T(z)$  temperature gradient, one of the basic control parameters.

These experimental conclusions are in a good agreement with those of aerodynamic numerical simulation which, in addition, provided the guidance for engineering solutions to overwhelm the deficiency.

### **Hot-wire measurements of a boundary-layer flow structure modified with spanwise-regular surface heating**

Investigation of velocity profiles in the boundary layer with local surface heating is necessary to get an insight into physical mechanisms of the thermal impact on a character and parameters of the boundary layer flow. It is important not only to find experimentally vortex structures displayed numerically but also to estimate their size, location, strength and development both in streamwise and spanwise directions. Besides, the correlation should be shown between the boundary layer structure and integral aerodynamic characteristics such as pressure, lift, drag and pitch moment coefficients.

The constant-temperature anemometer (CTA) system was used for direct measurements of velocity distributions in the model's boundary layer to find streamwise vortices developing due to the imposed  $T(z)$  regularity. To avoid the harmful microwave influence on the CTA equipment during the flow field measurements, the prototype model (Fig. A7.1, Appendix to Chapter VII) was used. The thermal control of the model was realized due to the *resistive heating* of the embedded array of streamwise elements.

The results in a form of averaged and fluctuating velocity profiles give the direct evidence of developing pairs of counter-rotating vortices between two neighboring heated strips. The obtained results can be found in relevant Quarterly reports as well as in the Appendix to Chapter VII. Further detailed investigations are necessary to set the full spatial correspondence of this structure to the forcing temperature boundary condition. It will be used for clear recommendations on optimized engineering solutions where the correlation between control and basic flow parameters is taken into account. Such a correlation will imply least losses of energy consumed for the proper organization of the spanwisely organized thermal fields.

### **Variations in the designed models with localized MW-heating. Other types of heaters.**

Model #11 had heated elements on its convex surface and the holder on its right side. It was tested with a convex surface faced upward to the MW radiation antenna. Model #12 has heated elements on its concave surface and the holder on its left side. It was tested with the concave surface faced upward.

All heated elements developed in MRTI were made from fine-dispersed bulk graphite strips flush-mounted into the model shells.

At free stream velocity  $U_0 = 15$  m/s, the model #11 showed no impact of the thermal control on lift and drag coefficients. However at  $U_0 = 20$  m/s, drag coefficients in the pre-stall region and even near the post-stall region were lower in the controlled case. Similar to the resistively heated model investigated earlier, the MW heating slightly diminished a stall angle and lift coefficients in the pre-stall region. But, the drag decrease prevailed over the lift drop that resulted in the raised **increment** of the lift-to-drag ratio in the pre-stall region as it is shown in Figs. Fig. 7.4 and 7.5.

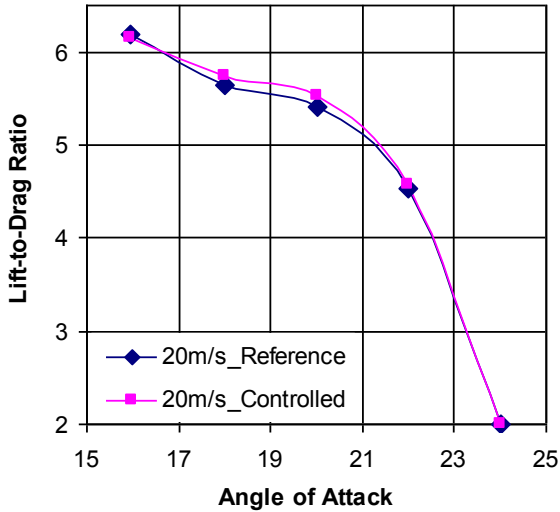


Fig. 7.4. Lift-to-drag ratio variation:  
model #11,  $U_0 = 20$  m/s

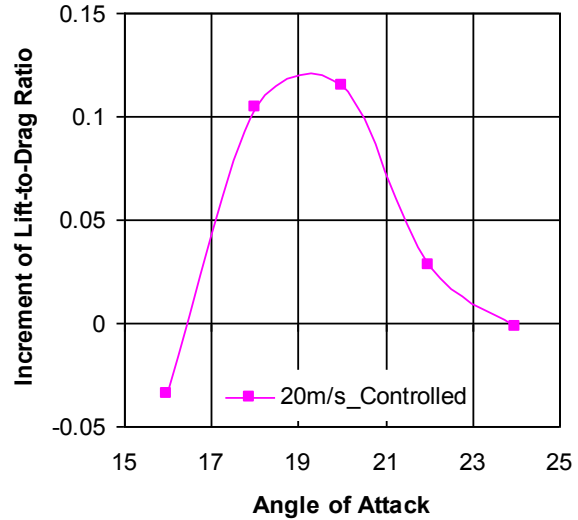


Fig. 7.5. Lift-to-drag ratio increment:  
model #11,  $U_0 = 20$  m/s

Thus measurement results show that a stall angle grows from  $8^\circ$  to  $10^\circ$  under thermal control. Drag and lift coefficients decrease at pre-stall angles of attack (to a greater extent at a higher free-stream velocity); lift-to-drag ratio grows.



Fig. 7.6. Destroyed surface of model  
#11\_2 because of the non-uniformity of the  
MW field

More measurement results including those obtained with 4 other types of MW-heated models and for other sets of experiment parameters can be found in the Appendix to this Chapter. They do not bring to essentially different conclusions than those formulated here. Aerodynamic characteristics can be improved at high angles of attack. However, effectiveness of the localized MW heating of the model surface using the proposed materials does not appear to be too impressive. Raised energy of the MW radiation could result in the local model destruction like that shown in Fig. 7.6.

Nevertheless, the obtained and perspective results are encouraging, e.g. for improvement of compressor stability of gas turbine engines on transient states due to delay of flow separation on concave surfaces of the blades.

## Comparative analysis of different types of MW-heated strips for flow control

Four types of microwave heated elements were developed and tested:

- (a) nichrome foil grid obtained by chemical etching and glued to paper drenched with thermosetting resin;
- (b) vitrified bulk carbon resistors flush-mounted in the model surface;
- (c) fine-dispersed bulk graphite mixed with heat-resistant lacquer, located in 0.5 mm wide slots inside models' surface;
- (d) graphite lead lines on the paper permeated and glued to the model with heat-resistant lacquer.

**The nichrome foil** heated elements were found to be least effective for flow control purposes; they showed insufficient values of  $\Delta T(z)$  to modify the flow structure, low uniformity of the heating along and across the thermal system and, accordingly, no noticeable changes of aerodynamic characteristics of models tested in the wind tunnel.

All the other types of MW heated elements can be characterized with similar advantages, disadvantages, and effectiveness:

**Vitrified bulk carbon resistors** required fine tuning before the model assemblage that was technologically inconvenient and, in addition, was impaired in the assembled model.

**Fine-dispersed bulk graphite heated elements** were technologically difficult to manufacture in the models and did not permit any tuning after the model assemblage.

**Graphite lead lines** on the paper were easiest technologically in laboratory conditions and provided possibilities for model modifications by gluing new patterns instead of fabrication of a sophisticated new model. However this type of heaters distorted the model shape and created some difficulties to clean pressure taps during elements gluing.

## Conclusions

1. Obtained results show feasibility of the developed thermal flow control concept based on the localized energy release using MW-heated streamwise elements. All the data obtained for the R800 models with different types of heated elements are consistent and prove a possibility to improve aerodynamic performance. Low effectiveness of this approach deals with current nonoptimal technological solutions of the method realization.
2. Another MW-based method of configured plasma arrays showed itself more efficient in terms of the aerodynamic performance improvement. Its drawbacks are common to the considered MW-heating method and relate to the MW energy scattering and nonuniformity in the wind-tunnel test section.
3. Among tested engineering solutions of the microwave-generated  $\Delta T(z)$  boundary condition, plasma arrays are more perspective for further investigations in the framework of the developed flow control concept. Further studies are to be focused on getting over the above mentioned drawbacks, on the development of reliable and aerodynamically acceptable plasma actuators as well as on a search of different types of discharges which can provide sufficient values and distribution of energy released in the flow.

## 7.2. Localized flow excitation with arrays of mechanical vortex-generators (prototype problem)

The prototype problem was formulated as a stage linking two MW-based approaches to the given-scale vortex generation for flow control: localized heating of the surface and arrays of localized plasma sources. A circular cylinder in a crossflow was chosen as a well studied case to refer to. The controlled case investigation started with a simpler prototype model with arrays of mechanical vortex-generators (Fig. 7.7) mimicking the plasma array. It enabled to determine optimal ranges of control parameters (e/g/ like a spanwise step between the vortex-generators) which could be recommended for design of a more sophisticated an expensive plasma-controlled model.

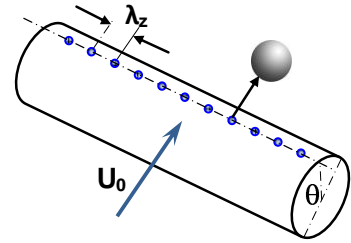


Fig. 7.7. Prototype problem formulation

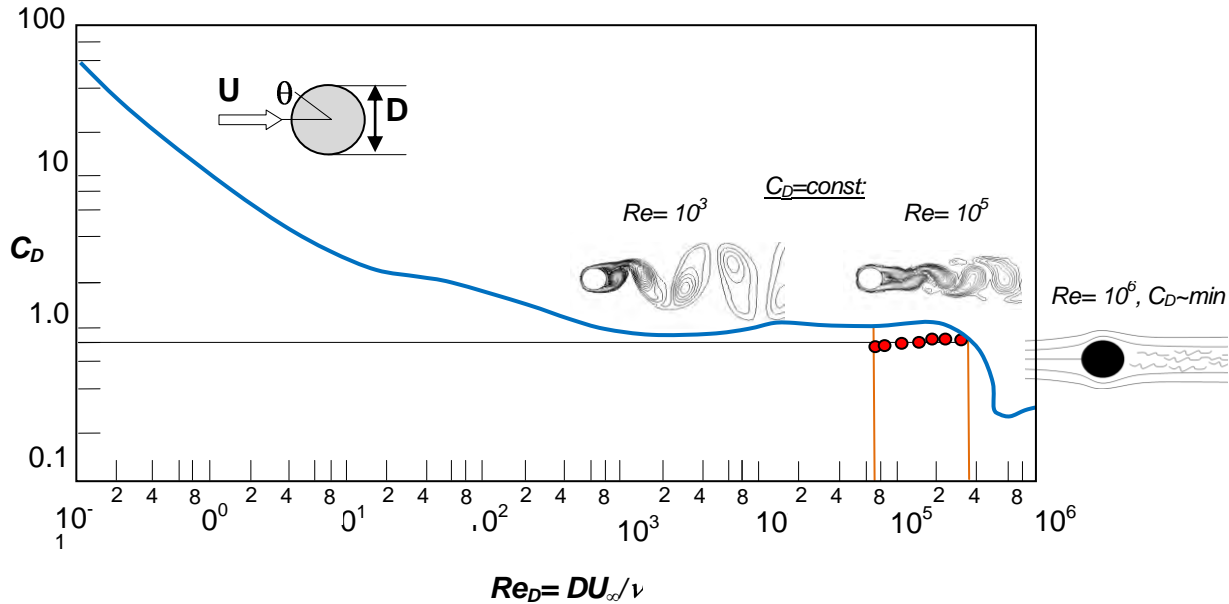


Fig. 7.8. Drag coefficient  $C_D$  of a smooth circular cylinder in a crossflow as a function of Reynolds number  $Re_D$ : blue curve – experiment, Schlichting, 1979; vortex shedding patterns – numerical visualization [1]; red points –present reference measurements)

Drag coefficients  $C_D \approx 0.8$  were obtained for two cylinders with the diameters of  $D=106.6$  mm and  $D=128.0$  mm within free-stream velocities  $U_0 \approx 15 - 44$  m/s, i.e. in the pre-critical range of  $Re_D$ . To clarify the flow physics, patterns of vortex shedding corresponding to growing Reynolds numbers are placed in Fig. 7.8 taken from [1].

<sup>1</sup> Lam K. M., Wei C. T., Characteristics of vortices shed from a circular cylinder and an inclined flat plate. Proc. 4<sup>th</sup> Int. Symposium on Computational Wind Engineering (CWE2006), Yokohama, 2006, pp. 649-652.

The controlled models with spherical vortex-generators were 7 at different angles of attack. Angle of attack  $\theta$  (Fig. 7.7) was zero when spherical turbulators were located in a horizontal central plane of the velocity vector and looked upstream. Measurements were carried out for several  $U_0$  velocities (or Reynolds numbers,  $Re_D$ , based on a cylinder diameter  $D$ ) and several spanwise steps  $\lambda_z$ .

Figure 7.9 shows drag and lift coefficient for  $Re_D \sim 1.25 \times 10^5$ . The vortex generator array with  $\lambda_z = 5$  mm demonstrated a considerable (**over 25%**) drop of drag coefficient at the angle of attack,  $\theta = 30^\circ$ . It occurs due the flow velocity increasing downstream the vortex-generator array where, accordingly, suction raised, as it is shown in Fig. 7.10. This case of the generated flow asymmetry results both in decreased drag and in growing lift. The similar situation is observed at other values of  $\theta$  for  $\lambda_z = 5$  mm. However for angles of attack  $\theta > 40^\circ$ , drag shows rapid recovery and reaches almost an initial value at  $\theta = 70^\circ$ . Under these conditions, lift coefficient drops even to negative values and recovers to zero above  $\theta = 100^\circ$ . Aerodynamic coefficients for  $\lambda_z = 10$  mm and 20 mm show similar behavior although they do not demonstrate such a significant drag drop (it reaches 19% at  $\theta = 30^\circ$ ). But unlike the small spanwise step case, the range of angles of attack with decreased drag values is considerably wider for larger values of  $\lambda_z$ . In addition, lift coefficient increments for larger  $\lambda_z$  are much higher exceeding 0.45 in a wide range of angles of attack. It should be noted that  $\lambda_z = 10$  mm is more effective in terms of flow control than 20 mm, which indicates that an optimal value of spanwise step can be found.

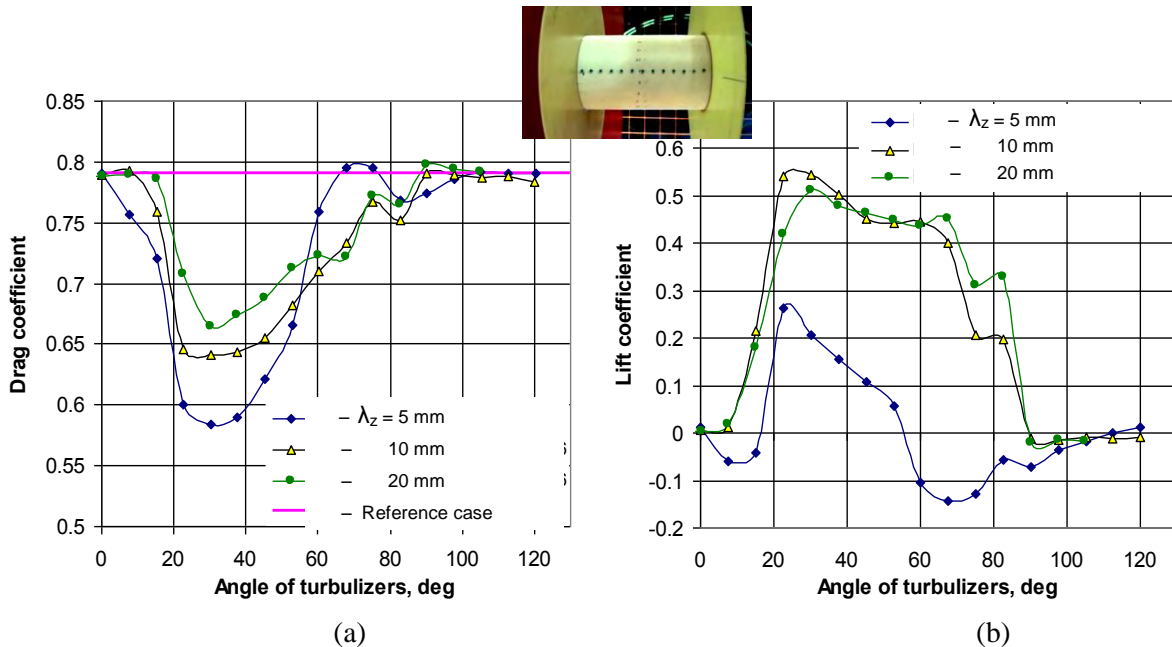


Fig. 7.9. Drag and lift coefficients for D-106.6 cylinder at  $Re_D \sim 1.25 \times 10^5$  for various values of  $\lambda_z$

Twice increased Reynolds number,  $Re_D = 2.47 \times 10^5$ , results in a similar character of aerodynamic coefficients depending on an angle of attack of the vortex-generator array. The shapes of the curves are close to those obtained for  $Re_D \sim 1.25 \times 10^5$  but quantitatively the results are quite different. Lift gain is even greater and reaches the value of 0.64. For  $\lambda_z = 20$  mm it remains high enough (of order of 0.45) up to  $\theta = 90^\circ$ .

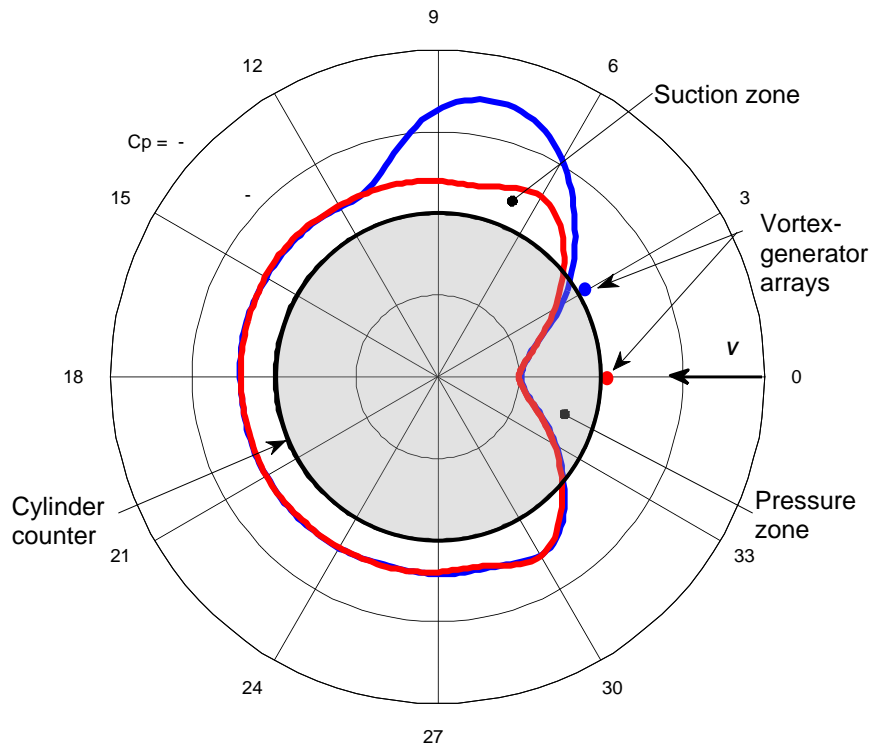


Fig. 7.10. Vector diagram of pressure distribution over  $D=106.6$  circular cylinder for azimuthal angles,  $\theta = 0^\circ$  (red) and  $30^\circ$  (blue), of the array of spherical vortex generators

Drag and lift coefficients for a bigger cylinder with  $D=128$  mm at  $Re = 248\,000$  are similar to those for  $D=106.6$  mm cylinder including values of lift coefficients. But at a higher Reynolds number the effect seemed to vanish. It can be explained with quite different (supercritical) flow regime around the cylinder shown in Fig. 3.1. for high Reynolds numbers. As such, it implies different mechanisms of flow modification and requires further studies.

### Summary

The physical phenomena involved into the developed flow-control strategy using MW-initiated plasma arrays are rather complex by their

very multidisciplinary nature. Therefore results obtained for flows around circular cylinders with the prototype arrays of mechanical vortex generators facilitate plasma experiments making them more time- and cost-efficient.

Two basic control parameters under consideration were an optimal value of a spanwise distance between the vortex initiators,  $\lambda_z$ , and an angle of attack between their spanwise array and a flow velocity vector,  $\theta^\circ$  (Figs. 7.7 and 7.10). These aerodynamically optimal values must be matched with those required electrodynamicly from a viewpoint of reliable ignition of plasma discharges along the whole array and their stable operation. Usually, a number of compromises is necessary to provide such operation in the environment of wind-tunnel experiments. The value of  $\lambda_z = 10$  mm was found in the prototype experiments to be optimal having shown the drag drop and the lift growth for angles of attack within  $\theta = 20^\circ - 80^\circ$  of the tested circular cylinder model (Fig. 7.9). Measurements of lift and drag coefficients were validated with the measured pressure distributions around the models.

Thus  $\lambda_z = 10$  mm is recommended for testing in electrodynamic experiments. It is found to be in a good agreement with technological electrodynamic possibilities to generate a system of multiple localized plasma discharges. Altogether, it defined a choice of parameters for the plasma-controlled circular cylinder together with the measurement ranges of Reynolds numbers and angle of attacks,  $\theta = 15^\circ - 90^\circ$ .

*Results for O-ring mechanical vortex-generators (symmetric excitation) are given in the Appendix to Chapter VII.*

### 7.3. Localized MW heating of flow with arrays of plasma discharges

**Plasma-controlled experiments with a circular cylinder** were planned as a logical continuation of the prototype problem of a circular cylinder controlled with an array of mechanical vortex generators. Test model (described in detail in Chapter V) was a cylinder of  $\sim 90$  mm in diameter. This diameter was chosen to satisfy both blockage criteria ( $\leq 10\%$  of test section cross-section area) and Reynolds number range of interest ( $10^5 - 2.5 \times 10^5$ ) for the accessible free-stream velocity range of 15 - 60 m/s.

The experiments aimed at the investigation of drag, lift coefficients and pressure distribution over a circular cylinder. MW pulse duration and repetition rate values were varied during the tests.

In the beginning it was found that the durability of the model is not sufficient to provide investigations in a wide range of test parameters without initiators repair. During testing, the discharge ignition tended to happen in the model interior that immediately stopped the wind-tunnel measurements to cover the model surface with graphite around the initiators. Therefore, tests were carried out for a limited range of flow and control variables like pulse duration,  $t$  / pulse repetition rates,  $F$ . Results of 2 sets of electrodynamic parameters are discussed below: (1)  $t=500 \mu\text{s}$ ,  $F=50$  Hz and (2)  $t=50 \mu\text{s}$ ,  $F=50$  Hz.

#### (1) EM mode: $t=500 \mu\text{s}$ at the repetition rate, $F=50$ Hz

This combination was taken according to the MRTI recommendations. Two test runs were performed at  $Re = 1.22 \times 10^5$  ( free-stream velocity,  $U_0= 20.5$  m/s). A downstream distance between heated wakes in a free stream was estimated to be about 0.4 m, i.e. 3 times larger than the cylinder diameter. Therefore, no significant aerodynamic gain could be expected. Figs 7.11 (a), (b) show drag and lift coefficient variations vs. angular position,  $\theta$ , of initiators of two test runs. Drag increment in the controlled case is found in the range of  $\theta = 15^\circ - 45^\circ$  decreasing to zero at  $\theta = 60^\circ$ . Drag reduction was obtained within  $\theta = 60^\circ - 75^\circ$ . Lift found in a reference case is a result of unsmooth cylinder surface caused by the bulged initiator tips. However the comparative experiment showed growing lift in the controlled case with the maximal value of  $\Delta C_y = 0.25$  at angle of attack of  $75^\circ$ . These results are in a good agreement with pressure distribution in Figs. 7.12(a) and (b) shown for  $\theta = 30^\circ$  and  $75^\circ$ .

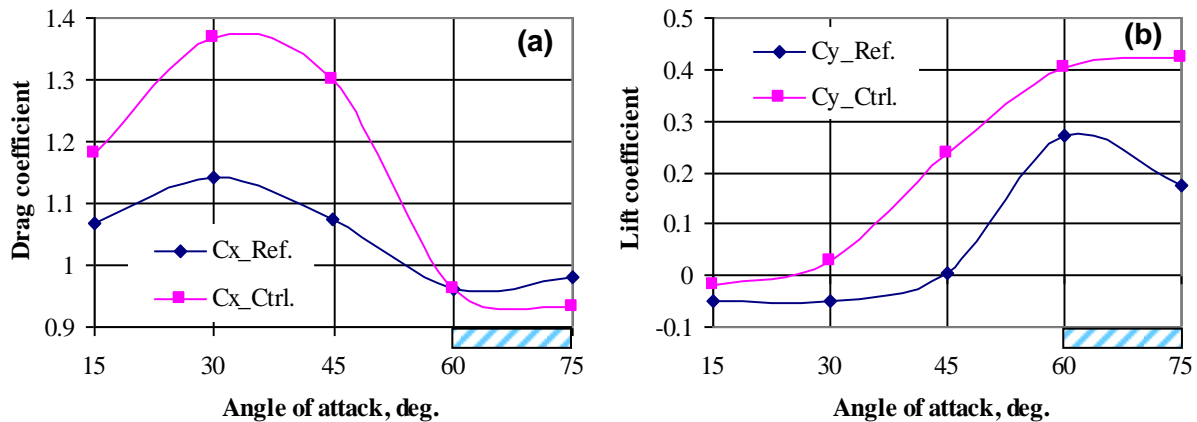


Fig. 7.11. Drag (a) and lift (b) coefficients vs. angular position of initiators:  $Re = 1.23 \times 10^5$ ,  $t=500 \mu\text{s}$ ,  $F=50$  Hz

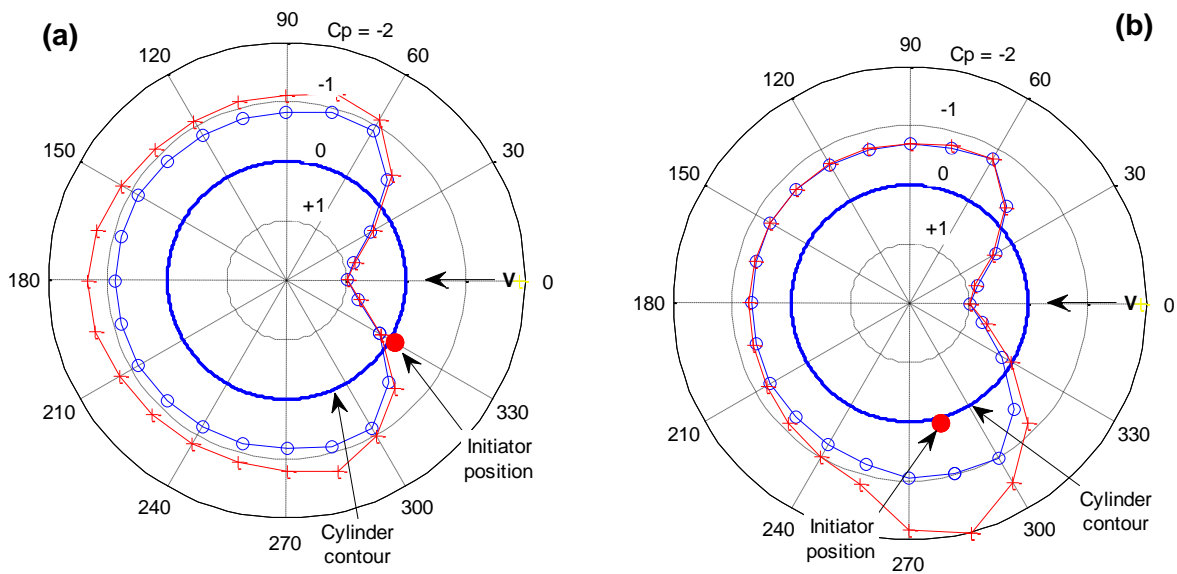


Fig. 7.12 Pressure distribution over

$Re = 1.23 \times 10^5$ ; (a) angle of initiators,  $\theta = 30^\circ$ ; (b)  $\theta = 75^\circ$

For  $\theta = 30^\circ$  suction over a cylinder surface is almost everywhere greater in the controlled case, especially in its aft part that results in growing drag. At the same time, the asymmetry of pressure distribution in the controlled case is not essential to increase lift substantially. For the initiators position of  $75^\circ$ , the picture is opposite. Suction increases only in the vicinity of initiators creating strong asymmetry of pressure distribution in the controlled case that results in significantly growing lift. Besides, suction increases mainly at the frontal part of the cylinder thus creating forward-directed suction force, which leads to drag reduction.

## (2) EM mode: $t=60 \mu s$ at the repetition rate, $F=500 \text{ Hz}$

Here, pulse duration was chosen as short as possible for reliable initiation of discharges, and the repetition rate was to provide a few thermal wakes over cylinder surface simultaneously drifting downstream. Measurements were carried out for  $Re = 1.23 \times 10^5$  and  $Re = 1.83 \times 10^5$  ( $U_0 = 20$  and  $30 \text{ m/s}$ ). Fig. 7.13 shows drag and lift coefficients depending on  $\theta$  at  $Re = 1.23 \times 10^5$ . In controlled case, drag behavior is similar to that for previous case only for  $\theta = 75^\circ$ . Lift coefficient behavior in looks similar to the previous one but its increments are smaller. It could happen because visually controlled energy of discharges (their brightness) decreased during the tests.

Pressure distributions are also in a good agreement with lift and drag behavior. They show that for this mode of MW radiation, suction growth in the aft part of the cylinder at  $\theta = 45^\circ$  is less than in the previous mode and pressure asymmetry is also less at  $\theta = 75^\circ$ .

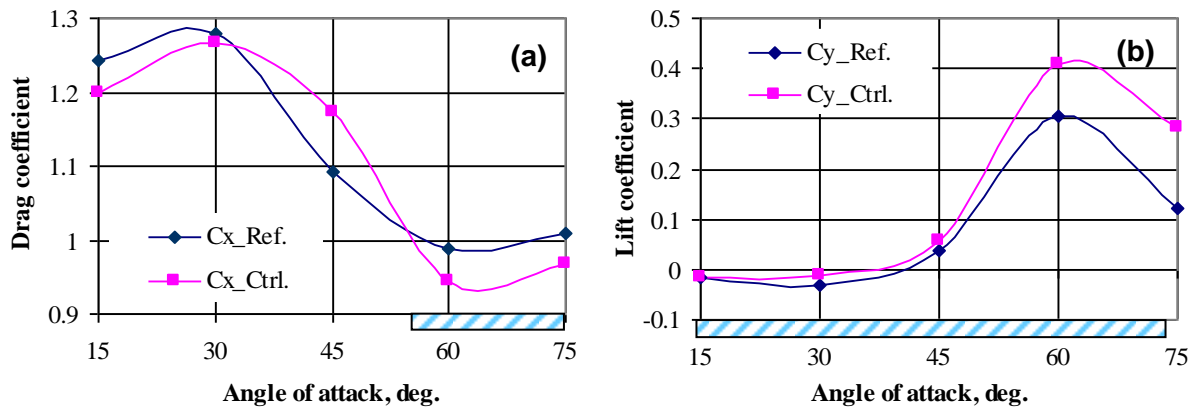
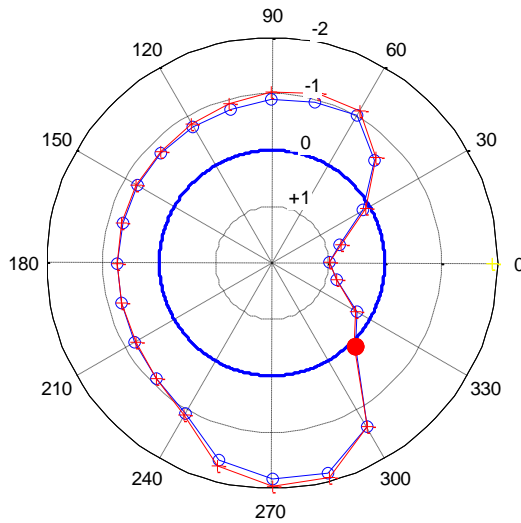


Fig. 7.13. Drag (a) and lift (b) coefficients vs. position of initiators:  $Re = 1.23 \times 10^5$ ;  $t = 60 \mu s$ ;  $F = 500 \text{ Hz}$



$Re = 1.83 \times 10^5$ ;  $t = 60 \mu s$ ;  $F = 500 \text{ Hz}$ ;  $\theta = 45^\circ$

For a greater free-stream velocity ( $Re = 1.83 \times 10^5$ ), it was found that the flow over the cylinder was much less receptive to thermal disturbances introduced with arrays of plasma discharges (Fig. 7.14). In this situation, mechanical disturbances of the flow field prevailed because of protrusions (Fig. 7.15) of plasma initiators as well as of the available surface step at the edge of two segments of the cylinder (2). Only subtle variations of drag and lift coefficients were found in the controlled case compared to the reference. Pressure distribution at  $\theta = 45^\circ$  is asymmetrical in both reference and controlled cases.

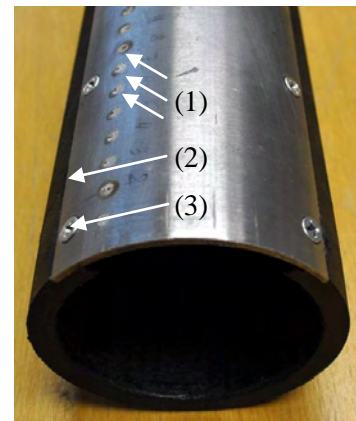


Fig. 7.15. Sources of surface roughness: (1) protrusions of initiators, (2) step between joined parts, (3) bracketry

## Summary

1. A circular cylinder controlled with an array of MW-initiated plasma discharges showed feasibility and practical ways to improve the aerodynamic performance of blunt bodies.
2. Life expectancy of plasma initiators is insufficient for extensive wind-tunnel testing. The plasma-controlled model design and manufacturing technology should satisfy both aero- and electrodynamic requirements especially for high-speed flows; electrodynamic adjustments of the model require further efforts.

### 7.3. Preliminary wind-tunnel testing of the Streamlined Aerodynamic Profile, “SAP”, controlled with an array of plasma discharges

In view of the complicated and laborious studies of plasma-controlled flow around slender bodies, the initial set of experiments was planned to give a clue and to estimate a scope of thorough future investigations. Thus the experiments were focused on the case of user-proven ring-type plasma actuators mounted at  $\bar{c} = 25\%$  on the “SAP” model lower surface (see Fig. 7.16 and model description in Chapter V).

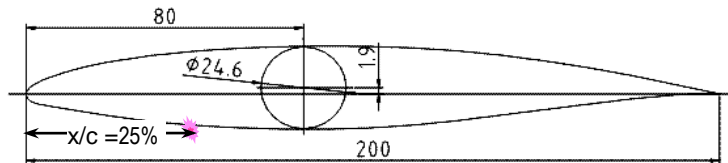


Fig.7.16. “SAP” with the array of plasma actuators at 0.25c

Angle of attack and Reynolds number values varied to find a gain in aerodynamic performance under a spectrum of conditions from a smooth to inevitably rough flow separation like in case of a circular cylinder.

Curves hereinafter are marked as follows: first three symbols refer to the Reynolds number,  $Re \times 10^5$ , “Ref” and “Ctrl” refer to the reference and controlled cases correspondingly. For example, “2.0\_Ref” means that a curve is obtained for the reference case at  $Re = 2.0 \times 10^5$ . Angle-of-attack axes,  $C_L$ , and  $C_m$  are reversed for convenience of the analysis.

#### Negative angles of attack

It was found for the earlier convex-concave R800 models that plasma discharges improved stall characteristics on the profile side where they were installed. Therefore to highlight the prospects, negative angles of attack were prioritized for the measurements at  $Re = (4.0, 5.0, 6.0) \times 10^5$ .

Figures 7.17 – 7.19 show drag, lift and pitch moment coefficients for  $Re = 4.0 \times 10^5$ . The flow control increases maximal lift coefficient  $C_L$  by  $\sim 10\%$  at a stall angle of  $11^\circ$  and flattens the post-stall lift decaying area compared to the reference case. Post-stall lift coefficients remain greater in the controlled case than the maximal reference lift up to  $\alpha = 16^\circ$ ; it can be interpreted as the flow

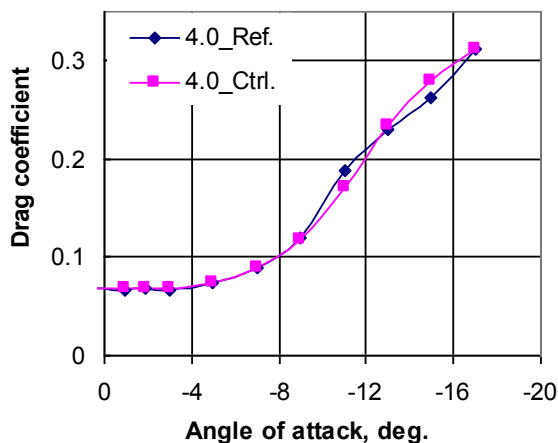


Fig. 7.17. Drag coefficient vs. angle of attack at  $Re = 4.0 \times 10^5$

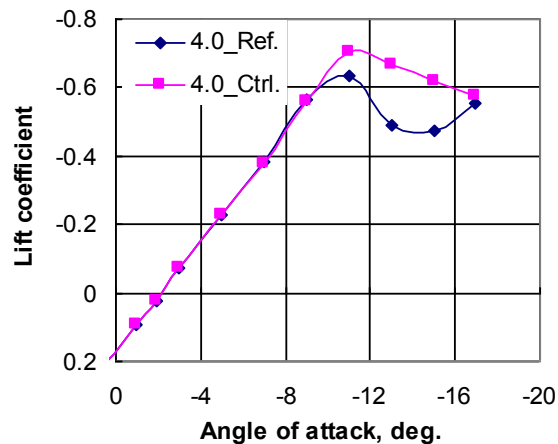


Fig. 7.18. Lift coefficient vs. angle of attack at  $Re = 4.0 \times 10^5$

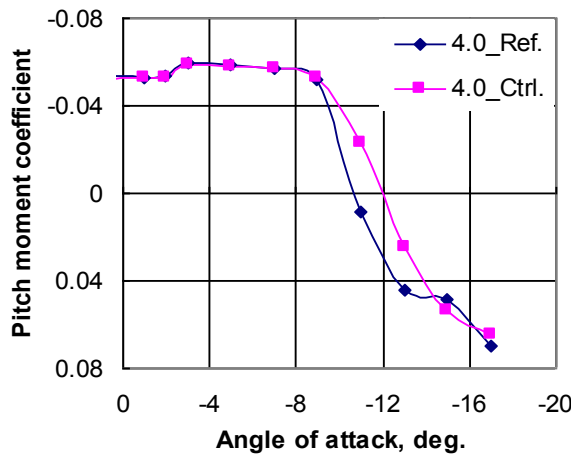


Fig. 7.19. Pitch moment coefficient vs. angle of attack at  $Re = 4.0 \times 10^5$

within roughly the same range of angles of attack and lift coefficient increments are close to those at  $Re = 4.0 \times 10^5$ . E.g. Figs. 7.20.–7.21 show drag and lift coefficients at  $Re = 5.0 \times 10^5$ . Pitch moment coefficients are in a good agreement with the discussed results.

#### Repeatability of measurement results

Accuracy of experimental data is an essential issue of all the measurements. It was evaluated from the statistical processing of experimental data obtained under the same conditions at different moments. It shows that all results are very close to each other and demonstrate the typically observed effects depending on Reynolds numbers. These effects, like a  $C_{L_{max}}$  growth, are consistent with the relevant theory and general knowledge of the problem.

separation delay by  $\sim 4^\circ$ . Drag coefficients decrease in the controlled case around the stall angle. Such a combined impact on lift and drag coefficients is advantageous for an aircraft because it leads to the reduced roll rate and to slower aircraft deceleration under pre-stall conditions.

Nose-down increment of a pitch moment coefficient (that corresponds to the nose-up increment for a normal flight) means that the suction grows in the “SAP” nose area under the applied plasma control. It was verified with the measured pressure distribution.

Negative angles of attack for  $Re = (5.0 \text{ and } 6.0) \times 10^5$  demonstrated the same flow-control tendencies. Drag coefficients remained lower

## VIII Chapter. ACHIEVEMENTS. REFERENCES. PROSPECTS.

**8.1. ACHIEVEMENTS:** Three large-scale scientific achievements are an important positive outcome of the Project # UKE2-1518-KV-07.

### (1) Verified proof of the developed flow-control concept based on minimal energy outlay

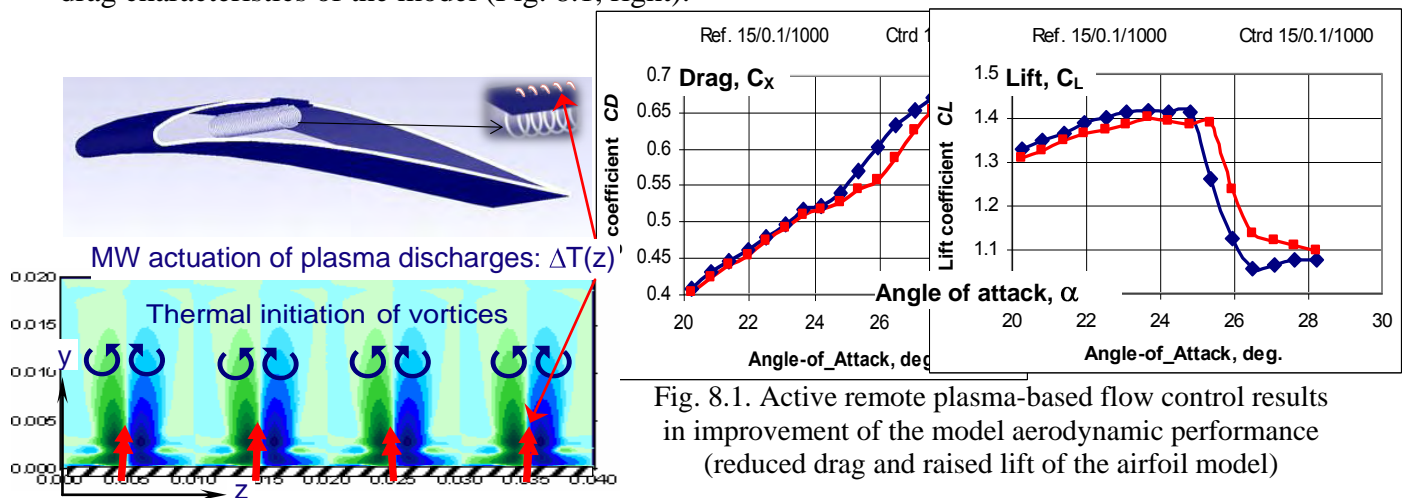
Fundamental investigations of boundary-layer stability and receptivity brought to the development of the innovative strategy of flow control at minimal energy outlay. The latter comes from the concept essence that is based on generation of inherent to flow streamwise vortices that does not require significant modification of the flow field. A number of adequate engineering solutions in the framework of this concept is found due to the concerted effort of specialists of the Institute of Hydromechanics, National Academy of Sciences of Ukraine, National Aviation University of Ukraine, and Moscow Radiotechnical Institute, Russian Academy of Sciences. The Project # UKE2-1518-KV-07 shows diversity of such approaches based on a spanwise-regular temperature boundary condition  $\Delta T(z)$  generated remotely with microwave radiation.

### (2) Engineering feasibility of the concept realization within a spectrum of possible solutions

It is the multidisciplinary nature of the project and close cooperation of professionals in the fields of aero- and electrodynamics that brought to the insight into the nature of fluid and electrodynamic problems involved. It enabled to match requirements in the both fields and to develop 2 different ways to generate the key  $\Delta T(z)$  boundary condition:

- localized MW heating of the surface with flush mounted arrays of streamwise strips, and
- MW initiation of plasma discharges using spanwise arrays of embedded actuators.

In addition, the prototype problem with spanwise arrays of mechanical vortex-generators was studied to show the integrity of the flow-control approach illustrated in Fig. 8.1, left. Initiated systems of vortices with a given scale near a surface can result in expected modification of lift and drag characteristics of the model (Fig. 8.1, right).



Various types of MW-initiated thermal arrays are designed and investigated in MRTI with their advantages and drawbacks discussed; most promising are mounted in the models and tested in the IHM wind tunnel. They are, e.g. ring-type (Fig. 8.1, top left) and newly designed linear G-shaped plasma actuators (Fig. 8.2). Though the latter consume low energy due to very small levels of the initiating electromagnetic field, they were shown to need further investigations to be successfully applied for boundary-layer control purposes.

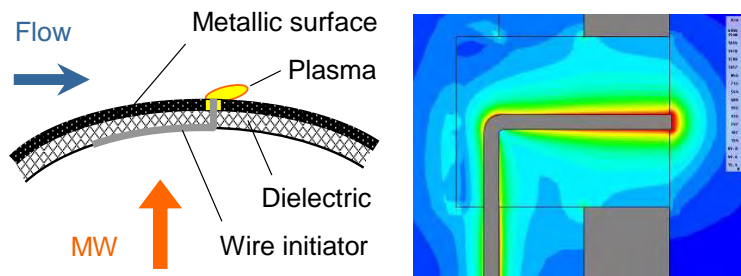


Fig. 8.2. Linear G-shaped plasma actuator (left) and MW-field pattern around it (right)

Operation of initiators was studied in the wind tunnel for various types of controlled models having proven the applicability of the developed methods both to streamlined and bluff bodies. Five years of continuous coordinated efforts gave birth to new ideas and the accumulated experience helps to distinguish most prospective of them.

**(3) Innovative Aerodynamic Complex for Interdisciplinary Research (ACIR) having no analogues in the world:** it is designed and optimized for a broad variety of fluid dynamic problems to solve now and in the future (Fig. 8.3). It was followed by the creation of the **Laboratory for Advanced Aerodynamics and Interdisciplinary Research (Advanced AIR)** at the Institute of Hydromechanics, National Academy of Sciences of Ukraine, Kiev

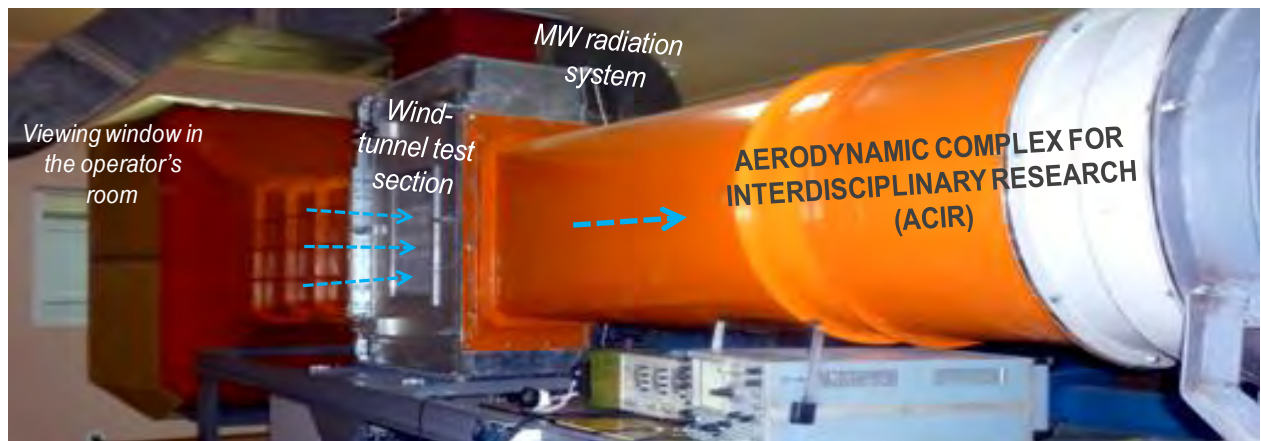


Fig. 8.3. Aerodynamic Complex for Interdisciplinary Research (ACIR)

The successful project implementation would not be possible without the development of the experimental base. As a result, the specialized **Laboratory for Advanced AIR** was created at the Institute of Hydromechanics, NASU. The Laboratory is equipped with two mutually complementary wind-tunnel facilities, automated systems of aerodynamic experiment control, data acquisition and processing, and the affiliated workshop for facility remodeling, fabrication and adjustments of test model. In addition to scientific research, it operates for training of relevant graduate and post-graduate students.

The unique **ACIR** is developed and optimized in a process of investigations related to advanced passive, active and remote methods of flow control based, in particular, on application of microwave radiation and plasma generation. For the latter case, it operates together with its electrodynamic twin built in MRTI to model the electrodynamic situation in the ACIR test section.

ACIR is designed so that to solve a number of various problems related to flow control including those dealing with operation of turbine blade cascades. **Together with the created Laboratory for Advanced AIR, it is open for mutually beneficial research.**

## **8.2. REFERENCES**

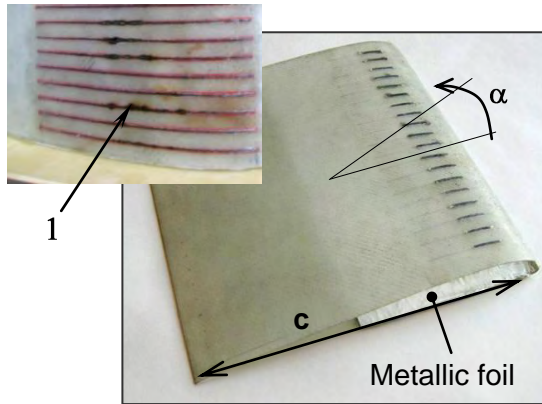
1. Tani, I. Production of longitudinal vortices in the boundary layer along a curved wall, **1962**, *J. Geophys. Res.*, **67** (8), 3075-3080.
2. Yurchenko, N., Delfs, J., Boundary layer control over an active ribletted surface, **1999**, *In: Fluid Mechanics and its Applications*, eds. G.E.A. Meier and P.R. Viswanath, Vol.53, 217-222, Kluwer Acad. Publishers.
3. Vynogradskyy, P., Laznyuk, P., Pavlovsky, R., Zhdanov, A., "Zero Free-stream Velocity Loads Processing in Weight Tests on 6-KETV Balance in TAD-2 Wind Tunnel of KIUCA", Herald of KIUCA, No. 2, Kiev, 1999, (In Ukrainian).
4. Yurchenko, N., Rivir, R., Pavlovsky, R., Vinogradsky, P., Zhdanov, A., Control of the profile aerodynamics using streamwise vortices generated in a boundary layer, **2003**, *Proc. World Congress "Aviation in the XXI-st Century"*, Kyiv, Ukraine, September 14-16, 2003.
5. Yurchenko, N., Optimization of flow about a turbine blade by means of turbulence scale control, **2007**, *AIAA Paper- 2007- 0524*.
6. Yurchenko, N., Vinogradsky, P., Physical mechanisms of turbulence control in near-wall flows under centrifugal forces – 2 parts, **2007**, *AIAA Paper-2007-4218*.
7. Yurchenko, N., MW-generated point plasma discharges as a novel approach to boundary-layer control, **2008**, *AIAA Paper-2008-1388*.
8. Yurchenko, N., Rozumnyuk, N., Zagumennyi, Ya., Numerical Simulation of Near-Wall Turbulence Structure Affected by MW-Generated Point Plasma Discharges **2008**, *AIAA Paper-2008-1440*
9. Yurchenko, N., Strategy of Turbulence Control Based on Flow Instability Mechanism, **2008**, *AIAA Paper-2008-4206*.
10. Vinogradsky, P., Yurchenko, N., Pavlovsky, R., Zhdanov, Aerodynamic Facility with MW-Systems for Flow Control Based on Localized Plasma Generation, **2008**, *AIAA Paper-2008-3939*.
11. Yurchenko, N., Speculation about near-wall turbulence scales, **2008** *Physica Scripta* **T132** 014011 (6 pp).
12. Yurchenko, N., Paramonov, Yu., Vinogradsky, P., Pavlovsky, R., Zhdanov, A., Control of flow characteristics using localized plasma discharges, **2009**, *AIAA Paper-2009-1227*.
13. Esakov, I., Grachev, L., Ravaev, A., Khodataev, K., Yurchenko, N., Vinogradsky, P., Zhdanov, A., Initiated Surface MW Discharge as an Efficient Active Boundary-Layer Control Method, **2009**, *AIAA-2009-0889*
14. Yurchenko, N.F., A method of active boundary-layer control over bodies of complex geometry, **2009**, *Patent of Ukraine № 45240 (registered on 26.10.2009)*
15. N. Yurchenko, N., Rozumnyuk, N., Vinogradsky, P., Kudryavtsev, V., Boundary-Layer Control Based on Localized Plasma Generation: Aerodynamic Problem, **2010**, *AIAA Paper-2010-1383*.
16. Vinogradsky, P., Yurchenko, N., Pavlovsky, R., Zhdanov, Lazarjan, M., Paramonov, Yu., Esakov, I., Ravaev, A., Boundary-Layer Control Based on Localized Plasma Generation: Wind-Tunnel Investigations. **2010**, *AIAA Paper-2010-1007*.

17. Yurchenko, N., Multidisciplinary research of transport phenomena in boundary layers, **2010**, *Proc. 21st International Symposium on Transport Phenomena, Kaohsiung City, Taiwan*.
18. Yurchenko, N., Research strategy for active flow control based on distributed thermal fields, **2010**, *Int. J. of Fluid Mechanics Research*, v. 57, No. 5, pp. 470-489.
19. Yurchenko, N., From Marine Animals to Plasma Aerodynamics, **2011**, *49th AIAA Aerospace Sciences Meeting (Invited lecture)*, *AIAA Paper-2011-1341*.
20. Yurchenko, N., Active Flow Control Based on Distributed Thermal Fields: Principles and Their Realization, **2011**, *AIAA Paper-2011-1076*
21. Yurchenko, N., Esakov, I., Interdisciplinary studies of flow control based on localized plasma discharges, **2011**, *Int. J. of Fluid Mechanics Research*, v.38, pp.272-289.
22. Esakov, I., Ravaev, A., Khodataev, K., Lavrov, P., Yurchenko, N., Vinogradsky, P., Zhdanov, A., Active Flow Control with MW-Generated Thermal Fields: Electromagnetic Modeling, **2011**, *AIAA Paper-2011-1077*
23. Yurchenko, N., Rozumnyuk, N., Paramonov, Yu., Tsymbal, V., Vinogradsky, P., Zhdanov, A., Impact of Spanwise Arrays of Plasma Discharges on Aerodynamic Performance, **2012**, *AIAA paper-2012-1029*
24. I. I. Esakov, K. V. Khodataev, A. A. Ravaev, P. B. Lavrov: Physical grounds of new-type electromagnetic vibrators and prospects of their application. AIAA Paper 2010-0834.
25. A. A. Ravaev, L. P. Grachev, I. I. Esakov, K. V. Khodataev, P. B. Lavrov: General features and application of electromagnetic vibrators located close to a metal plate-reflector in the field of microwave radiation. *VIII Workshop "Thermochemical Processes in Plasma Aerodynamics," July 12-14, 2010, St-Petersburg*, P. 40-41.
26. A. A. Ravaev, I. I. Esakov, L. P. Grachev, P. B. Lavrov: Main features and application of electromagnetic vibrators located near to a metal wall. *49<sup>th</sup> AIAA Aerospace Sciences Meeting, 4-7 January 2011, Orlando, Florida, USA*. Paper: AIAA-2011-1078.
27. Yurchenko N., Voropaev G., Pavlovsky R., Vinogradsky P., Zhdanov A. Flow control using variable temperature boundary conditions. *Proc. European Fluid Mechanics Conference, EFMC-2003, Aug. 24-28, 2003, Toulouse, France*.
28. Bychkov, I. Esakov, L. Grachev, A. Ravaev, K. Khodataev, N. Yurchenko. Initiated surface MW discharge in experimental investigations of new boundary layer control method. *VI Intern. Symp. "Thermo-Chemical Processes in Plasma Aerodynamics, May 12-14, 2008, St-Petersburg, Russia*. P. 27-29.
29. Kirill Khodataev. Various types of initiators for attached undercritical MW discharge ignition. *45th AIAA Aerospace Sciences Meeting 8-11 January 2007, Reno, NV*. Paper AIAA-2007-0431

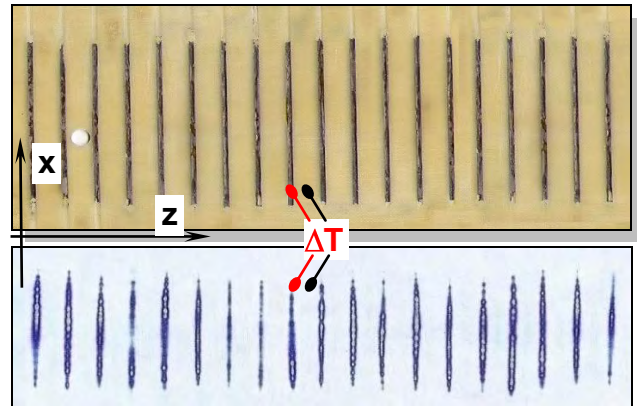
### 8.3. PROSPECTS

#### 8.3.1. MW potential as an engineering basis of the flow-control strategy grounded on generation and maintenance of spanwise-regular temperature boundary condition

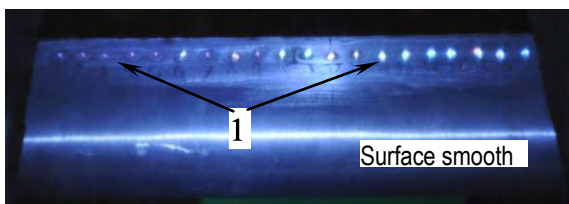
Microwave heating of embedded arrays of streamwise elements (Fig.8.4, a, b) proved its conceptual applicability to flow control due to registered regular  $T(z)$  surface temperature (Fig. 8.4, b). This method must be further developed in part of electrodynamic solutions eliminating nonuniform heating like one illustrated in Fig. 8,a top left). The correlated aerodynamic part should guide it in terms of optimal values of  $\Delta T(z)$ , extension and location of the controlled section over the model.



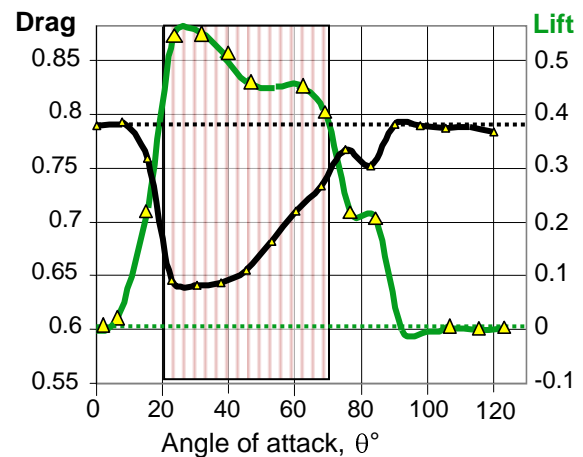
(a) Models fabricated for wind-tunnel testing with arrays of embedded MW-heated elements; 1— result of MW-field nonuniformity



(b) MW-heated graphite elements(top) and surface temperature array indicated with thermo-sensitive paper (bottom)



(c) Cylinder surfaces with arrays of prototype mechanical vortex-generators (top) and visibly “underdeveloped” plasma discharges (bottom) aimed to impose z-regular flow conditions; 1— result of MW-field nonuniformity



(d) Lift (green) and drag (black) coefficients of a circular cylinder controlled with an array of mechanical vortex generators:  $D=106.6$  mm,  $Re=1.24 \cdot 10^5$ ,  $\Delta z=10$  mm

Fig.8.4. Revealed weaknesses, advantages and prospects of MW-based realization of the developed flow-control strategy

A search of electrodynamically optimal solutions should also be continued in the framework of MW-initiated arrays of plasma discharges like the one shown in Fig. 8.1. These investigations are to be focused on a closer match to aerodynamic requirements formulated for various types of models. E.g. vortex generation using arrays of spanwise-regular mechanical disturbers showed itself as tried-and-true method with a range of angles of attack  $\theta=20-70^\circ$  where drag dropped and lift raised (Fig. 8.4,d). Considered as the prototype problem within the same flow-control strategy, it must have been successfully modified into the method of localized plasma discharges applied to curved surfaces. In practice, this future success will be achieved after fundamental tasks will be solved of reliable plasma ignition and technological requirements will be satisfied to the surface smoothness, operational easiness in flow conditions, etc.

Thus the obtained experience in a form of all the revealed advantages and drawbacks of the developed microwave methods of flow control as well as the insight into electro- and fluid dynamic problems can guarantee the improvement of the worked out and investigated engineering solutions. The created aerodynamic complex (ACIR, IHM) together with the electrodynamic analogue of its test-section (MRTI) provide the sufficient experimental base for implementation of well-qualified interdisciplinary flow-control investigations involving MW devices.

### 8.3.2. TEMs' potential to generate the given temperature boundary condition for flow control

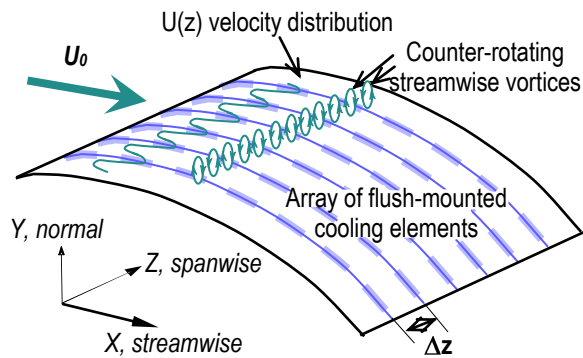


Fig. 8.5. Perspective solution of the flow-control problem using multi-element TEMs arrays

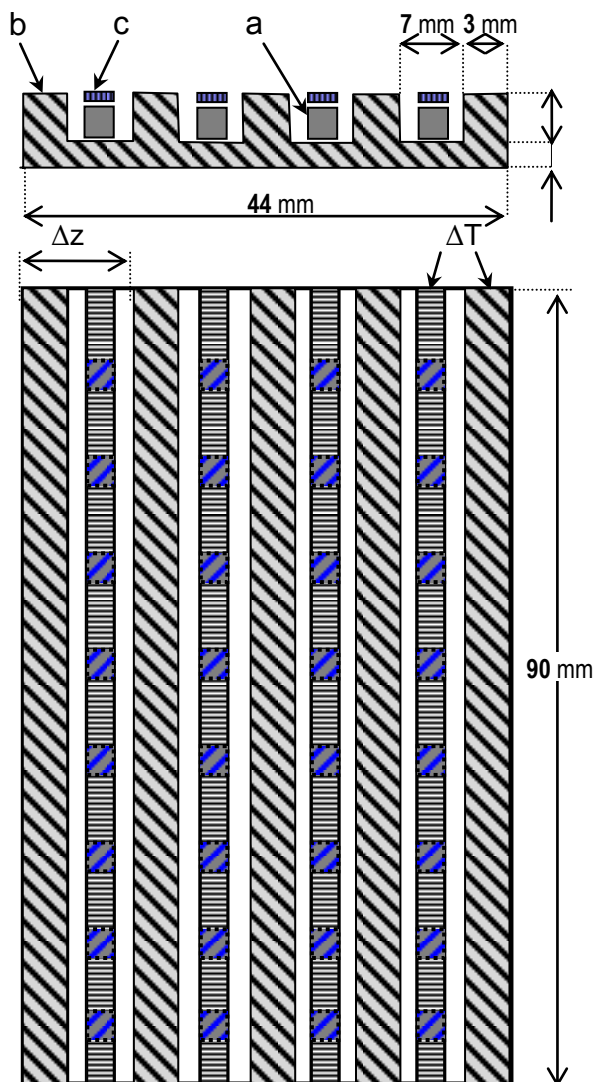


Fig. 8.6. Designed multi-element TEM: a) Peltier element; b) hot strips, copper; c) cold strips, copper.

The key project idea of turbulence control through selective surface heating triggered a novel engineering approach that is based on application of thermoelectric modules, TEMs (or Peltier elements), to create the necessary  $\Delta T(z)$  temperature gradient. It is shown schematically in Fig. 8.5. The feasibility of such an approach to flow control was investigated by the involved scientists of the **Institute of Semiconductor Physics (ISP)**, **National Academy of Sciences of Ukraine**, Kiev. For preliminary studies, they offered the design (Fig. 8.6) which consisted of alternate heated and cooled strips due to the applied arrays assembled from Peltier elements. The assembly of the 90x44x6 mm copper module is expected to provide the aerodynamically required spanwise temperature variation with a step of  $\Delta z = 10$  mm (Fig. 8.6). The accordingly fabricated system based on TEMs is shown in Fig. 8.7.

In experiments held in the ISP NASU, Peltier elements were chosen according to the aerodynamic requirements and the TEM system was assembled from 32 elements connected serially (Fig. 8.6).

#### Characteristics of the Peltier element:

Dimensions: 4.1x4.1x2.97 mm,  
 $I_{\max} = 2\text{A}$ ,  $U_{\max} = 0.8\text{V}$ ,  
 $Q_{\max} = 0.95\text{W}$ ,  $\Delta T_{\max} = 69^\circ\text{C}$ .

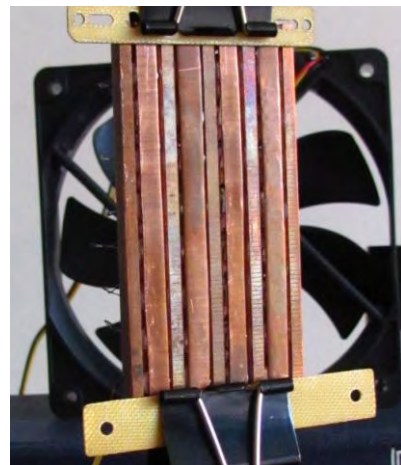


Fig. 8.7. Fabricated multi-element TEM

The following reasons were taken into consideration at the choice of Peltier elements:

- Small dimensions to satisfy the requirement of 10 mm temperature field periodicity ( $\Delta z$ , Figs. 8.5, 8.6) related to a typical size of models used in the ACIR wind-tunnel experiments;
- Appropriate temperature difference between hot and cold “poles” to create the  $\Delta T$ ;
- Availability of industrial elements to avoid customized devices at this stage of research.

To emulate an impact of the air flow on heat transfer from the module to fluid and thus on the achievable  $\Delta T$  as well as to estimate preliminary correlation between the Peltier elements, the module backside was actively cooled using a fan with a variable rotation speed (Fig. 8.7).

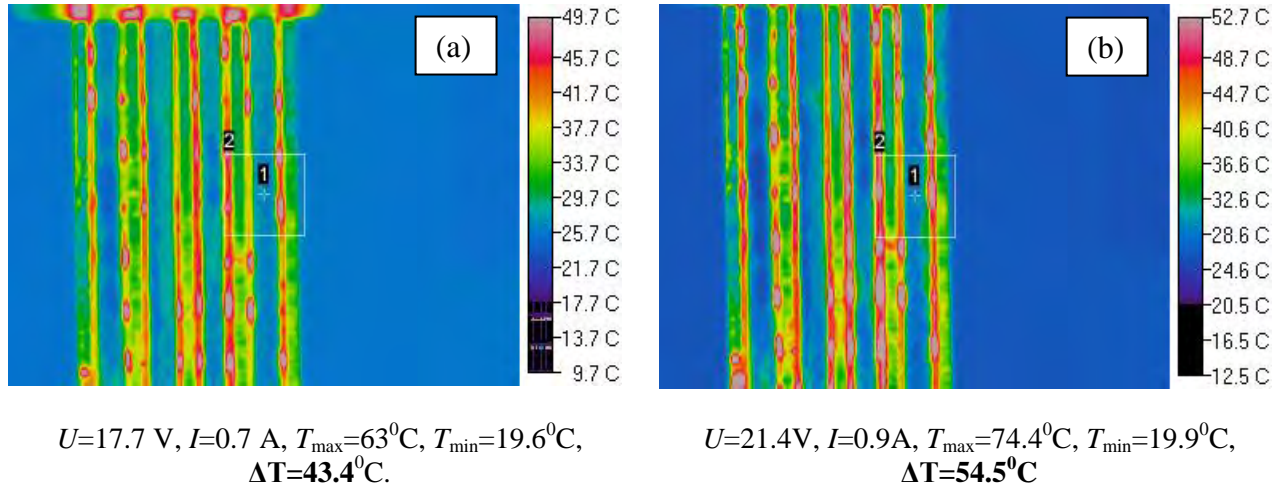


Fig. 8.8. Thermograms of the TEM at different operating modes: 1, 2 high and low temperature strips; (a) – ambient fluid; (b) – moderate air flow, 5 min measurements to reach thermodynamic equilibrium

Experiments showed that there exists univocal correspondence between the electric current through Peltier elements, achievable  $\Delta T$  temperatures, and flow velocity. E.g. it was found that the current growing from 0.7 A to 0.9 A at a constant flow rate resulted in  $\Delta T$  raised from 43°C to 54°C. On the contrary, intensified flow rate at constant (0.9 A) current causes the  $\Delta T$  drop from 54°C to 36°C. It should be taken into account in planning aerodynamic experiments with a variable free-stream velocity.

**Reliability of the TEM** is defined basically by Peltier elements used (32 pcs even for 44x90 mm area) and sensitivity of contact wires to heightened temperatures (>120 °C) at which the contact wires could be unsoldered from the Peltier elements.

**Testing of the TEM**, namely, temperature measurements of hot and cold strips were fulfilled using a thermal imager. The obtained results verified with thermocouple measurements are illustrated by thermograms of Fig. 8.8. A disagreement between two sets of results was found to not exceed 2°C.

## Conclusions

Maximal registered temperature difference  $\Delta T(z)=54.5^\circ\text{C}$  for the preliminary tested design at a given certified value for a single Peltier element,  $\Delta T=69^\circ\text{C}$ . Electric current through the one-stage Peltier elements was equal to 0.9A at a maximal permissible value of 2A that gives a certain reserve for a higher blow-off.

The shown one-stage TEM system enables generation and maintenance of  $\Delta T(z)\sim 55^\circ\text{C}$  with 10 mm spanwise step in the array. The power consumption was  $21.4\text{V}\times 0.9\text{A}=19.26\text{W}$  for the 90x44x6 mm

copper module of Fig. 8.6. Development of the array with two-stage Peltier elements will raise  $\Delta T$  under condition of similar power consumption. Impacts of the air flow and the construction itself is a subject for separate investigations.

Variation of both parameters, electric current and flow rate, demonstrated the potentiality of the TEM-based engineering solution that undoubtedly needs additional detailed investigations including possible modifications of the module design. E.g. the system can be optimized due to filling the air gaps between cold and hot strips with a proper thermal insulator to avoid heat exchange through radiation mechanism though the air is believed to be a good insulator.

Thus the significant improvement of the TEM system is expected at the expense of the optimized design, two-stage elements as well as application of customized devices and a better insight into mechanisms of the TEM behavior in the air flow. This is a key issue for the novel flow-control solution in terms of  $\Delta T(z)$  value, space scale flexibility and a range of the method applicability.

## APPENDIX, Ch II

### II-I. PURPOSE, DESIGN, AND DEVELOPMENT: Update process and current state

#### 2.2 ACIR upgrade and the present configuration

Experimental capability of the project implementation directly depends on the facility capacity for adjustments during the research process. In case of the ACIR (Aerodynamic Complex for Interdisciplinary Research), it relates both to electro- and aerodynamic requirements. As described earlier, the ACIR modification aims at the satisfaction of both kinds of requirements and enhancement of its potential due to a possible broader area of problems for fundamental research.

##### *New Eiffel Chamber Manufacturing*

The test section has internal width of 28 cm according to MRTI recommendations and is made of 20 mm thick steel sheets bolted together without welding, which prevents hogging and provides more precise geometry and better flow uniformity. Access door was enlarged to 1000 mm height and 600 mm width. It made the access more convenient to internal rooms of the test section and Eiffel chamber thus improving the operability and making test preparation procedures easier. A new 300 mm wide and 500 mm high, electrically shielded looking window together with a web camera mounted within the test section will enable much better visual observation of the model and picture/video taken during tests both from outside and inside of the test section.

##### *New Pressure Measurement Subsystem*

Old 8-point pressure measurement subsystem limits simultaneous measurements of aerodynamic loadings and static pressure distribution over a model surface. As mentioned above, in some cases pressure distribution characteristics are much more informative in controlled cases to catch flow-control effects. For instance, models with flow control applied to the concave surface demonstrated no change of lift coefficient but analysis of pressure distribution showed considerable pressure redistribution over the surface. This information is essential for deeper understanding of flow control mechanism and for a grounded choice of location of flow-control devices. Old subsystem made it necessary to perform several test runs under the same conditions but with different pressure taps attached to the same eight pressure transducers thus increasing a number of tests and, accordingly, labor cost.

That is why the new 25-point pressure measurement subsystem was developed and assembled (Fig. A2.1). It is based on Freescale's low-cost amplified pressure transducers of MPXV series. Actually, pressure transducers block contains 30 pressure sensors but only 25 of them are connected simultaneously to the data acquisition system.

The configuration includes 25 MPXV-5004 pressure transducers with measuring range up to 4 kPa and 5 MPXV-4006 transducers with measuring range of 6 kPa. The commutation is performed due to switches mounted inside the block in appropriate positions. This very configuration is determined by



Fig. A2.1 - point Pressure Measurement Block

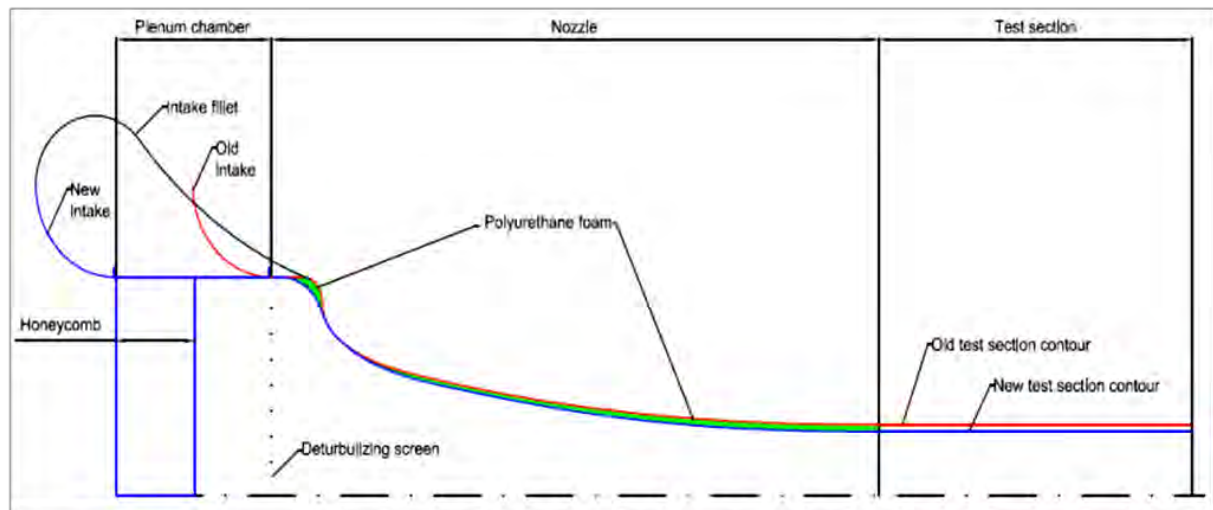


Fig. A2.2 Modification of the AFIR internal contour: horizontal section, right wall; the left one is symmetrical:

the fact that pressure coefficients in a nose part of the model at high angles of attack exceed the value of 5.0, and for dynamic pressure over 800 Pa this leads to transducers overshoot. Besides, the use of wide-range transducers at low free-stream velocities unreasonably diminishes output signals thus worsening accuracy of pressure measurements.

It is decided to use this subsystem with a new PCI1713 32-channel analog input board. A number of pressure measurement channels is selected taking into account simultaneous measurements of loads and static pressure. The first two channels are connected to precision pressure transducers Omega's PX653, measuring dynamic pressure in the test section during wind tunnel flow calibration. Only one of them is used in regular tests while another serves as a feedback signal source for fan control unit; so both channels are permanently connected to these transducers. Another three channels are used for loads measurements and are connected to 3-component strain gage. From the rest of 27 channels, 25 of them are connected to outputs of pressure transducers and the 26-th measures transducers supply voltage. This is made because MPXV-series transducers are ratiometric with respect to supply voltage and the output voltage varied during a test run and between calibrations in spite of a voltage stabilizer. Special calibration procedure accounting for voltage variation is used, which permits to improve repeatability of the results.

### ***Modification of the wind-tunnel internal contour***

This modification is intended to improve both aerodynamic and electrodynamic characteristics of the facility. According to recommendation of MRTI, a new test section was designed with the width 3 cm lower than previous one and is equal to 28 cm. This is expected to provide a more uniform distribution of electromagnetic field around a test model. In its turn, the new test section will require a proper adjustment of the nozzle and diffuser, i.e. the modification of the whole internal contour of the wind tunnel is launched for design and fabrication.

### ***Intake modification***

The performed smoke visualization of the flow around the intake section showed that spontaneous vortices could arise at the sharp edges of the intake. They pass through the deturbulizing screen into the nozzle and test section causing a certain flow instability responsible for data scattering.

To eliminate it, the intake bell was rounded by installation of appropriately curved glass-fiber sheets, which form intake fillet as shown in Fig. A2.2

### ***Plenum chamber formation***

To further improve the flow uniformity, a 40-cm long plenum chamber of constant cross-section

was installed between the intake and nozzle sections. It is planned to place there 20-cm long honeycomb, which would additionally improve the flow uniformity.

### *Nozzle section modification*

Modification was performed using polyurethane foam attached to the side walls of the nozzle section and leveled by special master profile according to the Vitoshinsky curve. After hardening of the polyurethane foam, it was smoothened using sandpaper, glazed, again smoothened with sandpaper until the desired surface shape and roughness was reached and finally painted. In the nozzle part adjacent to the test section, static pressure taps were remounted. Upper and lower walls of the nozzle were also smoothened to improve their shapes, which were a little distorted because of welding deformations during the manufacturing.

The above mentioned smoke visualization and CFD modeling of the flow also showed that radiuses of the nozzle contour in the very front part of the nozzle were too small, which caused flow separation in these corners. These radiuses were increased by filling them with polyurethane foam using the above mentioned procedure (see Fig. A2.2).

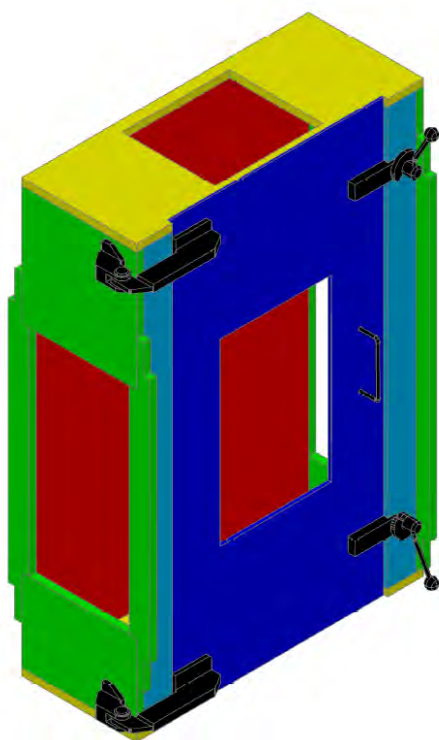


Fig. A2.3 Front-left view of the new test section:

Large access door with 300x500 mm window and 300x 260 mm upper window for the horn MW-radiation antenna

### *Test section*

Newly designed and manufactured test section has more precise geometry and is much more convenient for operation. It is made of thick metal sheets and assembled using bolts that prevent it from welding deformations. Long in a streamwise direction, the top window provides a greater range for the horn antenna displacement to adjust the electromagnetic situation around the test model. The new test section has a large access door to reach not only the model but also upper and lower sections of the Eiffel chamber. The large window in the access door allows better illumination of internal volume from outside and better observation of the model. It is planned to perform internal illumination in the test section using LED and to install a web-cam for remote observation and image capturing during testing.

Slotted upper and lower walls of the test section with a permeability ratio of 18% substantially decrease wind tunnel interference; as a result, aerodynamic corrections to angles of attack and aerodynamic coefficients would be much lesser thus making the flow around the test model closer to the unbounded one.

The test section heaviness reduces its vibrations and, accordingly, the vibrations of the strain gage balance thus improving accuracy of measured data.

The 20 mm-thick right wall of the test section tolerates rigid installation of the equipment both inside and outside of the test section enhancing operational capability of AFIR. It can be, e.g., dummy blades for the blade cascade testing, a hot-wire holder, etc.

### *Diffuser and fan*

For the available fan, the modification of the diffuser includes only side walls streamlining according to the narrower test section similarly to streamlining of the nozzle mentioned above. However it is planned to purchase a new fan with higher efficiency and a larger external diameter. It will enable higher free-stream velocities and lower flow swirling. Higher Reynolds numbers will

expand a range of experimental investigations and a scope of research problems.

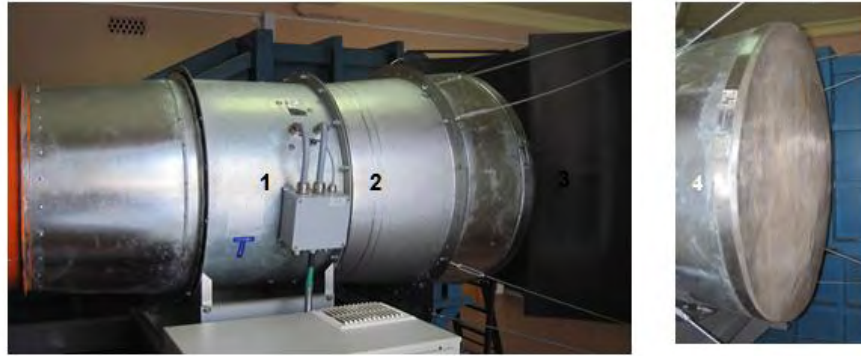


Fig. A2.4 Modified fan/engine section of the ACIR: (A)

1 – front conical duct; 2 – new fan; 3 – exhaust diffuser; 4 -  $\omega$ -shaped flow-reversing surface. (B) MW protection; MW-protecting screen

An outer 710 mm diameter of the new fan system appeared to be larger than the old one (630 mm). To match the new fan with the front part of the wind-tunnel diffuser, the 420 mm long section of a conical duct was fabricated to substitute the almost cylindrical old duct. To reduce full pressure losses at the outlet and to hide aft portion of the engine inside the duct, an additional 650 mm long diffuser was installed downstream of the fan with the exhaust diameter of 900 mm. To organize an outer flow, a specially designed and manufactured  $\omega$ -shaped flow-reversing plate was installed behind the exhaust diffuser. It enabled to diminish exhaust losses and to raise the wind tunnel efficiency.

### Strain gage modification

#### *Pitch-control mechanism*

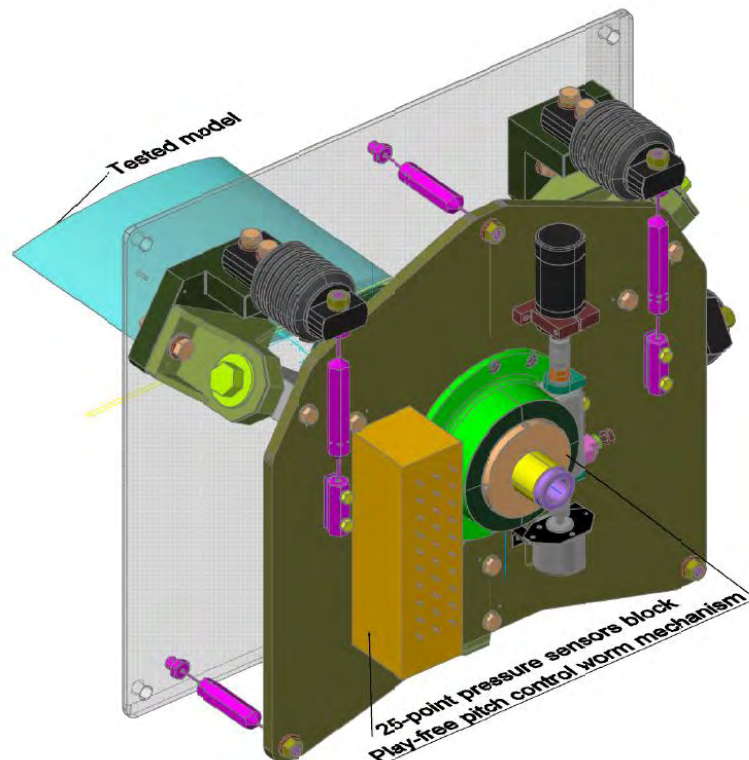


Fig. A2.5. Three-component strain gage balance with play free worm pitch control mechanism

The new play-free pitch-control worm gear mechanism was developed and manufactured in the "Antonov" State Enterprise. This mechanism also provides much more rigid model installation. It was

mounted on the strain gage with the same electric engine and incremental encoder as shown in Fig. A 2.5

### ***Honeycomb***

To complete the update process of wind tunnel structure, honeycomb was installed in settling chamber. The honeycomb is made of 1 mm thick high-impact polystyrene sheet and consists of 160 mm long rectangular cells with 40 by 40 mm cross section. Honeycomb is installed in the upstream portion of settling chamber right up to the outer protective/deturbulizing screen. The distance of 240 mm between the honeycomb and inner

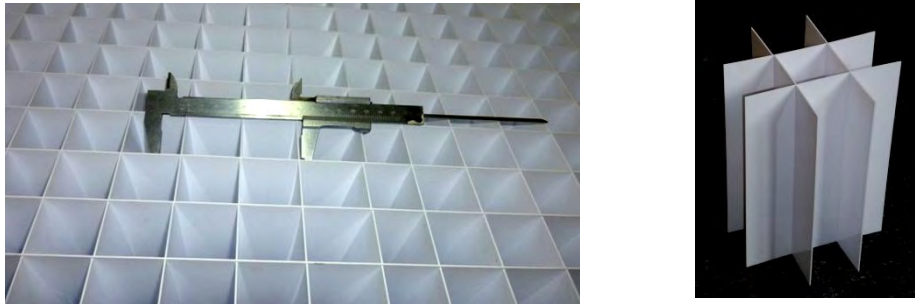


Fig. A2.6. A sample of the fabricated honeycomb fragment;  
(a) actual 4-cm size of cells (b)

deturbulizing screen is provided for dissipation of flow disturbances, generated by honeycomb. View of the honeycomb during its assemblage is given in Fig. A2.6 and 2.7



Fig. A2.7 Laboratory for Advanced Aerodynamics and Interdisciplinary Research:  
Rig fabrication for the honeycomb assemblage and mounting in the ACIR wind tunnel

## 2-3. DATA ACQUISITION AND CONTROL SYSTEM (DAS)

### *Pitch Control and Measurement Subsystem*

In order to decrease DAS CPU loading, it was decided to build autonomous microprocessor-based Pitch Control and Measurement Subsystem, which would permit permanent measurement of model pitch and provide servo drive for a model position based on the commands of DAS software obtained by the RS-232 interface. This subsystem has been realized using Atmega 8515 microcontroller and performs the following functions:

- simultaneous count of a number of pulses generated by the incremental encoder;
- recalculation of a number of pulses into an actual model pitch angle using calibration coefficients and initial model angle obtained from DAS software at the beginning of tests;
- output of an actual model angle on a separate LCD display;
- electric drive control according to the value of a necessary number of pulses obtained from DAS. The later is performed in two modes: quick and slow according to the difference between actual and desired position. Slow mode is realized using pulse-width modulation;
- switching between automatic and manual control modes from the exerciser. In a manual mode, the subsystem still provides permanent count of pulses and the data display both in quick and slow motion modes.

The subsystem electronics with appropriate programming is now completed and ready for integration into the DAS. The tuning is required after assemblage with a pitch control mechanism.

## 2-4. EXPERIMENTAL PROCEDURE AND DATA REDUCTION

### *Dynamic pressure measurement subsystem*

Two Omega's PX653 laboratory pressure transducers of high-precision were installed in the Data Acquisition System (DAS) to measure a difference between atmospheric and static pressure in the test section to calculate dynamic pressure. Their outputs were connected to 0 and 1 channels of the PCI1713 32-channel analog input board. The new software was developed to perform sensors calibration. Graphic user interface of the program with calibration results is shown in Fig. A2.8 Maximal errors are seen to be 0.46 Pa and 0.44 Pa for transducers (marked yellow), and standard deviation of errors was 0.19 Pa. These data correspond to maximal relative error of 0.04% and standard deviation of relative error equal to 0.02% (marked blue in Fig. A4.1). Also the calibration showed that errors are mainly defined by accuracy of the reference pressure measurement. It is necessary to improve resolution of visual observation of reference point of MKB-250 manometer.

The new 25-point pressure measurement block described in the QRT8 report was mounted on the floating plate of the 3-component strain gage balance as shown in Fig. A2.9 The block outputs were connected to channels 5 – 29 of the PCI-1713 board; channel 30 was given to the transducers power supply. Such an arrangement is necessary because Freescale's low-cost pressure transducers of MPXV series are ratiometric with respect to supply voltage. So in spite of a utilized voltage stabilizer, impact of output voltage variation on pressure measurements was found during test runs and between calibrations.

To improve the long-term stability of calibration data, special procedure of calibration and pressure calculation was developed using calibration data and supply voltage value. Each measured output voltage of a pressure transducer was normalized by a value of measured supply voltage and multiplied by 5 that is the rated supply voltage of MPXV series transducers equal to 5 V.

Resultant normalized values were used for calculation of both calibration function coefficients and measured pressure values.

These changes in calibration and testing procedures required corresponding modifications of the relevant software.

For the current set of tests, 25-point pressure measurement subsystem was configured so that 6 kPa

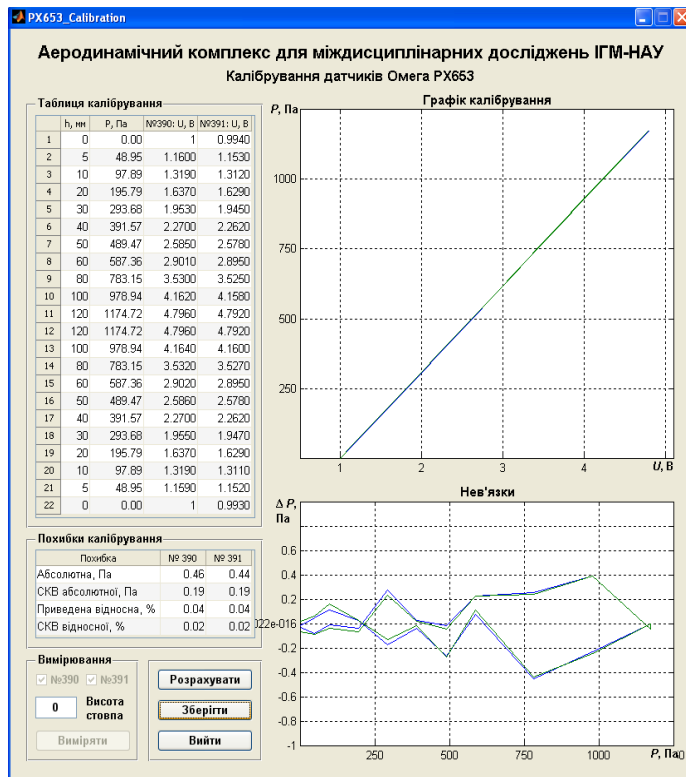


Fig. A2.8 Graphic user interface of software program for PX653 transducers calibration: calibration results are shown

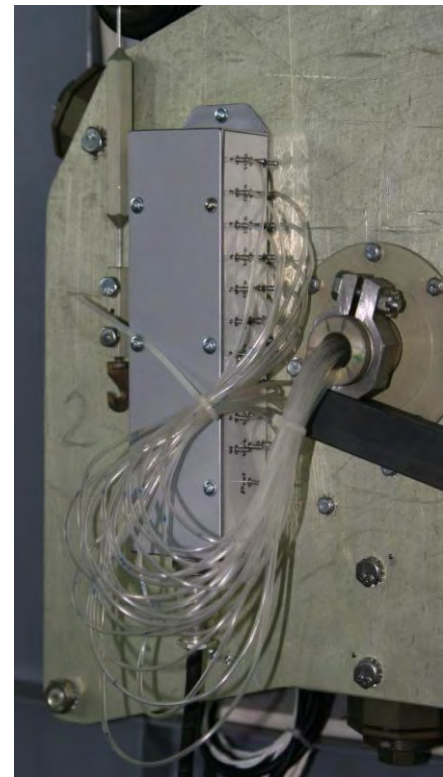


Fig. A2.9 25-point pressure measurement block mounted on the floating plate of the 3-component strain

transducers were connected to output wiring. The subsystem was calibrated using the same MKB-250 reference manometer in the pressure range from 0 to 250 mm H<sub>2</sub>O. With the calibration function considered to be linear, the following results were obtained. Maximal calibration error was 1.2 Pa, which corresponded to a relative error of 0.05% in the calibration range. It also should be noted that a considerable part of the total calibration error of a transducer could be referred to an error of reference pressure setting and measurement.

## Summary

ACIR remodeling embraced all the facility parts and functions to ensure its correct operation under conditions of microwave radiation and plasma generation for flow control.

The obtained results showed that the ACIR modification provided the expected velocity range up to 65 m/s for models with the considerably high blocking (high-drag bodies, profiles at stall angles of attack and profile cascades). It is a very important conclusion in view of the prospective experimental investigations which can be carried out in the ACIR. Flow field investigation resulted in the calculated correlation between pressure values obtained in the dynamic pressure measurement subsystem and true dynamic pressure in the test section.

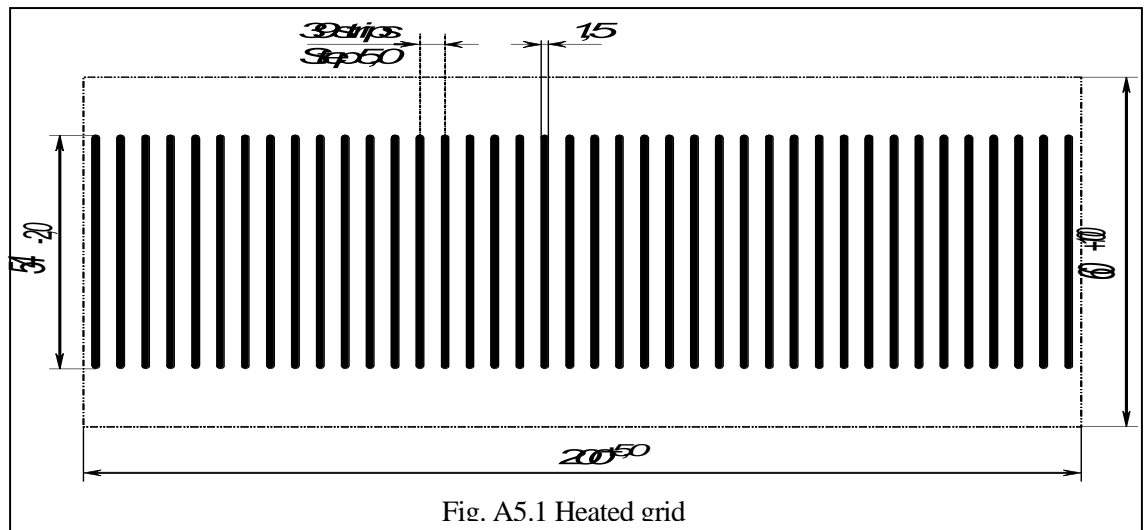
## APPENDIX, Ch. V

### 5-1. MODELS WITH FLOW CONTROL BASED ON PRINCIPLE OF HEATED ELEMENTS

#### 5.1.1 R800 airfoil with heated elements

##### Heated elements development and manufacturing

The geometry of heated elements was chosen similar to that used in resistively heated model. The main parameter is spanwise step, which has been chosen equal to 5 mm, at which the best results were obtained in previous project. The length of heated elements in streamwise direction is limited by MW radiation wavelength. According to recommendations of MRTI it should not be longer than 55 mm



(wavelength  $\lambda = 120$  mm). The layout of heating elements is shown in figure 1.

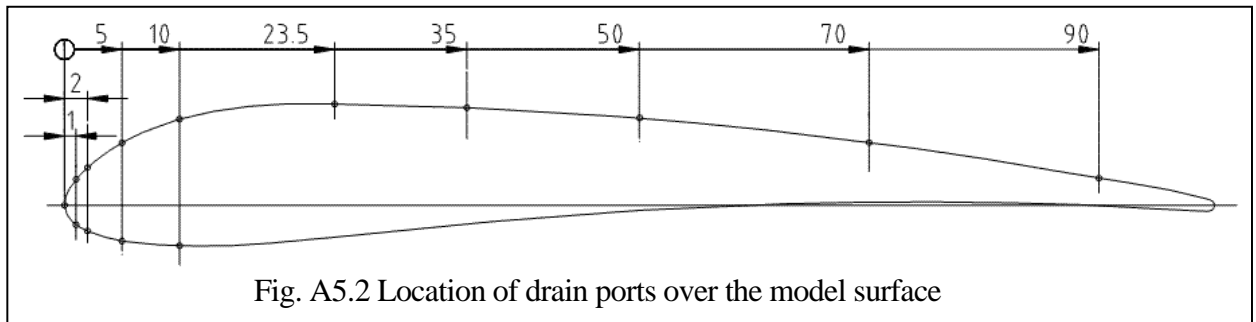
In order to simplify production of heated elements, to improve their uniformity and precision and to decrease a necessary number of models, it was decided to make it as a separate thin flexible sheet and to glue it onto the model surface over a desired section. The technology used to produce resistive-strain sensors was applied for this and ten 100 by 200 mm foils were obtained from the manufacturer. Each foil is a package of paper drenched with thermosetting resin and 8.4  $\mu\text{m}$  thick nichrome foil glued to it. Total thickness of the package is 45  $\mu\text{m}$ . The grid of heating elements is obtained by chemical etching. This permits to obtain very accurate and uniform set of heated elements. Usage of photographic mask enables to obtain similar foils made of different metals if required in the future.

##### Test model

Taking into account that pressure distribution is an essential factor for flow diagnostics and sometimes is more sensitive to flow variations, a model was fabricated with drain ports located according to the table below.

Table 1.1. Location of drain ports on the surface of test model #4 (in percents of cord)

Point #	1	2	3	4	5	6	7	8	9	10	11	12	13	14
Convex	0	1	2	5	10	23.5	35	50	70	90	-	-	-	-
Concave	-	-	-	-	-	-	-	-	-	-	1	2	5	10



### Fabrication and assemblage of test models

The adjusted and assembled models were controlled on their heating uniformity using thermosensitive paper. It was found that some unpredicted factors during the assemblage considerably deteriorated the heating uniformity so that a large fall-through appeared in left parts of both models.

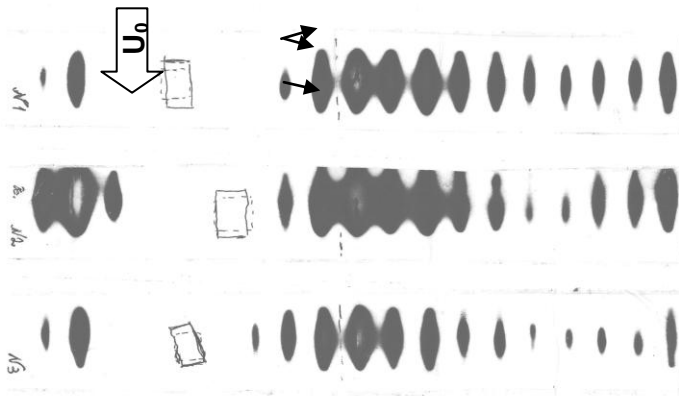


Fig. Ch. 5.3 Non-uniformity of MW heating for model #10 checked with the thermosensitive paper (top view): Black arrows show positions of center section of the model where drain ports were located; pen-drawn rectangles show positions of horn antenna flange (dash lines) relative to the wind-tunnel test section (solid lines)

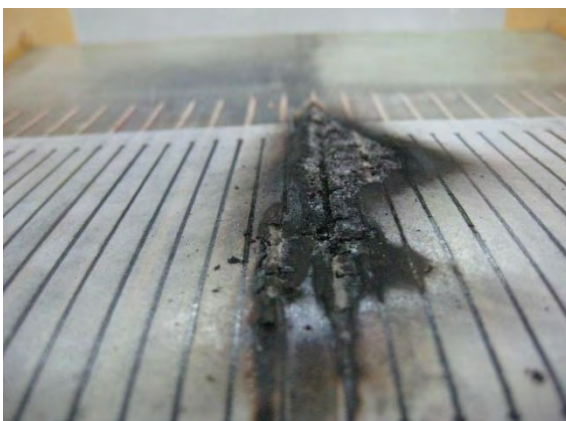


Fig. A5.4 The burn-out of the surface of model

The paper heater was absent in the central part of the model to enable pressure distribution measurements. Models' sketches are shown in Fig. A5.5 and A5.6.

Attempts to improve the situation did not show acceptable results. Thermal patterns obtained for the model #10 at three horn positions are shown in Fig. 3. Results for the model #09 were similar.

### Tested Models. Encountered problems and their explanation.

Four models were designed and fabricated for the planned set of tests. Two of them are modified available models designated as R800 #11\_2 and #12\_2, and the other two were newly made models #14 and #15. Such a great number of various tested models resulted from a search of most proper engineering solutions, first of all preventing the models from their burnout during tests or test preparation that happened even at low magnetron currents corresponding to the radiated power of 200 – 500 W.

All models have the same geometry, similar design and different types of heated elements developed and manufactured in MRTI. One of the heater versions in a form of paper sheets with graphite lead line pattern was glued to the model in NAU. All heaters had a spanwise step of 5 mm. The internal surface of the side opposite to that with heated elements was covered with the glued metal foil (reflector).

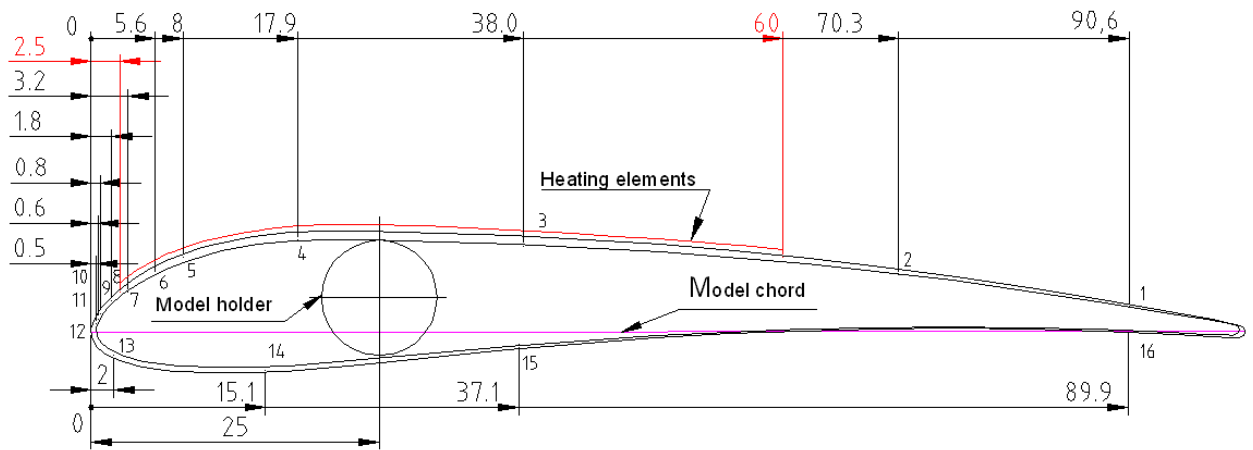


Fig. A5.5 Layouts of models #11\_2 and #15. Testing in a flight position at positive angles of attack

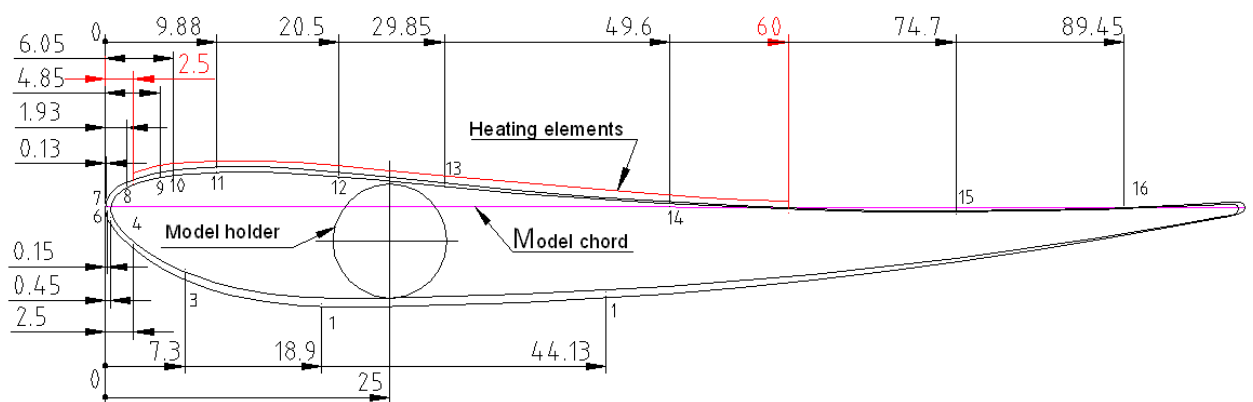


Fig. Ch 5.6 Layouts of models #12\_2 and #14. Testing in reversed position at negative angles of attack

Testing started from the models #11 and #12, which earlier had bulk graphite elements flush-mounted in slots over models' surface. The graphite elements were removed and surfaces were smoothed using appropriate filling. Instead, paper heaters were glued to the model surface in estimated locations. Models were named as #11\_2 and #12\_2. Both of them surface burned out on the surface including glass-fiber shells in several places (Fig. A5.4) during tuning of test conditions. These models were repaired by installation of new fabricated shells and named as #14 and #15. However, these models burned out too. It happened in central parts of the models having damaged drain taps together with tap pipes that made impossible pressure distribution measurement over the whole surface.

No significant difference between aerodynamic characteristics in reference and controlled cases was found during a limited number of performed test runs. It was validated with the assessments made by the MRTI team: the energy absorption concentrated in a place where it was high by itself. It decreased the fraction of power absorbed by the rest of the heated elements. So when for some reason a burnout occurred in a certain point, organic substances in model burnt out and were blown away but some of them consisting mainly of carbon remained in the model. Since carbon is a good absorber of microwave radiation, a considerable amount of radiated power was absorbed by the burnt portion of model leading to its further overheating while the rest of the heated elements remained almost cold.

## **Comparative analysis of different types of MW-heated strips for flow control**

Four types of heated elements were developed and tested:

- (a) nichrome foil grid obtained by chemical etching and glued to paper drenched with thermosetting resin;
- (b) vitrified bulk carbon resistors flush-mounted in the model surface;
- (c) fine-dispersed bulk graphite mixed with heat-resistant lacquer, located in 0.5 mm wide slots inside models' surface;
- (d) graphite lead lines on the paper permeated and glued to the model with heat-resistant lacquer.

**The nichrome foil** heated elements were found to be least effective for flow control purposes; they showed low heating, low uniformity of the heating along and across the thermal system and, accordingly, no changes of aerodynamic characteristics.

All the other heated elements had similar advantages and disadvantages as well as effectiveness.

**Vitrified bulk carbon resistors** required fine tuning before the model assemblage that was technologically inconvenient and, in addition, was impaired in the assembled model.

**Fine-dispersed bulk graphite heated elements** were technologically difficult to manufacture in the models and did not permit any tuning after the model completion.

**Graphite lead lines** on the paper were easiest technologically in laboratory conditions and provided possibilities for model modifications by gluing new patterns instead of fabrication of a completely new model. However this type of heaters distorted the model shape and created some difficulties to clean pressure taps during elements gluing.

## **5-2. MODELS WITH PLASMA FLOW CONTROL**

### **5.2.1 Initiators of plasma discharges**

MW-generated spanwise plasma arrays are more perspective for further investigations in the framework of the developed flow control concept. They are to be focused on getting over the above mentioned drawbacks as well as on studying and application (if possible) of different types of discharges characterized with lower temperatures but sufficient energy released in the flow.

### **5.2.3 Circular cylinder models**

#### ***Prototype cylindrical models with mechanical turbulators***

The prototype problem was formulated as a preparatory stage for studying flows around plasma controlled circular cylinder. The prototype measurements started from a reference case of a smooth cylinder in a crossflow to determine a range of basic flow parameters. Fig. A 5.7 shows obtained drag coefficients for the cylinder in the Reynolds number range of  $Re_D = (0.75 - 3.0) \times 10^5$ .

Drag coefficients in the pre-critical range of Reynolds numbers were found to be  $C_D \approx 0.8$ . The measurements were carried out in the wind tunnel of the Antonov's Aerodynamic Scientific and Technological Complex (ASTC) using the measurement system developed for the AFIR.

Two cylinders were tested with the diameters of  $D=106.6$  mm and  $D=128.0$  mm within free-stream velocities  $U_0 \approx 15 - 44$  m/s.

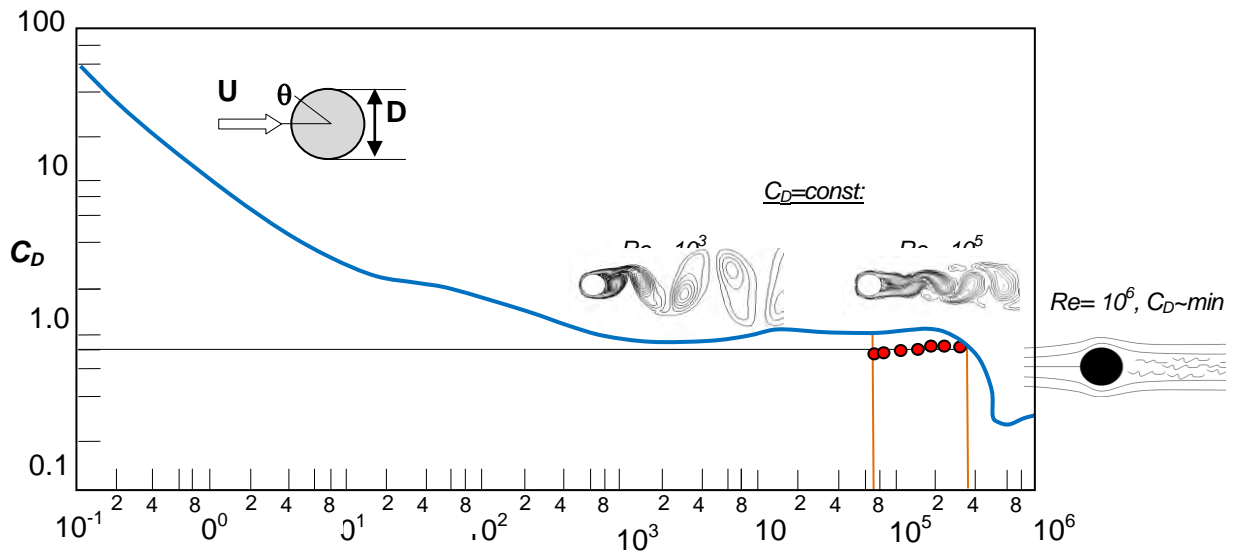


Fig. A5.7 Drag coefficient  $C_D$  as a function of Reynolds number  $Re_D$ : blue curve – experiment, Schlichting, 1979; vortex shedding patterns – numerical visualization [1]; red points – present reference measurements)

The prototype problem consists in the application of an array of mechanical vortex generators mounted along the cylinder generatrix with a fixed distance between the neighboring spherical generators (Fig. A5.8). Mimicking the plasma array application, such an arrangement was planned (1) to verify AFIR measurement possibilities and accuracy and (2) to get the guidance for the development of a plasma array in MRTI especially in terms of the optimal spanwise step between localized plasma discharges.

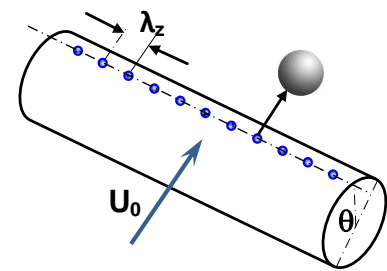


Fig. A5.8 Prototype problem formulation

Flow-control essence consists in the application of an array of mechanical vortex generators mounted along the cylinder generatrix with a certain  $\lambda_z$  distance between the neighboring spherical generators (Fig. A5.8). Mimicking the array of thermal sources in a form of localized plasma discharges, such an approach provides the guidance for the development of a plasma array in MRTI especially for the range of

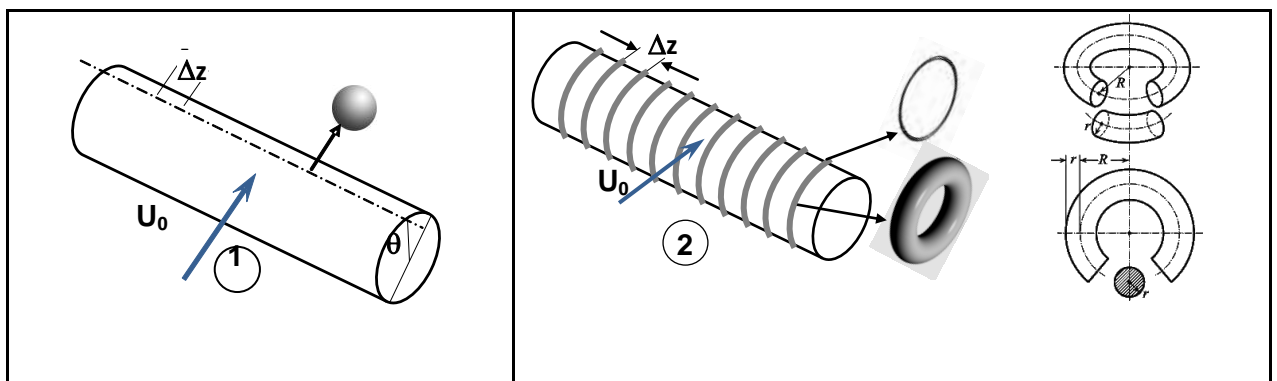


Fig. A5.9 Circular cylinder with an array of spherical disturbers

Fig. A5.9 Circular cylinder with an array of O-ring disturbers

optimal  $\lambda_z$  values from a viewpoint of the aerodynamic performance improvement for a given range of Reynolds numbers.

O-ring disturbers represent smooth rings with a round cross section of two diameters,  $d=2.5$  mm and 4.6 mm which are uniformly distributed with a  $\Delta z$  step along cylinder models of two diameters,  $D=106.6$  mm and 128 mm. Figs A5.8 and A 5.9 show fabricated models with the two types of disturbers.

#### *Cylindrical model with linear plasma initiators*

During model preparation, it appeared to be impossible to keep the model surface smooth after multiple disassembling - assembling. That is why the special effort is to be planned to develop the appropriate technology of model fabrication and exploitation. Meanwhile, overhanging parts of screws were snagged by a broach file, cavities and shoulders were smoothed by plasticine to satisfy aerodynamic requirements.

#### 5.2.4 Streamlined airfoil profile

Five inserts with plasma arrays of nineteen flush-mounted ring initiators were fabricated for the both surfaces of the model so that to get a plasma array at different locations along a chord. A spanwise step between the initiators is  $\Delta z=10$  mm.

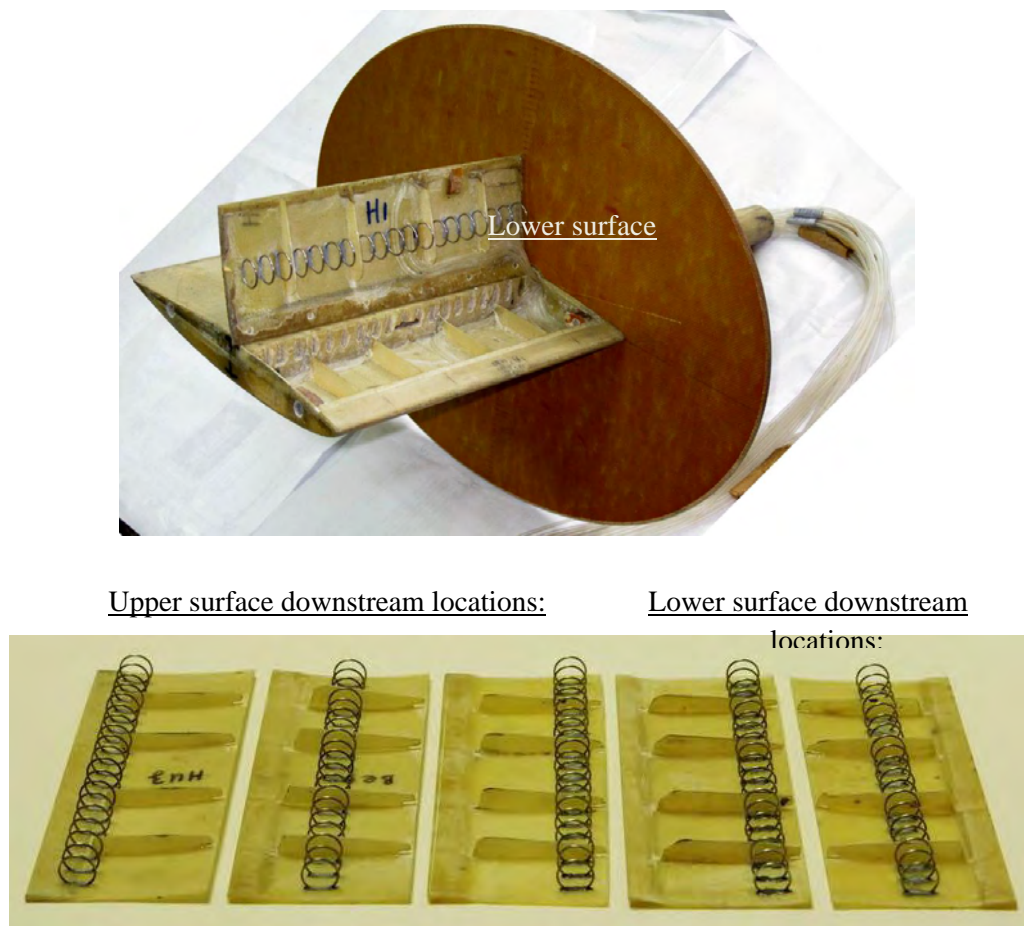


Fig. A5.10 “SAP” model (top) with the left endplate removed, the insert is opened.

Five inserts (bottom) providing different chordwise locations of plasma arrays on the both model surfaces.

Typically, the controlled model is equipped with 25 pressure taps connected to pressure probes to measure pressure distributions around the models. Internal and external sides of the inserts are shown in Figs. A5.10, a - b. The holder with pressure tubes is seen to the right of the model.

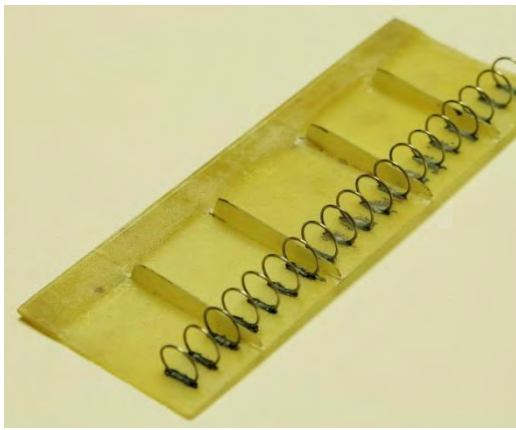


Fig. A5.11, a. Inside view of the insertion with ring-type initiators

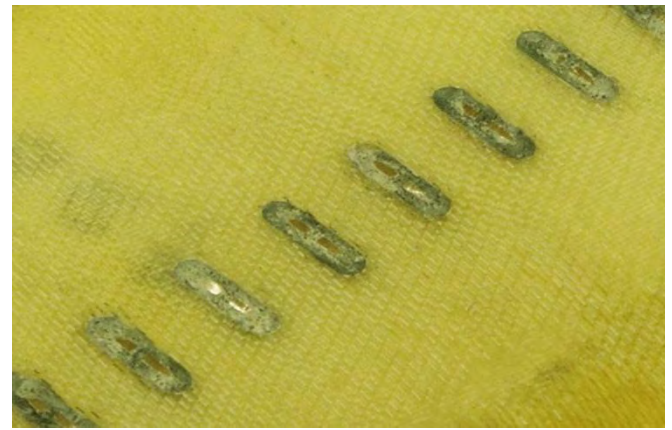
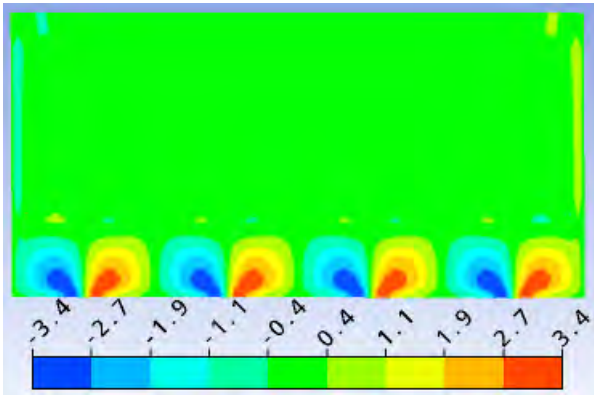


Fig. A5.10, b. Outside view of the insertion with ring-type initiators

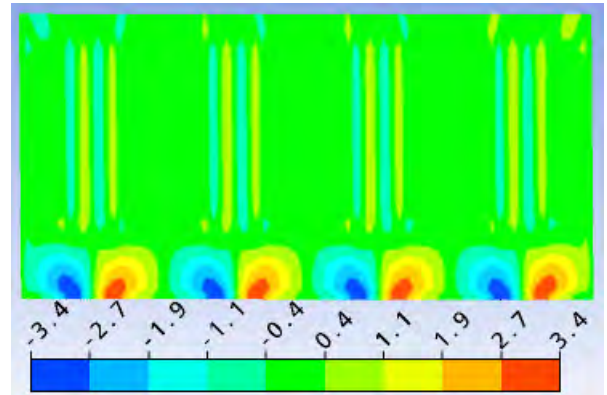
Thus the measurements were focused on the case of ring-type plasma initiators mounted only on the lower surface of the model at their only relative location of  $\bar{c} = 25\%$  along a chord on the lower “SAP” surface. Angle of attack and Reynolds number values varied to find a gain in aerodynamic performance under a spectrum of conditions from a smooth flow to inevitably rough flow separation like in case of a circular cylinder.

## Attachment Ch.6

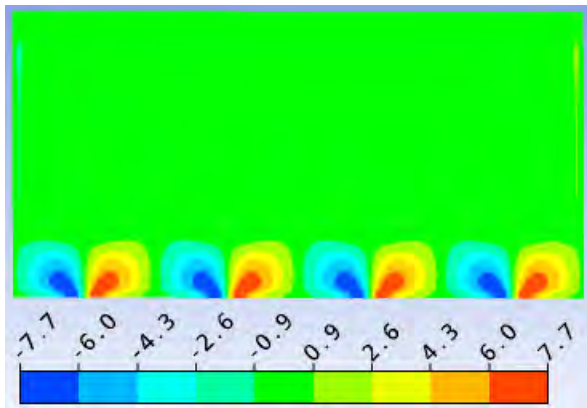
The flow structure over convex surface with surface thermal elements (6.2.2).



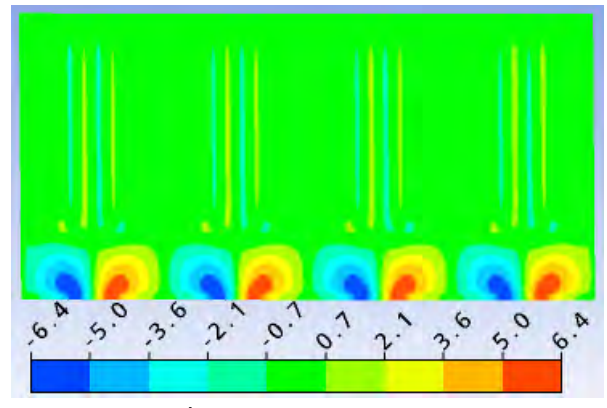
(a)  $\Delta T=100^\circ\text{C}$ ,  $\lambda_z=10$  mm,  $d_{\text{element}}=1$ mm



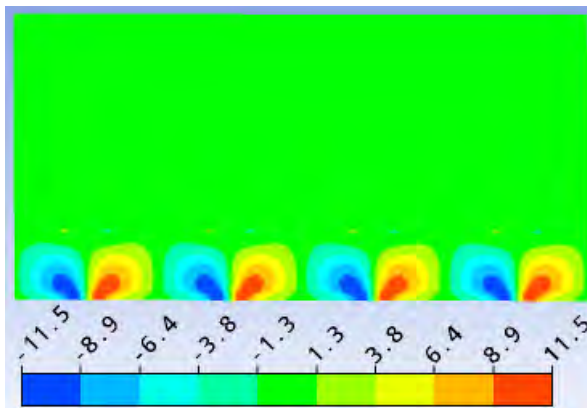
(d)  $\Delta T=50^\circ\text{C}$ ,  $\lambda_z=10$ mm,  $d_{\text{element}}=2$ mm



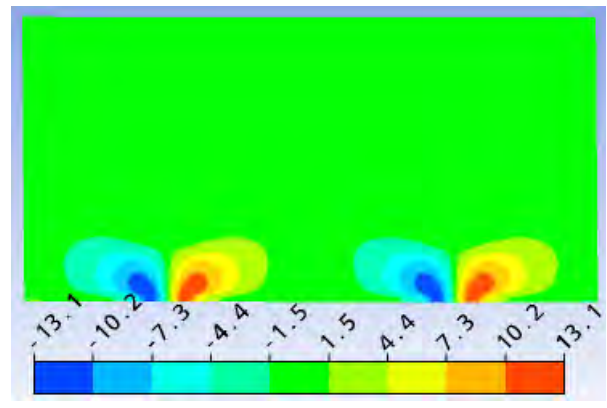
(b)  $\Delta T=200^\circ\text{C}$ ,  $\lambda_z=10$  mm,  $d_{\text{element}}=1$ mm



(e)  $\Delta T=100^\circ\text{C}$ ,  $\lambda_z=10$  mm,  $d_{\text{element}}=2$ mm



(c)  $\Delta T=300^\circ\text{C}$ ,  $\lambda_z=10$  mm,  $d_{\text{element}}=1$ mm



(f)  $\Delta T=200^\circ\text{C}$ ,  $\lambda_z=16$ mm,  $d_{\text{element}}=2$ mm

Fig. A.6.2.1. The effects of the element width  $d_{\text{element}}$  and temperature gradient  $\Delta T$ . Contours of longitudinal vorticity in the YZ cross-section at  $x = 0.26$  m

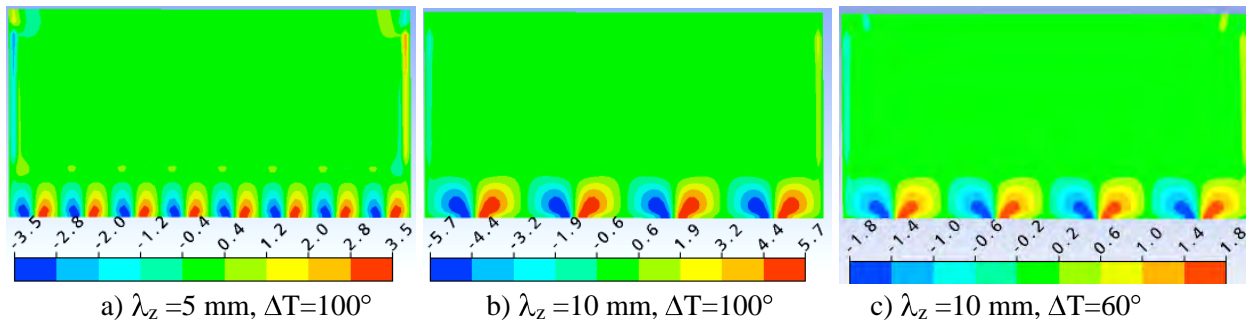


Fig. A.6.2.2. The effect of spanwise spacing  $\lambda_z$  and temperature gradient  $\Delta T$ . Streamwise vorticity over the convex surface;  $U_0 = 30$  m/s

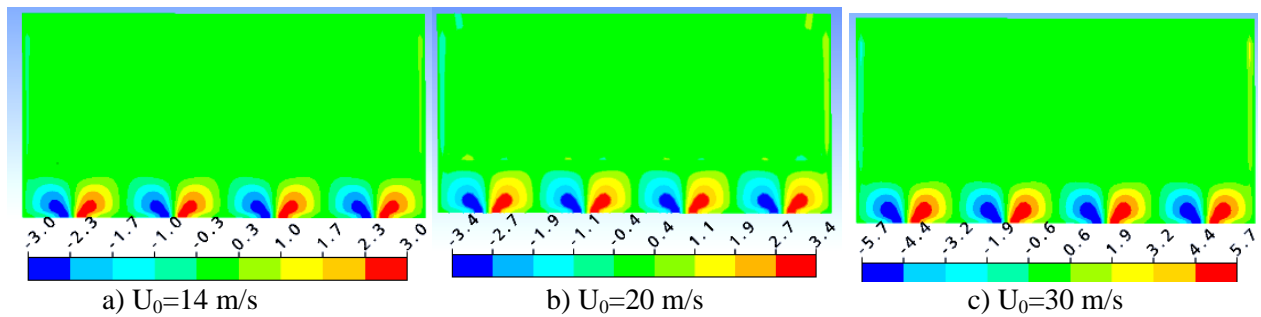


Fig. A.6.2.3. The effect of the free-stream velocity at  $\Delta T = 100^\circ\text{C}$ ,  $\lambda_z = 10$  mm,  $d_{\text{element}} = 1$  mm

### The flow structure over the airfoil with surface thermal elements (6.2.3).

Table A.6.1. Geometrical parameters of the control system shown in Fig. A.6.2.4-

	$L_{\text{element}}$	$L_{\text{tip}}$	$L_{\text{gap}}$
Case 1	112mm	10mm	-
Case 2	55mm	10mm	2mm
Case 3	45mm	10mm	12mm
Case 4	35mm	20mm	22mm

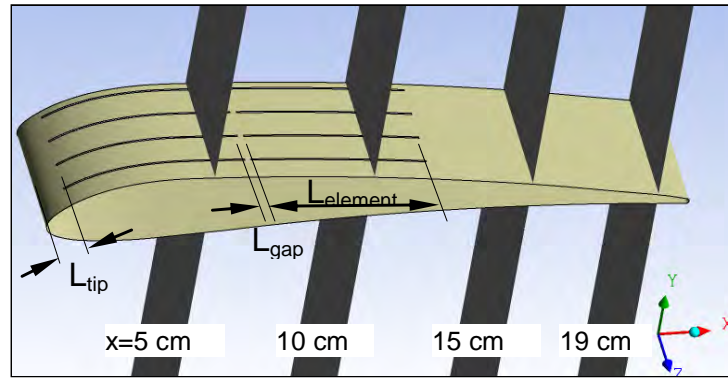
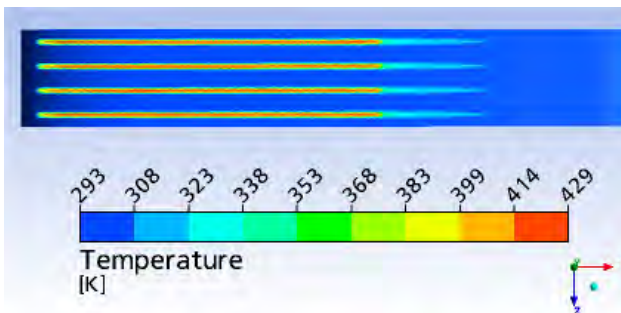
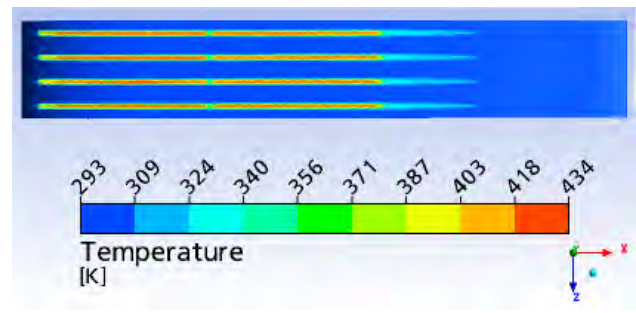


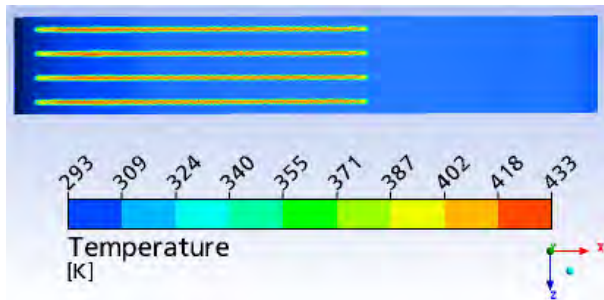
Fig. A.6.2.4. Geometry of the heated array for Table A.6.1; cross-section planes for the vorticity contours in Fig. A.6.2.5 - Fig. A.6.2.11



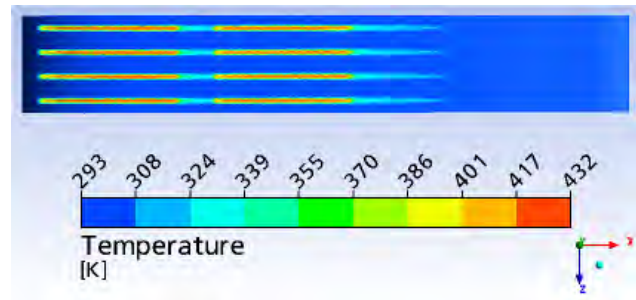
a) Case 1,  $\alpha=0^\circ$



c) Case 2,  $\alpha=0^\circ$



b) Case 1,  $\alpha=12^\circ$



d) Case 3,  $\alpha=0^\circ$

Fig. A.6.2.5. Temperature contours on the profile surface at different sizes of heated elements ( $U_0=15\text{m/s}$ ,  $\Delta T=150^\circ\text{C}$ .)

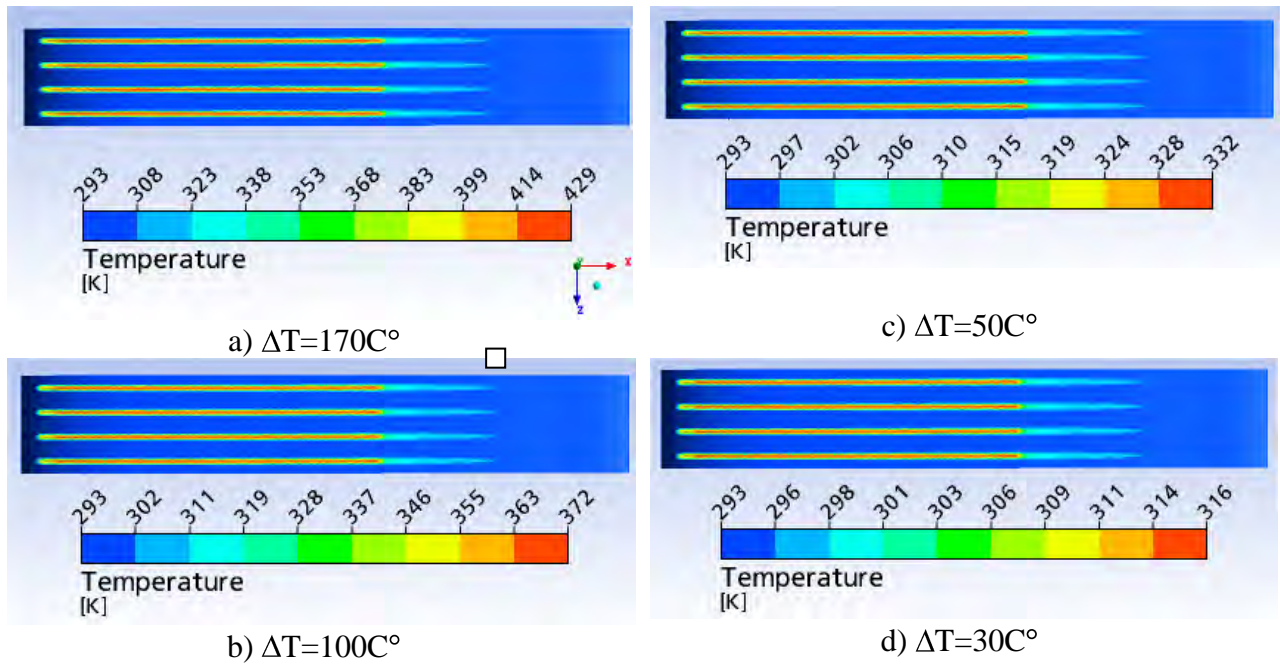


Fig. A.6.2.6. Temperature contours on the airfoil surface at different temperature gradients applied to the heated elements (**Case 1**,  $U_0=15\text{m/s}$ ,  $\alpha=0^\circ$ )

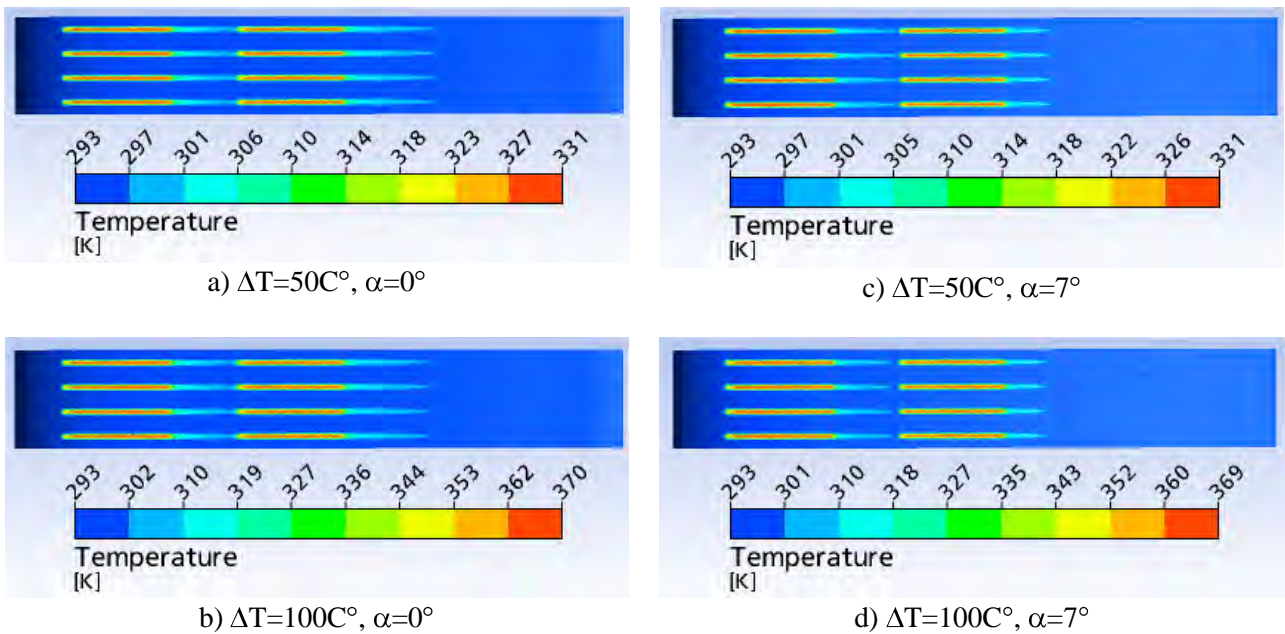


Fig. A.6.2.7. Temperature contours on the profile surface at different  $\Delta T$  and  $\alpha$  (**Case 4**,  $U_0=15\text{m/s}$ ,  $\Delta T=150C^\circ$ )

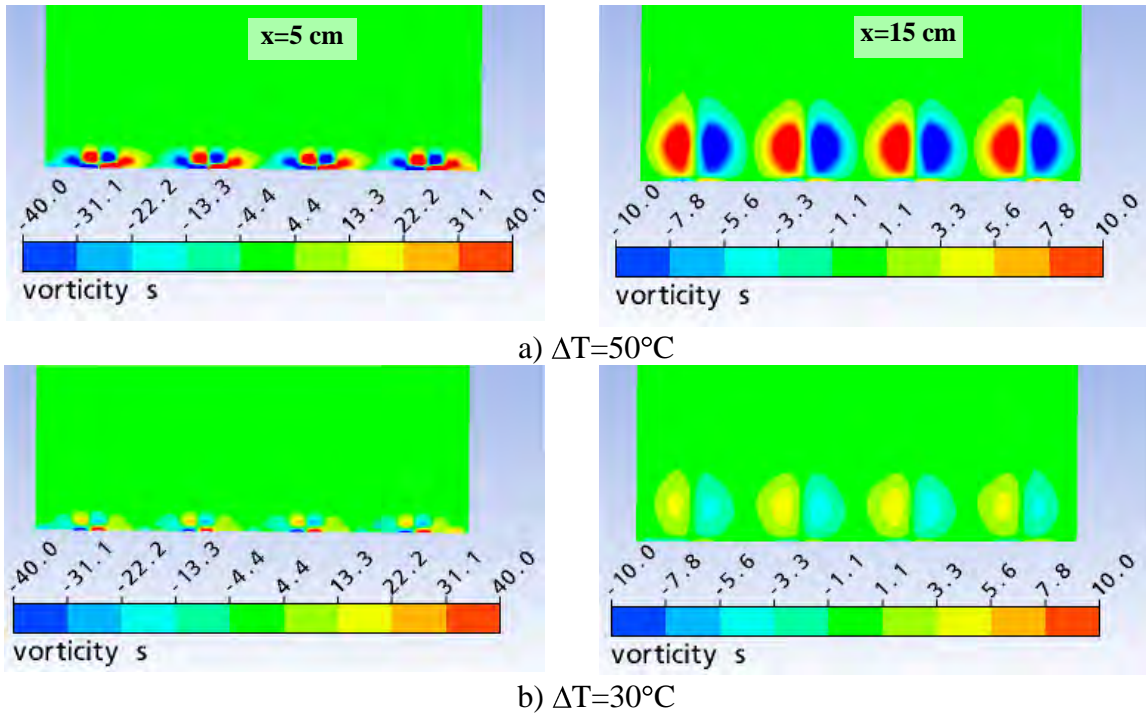


Fig. A.6.2.8. Longitudinal vorticity in different downstream cross-sections (left and right columns) at different temperature gradients: **Case 1**,  $U_0=15\text{ m/s}$ ,  $\alpha=0^\circ$

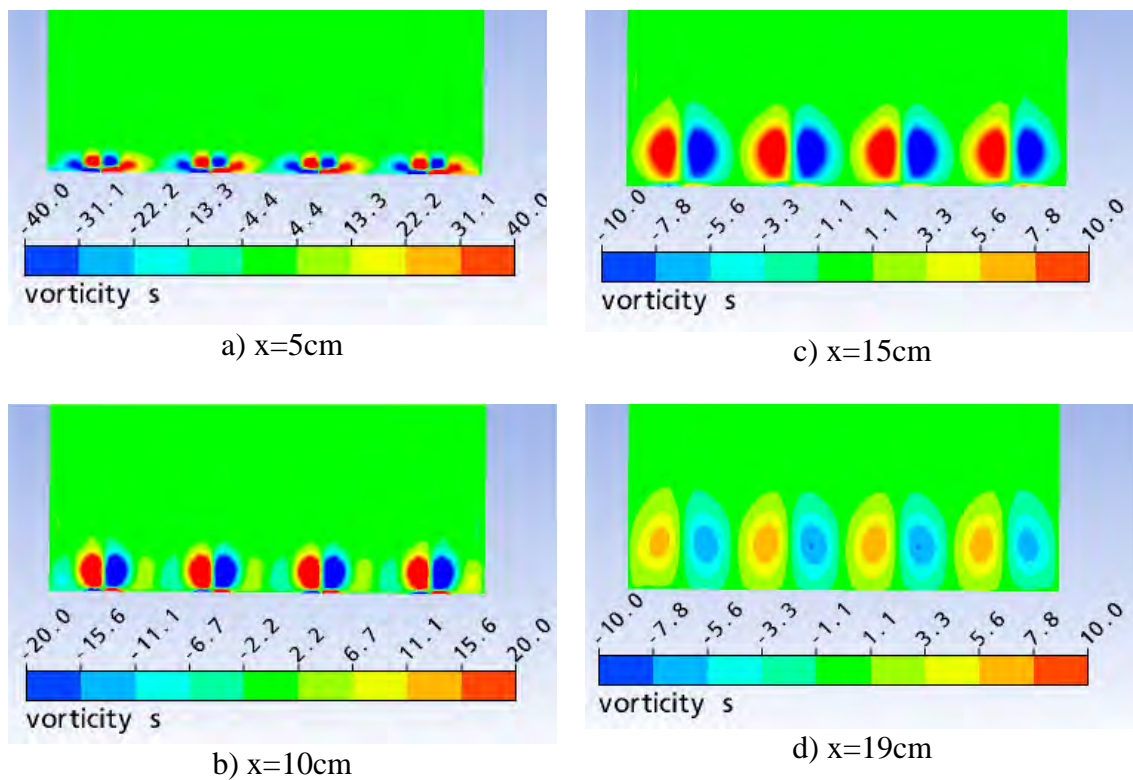


Fig. A.6.2.9. Longitudinal vorticity contours in different downstream cross-sections:  
**Case 1**,  $\alpha=0^\circ$ ,  $U_0=15\text{m/s}$ ,  $\Delta T=100^\circ\text{C}$

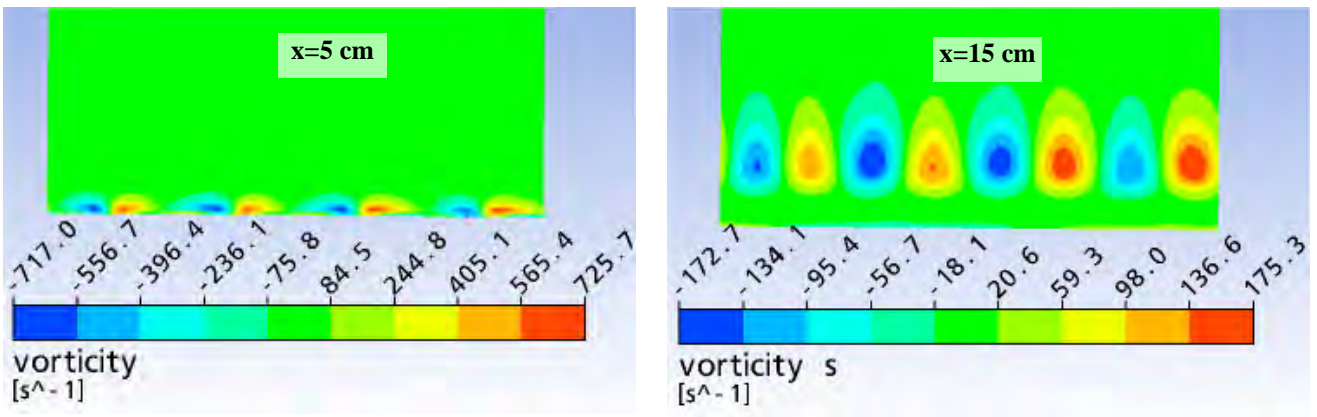


Fig. A.6.2.10. Downstream development of longitudinal vorticity at an increased angle of attack:  
**Case 1**,  $U_0=15\text{m/s}$ ,  $\alpha=12^\circ$

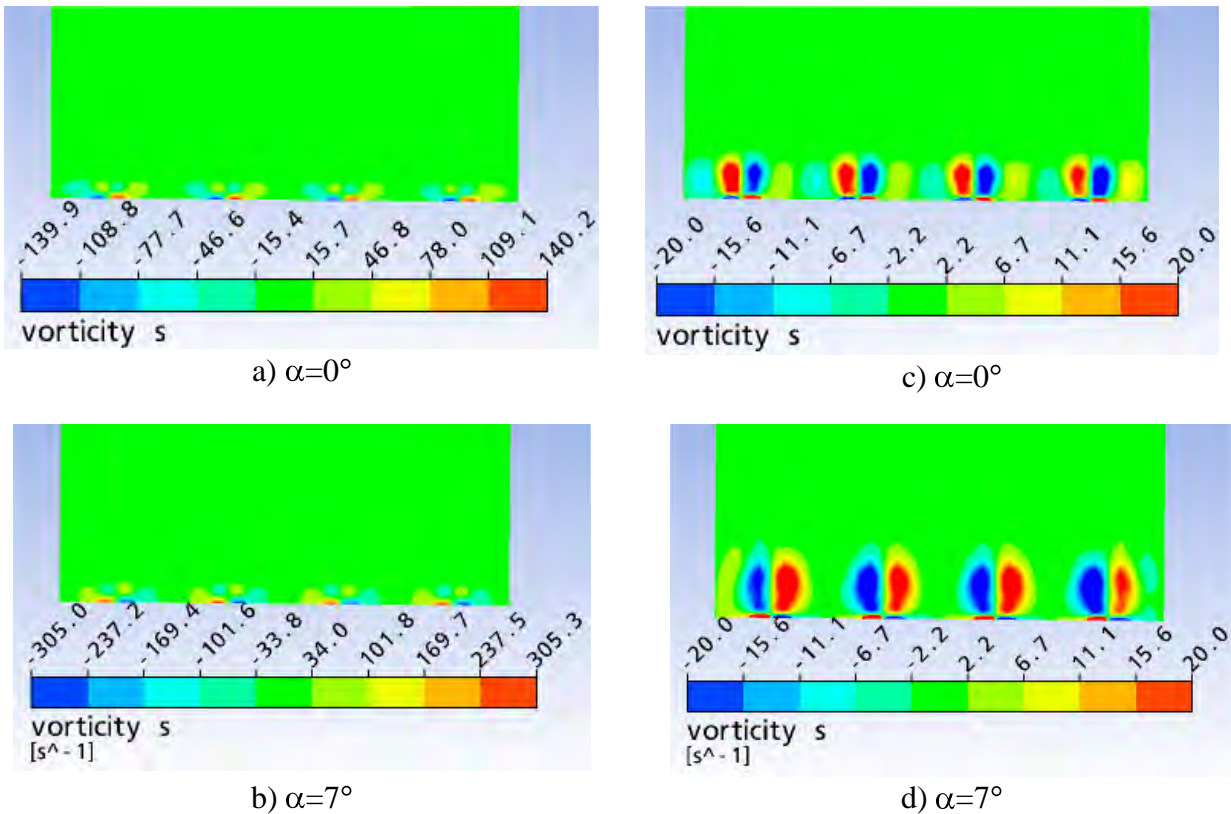


Fig. A.6.2.11. Longitudinal vorticity contours at  $x=5$  cm (left column) and  $x=10$  cm (right column)  
at different angles of attack: **Case 4**,  $U_0=15$  m/s,  $\Delta T=100^\circ\text{C}$

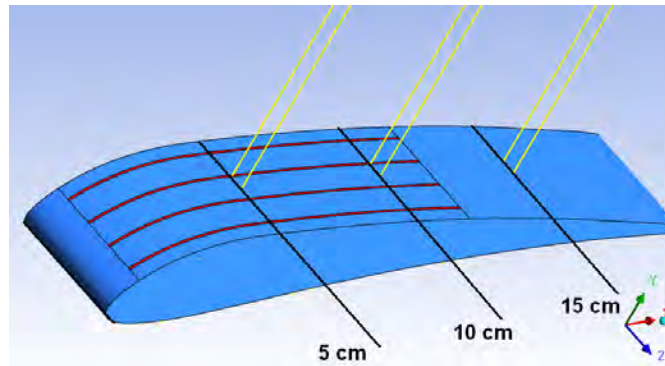


Fig. A.6.2.12. Yellow lines show lines for plots in Figs.A.6.2.13 – A.6.2.17 (Case 1 in Table A.6.1, the angle of attack  $\alpha=0^\circ$ , free-stream velocity  $U_\infty=30$  m/s; temperature gradient  $\Delta T_z=170^\circ\text{C}$ ).

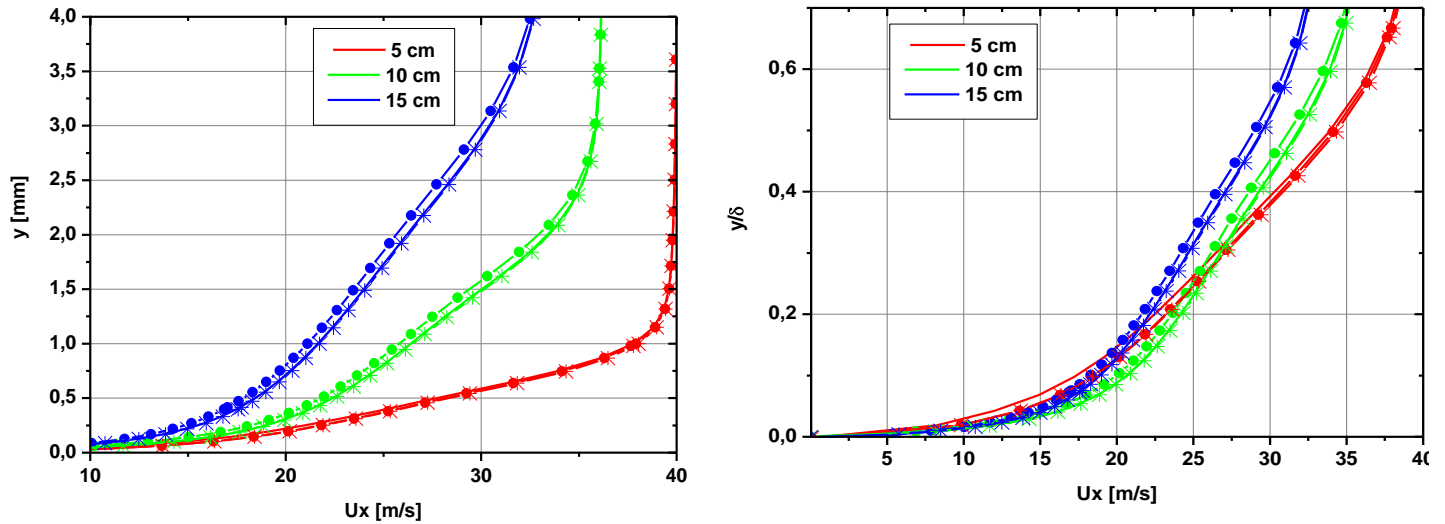
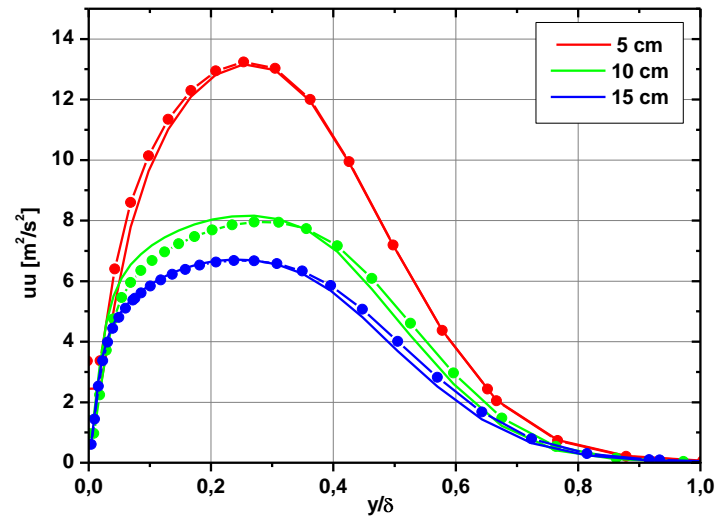
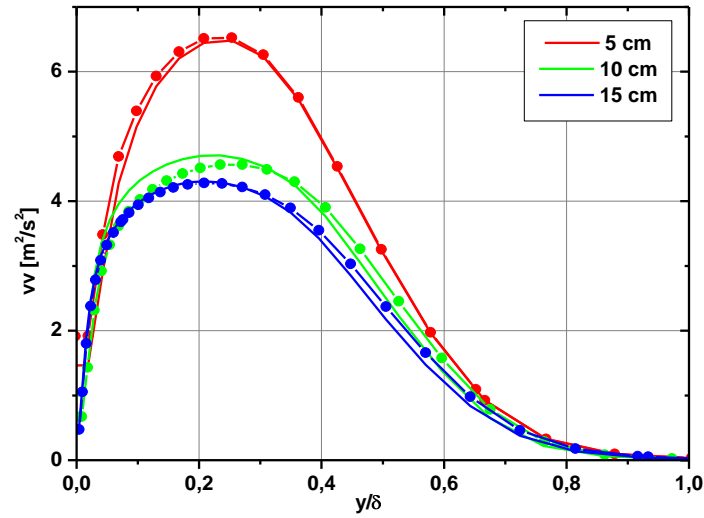


Fig. A.6.2.13. Longitudinal velocity vs a) vs absolute distance from the wall; b) non-dimensional normal coordinate.

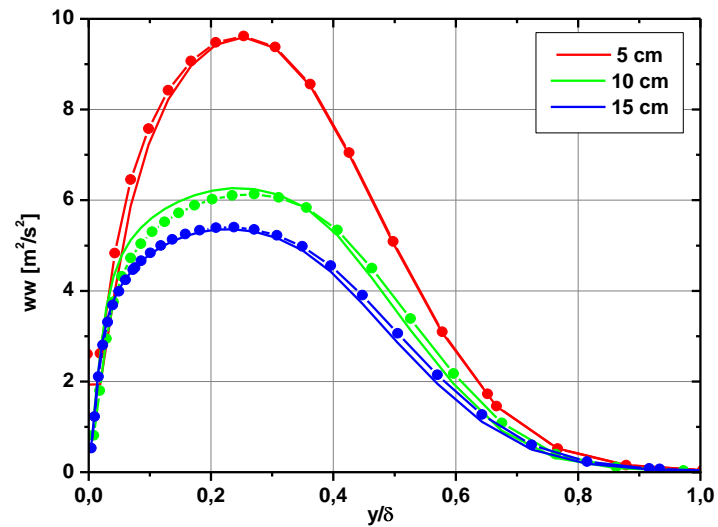
Solid lines correspond to the heated element, circles – to the middle between elements, crosses – to the reference case (no heating)



a)

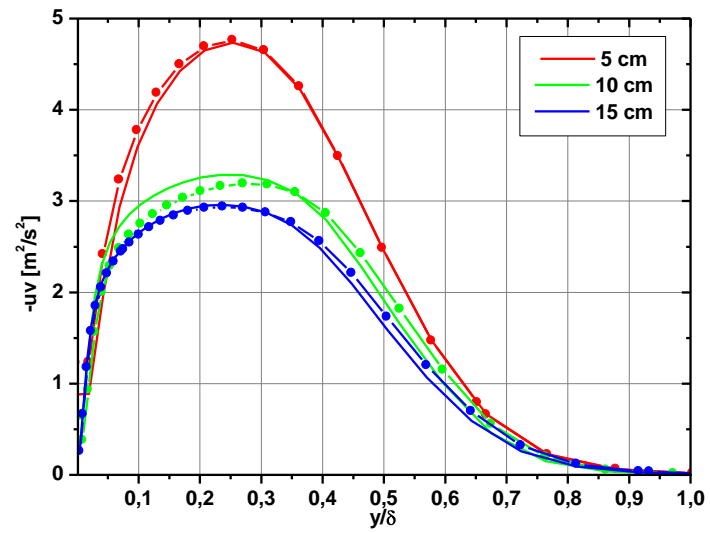


b)

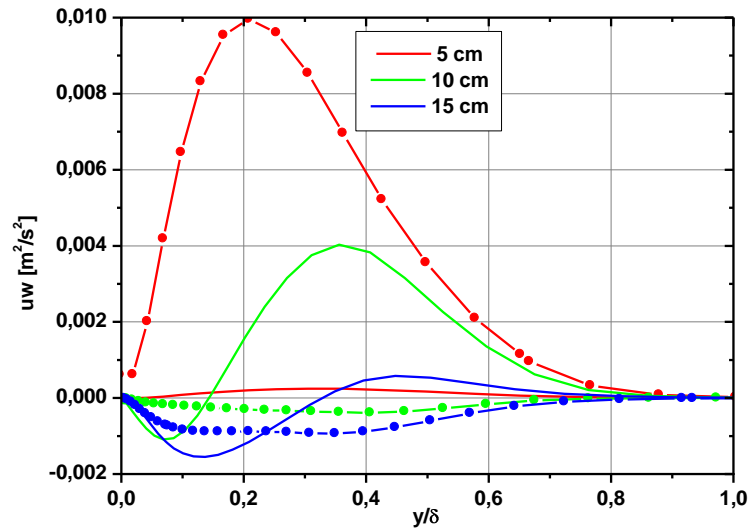


c)

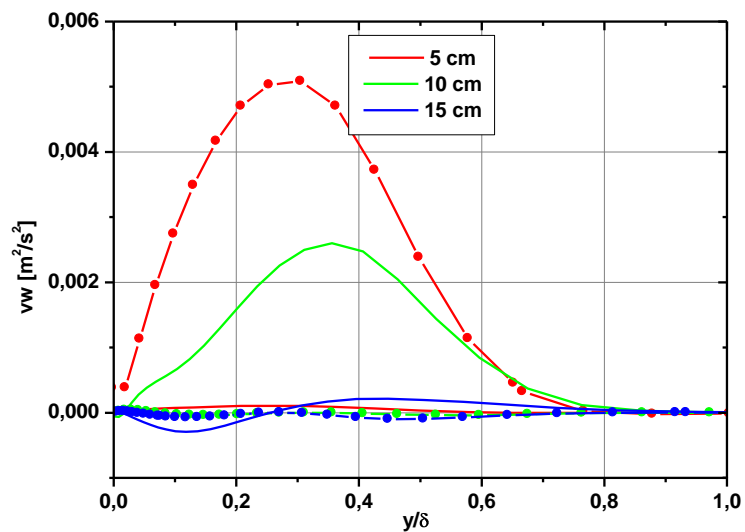
Fig. A.6.2.14. Reynolds stress values a)  $uu$ , b)  $vv$ , c)  $ww$  across the boundary layer thickness. Solid lines correspond to the location of heated elements, circles – to the middle between them.



a)



b)



c)

Fig. A.6.2.15. Reynolds stress values a)  $-uv$ , b)  $uw$ , c)  $vw$  across the boundary layer thickness

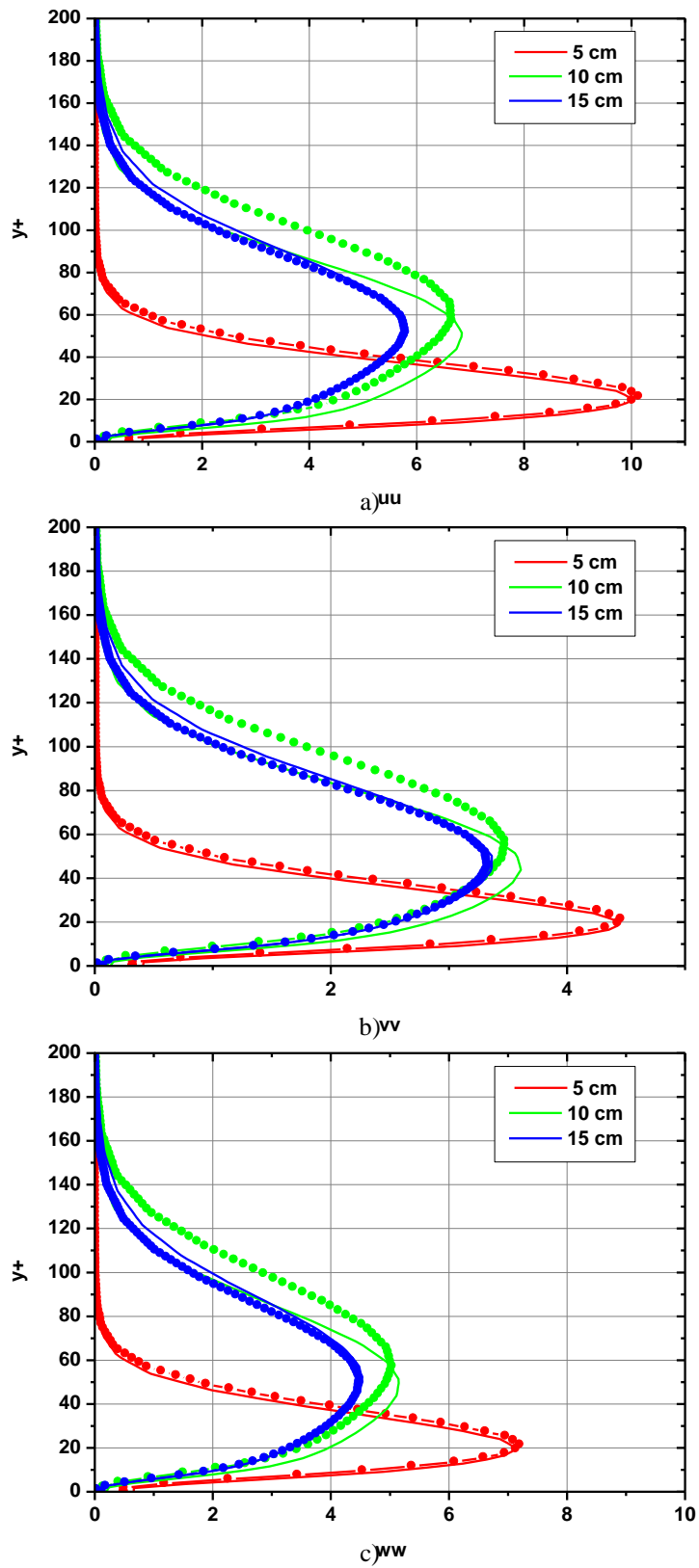


Fig. A.6.2.16. Reynolds stresses values a)  $uu$ , b)  $vv$ , c)  $ww$  versus  $y^+ = yu_\tau/\nu$  (where  $u_\tau = \tau_w/\rho$ ,  $\tau_w$  is local shear stress on the wall)

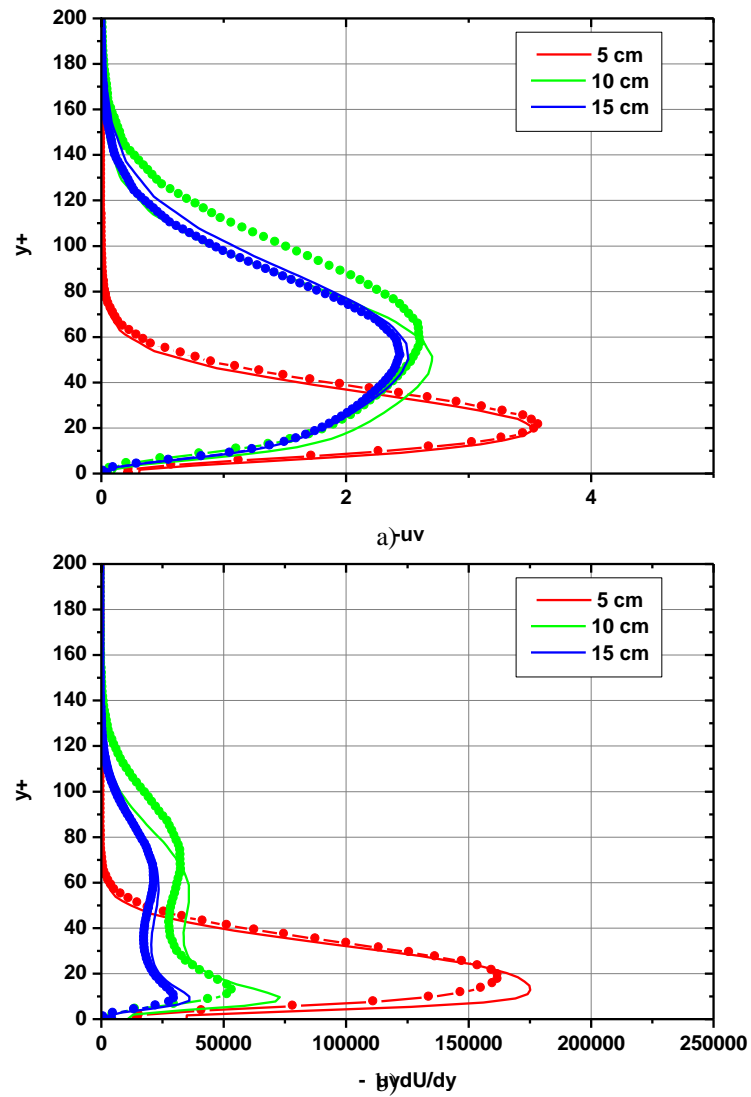


Fig. A.6.2.17. a) Reynolds stresses- $uv$  and b) the production term  $-uv \partial U / \partial y$  versus  $y^+ = y u_\tau / \nu$  (where  $u_\tau = \tau_w / \rho$ ,  $\tau_w$  is local shear stress on the wall)

## The flow about a cylinder with arrays of plasma discharges (6.4.1, 6.4.2)

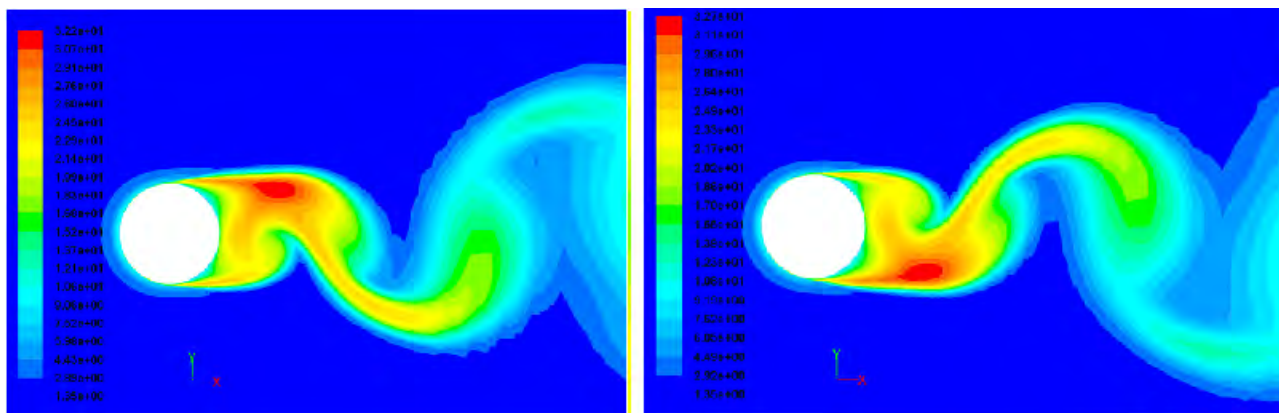


Fig. A.6.4.1. Turbulence intensity in the middle cross-section at the moments of minimum and maximum lift for the reference case

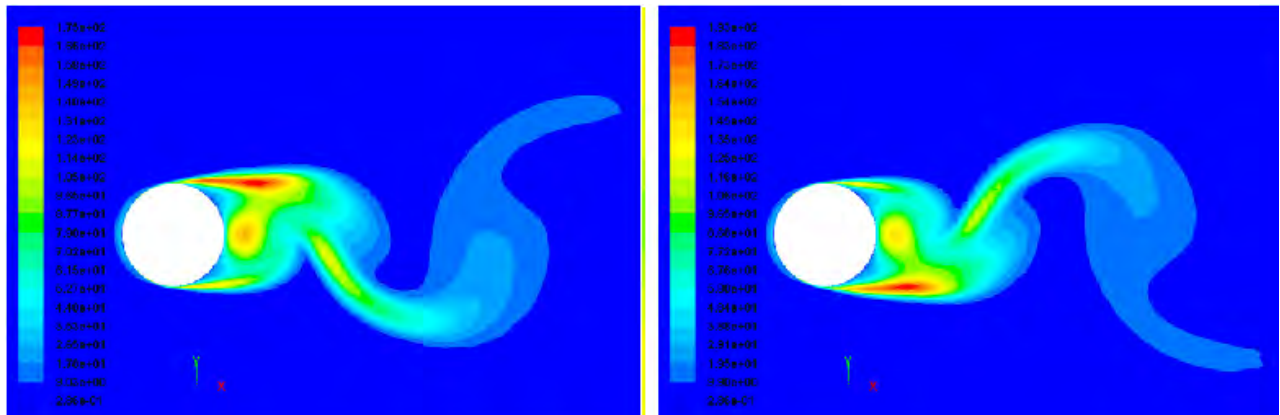


Fig. A.6.4.2. Reynolds stress  $uu$  in the middle cross-section at the moments of minimum and maximum lift for the reference case.

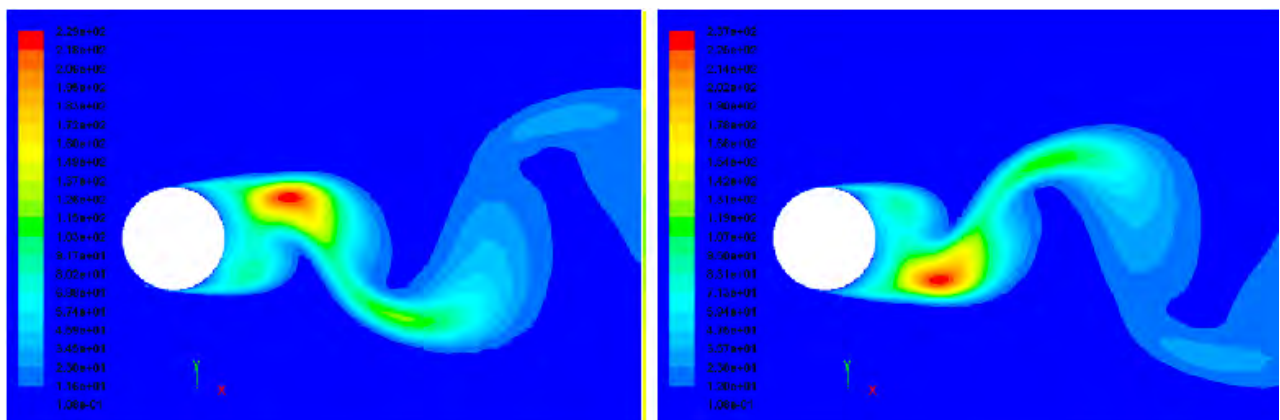


Fig. A.6.4.3. Reynolds stress  $vv$  in the middle cross-section at the moments of minimum and maximum lift for the reference case.

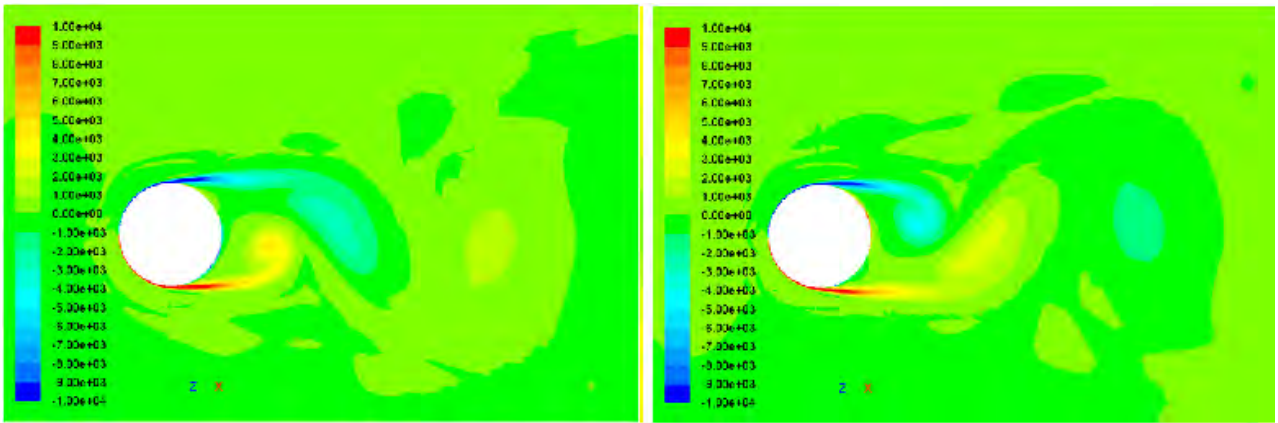


Fig. A.6.4.4. Spanwise vorticity in the middle cross-section at the moments of minimum and maximum lift for the reference case ( $U_0=40$  m/s).

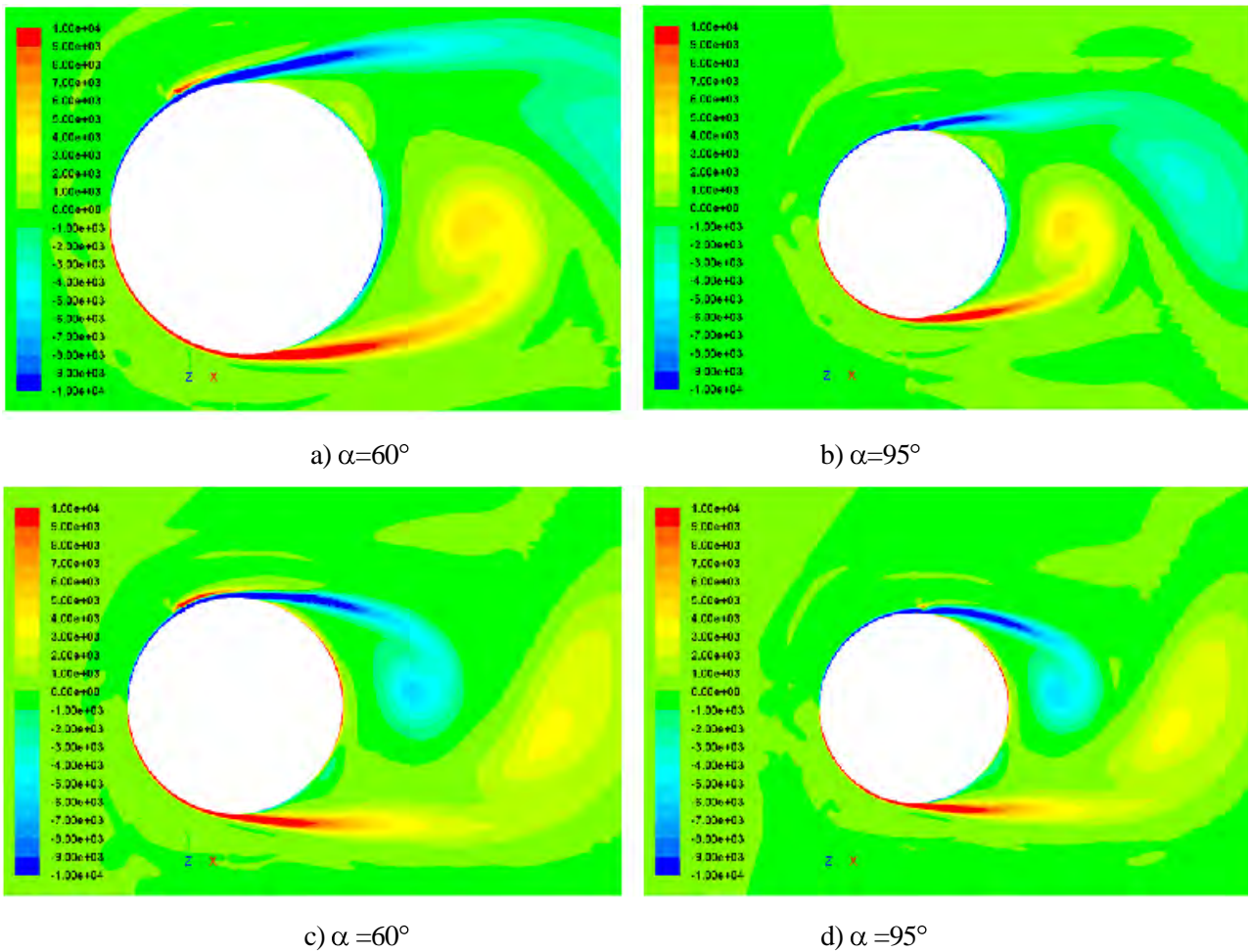
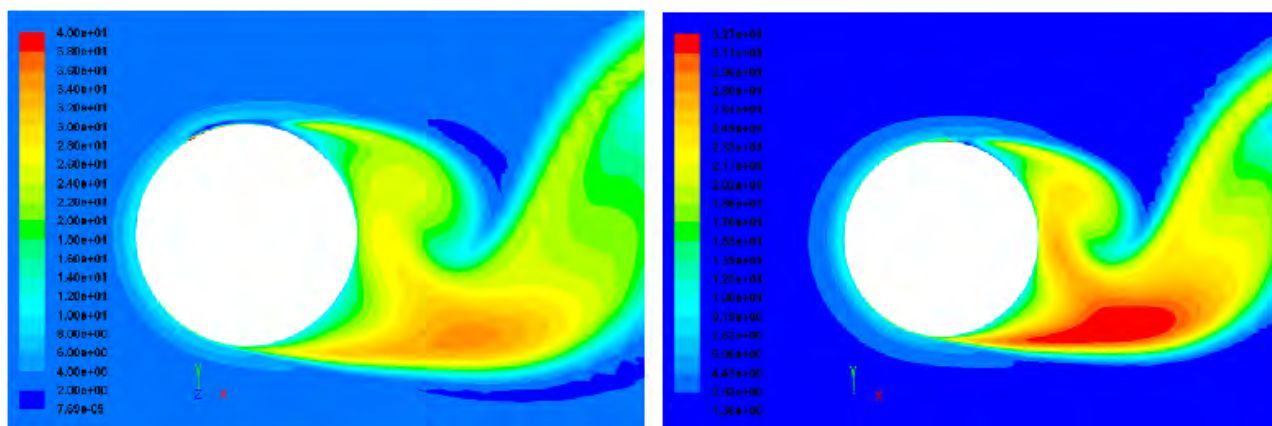


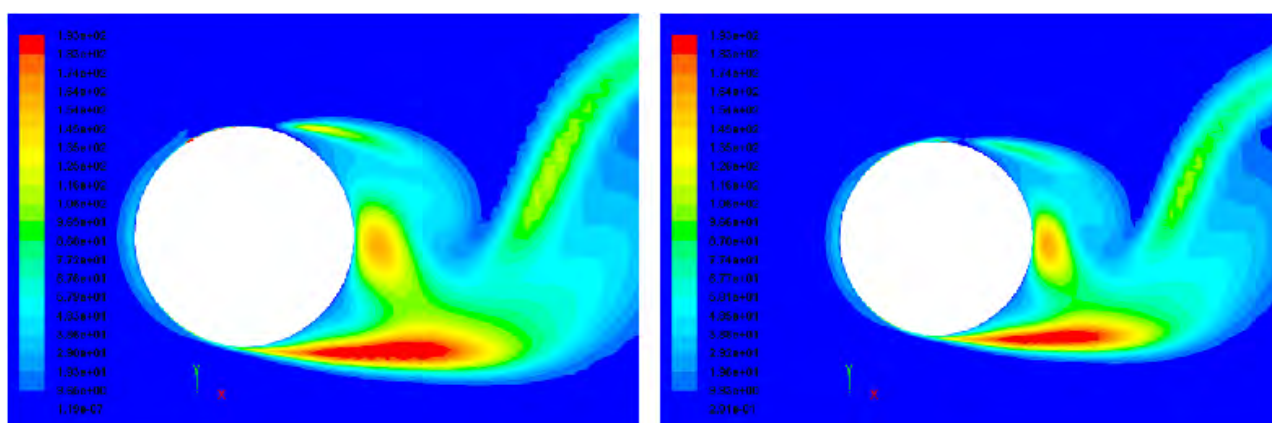
Fig. A.6.4.5. Spanwise vorticity in the middle cross-section in presence of the sources at the moments of minimum (a, b) and maximum (c, d) lift ( $\Delta z=1$ ,  $\Delta T=1000$  °C,  $U_0=40$  m/s).



a)  $\alpha = 60^\circ$

b)  $\alpha = 95^\circ$

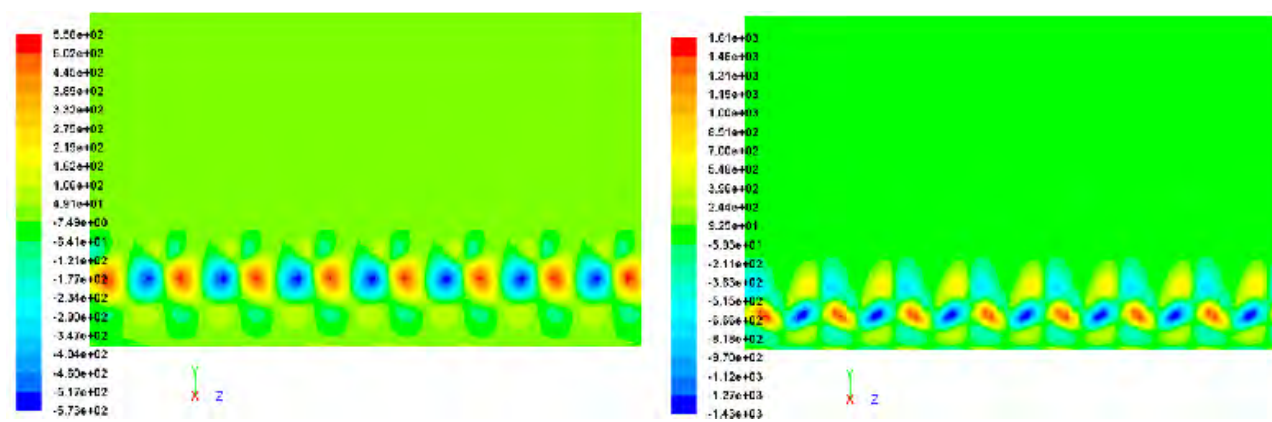
Fig. A.6.4.6. Turbulence intensity in the middle cross-section at the moments of maximum lift  
( $\Delta z=1$ ,  $\Delta T=1000^\circ\text{C}$ ,  $U_0=40\text{ m/s}$ )



a)  $\alpha = 60^\circ$

b)  $\alpha = 95^\circ$

Fig. A.6.4.7. Reynolds stress  $uu$ . See the legend in Fig. A.6.4.6.



a) minimum lift

b) maximum lift

Fig. A.6.4.8. Longitudinal vorticity in the transversal cross-section at the streamwise distance  $x=2\text{ cm}$  from the cylinder center;  $\alpha = 95^\circ$

**The flow about a "SAP" model (6.4.3)**

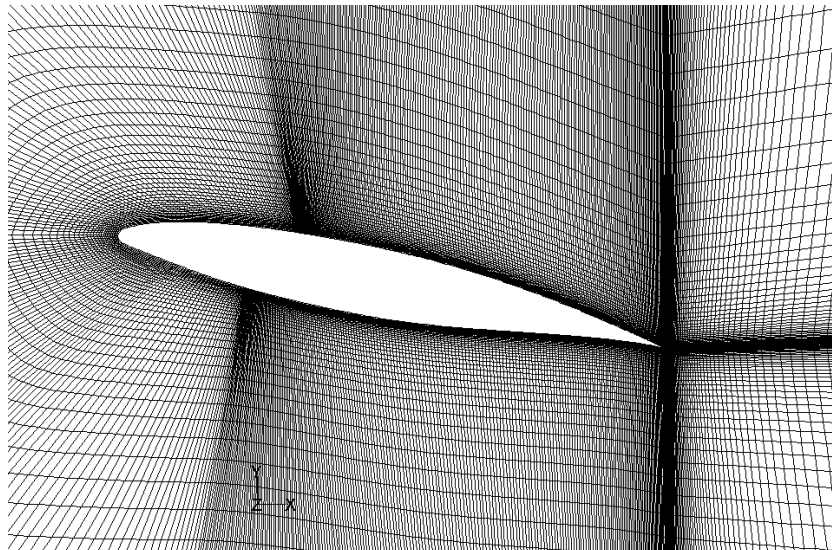
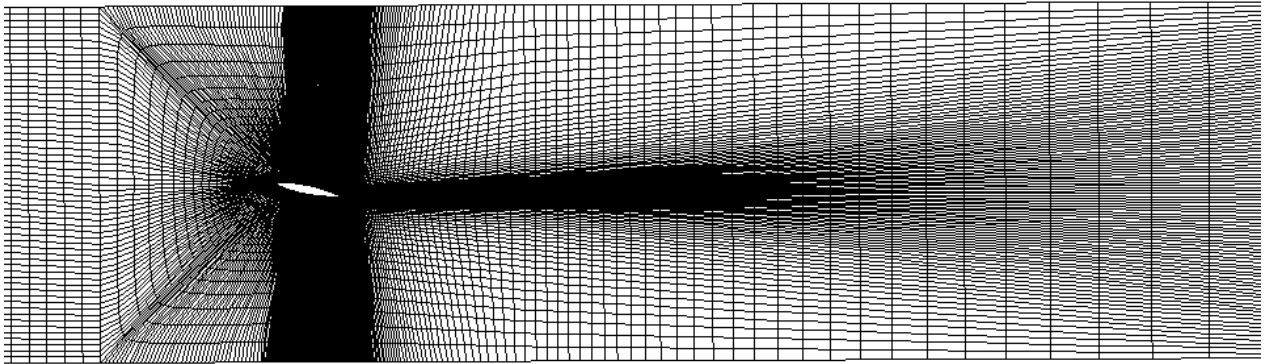
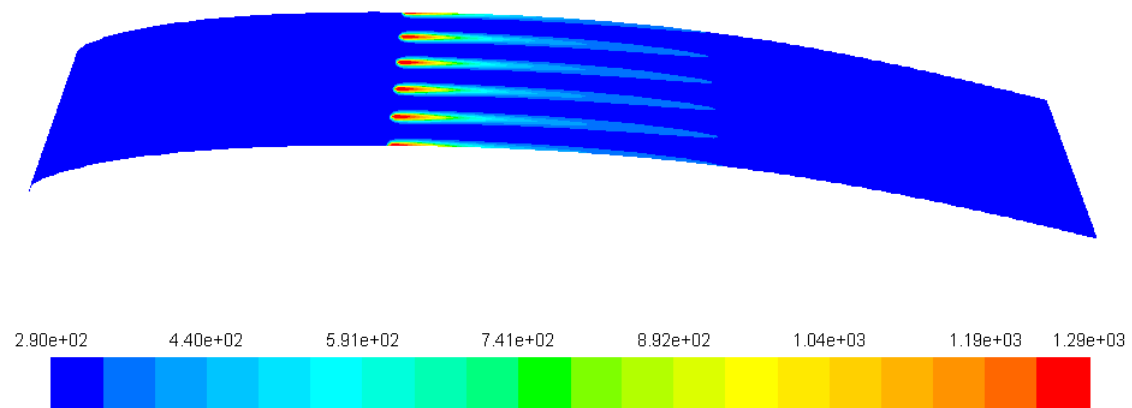
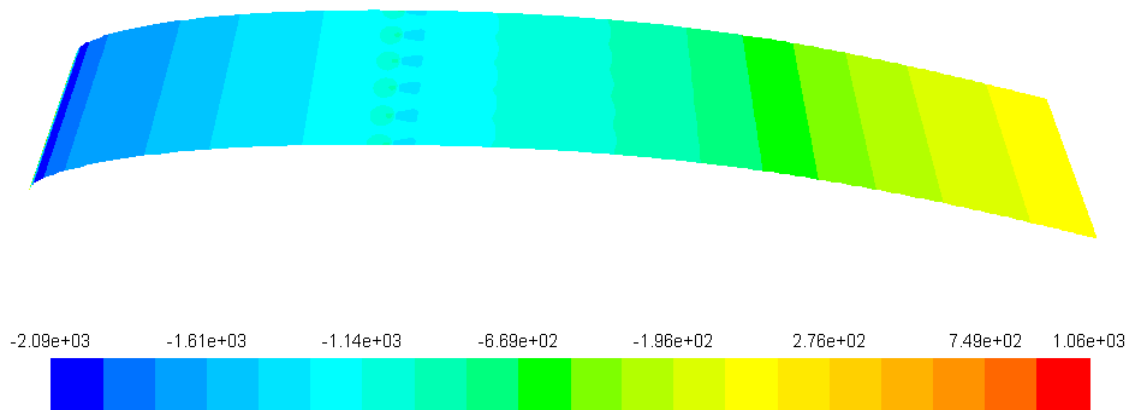


Fig. A.6.4.9. Frontal view of the calculation mesh.



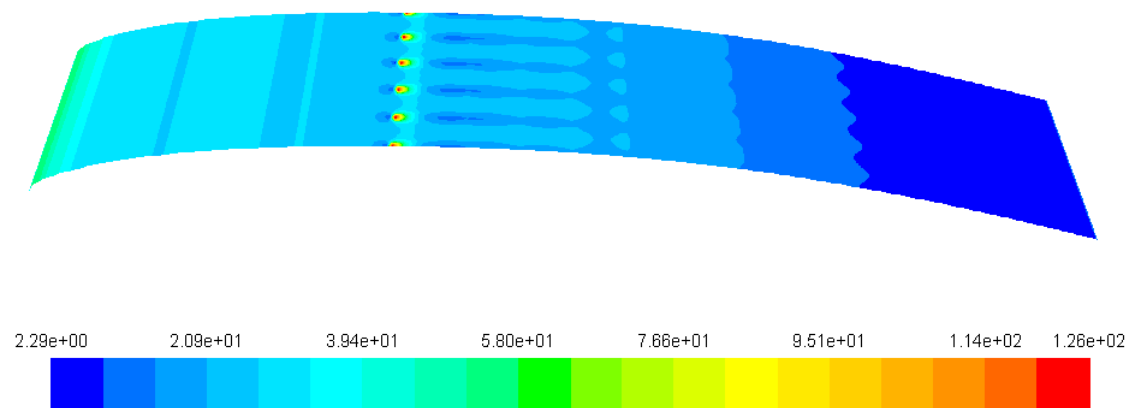
Contours of Static Temperature (k)

Aug 08, 2012



Contours of Static Pressure (pascal)

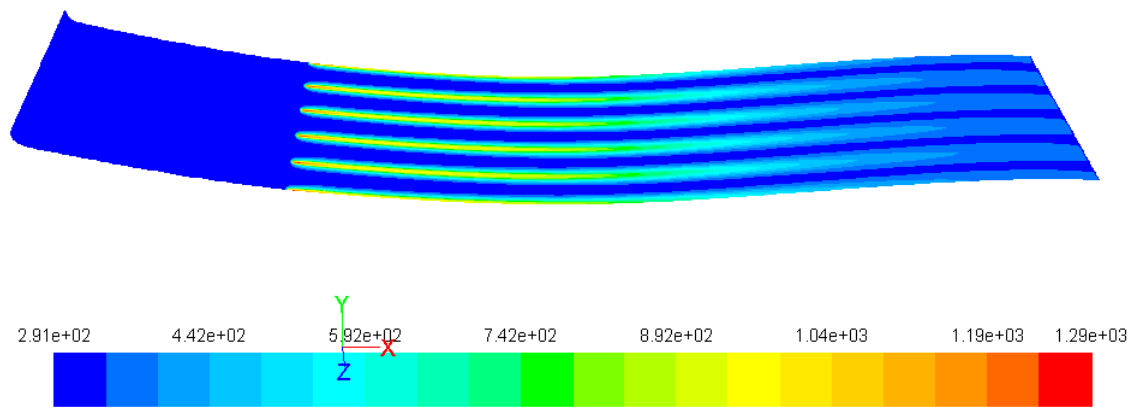
Aug 08, 2012



Contours of Wall Shear Stress (pascal)

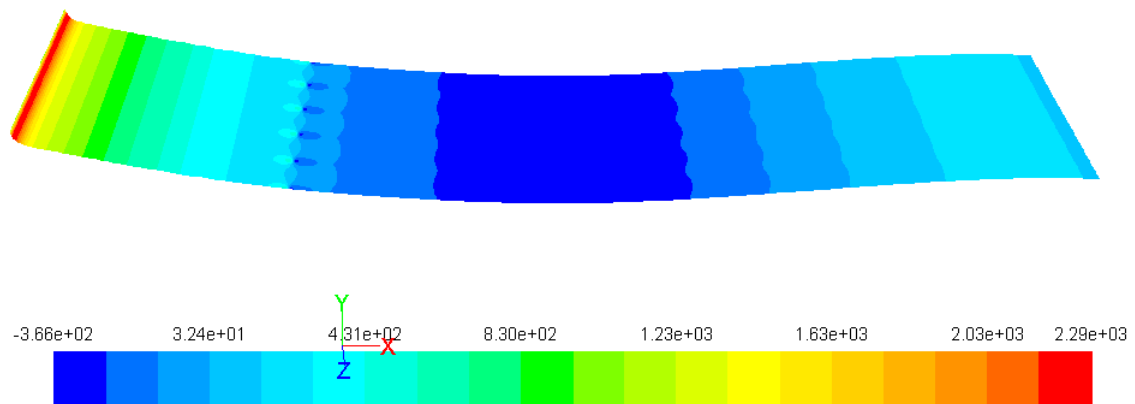
Aug 08, 2012

Fig. A.6.4.10. Temperature, pressure and shear stress distributions on the *upper* airfoil surface at  $\alpha=4^\circ$  in case of thermal arrays located at  $x=6.8$  cm on this surface.



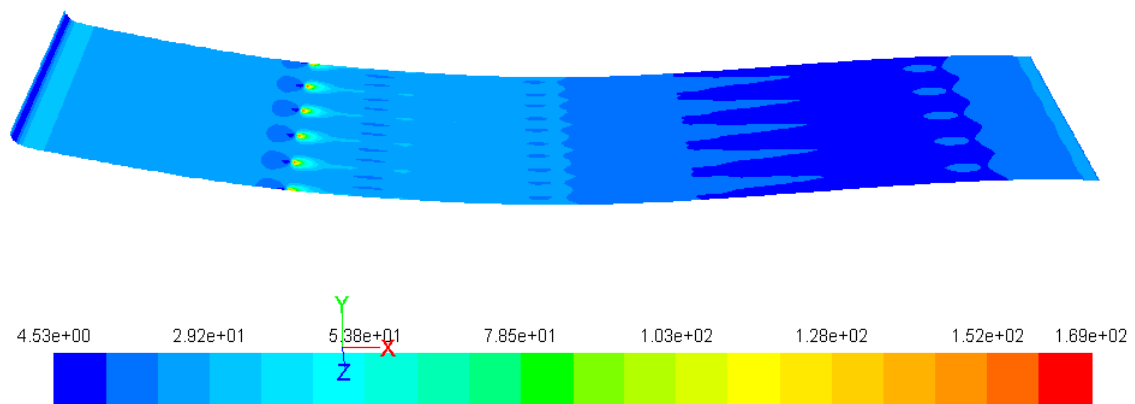
Contours of Static Temperature (k)

Aug 08, 2012



Contours of Static Pressure (pascal)

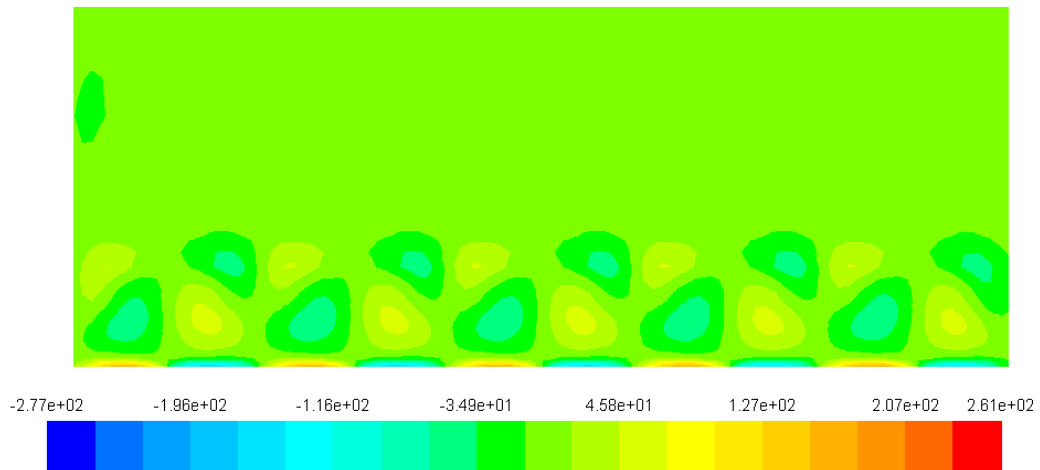
Aug 08, 2012



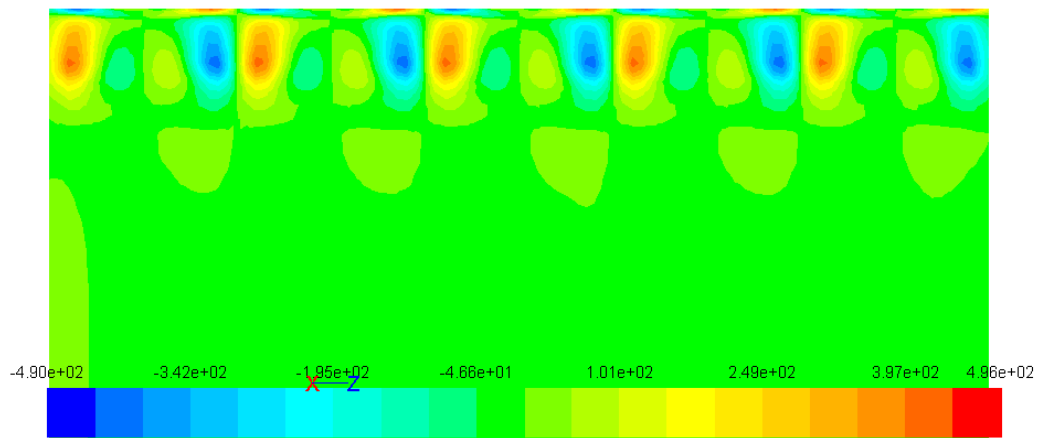
Contours of Wall Shear Stress (pascal)

Aug 08, 2012

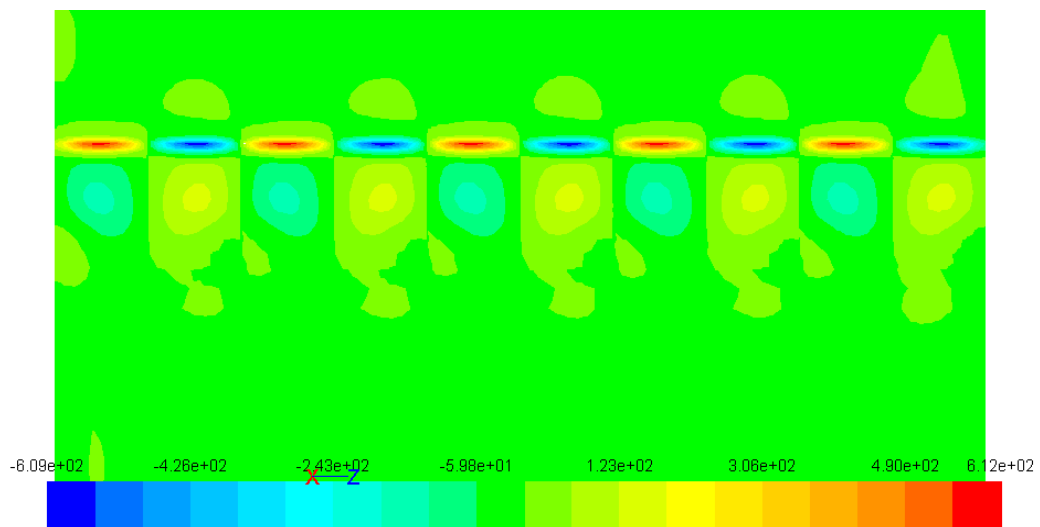
Fig.A.6.4.11. Temperature, pressure and shear stress distributions on the *lower* airfoil surface at  $\alpha=4^\circ$  in case of thermal arrays located at  $x=4.9$  cm on this surface.



(a)  $x=15\text{cm}$ , sources on the *upper* surface



(b)  $x=15\text{ cm}$ , sources on the *lower* surface



(c)  $x=20\text{ cm}$ , sources on the *lower* surface

Fig. A.6.4.12. Longitudinal vorticity in the transversal cross-sections at  $\alpha=4^\circ$

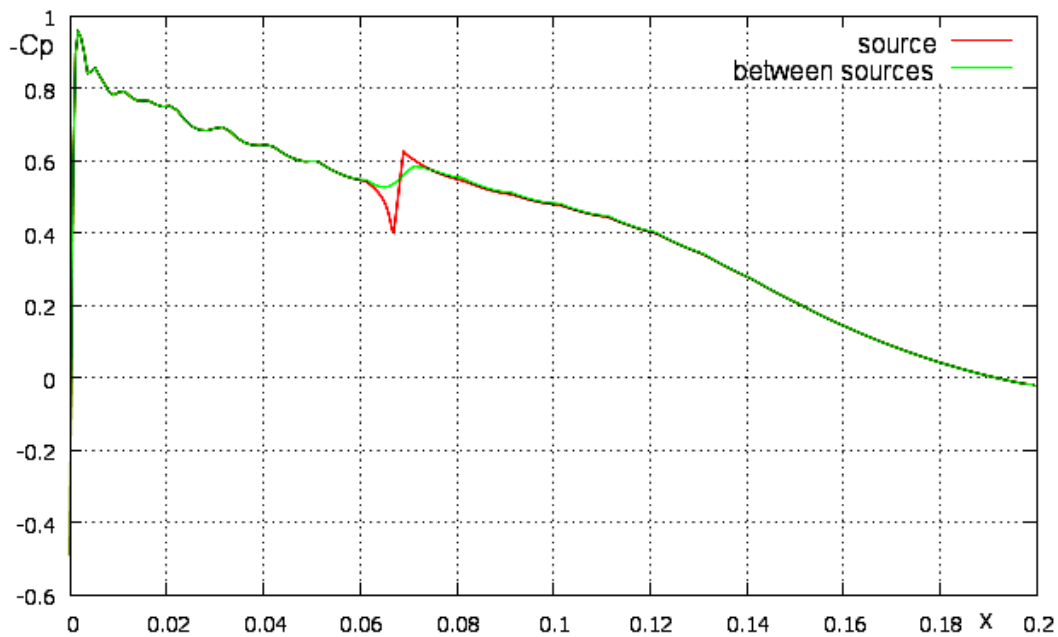


Fig. A.6.4.13. Pressure coefficient along the *upper* surface of the “SAP” at  $\alpha=4^\circ$  with the thermal array installed at 6.8 cm (0.34c) from the leading edge: red and green curves correspond to pressure distributions downstream of a thermal source,  $z=0$ , and along lines between the adjacent sources,  $z=\Delta z/2$ .

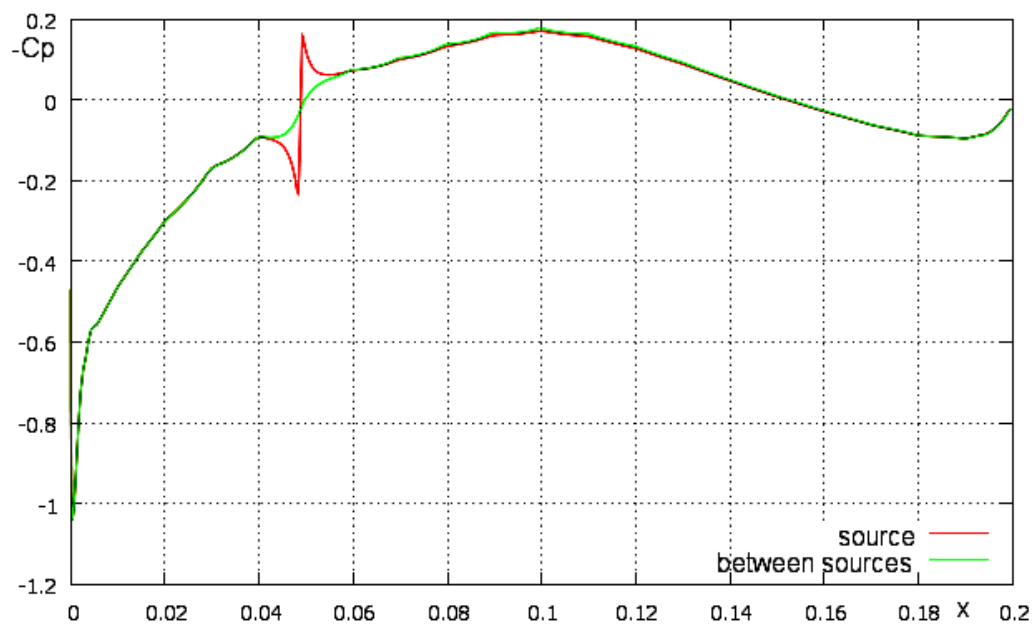


Fig. A.6.4.14. Pressure coefficient along the *lower* surface of the “SAP” at  $\alpha=4^\circ$  with the thermal array installed at 4.9 cm (0.25c) from the leading edge: red and green curves correspond to pressure distributions downstream of a thermal source,  $z=0$ , and along lines between the adjacent sources,  $z=\Delta z/2$ .



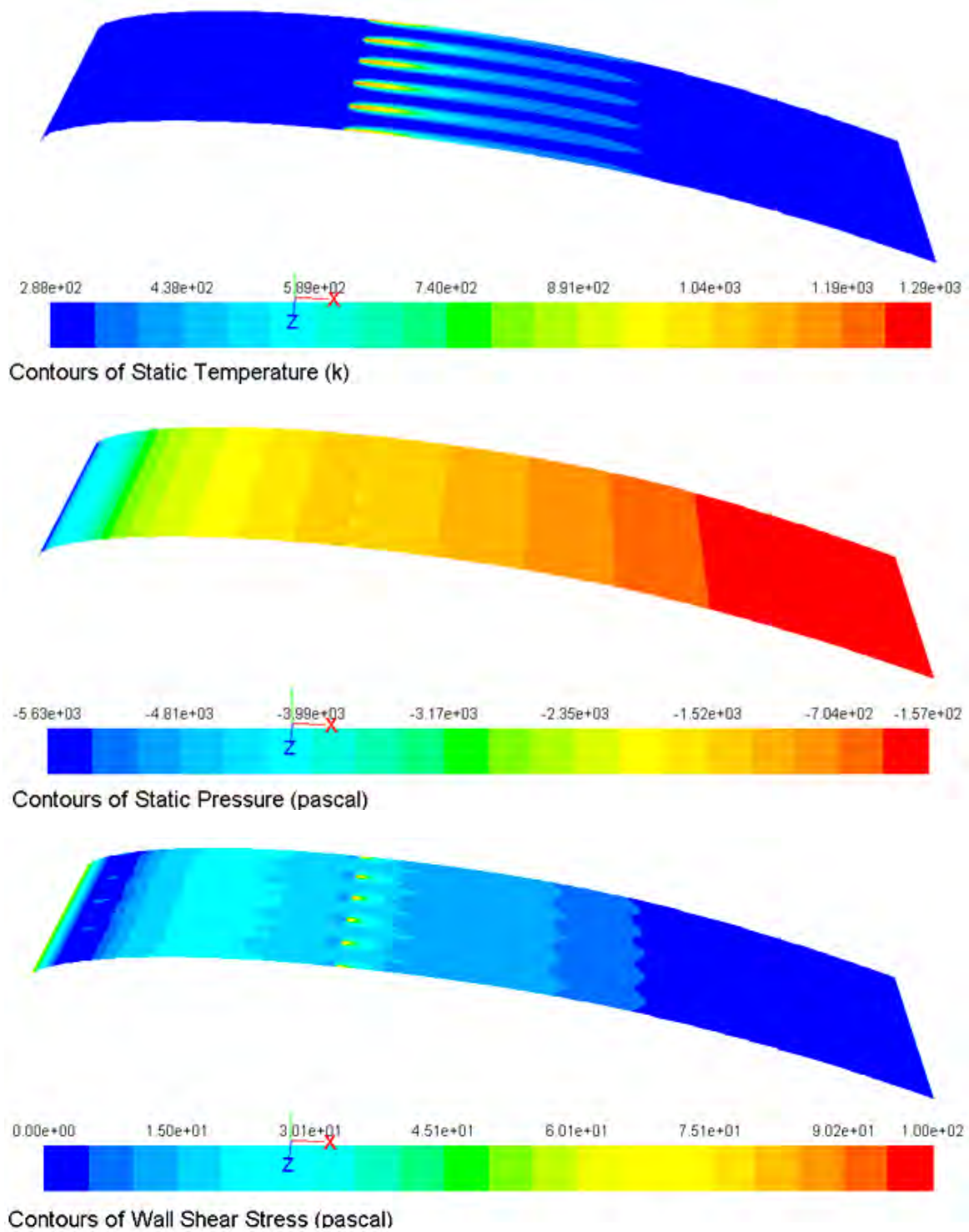


Fig. A.6.4.15. Temperature, pressure and shear stress distributions on the *upper* airfoil surface at  $\alpha=8^\circ$  and heat sources located at  $x=6.8\text{cm}$  on this surface.

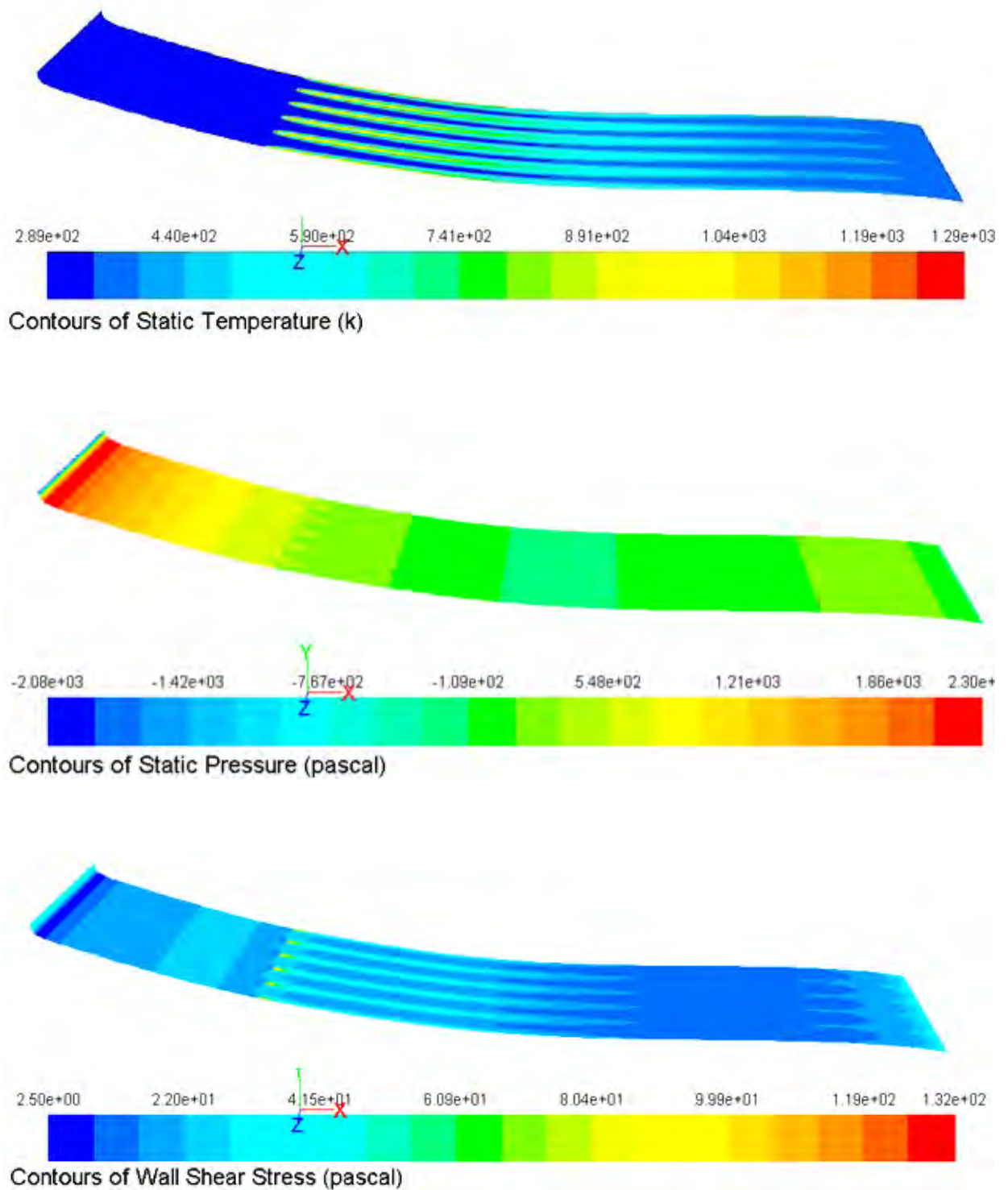
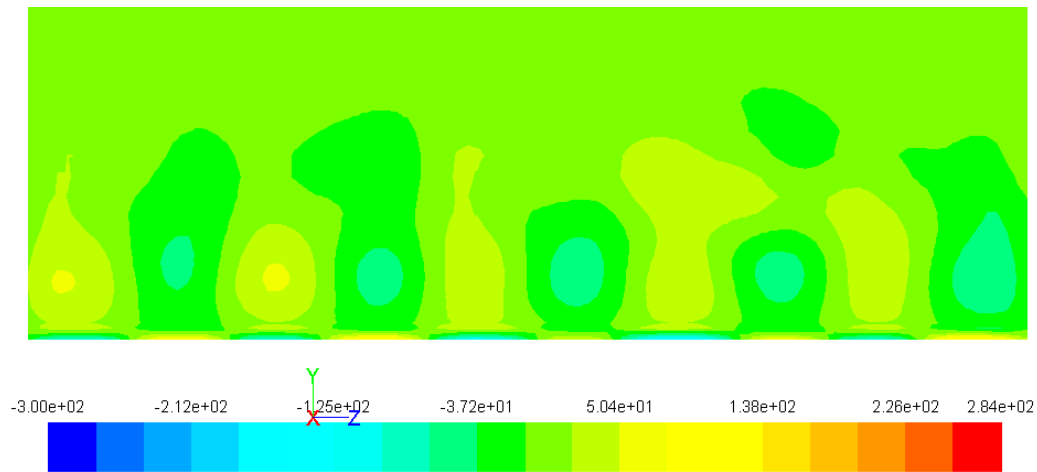
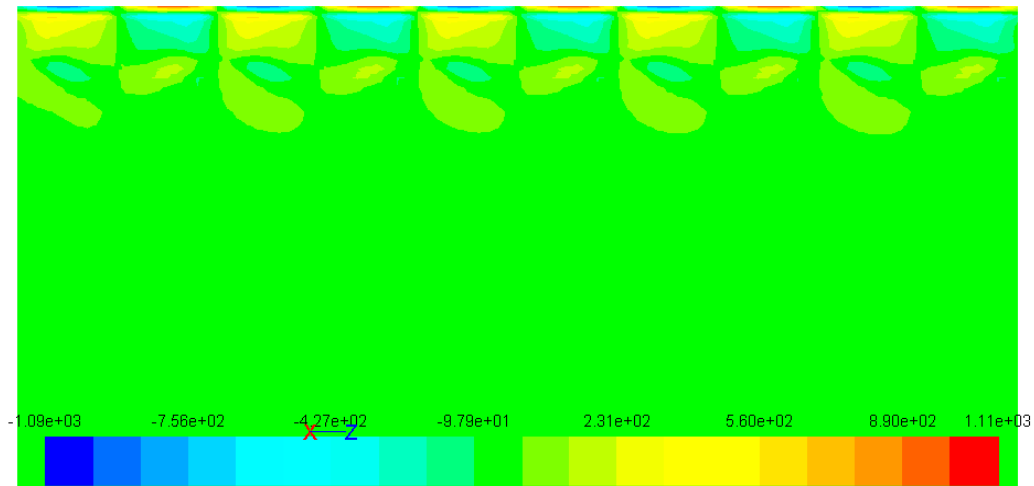


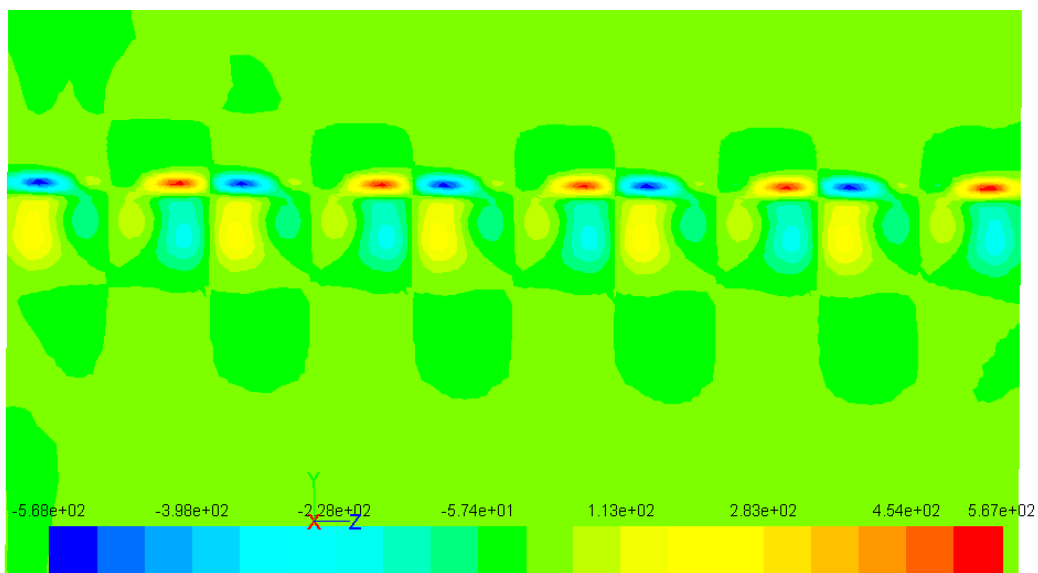
Fig.A.6.4.16. Temperature, pressure and shear stress distributions on the *lower* airfoil surface at  $\alpha=8^\circ$  and heat sources located at  $x=4.9\text{cm}$  on this surface.



(a)  $x=15\text{cm}$ , sources on the *upper* surface



(b)  $x=15\text{cm}$ , sources on the *lower* surface



(c)  $x=20\text{cm}$ , sources on the *lower* surface

Fig. A.6.4.17. Longitudinal vorticity in the transversal cross-sections at  $\alpha=8^\circ$   
**Distribution A: Approved for public release; distribution is unlimited.**

## APPENDIX, Ch. VII

### HOT-WIRE MEASUREMENTS OF A BOUNDARY-LAYER STRUCTURE MODIFIED WITH SPANWISE-REGULAR SURFACE HEATING

#### The purpose of wind-tunnel tests

These experiments are aimed to catch streamwise vortices by direct measurements of velocity distributions in the model's boundary layer. Correct application of the hot-wire constant-temperature anemometer (CTA) system requires certain practice and experience in addition to manuals and extensive published reviews. Therefore the initial cycle of experiments provided this necessary experience in handling, tuning and performing measurements using CTA.

The purchased 2-channel CTA blocks have two output ports each, one of the outputs of the so-called DC signal being of a low frequency band of order of a hundred Hertz. This signal corresponds to a mean velocity of the flow. Another one, the AC signal, corresponds to velocity fluctuations and has mean value equal to zero. This is made to raise accuracy of measurements of low-level fluctuations within several percents to a fraction of percent of full signal and thus could experience substantial losses when being digitized by lo-bit digital-analog converters (ADC) in case if these two signals are combined into one. Separate measurements of DC and AC signals make it possible to set appropriate gains for each measuring channel and to use the full range of ADC for both signals.



Fig. A7.1. R800 model in the test section with CTA probe holder

The first step of measurements consists in a number of tunings, in particular of frequency characteristics of servo-amplifier. Performing this operation, it was found that at high response frequencies of order of 20 kHz servo amplifier tends to self-excitation. It resulted in a very high level of signal noise that made impossible measurements of fluctuation velocities. This undocumented behavior required considerable efforts to understand it and to set a lower response frequency taking into account that such high frequencies are not inherent to low-speed subsonic flows.

The procedure of CTA calibration versus velocity in the empty wind tunnel showed that during even one testing day it is desirable to repeat such calibrations because of

high sensitivity of the CTA output to flow temperature.

#### Results and discussion

To avoid the harmful microwave influence on the CTA system during the flow field measurements, the prototype model (Fig. A7.1) was used where the thermal control was realized due to resistive heating of the embedded array of streamwise elements. Normal velocity profiles for reference and controlled cases are shown in Figs. A7.2 and A7.3 (averaged velocity) and Figs. A7.4 and A7.5 (fluctuating velocity) in a form of its standard deviation.

In the reference case, the averaged velocity profile is a typical one for a turbulent boundary layer. A level of flow fluctuations is practically constant and close to the one in the empty test section at a given free-stream velocity. Some inflections of curves (Figs. A7.2 and A7.4) at  $h = 1.5$  and  $h = 3$  mm can perhaps indicate a presence of unstable streamwise vortices naturally developing over a concave surface.

In the controlled case with heated streamwise elements, additional inflections of curves occur (Figs. A7.3 and A7.5). It is typical for fluctuating velocity profiles which have 2 maximums in a near-wall region. It can be interpreted so that streamwise vortices thermally generated in the boundary layer have a considerably higher intensity than those of a reference case.

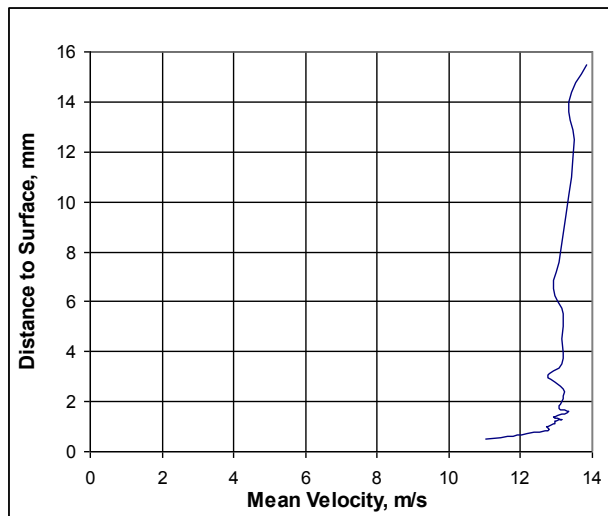


Fig. A7.2. Velocity profile for reference case

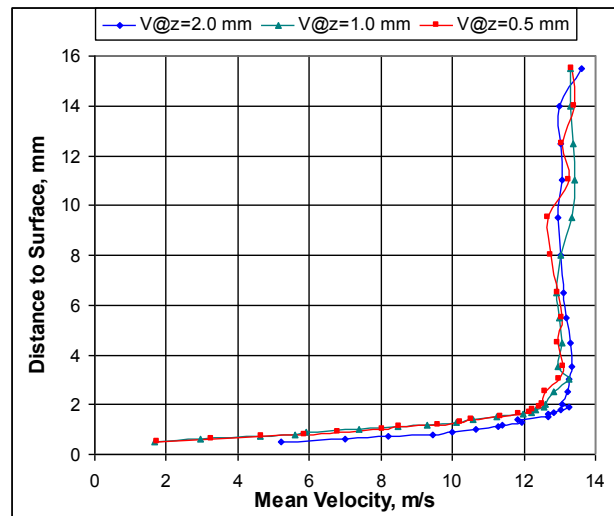


Fig. A7.3. Velocity profile for controlled case

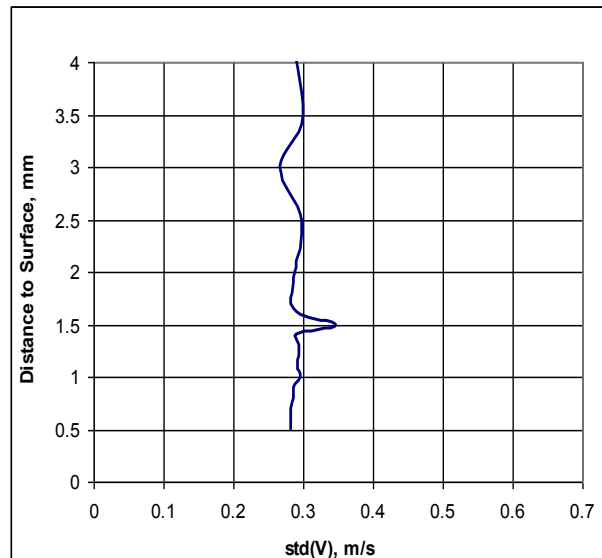


Fig. A7.4. Velocity fluctuation for reference case

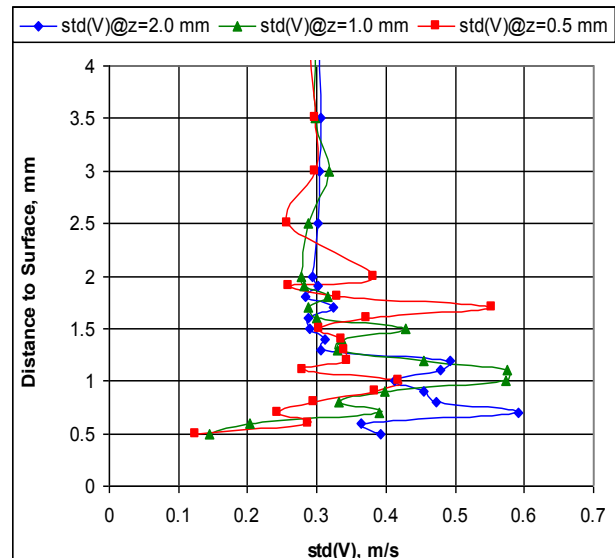


Fig. A7.5. Velocity fluctuation for controlled case

This 2-maximum character of the fluctuating velocity distributions is found in various spanwise sections of the boundary layer along  $\lambda_z$ . The main global maximum is accompanied with a less pronounced one located farther away from the wall. Some plots show other smaller maximums

in the very vicinity of the wall. It can indicate the meandering of the vortical system or the development of a multi-deck vortical structure what was shown numerically for certain cases.

Closer to the vertical plane of a heated element, the fluid is displaced farther away from the wall. It shrinks the distance between the above mentioned peaks from 0.5 mm at  $z = 2.0$  mm to 0.3 mm at  $z = 0.5$  mm that shifts up the maximum of the fluctuating velocity by 1 mm. New peaks with lower intensity arise under the basic maximum. It can be an evidence of developing additional vortex pairs adjacent to the heated elements competing with the basic generated vortical structure. Similar vortical patterns were obtained numerically under conditions of heating insufficient to maintain the basic vortex pairs corresponding to the given  $\lambda_z$ . In other words, the  $\lambda_z$  distance can be too big for the applied temperature gradient to get a sustainable forced system of streamwise vortices with the given spanwise periodicity of parameters.

Comparing fluctuating velocity profiles, one can see that the level of fluctuations in the vicinity of the wall above heated elements (red curve of Fig. A7.5) is lower than that between the heated elements or in a reference case. It must be affected by averaged local outward flows above the heated strips which move maximums of the fluctuating velocity out of the wall. Moving a vertical measuring section spanwisely to the position between the neighboring strips, one gets the fluctuating velocity maximum closets to the wall (blue curve of Fig. A7.5). It is the location between two counter-rotating vortices bringing fluid inward, into a wall-adjacent area of the boundary layer.

Thus the obtained results give the first direct evidence of developing pairs of counter-rotating vortices between two neighboring heated strips. Of course, to get this structure fully corresponding to the forcing temperature boundary conditions, further investigations are required which will result in clear recommendations about the correlation between control parameters  $\lambda_z$  and  $\Delta T(z)$  and basic flow parameters. Such a correlation will imply least losses of the energy consumed for the proper organization of the spanwise organized thermal fields. In its turn, the experimental investigation is to be guided by the matched numerical studies that proved to be the correct approach to the formulated flow-control problem.

### **Testing program and procedure**

Full pressure was measured in a boundary layer of a concave surface of the resistively heated model with the geometry and size of the models used for MW-controlled experiments. The model with a chord of 200 mm had several sections of streamwise flush-mounted wires heated with the applied voltage. Three downstream sections on the concave surface are characterized with 5 mm spanwise distance between the heated elements. Measurements were performed using miniature Pitot tube, MPT (full pressure probe) as shown in Fig. 4.1. The model was installed in the wind-tunnel test section at an angle of attack  $\alpha = 8^\circ 40'$  as shown in Fig. 4.2.

Measurements were performed at heating of two front control sections at six downstream distances from the model leading edge:  $x = 88, 97, 106, 113, 135$ , and  $155$  mm with. At chord positions  $x = 106$  and  $154$  mm, measurements were performed for twelve spanwise positions beginning from  $z = 0$  to  $z = 5.5$  mm (see Fig. 4.1). In the rest of chord positions, measurements were performed for two spanwise positions:  $z = 0$  to  $z = 2.5$  mm.  $z = 0$  corresponds to the probe position directly above the heated element and  $z = 2.5$  mm corresponds to the probe position between two adjacent heated elements. At spanwise positions of  $z = 0$ ,  $z = 2.5$  mm (and  $z = 5.0$  mm where applicable) reference measurements were performed.

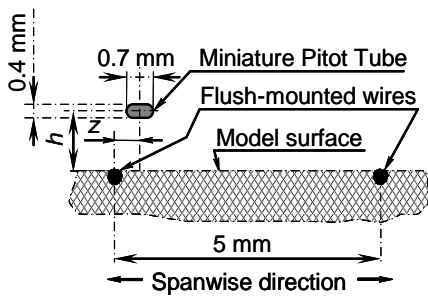


Figure 4.1. Cross-section of resistively heated model and MPT: downstream view

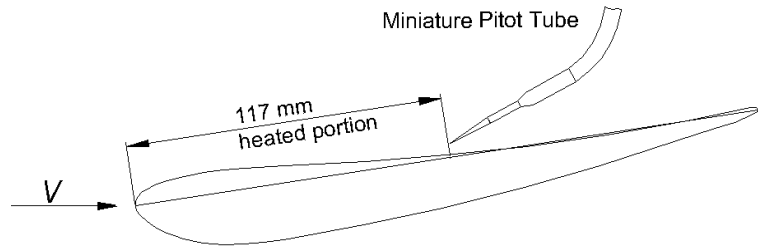


Figure 4.2. Scheme of measurements: resistively heated model at  $\alpha=8^{\circ}40'$

Full pressure values were measured during 4 s at a sampling rate of 5000 samples per second (sps) and velocity values were calculated for each measured pressure value. Averaged and fluctuation velocity values (in a form of velocity standard deviation) were calculated at each probe position using a whole sample of velocity values.

## Results and discussion

Investigation of velocity profiles in the boundary layer with local surface heating is necessary to get an insight into physical mechanisms of local thermal impact on a character and parameters of the boundary layer flow and finally on the forces acting on the body in such a flow. It is essential not only to find experimentally vortex structures displayed numerically but also to estimate their size, location, strength and development both in streamwise and spanwise directions. Besides, the correlation should be shown between the boundary layer structure and integral aerodynamic characteristics of the body in a form of pressure coefficients as well as lift, drag and pitch moment coefficients.

Earlier within the framework of this project, mean and fluctuating velocity profiles were studied over a concave surface of resistively heated R800 model with streamwise heated elements. This study showed formation of streamwise vortices in accordance with the heating elements layout. Vertical velocity profiles were measured at one downstream section between two heated elements with 0.1 mm step at angles of attack of  $\alpha=+19^{\circ}$  and  $\alpha=+8^{\circ}40'$  (QRT4 and QRT6 respectively). Heated elements with 5-mm spanwise spacing were organized into three independent downstream sections covering almost 90% of the entire surface.

In the present cycle of experiments, only front and middle sections were heated. The downstream end of the middle section was located at 117 mm from the leading edge, which corresponded to a relative cord position of  $\bar{x}=58.5\%$ . As mentioned above, measurements of velocity profiles were carried out at several downstream sections to obtain flow characteristics over both a heated section itself and in the wake behind it.

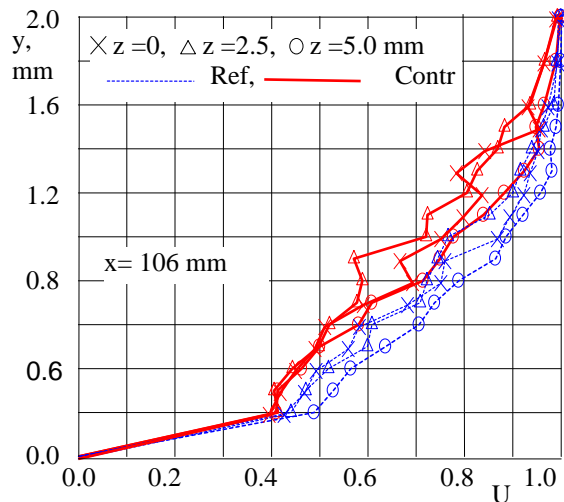


Fig. 4.3. Vertical profiles of averaged velocity **above** the heated section of the model in reference and controlled cases

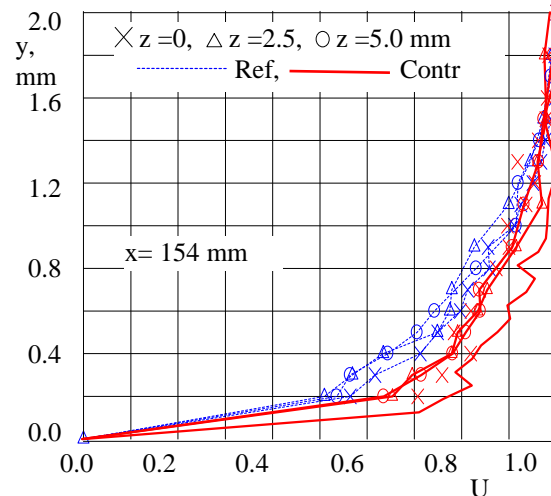


Fig. 4.4. Vertical profiles of averaged velocity **in a wake downstream of** the heated section in reference and controlled cases

Figs. 4.3 and 4.4 compare mean velocity profiles in the boundary layer at different cord positions. Fig. 4.3 shows velocity profiles in the boundary layer with and without local heating at  $x = 106$  mm and Fig. 4.4 deals with data obtained in the section of  $x = 154$  mm that is 37 mm downstream of the aft edge of the middle heated section. These two cases differ noticeably. Mean velocity profiles are less full over a heated section. Inflectional type of profiles gives an evidence of developing vortex structures in boundary layer. Boundary layer thickness and displacement thickness grow in case of local heating compared to the reference case. Flow velocity in a near-wall region in the controlled case is lower than in the reference one; lower velocity gradients on the wall impose lower shear stress.

The situation is opposite in the wake downstream of the heated elements. In a near-wall region, flow velocity is higher in the controlled case and, accordingly, the velocity gradient is greater than in the reference case. Displacement thickness in the wake decreases. Inflection of velocity profiles in the wake is lower that can be interpreted as a lower intensity of generated vorticity. The whole vortical structure in the wake is pressed to the concave surface by the outer flow and washed out. Finally, the near-wall fluid mixing results in velocity profiles typical for a turbulent boundary layer.

It should be mentioned that since the full pressure probe measures only a streamwise component of flow velocity, it must be taken into account at interpretation of the obtained results.

Figs. 4.5 and 4.6 show the boundary layer structure in a spanwise direction between two adjacent heated elements for the heated part of the model (Fig. 4.5) and for the downstream part in the wake zone (Fig. 4.6). Sequences of velocity profiles measured in a spanwise direction have similar typical features as those found for the chordwise direction. Detailed investigations of velocity fields (see QRT4 and QRT6 reports) showed a wavy character of velocity variations with a period equal to a half of the spacing between the heated elements (2.5 mm in our case). Fluctuating velocity profiles are in a good agreement with the previous observation about the spanwise flow field periodicity which appeared to be different over a heated section and downstream of it. Dashed lines in Figs. 4.5 and 4.6 indicate the variation of a height of fluctuating velocity peaks. Over the heated section of the model, this height has period equal to a half of the spacing between the heated elements (2.5 mm). In the

wake part, this period grows to the whole value of spacing (5.0 mm). Probably greater energy of thermal disturbances over the heated surface causes formation of an additional vortex pair, i.e. generates a half smaller flow structure compared to the scale of the disturbing factor (spacing between the heated elements). Downstream dispersion of this energy makes it possible to support only one pair of vortices between the adjacent heated elements, i.e. the spanwise scale of regular vortices doubles in the wake without a direct contribution of energy. Besides, a peak of the fluctuating velocity across a boundary-layer thickness moves up over the surface in the controlled case compared to the flow over the “cold” (reference) surface.

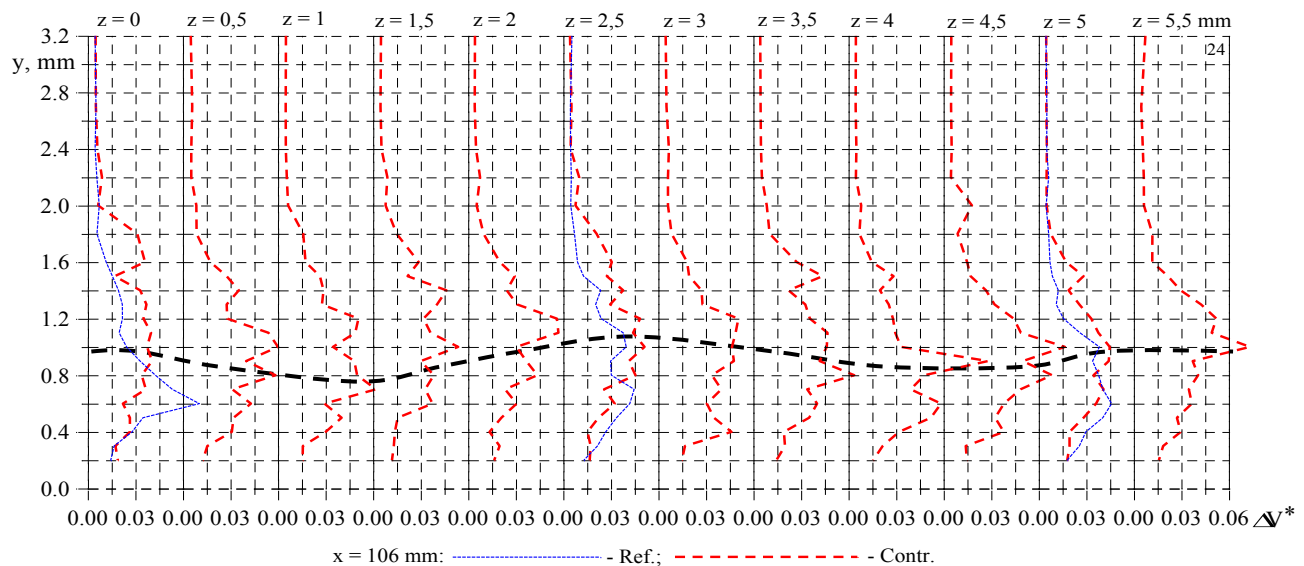


Figure 4.5. Variation of vertical fluctuating velocity profiles in a spanwise direction over the heated section of the model **between** heated elements in reference and controlled cases

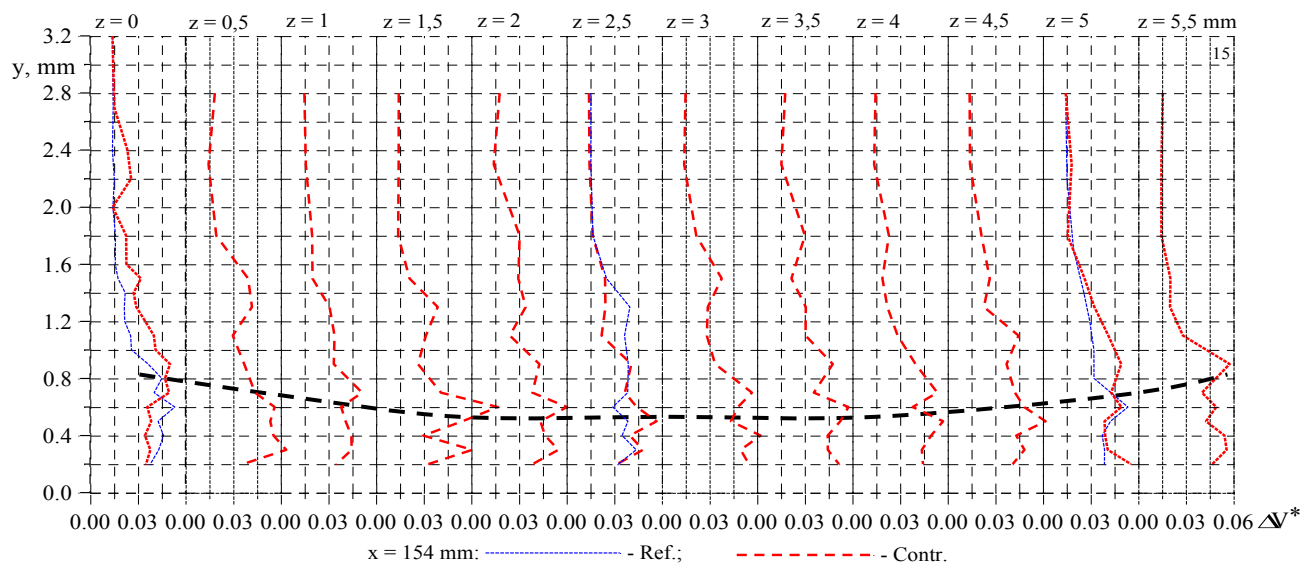


Figure 4.6. Variation of vertical fluctuating velocity profiles in a spanwise direction **in the wake downstream** of the heated section in reference and controlled cases

Figs. 4.7 and 4.8 show mean velocity profiles in different streamwise sections with and without local spanwise-regular heating. Measurements were carried out for two spanwise positions: directly above a heated element (or behind it in the wake) –  $z = 0$  and between adjacent heated elements –  $z = 2.5$  mm. Analysis should account for flow conditions in the reference case: velocity grows from the leading towards the trailing edge where fluid is pressed to the surface by the outer flow. Black lines show variation of a boundary layer thickness along the model's chord in the controlled and reference cases. In the controlled case, the boundary layer is thicker over the heated section (to  $x = 113$  mm). In the wake ( $x = 135$  mm and  $x = 155$  mm), the influence of heating decays and the boundary layer thickness approaches to that of the reference case.

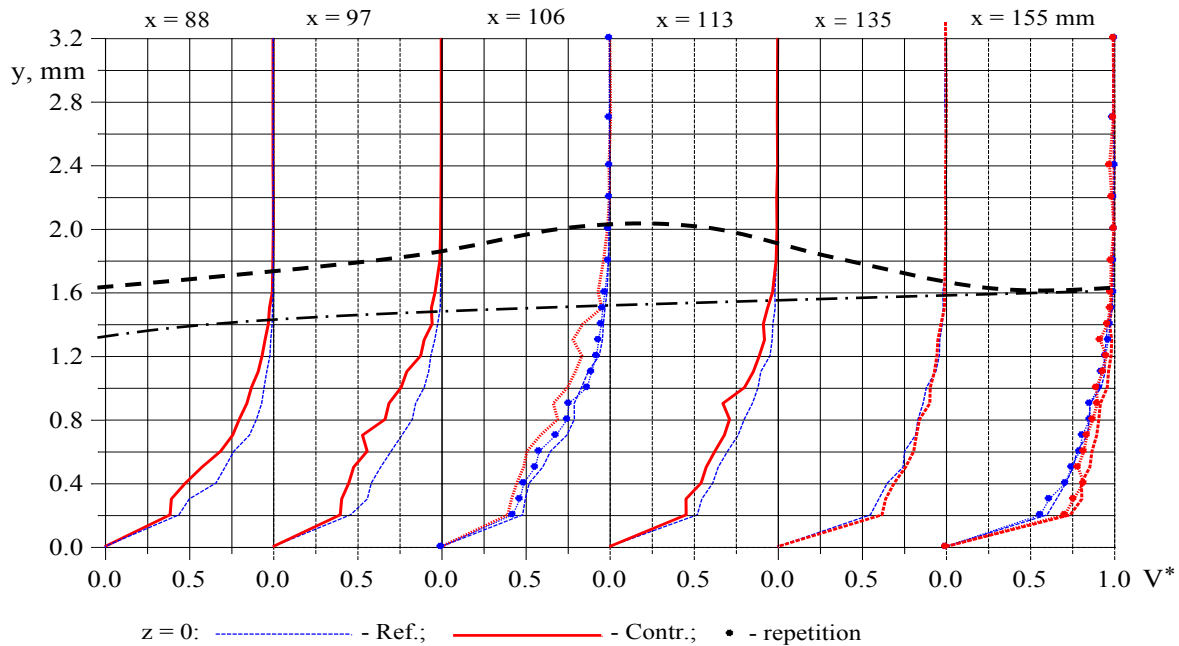


Figure 4.7. Variation of vertical profiles of mean relative velocity in streamwise direction **above** heated element in reference and controlled case

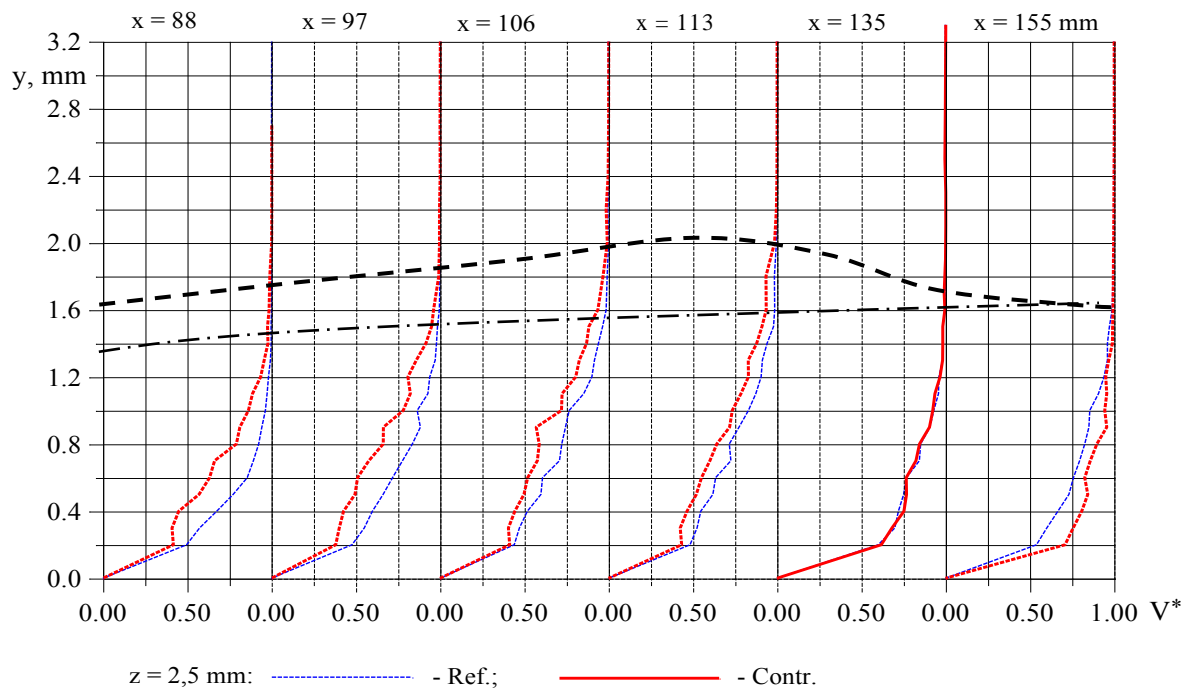


Figure 4.8. Variation of vertical profiles of mean relative velocity in streamwise direction **between** heated elements in reference and controlled case

## SUMMARY

1. Measurement of the boundary layer vortical structure revealed a number of features characteristic to the flow over a concave surface of the model containing a section of heated spanwise-regular elements.
2. The space scale of vortices generated over the heated section is half less that the scale of the thermal control factor (a spacing between the heated elements). It is in agreement with the numerical results for situations of insufficient thermal energy delivered into a boundary layer (low spanwise temperature gradient, too narrow heated elements or too large spacing between the thermal sources).
3. Scales of streamwise vortices downstream of the heated section doubles becoming equal to the spacing between the elements. Vortex shape in a spanwise cross-section transforms from almost circular over a heated section to a flat stretched along a span in the wake downstream of the heated area.
4. Velocity gradient in the vicinity of the heated surface section decreases thus showing a tendency to decreasing shear stress values. It is to be confirmed with results of direct measurements of aerodynamic coefficients.

To the paragraph: 7.1. *Localized MW heating of the surface*

### Model #10 Testing

#### Program and data reduction

Model #10 was tested at pre-stall to post-stall negative angles of attack  $\alpha = -4^\circ$  to  $-14^\circ$ . Five test runs were performed: three runs with pressure ports #6 to #13 connected to pressure transducers and two – with connected pressure ports #1 – 5, 14, 15. For lift, drag, and pitch moment coefficients all data were combined into one sample and averaged for each angle of attack. For pressure coefficients, respective data were processed in the similar way.

#### Wind-tunnel results

Measured lift, drag, and pitch moment coefficients are shown in Figs. 3.12-3.14; here, angle-of-attack and lift coefficient axes have reverse directions. Separation on the concave surface started at  $\alpha = -6^\circ$ . It caused increase of drag and pitch moment coefficients in the post-stall region; lift coefficients went on rising up to  $\alpha = -10^\circ$ .

Switched on flow control made no significant influence on the lift coefficient. This is typical for R800 model with the control applied to its concave surface which redistributed pressure so that lift coefficient variations were minimal. Drag coefficients somewhat changed at  $\alpha = -6^\circ$  to  $-10^\circ$ .

Figs. 3.15 – 3.20 show pressure coefficient variations in several drain ports. Pressure ports #10 (results of Fig. 3.17) and #11 (Fig. 3.18) are located correspondingly at the front and rare edges of the heated elements (see Fig. 3.2). At

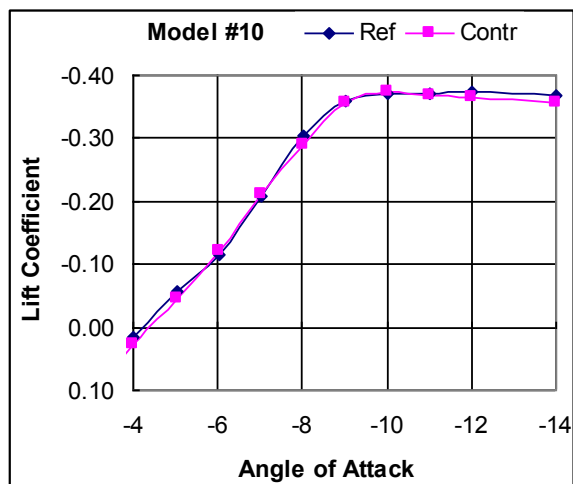


Fig. 3.12. Lift coefficient for model #10

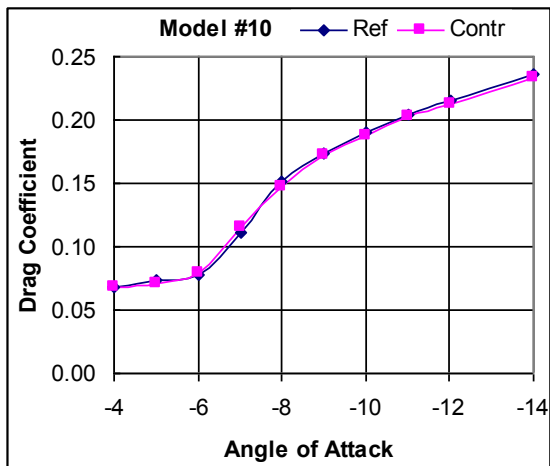


Fig. 3.13. Drag coefficient for model #10

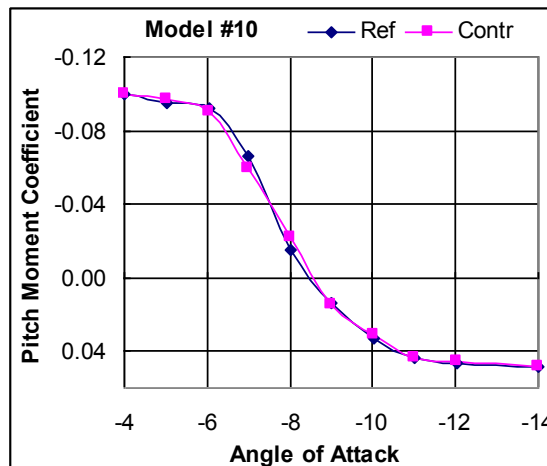


Fig. 3.14. Pitch moment coefficient for model #10

pre-stall angles little differences are observed in reference and control cases in the nose part of the model. Suction is less in the controlled case beginning from  $\alpha = -6^\circ$  in the very front part of the surface upstream of the heated elements. The situation is opposite in the part of the concave surface downstream of the heated elements. It explains a little difference between lift coefficients in reference and controlled cases.

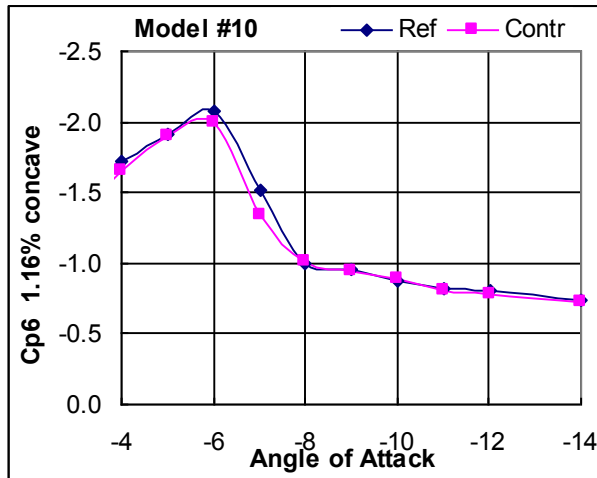


Fig. 3.15. Pressure coefficient at 1.16% of chord ( $x = 2.3$  mm) on the **concave** surface of model #10

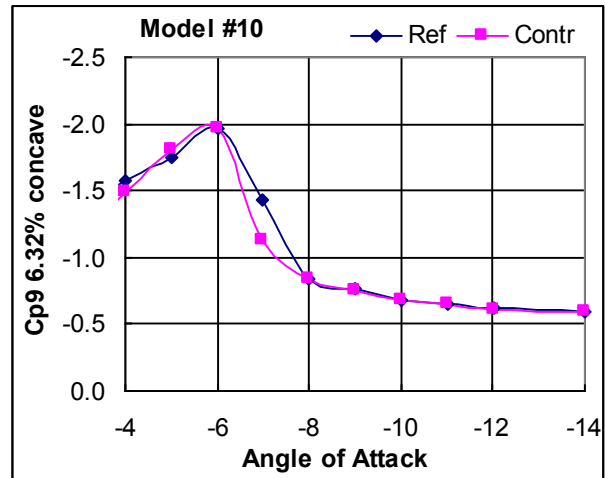


Fig. 3.16. Pressure coefficient at 6.3% of chord ( $x = 12.5$  mm) on the **concave** surface of model #10

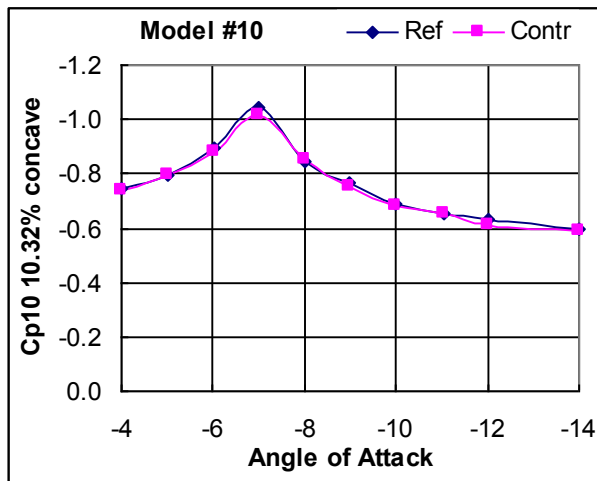


Fig. 3.17. Pressure coefficient at 10.3% of chord ( $x = 20.4$  mm) on the **concave** surface of model #10

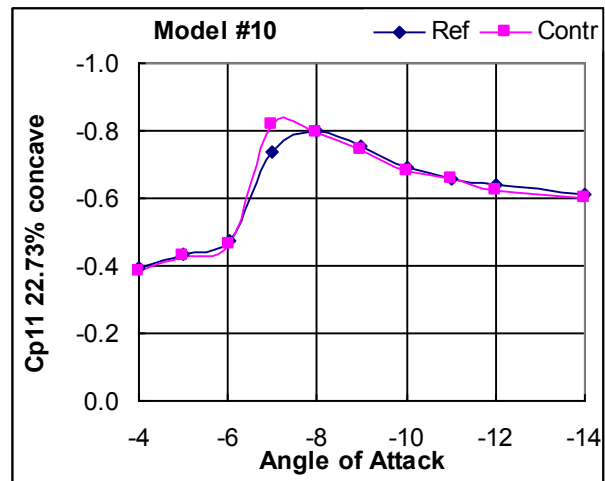


Fig. 3.18. Pressure coefficient at 22.7% of chord ( $x = 44.95$  mm) on the **concave** surface of model #10

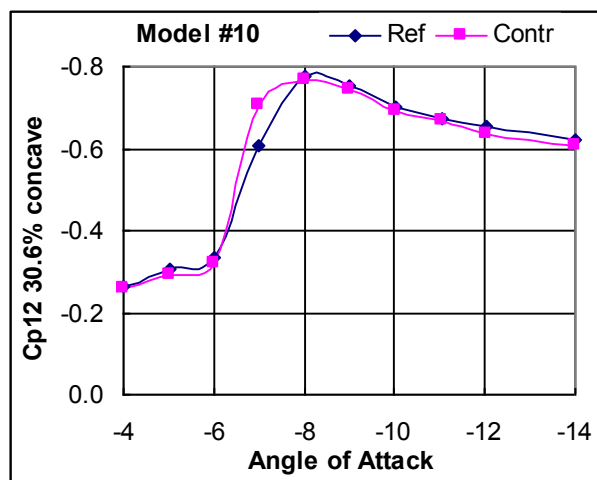


Fig. 3.19. Pressure coefficient at 30.6% of chord ( $x = 60.5$  mm) on the **concave** surface of model #10

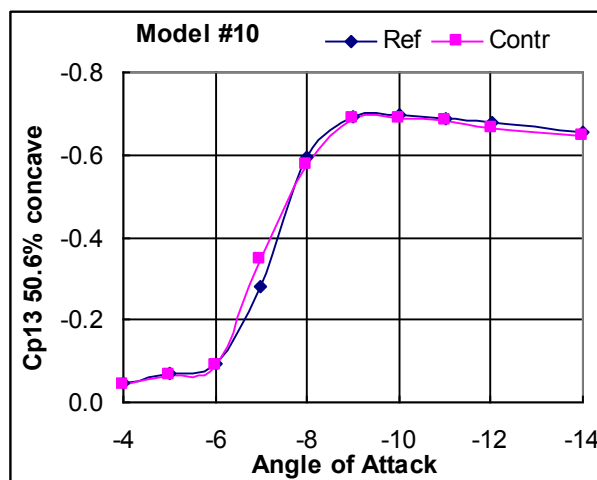


Fig. 3.20. Pressure coefficient at 50.6% of chord ( $x = 100.1$  mm) on the **concave** surface of model #10

#### Test results for the model #09 (thermal control section over a convex surface)

Figures 4.4 through 4.6 show variation of lift, drag, and pitch moment coefficients depending on angles of attack in reference ("r") and controlled ("c") cases for two test runs. The obtained results show almost no difference in  $C_L$  and  $C_D$  behavior in a pre-stall region. But a stall angle in the "prototype" controlled case is less by 1 deg then in the reference case, which is similar to the behavior in microwave controlled case (see QRT7 report). In a pre-stall region, no meaningful variations of lift and drag coefficients were registered. Pitch moment coefficients cannot be compared by absolute values because of different position along a model's chord, at which they were measured in AFIR and UTAD-2. Stall angles and lift curve slopes are also different in these sets of tests because test sections of these wind tunnels are of different types and sizes and no corrections were applied. It should be noted that the behavior of pitch moment coefficient in "prototype" tests is non-monotonous showing substantial waviness. This phenomenon will be discussed below.

Pressure coefficients behavior is in a good agreement with that for lift and drag coefficients in almost all pressure ports. Some of them are shown as an example in Figs. 4.7, a-d. On a convex surface, suction increases with an increased angle of attack (pressure coefficients become more negative) up to the stall. When stall occurs, abrupt drop of suction is observed in a front part of the model where  $C_p < -1$  and certain increase of suction appears in the aft part where  $C_p > -1$ . On the concave surface at pre-stall angles, pressure varies according to the critical point location (Fig. 4.7, c, d). The stall is manifested with an abrupt change of pressure and pressure redistribution over the whole model surface. At stall conditions, velocity over convex surface drops and the critical point on a concave surface shifts towards the leading edge of the model.

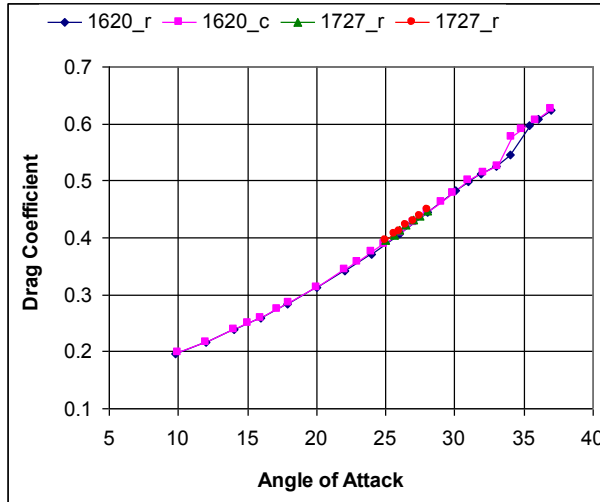


Fig. 4.4. Drag coefficient for the #09 model vs. angle of attack. Averaged data

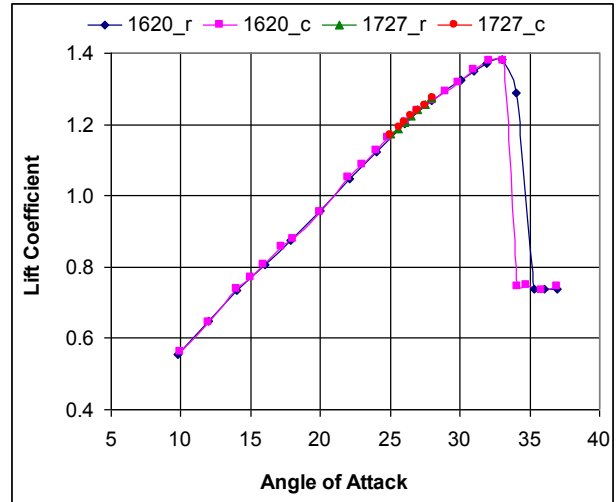


Fig. 4.5. Lift coefficient for the #09 model vs. angle of attack. Averaged data

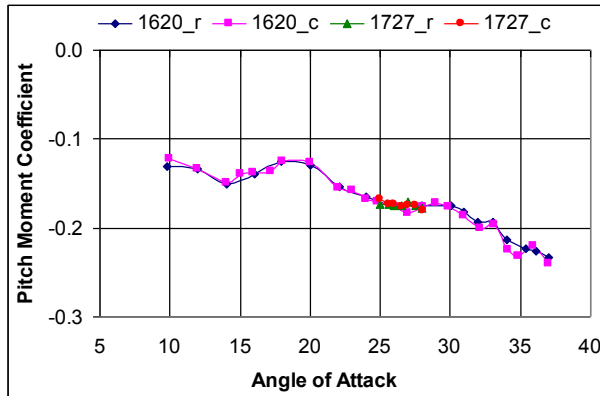
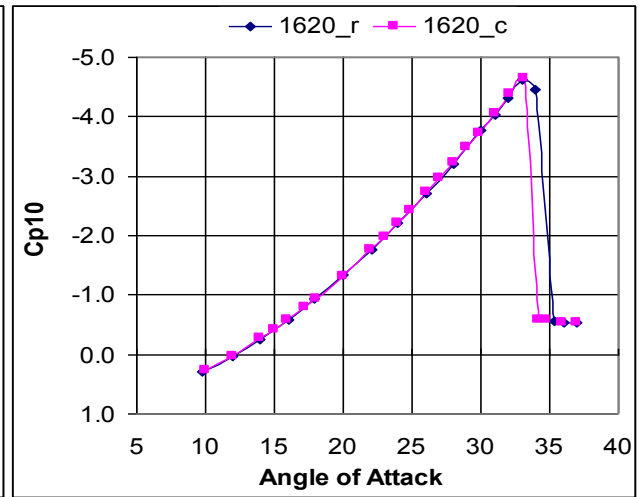
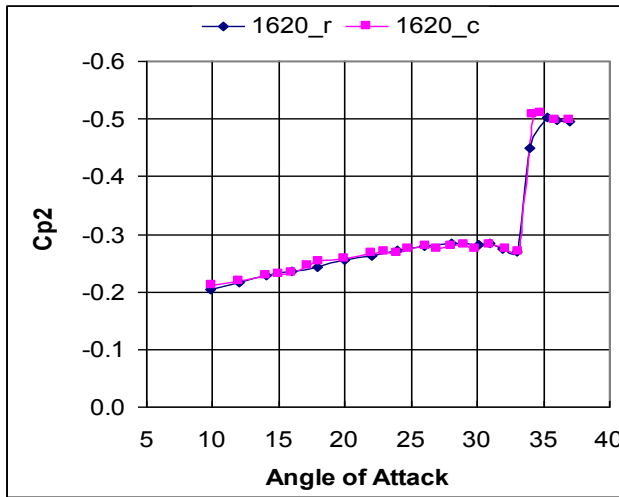


Fig. 4.6. Pitch moment coefficient for the #09 model vs. angle of attack. Averaged data

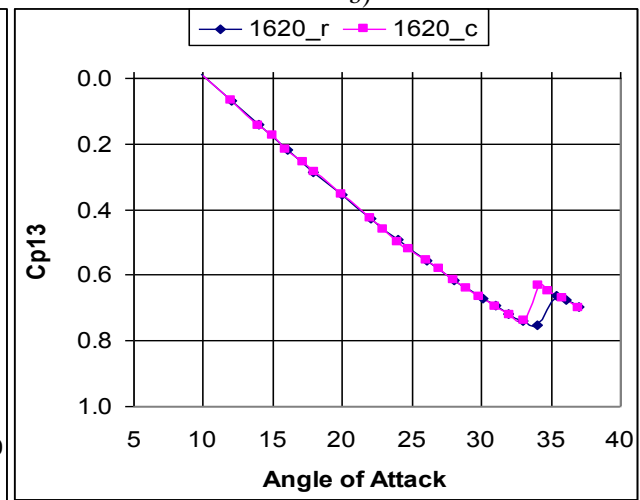
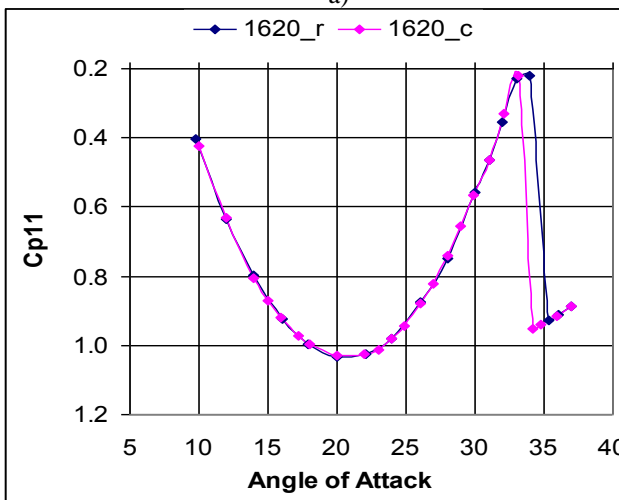
Monotonous suction rise with angle of attack in a pre-stall region on a convex surface is violated in pressure ports #3 and #4 (Fig. 4.8, a, b). Suction drops at  $Cp3$  within the angle-of-attack range,  $\alpha = 10 - 14$  deg. and at  $Cp4$  within  $24 - 27$  deg. It can be interpreted so that some flow disturbances over the surface exist which move upstream with an increasing angle of attack. A separation bubble can cause such behavior; it can be confirmed with visualization tests. These tests were conducted using easy to implement oil dot method; the results are presented below.

Time series for the #09 model was obtained at  $\alpha = +27^\circ$ . Heating was switched on at the 40-th second and switched off at the 210-th. Lift, drag, and pitch moment coefficients are shown in Fig. 4.9; heating did not result in their variation. A kind of monotonous drift of all the coefficients can be explained with decreasing air density with growing temperature. Air temperature is not monitored in the UTAD-2 in a course of experiments. So in fact, the obtained data could represent just random errors of the AVMKt 3-component strain gauge balance of the UTAD-2 wind tunnel.



a)

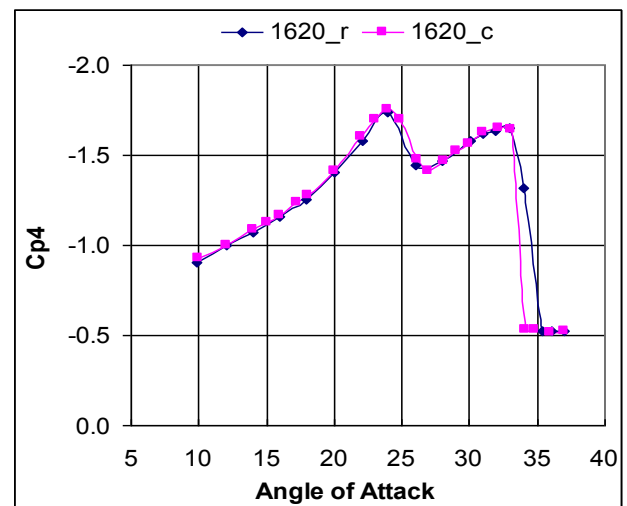
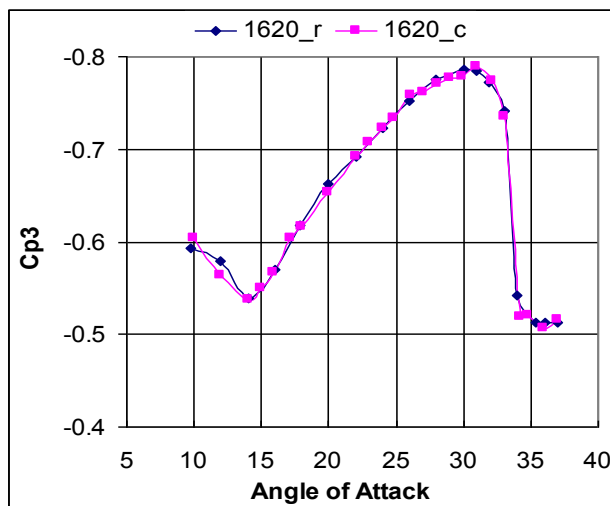
b)



c)

d)

Fig. 4.7. Pressure coefficients vs. angle of attack for the #09 model



a)

b)

Fig. 4.8. Pressure coefficients Cp3 and Cp4 vs. angle of attack for the #09 model

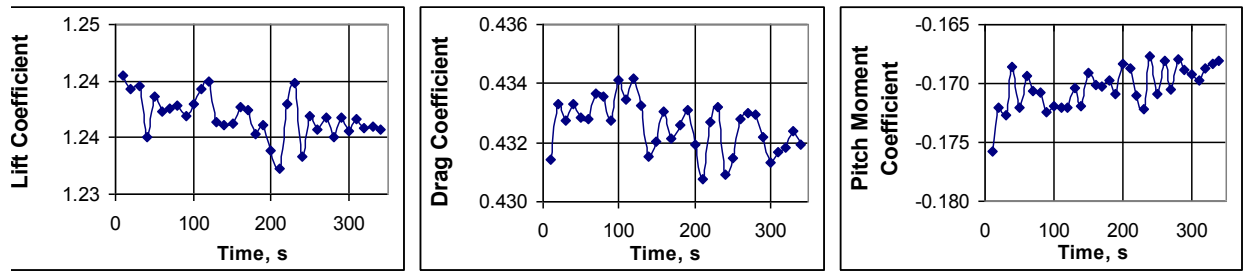


Fig. 4.9. Time series of lift, drag, and pitch moment coefficients for the #09 model at  $\alpha = +27^\circ$

### Test results for the model #10 (thermal control section over a concave surface)

Figures 4.10 – 4.12 show variation of lift, drag, and pitch moment coefficients vs. angle of attack in reference ("-r") and controlled ("-c") cases for two test runs (note reverse direction of angle-of-attack and  $C_L$  axes). No meaningful difference in lift, drag, and pitch moment coefficients is observed. Here too pitch moment coefficient demonstrates some waviness in pre-stall region (see paragraph 4.2).

The same is true for pressure coefficient varying with an angle of attack. Examples of pressure

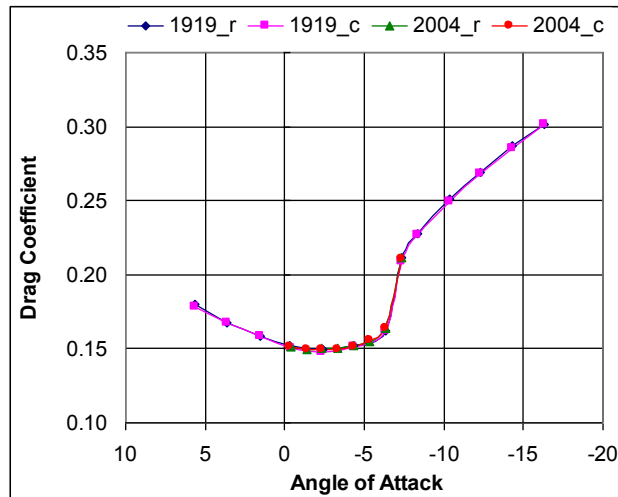


Fig. 4.10. Drag coefficients for the #10 model vs. angle of attack. Averaged data

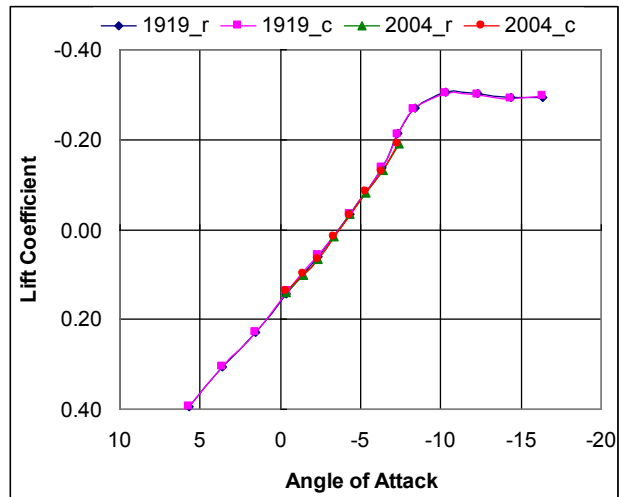


Figure 4.11. Lift coefficients for the #10 model vs. angle of attack. Averaged data

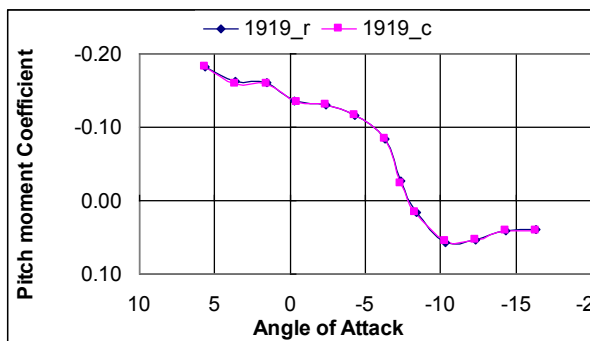


Fig. 4.12 Pitch moment coefficients for the #10 model vs. angle of Attack. Averaged data

plots are shown in Fig. 4.13 a, b. Similar to the model #09, some waviness of pressure curve for  $C_{p11}$  for  $\alpha = 5.7 - 0$  deg. together with the behavior of a pitch moment in the same range of angles of attack can be explained with an arising separation bubble, which migrates forward while angles of attack decrease.

Time series for the model #10 are similar to that for the model #09 in terms of data scattering, general drift direction and a value per given time, and there is no need to present them in the report.

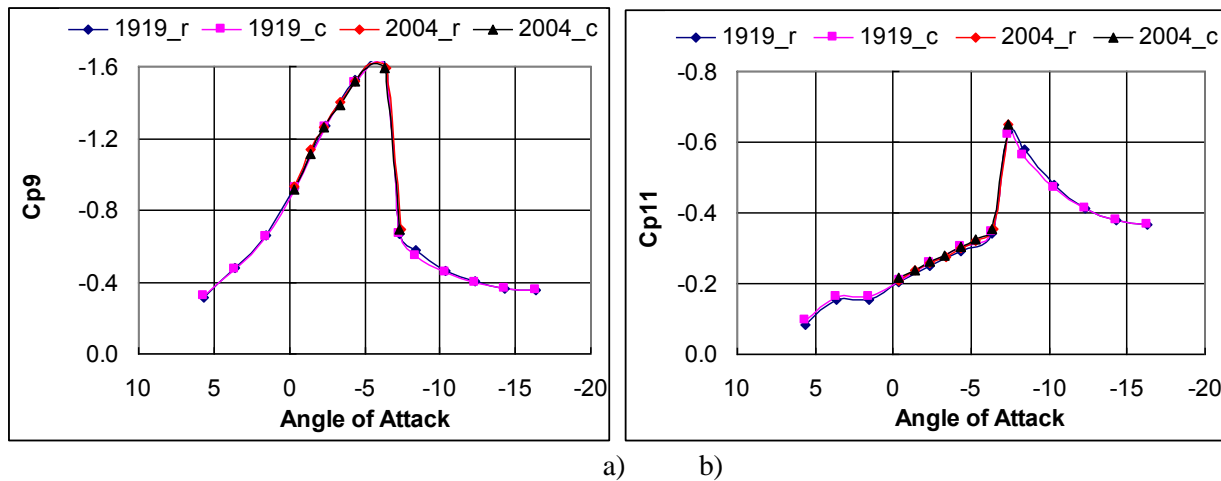


Fig. 4.13. Pressure coefficients vs. Angle of attack for the #10 model

### Visualization experiments

The method of oil dots was used to see streamlines over the model surface. For these tests the slurry of fine-dispersed carbon black in mineral oil was used. The model was set at a desired angle of attack, oil dots were put onto the model surface. The tracks left by oil dots in the flow during their motion along the model surface were registered. It was found that the separation did bubble appear on both models in a sufficiently wide range of angles of attack.

Figs. 4.14 a, b show flow visualization over a convex surface of the #09 model. It is seen that the separation bubble begins at  $\alpha=12^{\circ}06'$  at approximately  $x_f \approx 20\%$  of a model chord near the rear edge of heated elements and the flow reattaches at  $x_f \approx 30\%$ . At  $\alpha=26^{\circ}20'$  the bubble moves upstream starting at  $x_f \approx 8\%$  and the flow reattachment occurs at  $x_f \approx 15\%$ . This proves the earlier assumption about the separation bubble which moves upstream with increasing angle of attack.

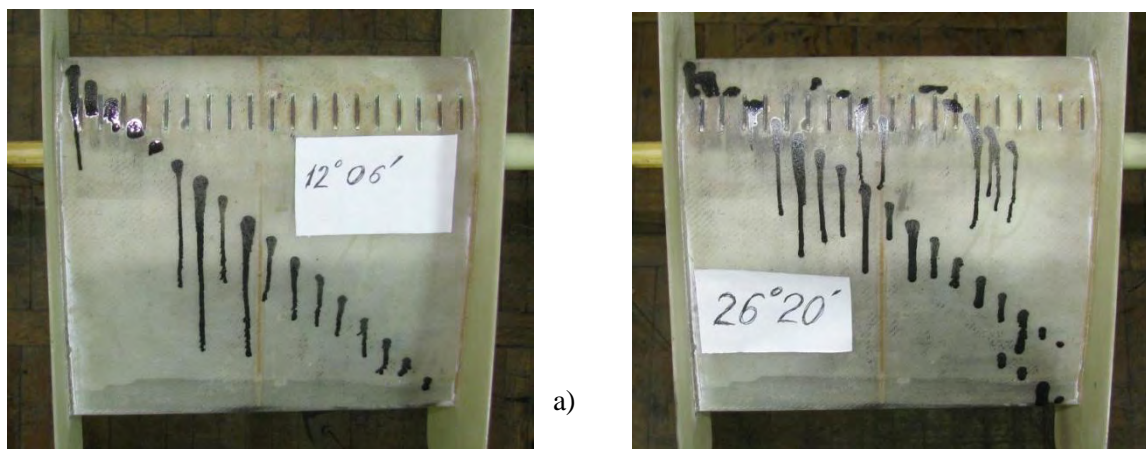


Figure 4.14. Streamlines on the surface of the #09 model

Fig. 4.15 shows flow visualization over a concave surface of the #10 model. Here the separation bubble exists up to positive angles of attack and is located upstream of heated elements in the very nose part of the model. With an angle of attack decreasing towards higher negative values, the bubble became shorter in a chordwise direction and moved slightly upstream.

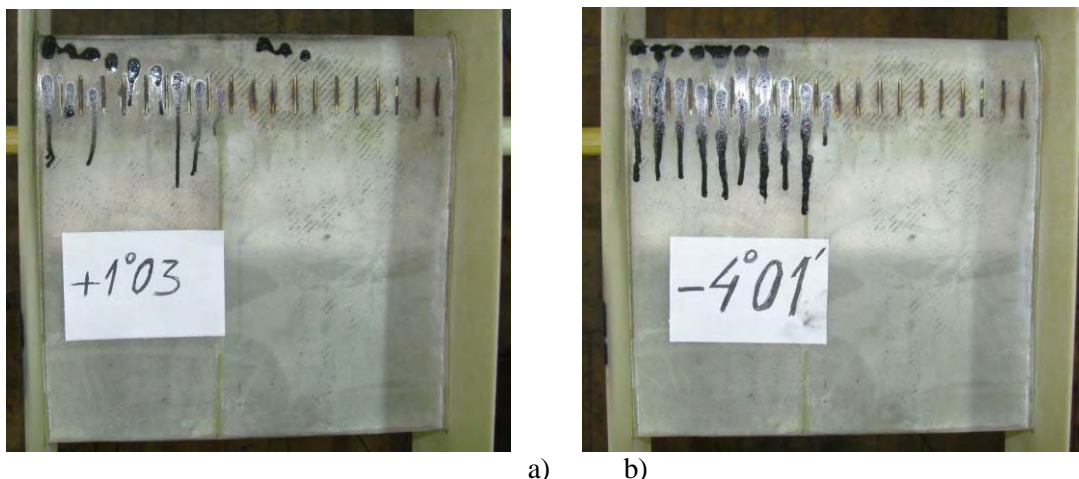


Figure 4.15. Streamlines on the surface of the #10 model

It should be mentioned, that the analysis of models quality showed slight manufacturing defects of leading edges of both models. Flow visualization showed that the R800 test model is very sensitive to the geometry irregularity, thus the special care is to be taken to precise reproduction of the model geometry, especially in its leading edge part.

The results of flow visualization show that separation bubble sits upstream or over a short (of the TVO resistor length) thermal control section on the model surface in the tested range of angles of attack. Evidently, it kills the very possibility of flow control using imposed thermal disturbance what was demonstrated by obtained results of weight tests. Only high positive angles of attack of the #09 model resulted in the flow reattachment upstream of the heated elements where a difference between reference and controlled cases was found. This gain is small because of the separation happened upstream and of intense downstream mixing of fluid which made the available temperature boundary condition too weak to reorganize favorably the boundary-layer structure.

### Concluding remarks, 8 Quarter

- Weight tests in the UTAD-2 wind tunnel showed zero flow control effects on models #09 and #10 with short TVO elements heated with applied voltage. Inefficient heating was aggravated with an early flow separation over the model compared to the downstream location of the control section.
- Considerable efforts aimed at AFIR modernization:
- New 25-point pressure measurement system was developed and put into operation. It included the relevant software development. These measures will considerably reduce labor cost of experiment.
- New gear drive for pitch control mechanism was developed and is being fabricated.

Microprocessor-based drive control electronics was developed, assembled, and tested. New test section is designed and optimized for more uniform distribution of MW field to provide heating uniformity of the control section. It is also expected to decrease random errors of weight testing

## Variations in the designed models with localized MW-heating

Model #11 has heated elements on its convex surface and the holder on its right side. It was tested with a convex surface faced upward to the MW radiation antenna. Model #12 has heated elements on its concave surface and the holder on its left side. It was tested with the concave surface faced upward.

All heated elements were developed in MRTI. Heated elements made from fine-dispersed bulk graphite were flush-mounted into the shells of models #11 and #12 in MRTI.

Table 2.1: Test program for models #11 and #12 with MW-heated elements

Model number	Free-stream velocity, m/s	Angle of attack variation		Number of test runs	Model position in the wind tunnel
		Range, deg.	Step, deg.		
#11	15	+16 to +24	2	2	Flight*
#11	20	+16 to +24	2	1	Flight
#11	26	+16 to +29	2	2	Flight
#12	15	+2 to -14	2	2	Tunnel
#12	20	+2 to -14	2	2	Tunnel

\* – In the “flight position”, the model convex surface looks upward; in the “tunnel position”, the concave surface looks upward; “tail upstream” designate the model position with its trailing edge directed upstream

### 2.3. Test program and procedure

Effectiveness of the boundary layer control was estimated from the analysis of modified aerodynamic characteristics. The scope of experiments is described in Table 2.1. Angle of attack range for each model was chosen so that to cover angles where aerodynamic characteristics were expected to be the most sensitive to applied flow control. Two or more test runs at certain test conditions were necessary to check or define more exactly the behavior of aerodynamic characteristics at different angles of attack or at different angle of attack range. The values for repeated angles were averaged and all data for certain conditions were combined into one sample.

Test procedure was set as follows: after zero-velocity load measurement, a desired free-stream velocity was set in the wind tunnel; the model was positioned at an initial angle of attack and all parameters were measured under reference conditions (no heating, MW radiation was «OFF») during 8 s with a sampling rate of 1000 samples per second. Then the MW system was turned «ON» and after 2 - 3 seconds, measurements were carried out under controlled conditions for various angle-of-attack values. Dynamic pressure, aerodynamic loadings, and static pressures in pressure taps were measured during these tests. Microwave radiation power was preset before a test run.

Measurements were accompanied with periodic visual check-up of general model state, and the surface heating was estimated with thermo-sensitive paper.

In addition, several test runs were performed to debug modified software and to control functioning of the modified AFIR.

## 2.4. Results and Discussion

### 2.4.1. Model #11 Results

At free stream velocity  $U_0 = 15$  m/s, the model #11 did not different characteristics in reference and controlled cases (Figs. 2.6 and 2.7). No reasonable explanation is still found for this because model has been tuned directly before tests and heating has been checked using thermo sensitive paper.

At  $U_0 = 20$  m/s, the situation is quite different being characterized with noticeably different aerodynamic coefficients. Drag coefficients in the pre-stall region and even near the post-stall region are lower in the controlled case (Fig. 2.8). Similar to the resistively heated model investigated earlier, the spanwise-regular heating slightly decreases a stall angle and lift coefficients in the pre-stall region (see Fig. 2.9). However, the drag decrease prevails over the lift drop so that an **increment** of the lift-to-drag ratio grows in the pre-stall region as it is shown in Figs. 2.10 and 2.11.

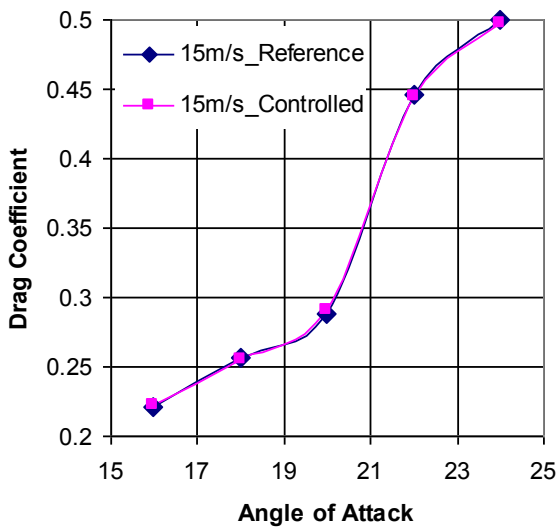


Figure 2.6. Drag coefficient variation:  
model #11 at  $U_0 = 15$  m/s

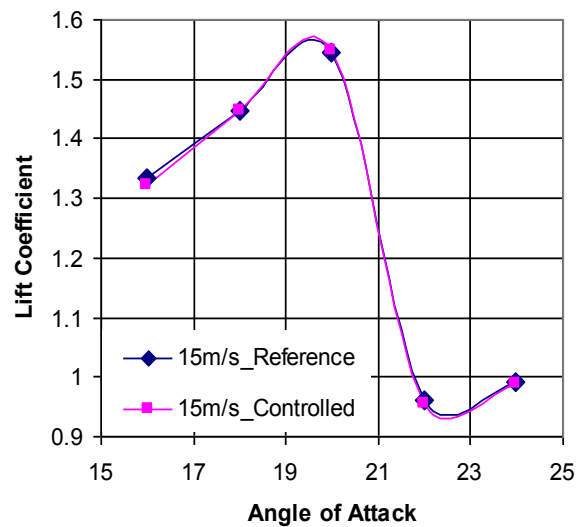


Figure 2.7. Lift coefficient variation:  
model #11,  $U_0 = 15$  m/s

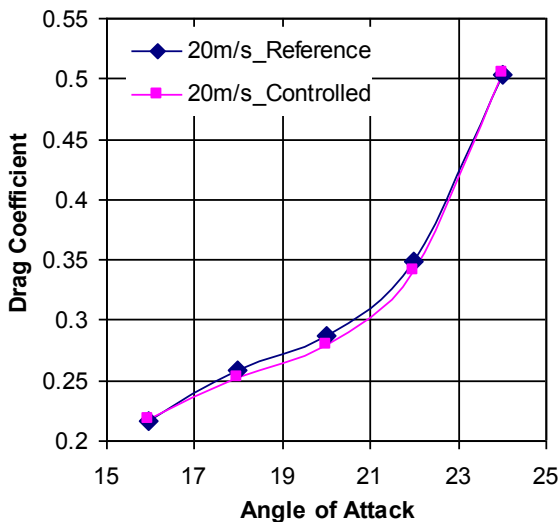


Figure 2.8. Drag coefficient variation:  
model #11,  $U_0 = 20$  m/s

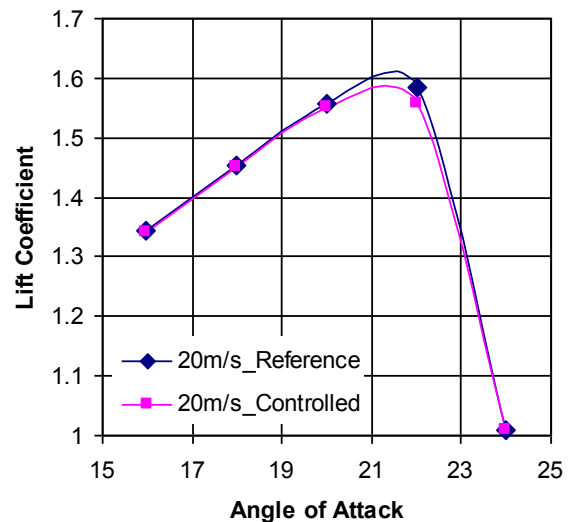


Figure 2.9. Lift coefficient variation:  
model #11,  $U_0 = 20$  m/s

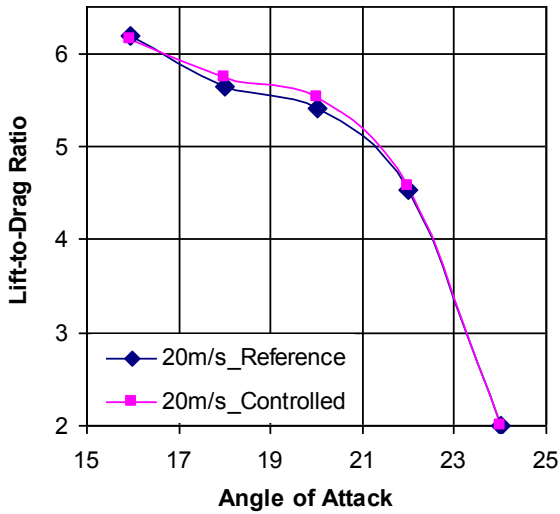


Figure 2.10. Lift-to-drag ratio variation:  
model #11,  $U_0 = 20$  m/s

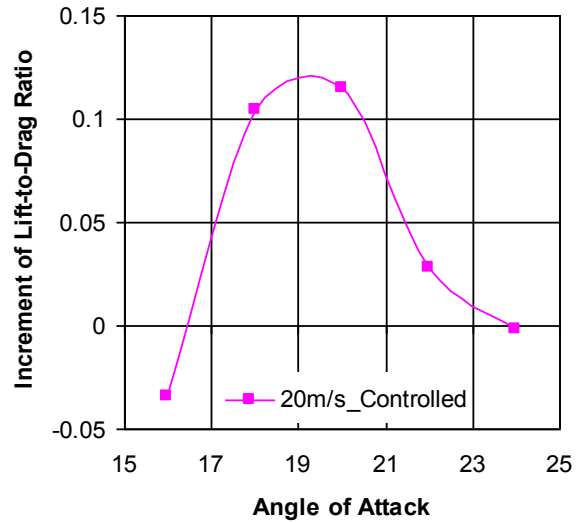


Figure 2.11. Lift-to-drag ratio increment:  
model #11,  $U_0 = 20$  m/s

These effects can be interpreted on basis of the analysis of static pressure distribution over the model in a vector form (Fig. 2.12). In the leading part of the model, the suction is greater in the controlled case and the vectors are directed upstream thus decreasing drag. Vertical component is small enough and is applied to a short forward piece of the model. So it does not create a significant lift increment. At the same time, low decrement of suction on a considerable part of the convex surface (within  $\approx 20\% - 90\%$  of chord) lead to a small general lift decrease as it is seen in Fig. 2.11.

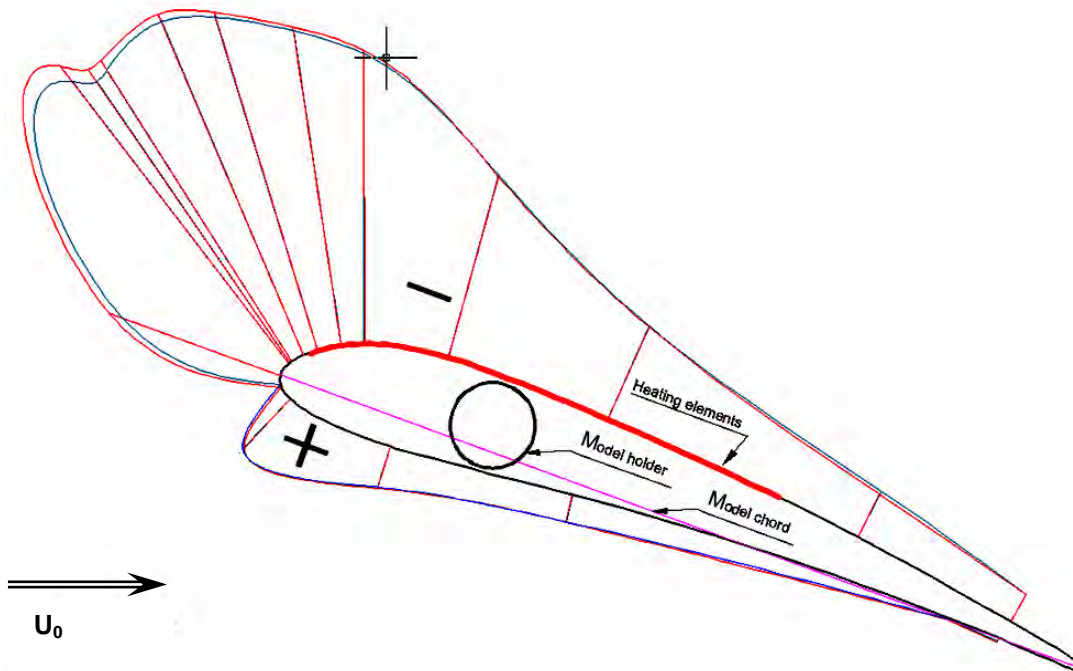


Figure 2.12. Static pressure distribution over model #11 at  $U_0 = 20$  m/s and  $\alpha = 20^\circ$ :  
blue lines refer to the reference, red lines – controlled case

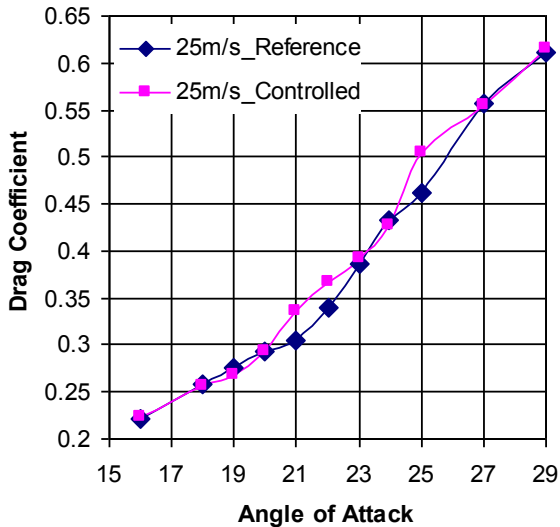


Figure 2.13. Drag coefficient variation:  
model #11,  $U_0 = 25$  m/s

At  $U_0 = 25$  m/s, flow in the stall region is highly unstable and the stall region itself covers the range of  $\alpha = 19^\circ - 25^\circ$ . The repeated measurements showed that the flow over the model here is alternatively separated and nonseparated, so that it can be characterized only in a probability sense. Mean values of aerodynamic coefficients are determined as the probability of one or another type of flow and application of flow control changes these probabilities. Since this alteration is a random process and its observed periodicity is of order of one to several seconds, it is evident that the 8 s measurement time is insufficient to obtain statistically definite values of aerodynamic coefficients. Figs. 2.15 and 2.16 give an illustration of measured drag and lift coefficients depending on angles of attack.

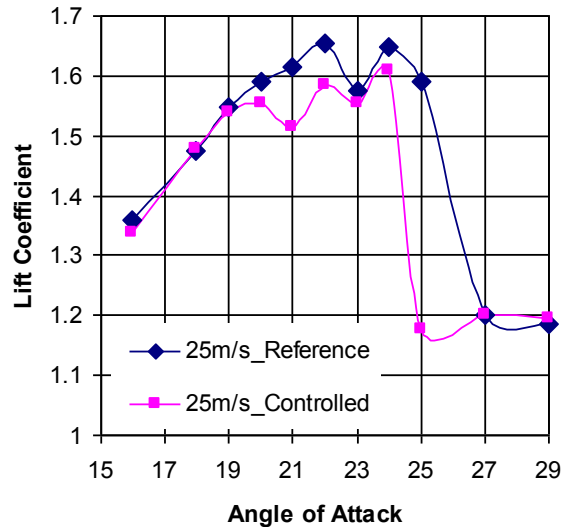


Figure 2.14. Lift coefficient variation:  
model #11,  $U_0 = 25$  m/s

#### 2.4.2. Model #12 results

These tests were carried out for negative angles of attack; therefore lift coefficient, lift-to-drag ratio, and angle-of-attack axes are reversed in the figures to get a conventional plots appearance. Accordingly, a further shift towards negative values of lift coefficients and lift-to-drag ratio due to flow control will be referred here to their increase (i.e. “negative growth”).

At  $U_0 = 15$  m/s, the model #12 demonstrates insignificant change of drag and somewhat decreased lift coefficients in the pre-stall region. At stall angles of  $8^\circ$  to  $10^\circ$ , growth of lift coefficients goes together with the growth of drag coefficients (Figs. 2.15 and 2.16).

This regime and the profile shape are not typical and therefore are not intended for direct aircraft applications. However their investigation and obtained results can be used to improve compressors stability of gas turbine engines on transient states by delaying flow separation on the concave surfaces of the blades.

At  $U_0 = 20$  m/s, the stall angle grows from  $8^\circ$  to  $10^\circ$ . At the pre-stall angle of attack, both drag and lift coefficients decrease more noticeably than at  $U_0 = 15$  m/s. However their increments at stall and post-stall angles are lower (Figs. 2.17 and 2.18). It can be interpreted as a result of relatively decreased energy release from the heated elements in the higher-velocity flow at the same radiated MW energy.

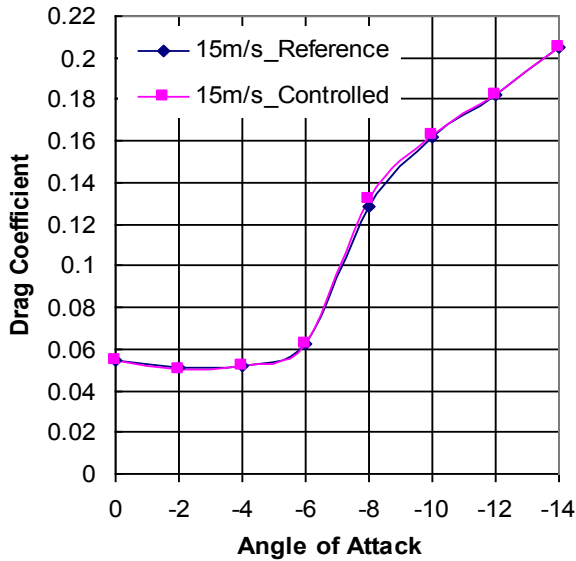


Figure 2.15. Drag coefficient variation:  
model #12,  $U_0 = 15$  m/s

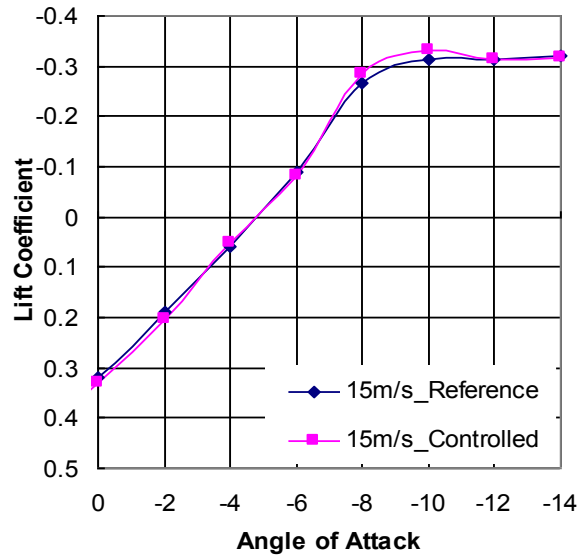


Figure 2.16. Lift coefficient variation:  
model #12,  $U_0 = 15$  m/s

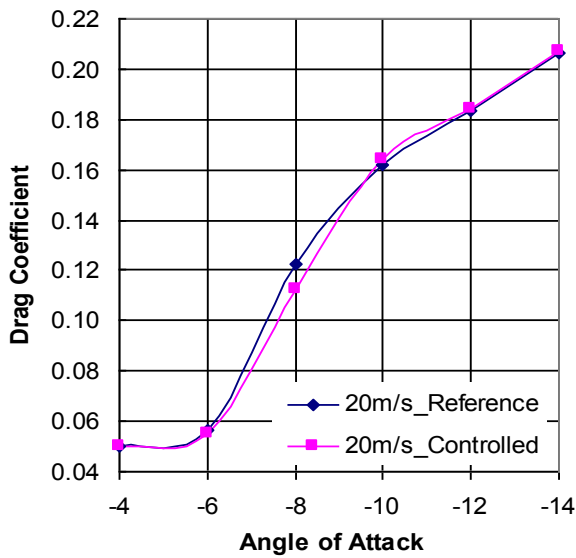


Figure 2.17. Drag coefficient variation:  
model #12,  $U_0 = 20$  m/s

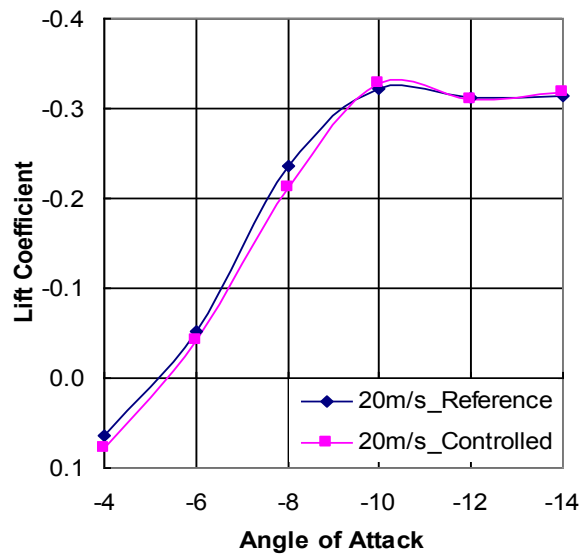


Figure 2.18. Lift coefficient variation:  
model #12,  $U_0 = 20$  m/s

Two MW-controlled models are fabricated and tested in the modified wind tunnel. Measurement results show that a stall angle grows from  $8^\circ$  to  $10^\circ$  under thermal control. Drag and lift coefficients decrease at pre-stall angles of attack (to a greater extent at a higher free-stream velocity); lift-to-drag ratio grows. Obtained results can be used to improve compressors stability of gas turbine engines on transient states by delaying flow separation on the concave surfaces of the blades.

# NEXT STAGE (11 QRT OF THE PROJECT) OF AERODYNAMIC EXPERIMENTS ON MW-BASED FLOW CONTROL

## 3.2. Test Program and Procedure

Experiments aimed at effectiveness investigation of applied boundary-layer control through variation of aerodynamic characteristics. Test scope is shown in Table 3.1. The whole range of angles of attack was investigated to search for any variation of flow characteristics. Two or more test runs were made at given experimental conditions to determine exactly the behavior of aerodynamic characteristics at different angles of attack. In addition to the shown conditions, six methodological test runs were performed to check AFIR functioning.

Table 1.1. Test program for model R800#13\_2:  
39 heated elements with 5 mm spanwise step

File	V, m/s	$\alpha^\circ$ start : end: step			Magnetron current, A
July 2010					
P28_1446	15	18	24	1	0.2
P28_1459	15	18	24	1	0.3
P28_1509	15	18	24	1	0.4
P28_1519	15	18	24	1	0.5
P28_1717	15	16	23	1	0.4
P28_1618	20.5	18	25	1	0.3
P28_1627	20.5	18	25	1	0.5
P28_1639	26	18	26	1	0.5
P28_1701	26	17	27	1	0.6
August 2010					
P26_1411	15.3	7.9	17.9	0.5	0.4
P27_1119	15.6	7.9	17.9	0.5	0.6
P27_1155	15.4	-2	8.4	0.5	0.6

Test procedure was set as follows: after zero-velocity loads measurements, wind tunnel started and desired free-stream velocity was set; the model angle of attack was set to an initial value and all parameters were measured for the reference conditions (no heating, MW «OFF») during 8 s with a sampling rate of 1000 samples per second; MW system was turned «ON» and after 2-3 s pause, measurements started for the controlled case; a new angle of attack was set and procedure was repeated up to the final value of angle of attack. Dynamic pressure, aerodynamic loadings, and static pressure values in 20 pressure taps were measured during the tests together with current angle of attack. Microwave radiation power was preset before a test run. During testing, visual check-up of general model condition was periodically performed.

## 3.3. Results and Discussion

### *Preliminary Testing of Heating and Post-test Model Inspection*

Before aerodynamic testing, the heating pattern was tested in the still air using thermo-sensitive paper attached to the model. At relatively low magnetron currents up to 0.3 A no heating was registered but at currents of ~0.5 A the central line burned out. All the other heated elements did not display themselves on the thermo-sensitive paper but touching the model, one could find the surface slightly heated approximately by 20°C. This fact made to expect some variation of aerodynamic characteristics in the controlled case.

Inspection of the model after tests showed that no burnout of heated elements occurred. This proved low temperature values during testing.

Examination of pressure behavior on the concave surface of the model showed that pipes connecting pressure taps from #1 to #10 (see Fig. 3.1) had leakages, therefore obtained pressure distribution was invalid.

### *High angles-of-attack results*

Four test runs were performed at 15 m/s free-stream velocity. Two tests (logs P28\_1446 and P28\_1509) showed similar results with somewhat higher lift coefficient and lower drag coefficient values at pre-stall angles of attack of  $\approx 21$  and  $\approx 22$  deg. (Figs. 3.3 and 3.4). This is verified by pressure distribution of Fig. 3.5 over the model surface. It shows that suction over the convex surface in the controlled case was slightly greater than in the reference case that resulted in growing lift and dropped drag.

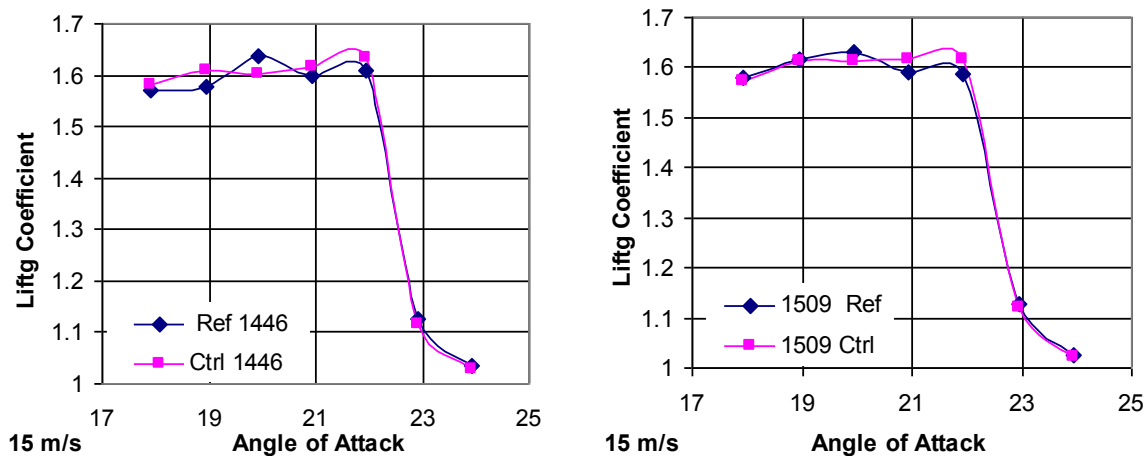


Figure 3.3. Lift coefficients vs. angle of attack in reference (Ref) and controlled (Ctrl) cases for the model R800#13\_2

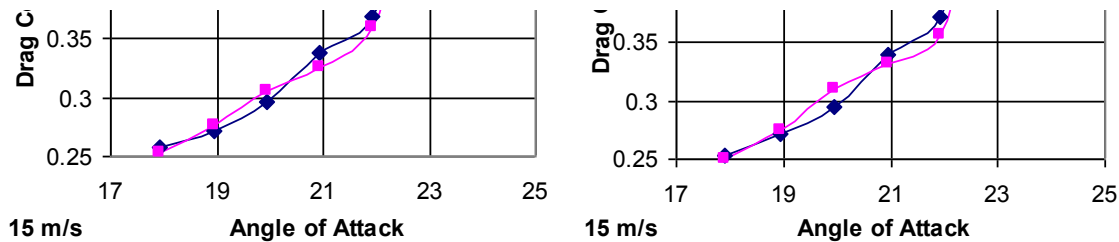


Figure 3.4. Drag coefficients vs. angle of attack in reference (Ref) and controlled (Ctrl) cases for model R800#13\_2

However two other tests for the same flow parameters (logs P28\_1459 and P28\_1519) showed different results (Figs. 3.6 and 3.7) with the stall started approximately one deg. earlier and with much greater lift drop in the controlled case in a post-stall region compared to the reference case. At that, drag coefficients at  $\alpha=22^\circ$  were similar in the controlled case and differed both qualitatively and quantitatively in the reference case. It is an indication of strong instability of the flow at pre-stall and stall angles of attack in the reference case. The application of flow control evidently stabilizes the flow

to a certain extent. Figs. 3.3, 3.4, 3.6, and 3.7 display smoother lift and drag curves in the controlled case. This observation is consistent with many other earlier obtained results not yet clearly declared.

The above analysis relates to the air velocity  $U_0=15$  m/s. At higher velocities, data scattering grows and no trustworthy changes of aerodynamic characteristics were found. It results from the very low energy delivered to the flow by heated elements. Similar situation was observed in the framework of an earlier project with the resistive heating of streamwise elements where meaningful results were obtained only at  $U_0=15$  m/s.



Figure 3.5. Pressure distribution over model R800#13\_2 in reference (blue lines) and controlled (red

### ***Low Angles of Attack Results***

Since encouraging results were obtained at low angles of attack for the earlier tested resistively heated model, here the similar experiment was planned. Improvement of aerodynamic characteristics of a MW heated model was found in a very narrow range of angles of attack, about  $1^\circ$ . These measurements were performed with  $0.5^\circ$  angle-of-attack step twice for reference and twice for controlled conditions at every single angle of attack. All the data were averaged.

Figs. 3.8 and 3.9 show variation of lift and drag coefficients depending on angles of attack. It is evident that no meaningful results were found in the controlled case compared to the reference. Scattering of values in certain points can be referred to random errors which were not reproduced in other tests.

Analysis of pressure distribution over the model surface is a more sensitive mean to distinguish an impact of flow control. Fig. 3.10 shows pressure values varying with an angle of attack at #15 pressure tap with most pronounced suction and sensitivity to flow control. However even here, absolute values of pressure variations are small. Conformity can be found between lift and suction

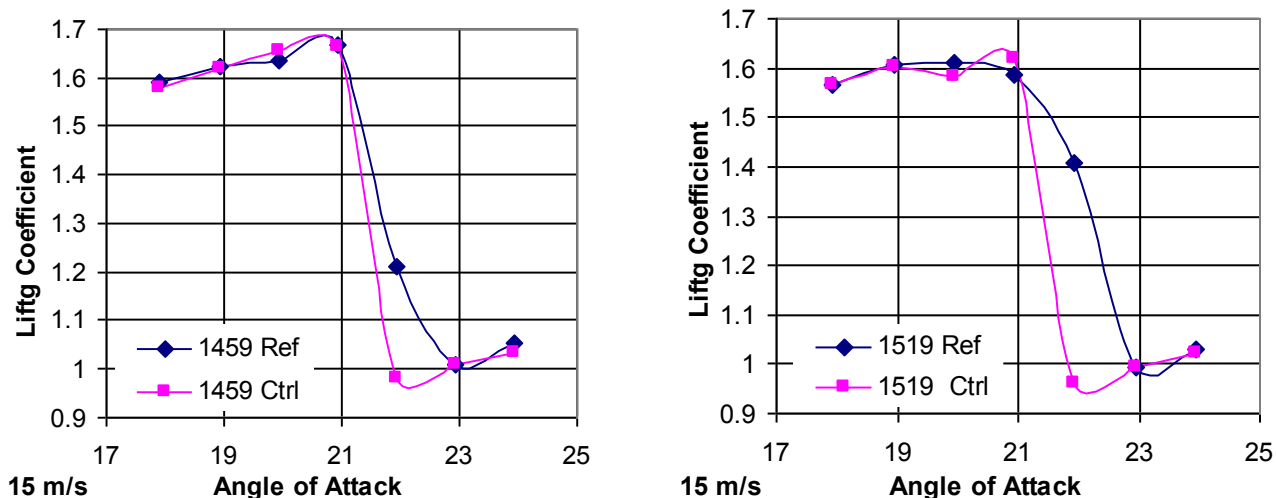


Figure 3.6. Lift coefficients variation vs. angle of attack in reference (Ref) and controlled (Ctrl) cases for model R800#13\_2

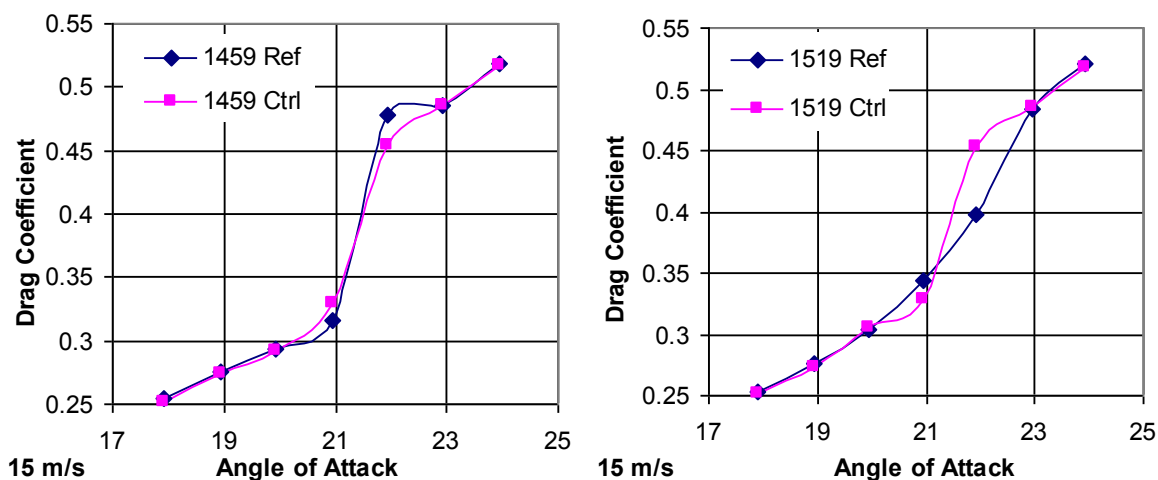


Figure 3.7. Drag coefficients vs. angle of attack in reference (Ref) and controlled (Ctrl) cases for model R800#13\_2

increments at angles of attack within  $10^\circ - 12^\circ$  and within  $13^\circ - 14^\circ$ . Similar situation is observed for adjacent pressure taps #14 and #16 (see Fig. 3.1). Undoubtedly, such pressure distribution should result in corresponding change of lift and drag coefficients. However, it is to be clearly demonstrated that these variations take place due to the applied flow control rather than represent random errors. That is why additional measurements are required under the condition of more efficient transfer of thermal energy to the flow.

### Summary

Aerodynamic characteristics can be improved at high angles of attack using the developed flow control approach based on a spanwise-regular heating of the surface. However, effectiveness of MW heating of the model surface made from the proposed materials appeared to be low.

Accordingly, aerodynamic characteristics were not found to show significant improvements at low angles of attack. The changed characteristics at moderate angles of attack could be referred to the flow control impact after additional verification of the obtained results.

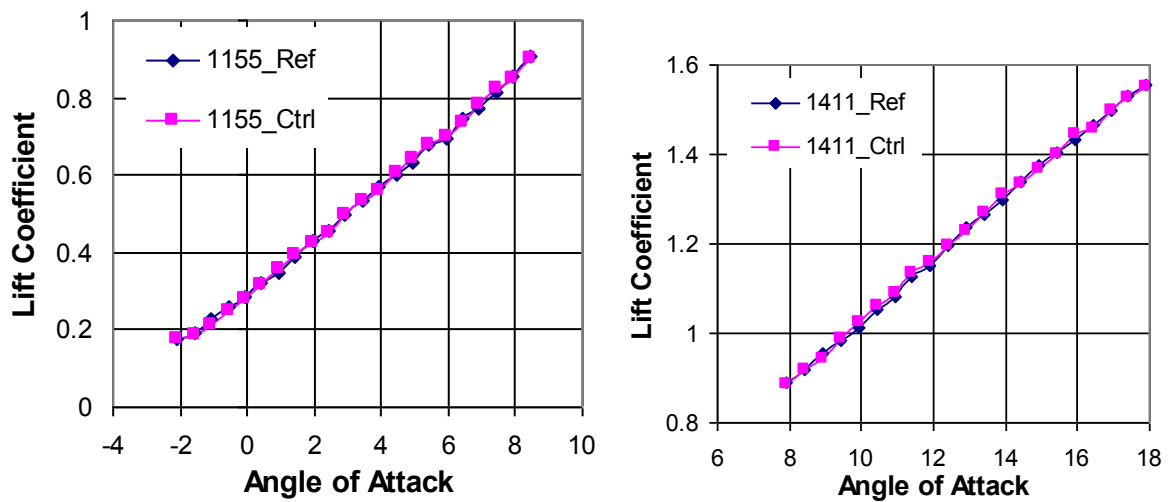


Figure 3.8. Lift coefficients variation vs. angle of attack in reference (Ref) and controlled (Ctrl) cases for model R800#13\_2;  $U_0 = 15$  mps

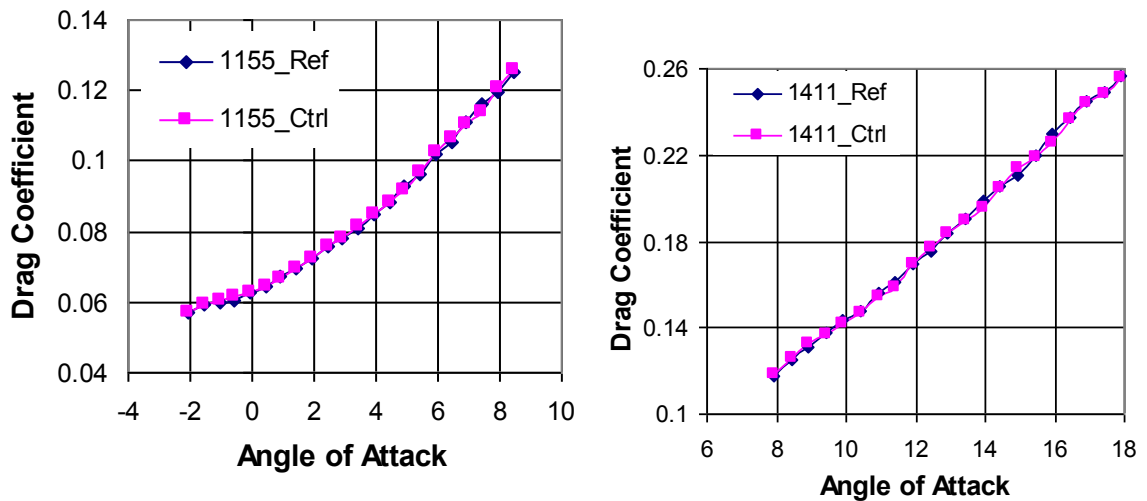


Figure 3.9. Drag coefficients vs. angle of attack in reference (Ref) and controlled (Ctrl) cases for model R800#13\_2;  $U_0 = 15$  mps

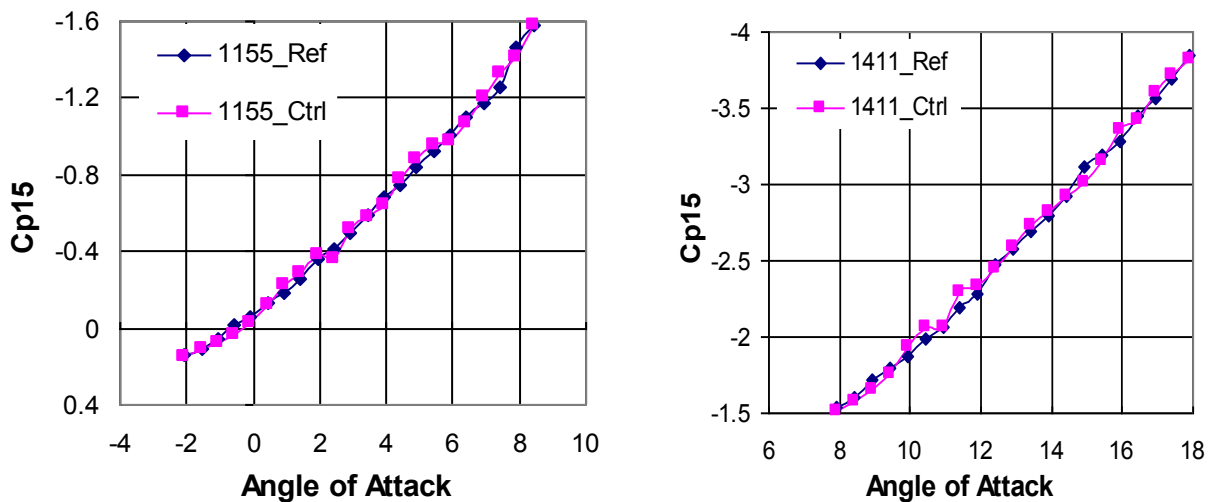


Figure 3.10. Pressure coefficients vs. angle of attack in reference (Ref) and controlled (Ctrl) cases for pressure tap #15 on model R800#13\_2;  $U_0 = 15$  mps

### Tested Models. Encountered problems and their explanation.

Four models were designed and fabricated for the planned set of tests. Two of them are modified available models designated as R800 #11\_2 and #12\_2, and the other two were newly made models #14 and #15. Such a great number of various tested models resulted from a search of most proper engineering solutions, first of all preventing the models from their burnout during tests or test preparation that happened even at low magnetron currents corresponding to the radiated power of 200 – 500 W.

All models have the same geometry, similar design and different types of heated elements developed and manufactured in MRTI. One of the heater versions in a form of paper sheets with graphite lead line pattern was glued to the model in NAU. All heaters had a spanwise step of 5 mm. The internal surface of the side opposite to that with heated elements was covered with the glued metal foil (reflector). The paper heater was absent in the central part of the model to enable pressure distribution measurements. Models' sketches are shown in figures 3.1 and 3.2.

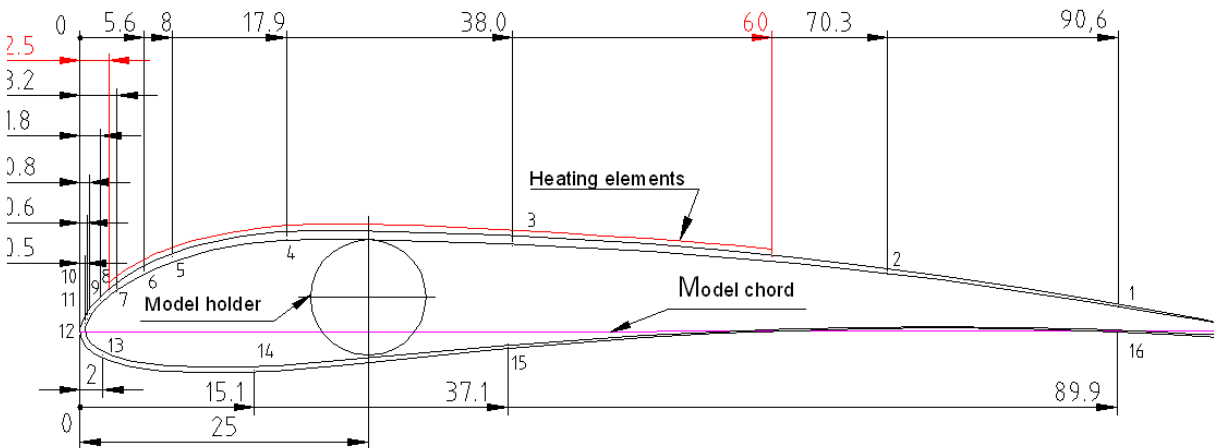


Fig. 3.1. Layouts of models #11\_2 and #15. Testing in a flight position at positive angles of attack

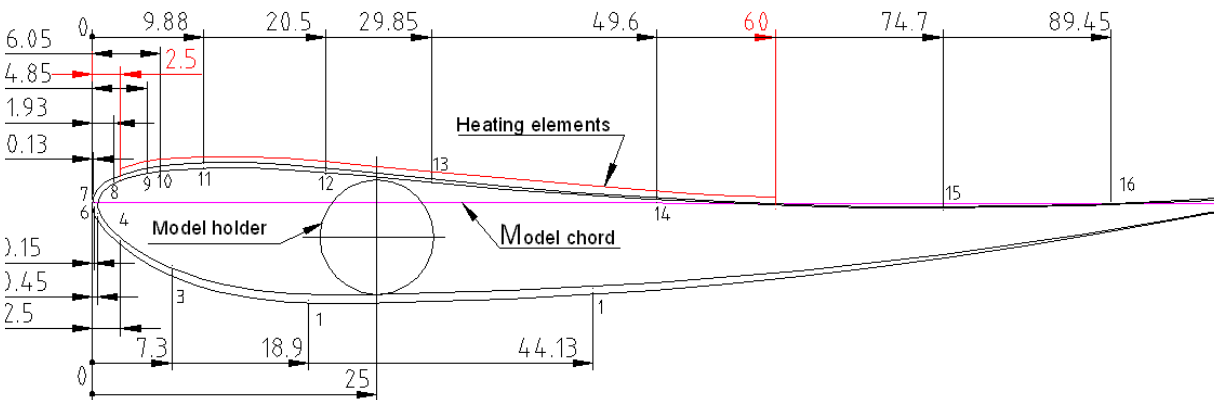


Fig. 3.2. Layouts of models #12\_2 and #14. Testing in reversed position at negative angles of attack

Testing started from the models #11 and #12, which earlier had bulk graphite elements flush-mounted in slots over models' surfaces (see QRT-10 Report). The graphite elements were removed and surfaces were smoothed using appropriate filling. Instead, paper heaters were glued to the model surface in estimated locations. Models were named as #11\_2 and #12\_2. Both of them surface burned



Fig. 3.3. The burn-out of the surface of model #11\_2

out on the surface including glass-fiber shells in several places (Fig. 3.3) during tuning of test conditions. These models were repaired by installation of new fabricated shells and named as #14 and #15. However, these models burned out too. It happened in central parts of the models having damaged drain taps together with tap pipes that made impossible pressure distribution measurement over the whole surface.

No significant difference between aerodynamic characteristics in reference and controlled cases was found during a limited number of performed test runs. It was validated with the assessments made by the

MRTI team: the energy absorption concentrated in a place where it was high by itself. It decreased the fraction of power absorbed by the rest of the heated elements. So when for some reason a burnout occurred in a certain point, organic substances in model burnt out and were blown away but some of them consisting mainly of carbon remained in the model. Since carbon is a good absorber of microwave radiation, a considerable amount of radiated power was absorbed by the burnt portion of model leading to its further overheating while the rest of the heated elements remained almost cold.

### Test Scope and Procedure

In spite of the encountered problems described above, aerodynamic testing of some models was performed. Test procedure was identical for all weight tests with heated elements. After zero-velocity loads measurement, wind tunnel was started and measurements in the flow were performed at each angle of attack in series: reference case measurements during 8 s were followed by measurements of the same duration in controlled cases. Here MW system was switched on and a model was preheated within 2 s. After measurement completion at a given angle of attack, a new angle was set and model was cooled in the flow during 15 s. During this procedure, the following output signals were measured: dynamic pressure, 3 components of loading on the balance, static pressure in the pressure taps on the model surface. Mean values were calculated and according to the calibration function of respective measuring channels, physical values were calculated. Then lift, drag, pitch moment, and pressure coefficients were calculated:

$$c_x = \frac{X}{qS}; c_y = \frac{Y}{qS}; c_m = \frac{M_z}{qSb_A}; c_{p_i} = \frac{\Delta p_i}{q}, \quad (3.1)$$

where  $c_x$ ,  $c_y$ ,  $c_m$ ,  $c_{p_i}$  are drag, lift, pitch moment and pressures coefficients;  $X$ ,  $Y$ ,  $M_z$  are drag, lift, and pitch moment, and  $\Delta p_i$  is the difference between pressure in a pressure tap and static pressure in the test section;  $S$  is model reference area;  $b_A$  is mean aerodynamic chord;  $q = \rho V_\infty^2 / 2$  is dynamic pressure;  $U_0$  is a free-stream velocity and  $\rho$  is air density.

Test scope is given in table 3.1.

Table 3.1. Test scope summary

Model	File	$U_0$ , m/s	$\alpha^\circ$ Start : end: step			Magnetron current, A	Remarks
R800#12_2	P27_1618	15.5	4	-16	-4	0	Software testing
R800#12_2	P27_1632	15.4	-5	-16	-1	0.2	
R800#14	P11_1910	15.5	2	-4.5	-0.5	0.16	
R800#11_2	P28_1320	15.4	18	21	1	0.16	Software testing
R800#11_2	P28_1404	15.4	18	23	1	0.16	
R800#15	P01_1723	15.4	18	25	1	0.16	
R800#15	P04_1638	15.5	8	20	0.5	0.16	
R800#15	P06_1719	15.6	8	24	0.5	0.2	
R800#15	P08_1527	10.3	8	21	0.5	0.25...0.30	Model after repair

## Results and discussion

### 3.3.1. Models at positive angles of attack

**Model #11\_2** enabled to perform only one test run, during which the through hole appeared because of the model burnout (see Fig. 3.3). No appreciable difference was found in lift, drag and pressure coefficients except values obtained for the angle of attack of  $20^\circ$  where both lift and drag coefficients were greater in the control case (Fig. 3.4).

Pressure coefficients demonstrated similar behavior. As an example, pressure coefficients are shown for drain taps #9 located at 1.8% of chord on the convex side and #14 at 15.1% of chord on the concave side (Fig. 3.5). Greater suction on the convex surface is combined with greater pressure on the concave surface creating greater lift and greater drag that is in a disagreement with optimal flow control where lift increment is associated with drag decrement. In given case, the obtained difference can be considered rather as a result of spontaneous and relatively long-duration flow separation and reattachment at high angles of attack, where flow instability is high. Then one of flow configurations could be caught mainly by one sample while another configuration – by the other.

Four test runs were performed with the **model #15**. Only first three of them were consistent. The fourth test was performed after an attempt to repair the model with new heated elements mounted. This model demonstrated a stall angle  $1...1.5^\circ$  less than in previous tests and no changes in its aerodynamic characteristics.

Drag and lift coefficient variations vs. angle of attack for the model R800 #15 are shown in Fig. 3.6 where data of first three runs were combined and mean values were calculated. It is seen that the flow instability in pre- and post-stall region leads to greater data scattering. Generally, lift and drag coefficients at high angles of attack are similar to those obtained in tests of the model R800 #13\_2 (see Figs. 3.3, 3.4, and 3.6 in QRT11 Report). Here again in the controlled case, some drop of lift coefficient is observed at  $\alpha = 2^\circ$  lesser than the stall angle followed by the lift growth. For the both models, stall angles in the controlled case are slightly less than in the reference case.

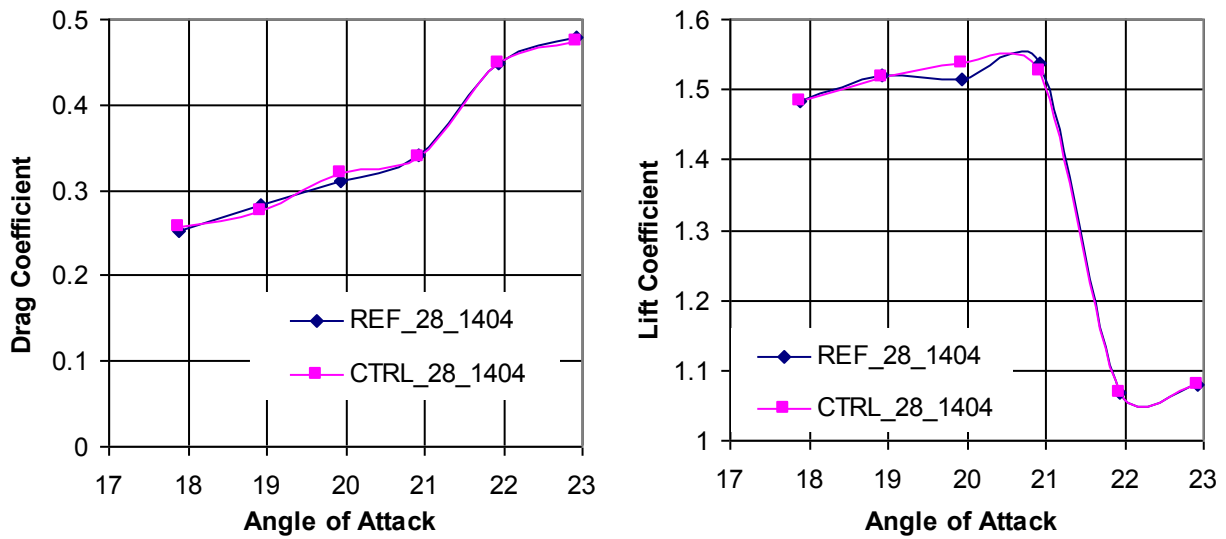


Fig. 3.4. Drag and lift coefficients variation vs. angle of attack for model R800 #11\_2

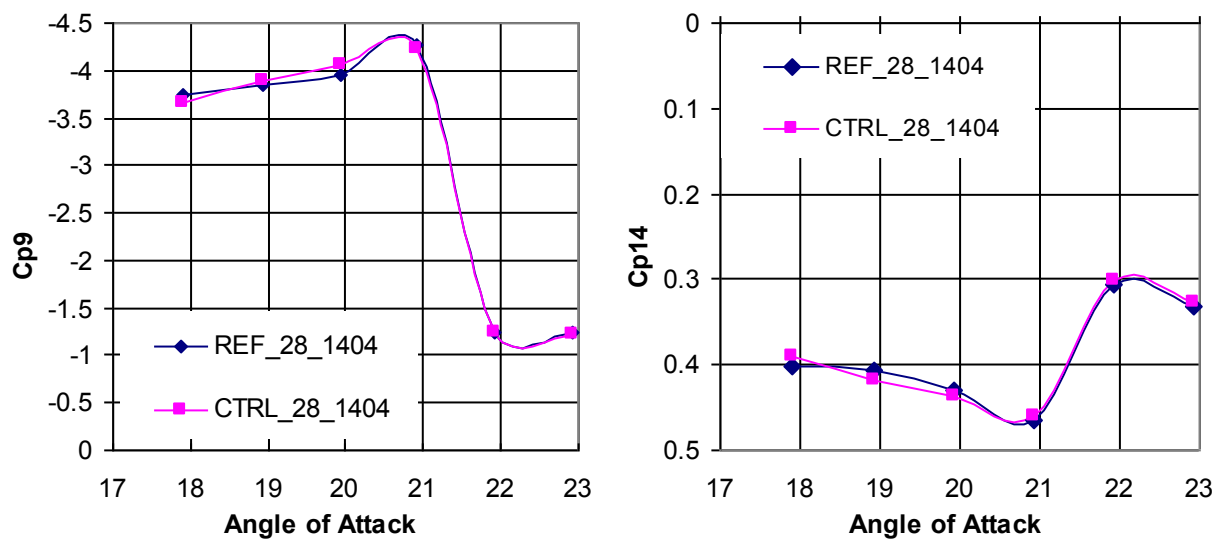


Fig. 3.5. Pressure coefficients variation vs. angle of attack for model R800 #11\_2

In addition, it should be noted that flow becomes more stable and characteristic curves are smoother in the controlled case. This was also observed in other tests during the project implementation.

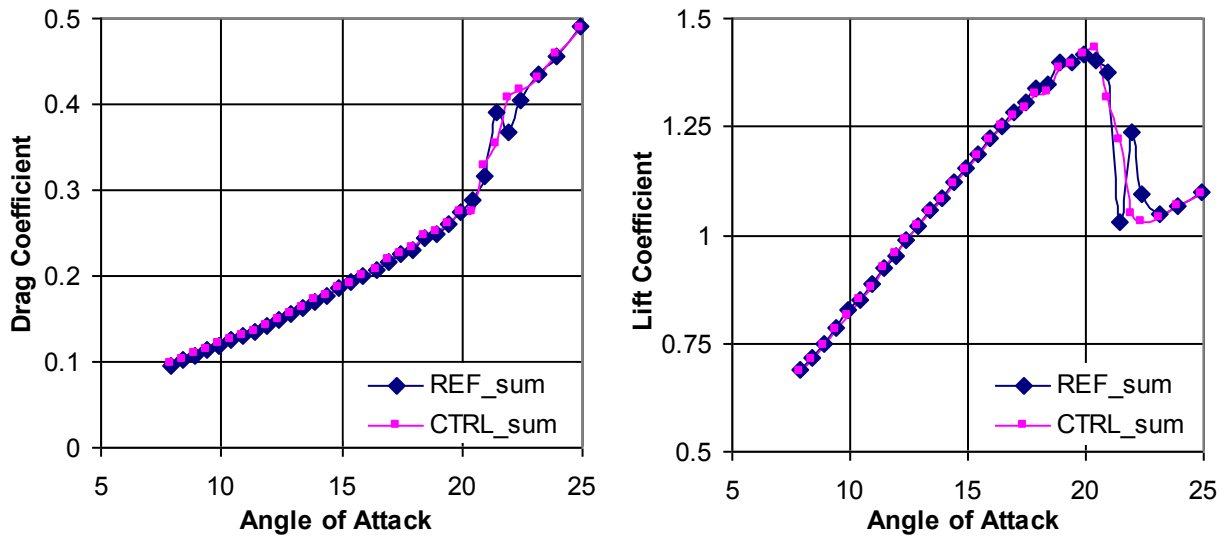


Fig. 3.6. Drag and lift coefficients variation vs. angle of attack for model R800 #15. Combined data

At low angles of attack no meaningful differences were observed. Figures 3.7 and 3.8 show increments of drag and lift coefficients in the controlled case calculated as:

$$dc_i = c_{i\text{Ctrl}} - c_{i\text{Ref}},$$

where  $dc_i \in dc_x, dc_y$  is respective coefficient increment;  $c_{i\text{Ctrl}}, c_{i\text{Ref}}$  are values of corresponding coefficients in controlled and reference cases respectively. It is seen that coefficient increments show no systematic variations and often have different signs. This is again consistent with the data obtained for the model R800 #13\_2 (see Figs. 3.8 and 3.9 in QRT11 Report).

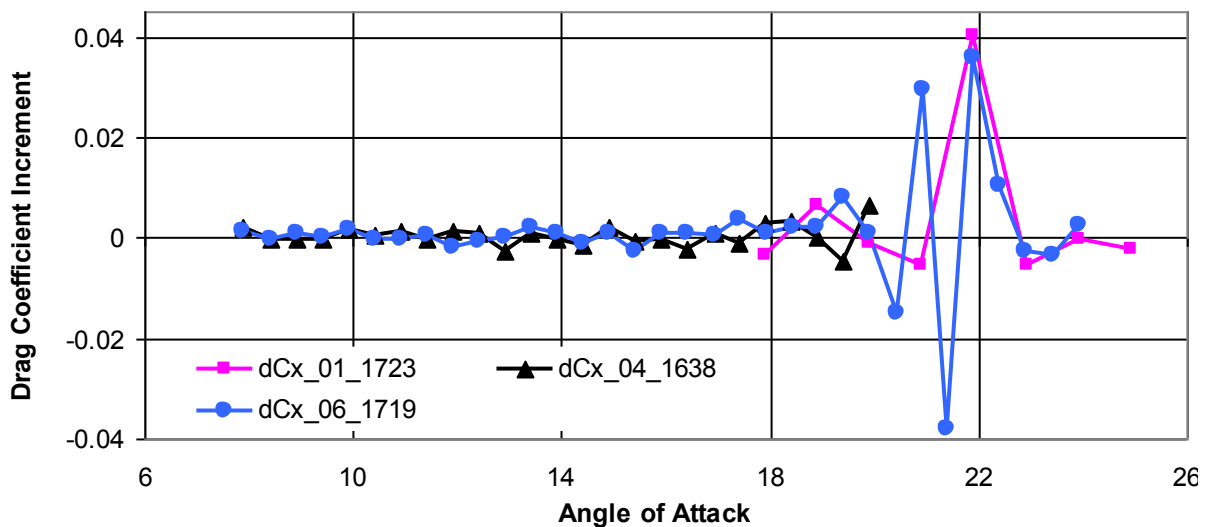


Fig. 3.7. Drag coefficient increment vs. angle of attack for model R800 #15

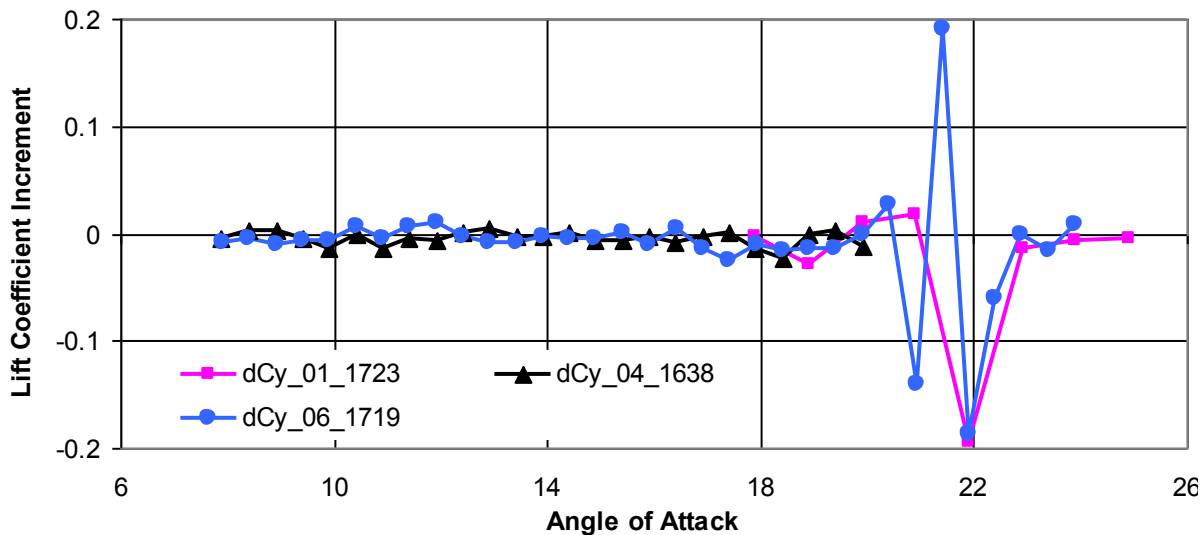


Fig. 3.8. Lift coefficient increment vs. angle of attack for model R800 #15

### 3.3.2. Models at negative angles of attack

No aerodynamic characterization can be given to the model R800 #14 because its heating elements burnt out heavily together with the model shell during the first test. The model was damaged severely with a formed through hole.

One test with MW heating was possible with the model #12\_2 of the same layout (see Fig. 3.2). This model also burned out during the test run but without a through holes. At pre-stall angles of attack, lift and drag coefficients in the controlled case are slightly greater than in the reference case. This is similar to lift and drag behavior of model R800 #12 (see Figs. 3.16, 3.17, and 3.6 in QRT10 Report). However in post-stall region model #12\_2 demonstrates lift drop while model #12 still sustains higher values of lift coefficient in the controlled case.

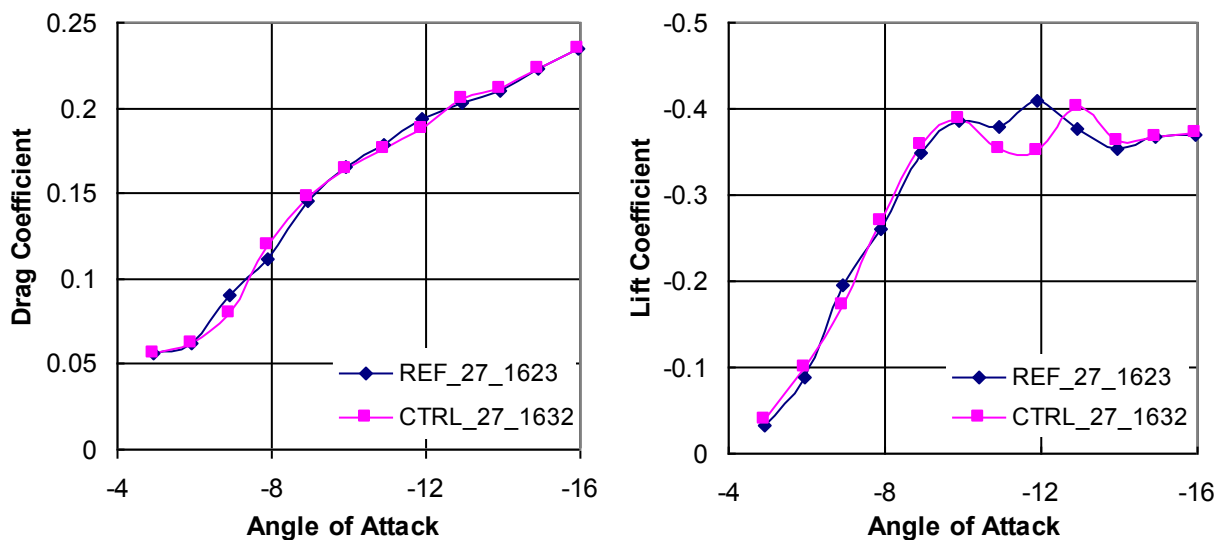


Fig. 3.9. Drag and lift coefficients variation vs. angle of attack for model R800 #12\_2. Combined data

Measurements of surface pressure distribution were not possible because drain taps and pipes broke out at the model burn-out.

## SYMMETRIC FLOW EXCITATION: Passive flow control over a circular cylinder with mechanical O-ring vortex-generators

Two cylinders were tested with the diameters of  $D=106.6$  mm and  $D=128.0$  mm within a range of free-stream velocities,  $U_0 \approx 15 - 44$  m/s. Two flow-control tasks are studied with a symmetrical (Figs. 2.1, 2.3) and asymmetric (Figs. 2.2, 2.4) flow excitation. It is planned, first of all, as a linking, preparatory stage for investigations with plasma arrays; in particular, it should reveal an optimal  $\Delta z$  space scale of introduced disturbances in terms of the best aerodynamic performance. Secondly, the results obtained for the two different flow situations will assist to get an insight into physical mechanisms of processes responsible for the improvement of the aerodynamic performance.

Spherical disturbers (turbulators) are described in the previous stage of investigations (see, the FINAL REPORT on the Project as well as 14 Qrt Report, Fig. 2.1 below); O-ring disturbers are smooth rings with a round cross section of two diameters,  $d=2.5$  mm and  $4.6$  mm which are uniformly distributed with a  $\Delta z$  step along cylinder models of two diameters,  $D=106.6$  mm and  $128$  mm. Figs 2.3. and 2.4 show fabricated models with the two types of disturbers.

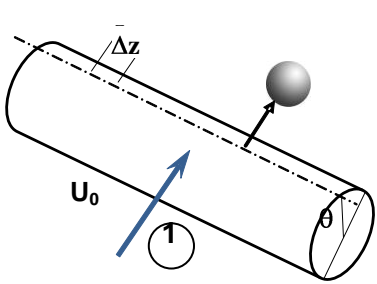


Fig. 2.1. Circular cylinder with an array of spherical disturbers

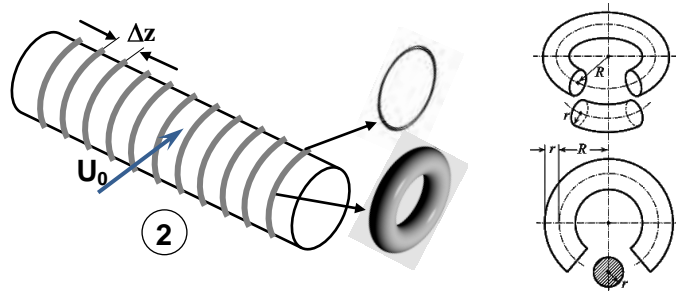


Fig. 2.2. Circular cylinder with an array of O-ring disturbers

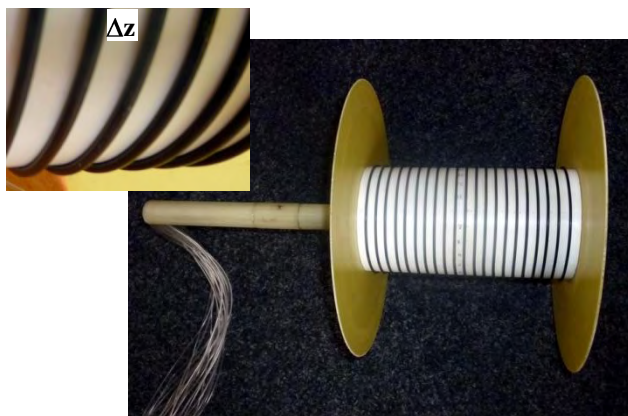


Fig. 2.3. Modeling of a symmetrical flow around a cylinder with rings at a  $\Delta z$  distance from each other

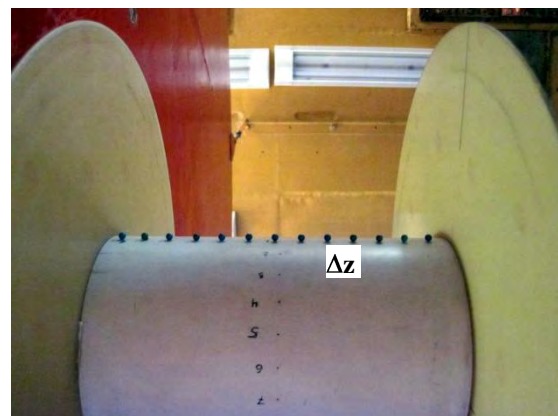


Fig. 2.4. Modeling of an asymmetric flow around a cylinder with spanwise-regular spherical disturbers

## Results and discussion

### *Results for O-ring turbulators*

Measurement results are planned to demonstrate an impact of the symmetric flow disturbance with O-rings placed on the cylinder model at a certain distance  $\Delta z$  from each other. Two sizes of these symmetric flow disturbers were used in the experiments described below, with the diameter,  $d=2.5$  mm and 4.6 mm. The spanwise distance between them varied from 5 to 18 mm so that similar non-dimensional scale parameters,  $d/D$ ,  $\Delta z/d$  and  $\Delta z/D$  could be formed and tested at the same non-dimensional flow parameter,  $Re_D$ .

The table below shows a scope of experimental conditions for the  $D=128$  cylinder with O-ring turbulators.

O-ring section d, mm	d/D	Spanwise step $\Delta z$ , mm	$\Delta z/d$	$\Delta z/D$	Free-stream velocity $U_0$ , m/s	$Re_D \times 10^{-5}$
2.5	0.0195	21	8.4	0.164	15.9	1.23
					26.5	2.04
					31.7	2.44
					42.3	3.26
		10	4.0	0.078	16.3	1.26
					21.5	1.65
					26.5	2.04
					31.7	2.44
					37.1	2.85
					42.3	3.26
		5	2.0	0.039	16.1	1.24
					21.2	1.63
					26.7	2.05
					31.9	2.46
					37.0	2.85
					42.3	3.26
4.6	0.0359	9	1.96	0.070	16.0	1.23
					21.5	1.66
					31.7	2.44
					42.3	3.26

O-ring section d, MM	d/D	Spanwise step $\Delta z$ , MM	$\Delta z/d$	$\Delta z/D$	Free-stream velocity $U_0$ , m/s	$Re_D \times 10^{-5}$
		18	3.91	0.141	16.1	1.24
					21.5	1.66
					26.4	2.03
					31.7	2.44
					37.1	2.86
					42.2	3.25

A scope of test parameters for the D=106.6 cylinder with O-ring turbulators is given in the following table:

O-ring section d, MM	d/D	Span-wise step $\Delta z$ , MM	$\Delta z/d$	$\Delta z/D$	Free-stream velocity $U_0$ , m/s	$Re_D \times 10^{-5}$
2.5	0.0195	20	8.0	0.188	16.4	1.06
					19.4	1.25
					27.8	1.79
					38.1	2.46
2.5	0.0195	17.5	7.0	0.164	16.3	1.05
					19.5	1.26
					27.6	1.77
					38.1	2.45
		10	4.0	0.094	16.0	1.03
					19.3	1.24
					27.7	1.79
					38.1	2.45
		5	2.0	0.047	16.3	1.05
					19.2	1.24
					27.5	1.77
					38.1	2.45

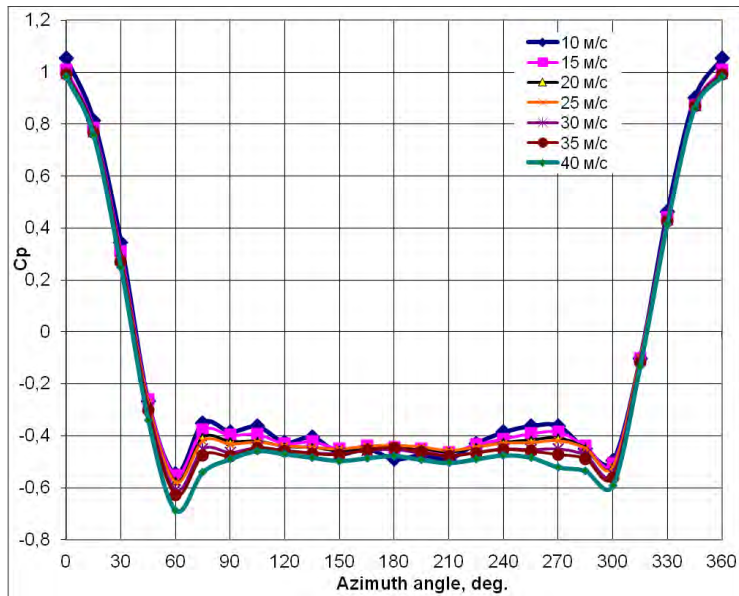


Fig. 2.5. Pressure distributions around a circular cylinder for different Reynolds numbers  $Re_D$

From a set of pressure distribution graphs in Fig. 2.5, one can see that O-ring turbulators cause earlier flow crisis and shift separation downstream from the cylinder middle compared to the reference case. This leads to drag reduction. Fig. 2.6 shows that at  $Re=2.46 \times 10^5$ , the flow along the reference model is subcritical with a separation line in the middle ( $\theta=90^\circ$ ). The O-rings transfer the flow into the supercritical mode with separation shifted to  $\theta=120^\circ$ . In this case, additional suction arises in a frontal part of the cylinder that produces a suction force and results in a corresponding drag reduction. The reference cylinder shows an earlier flow separation at  $Re=3.25 \times 10^5$  than the cylinder with O-ring turbulators even at a lower  $Re$ .

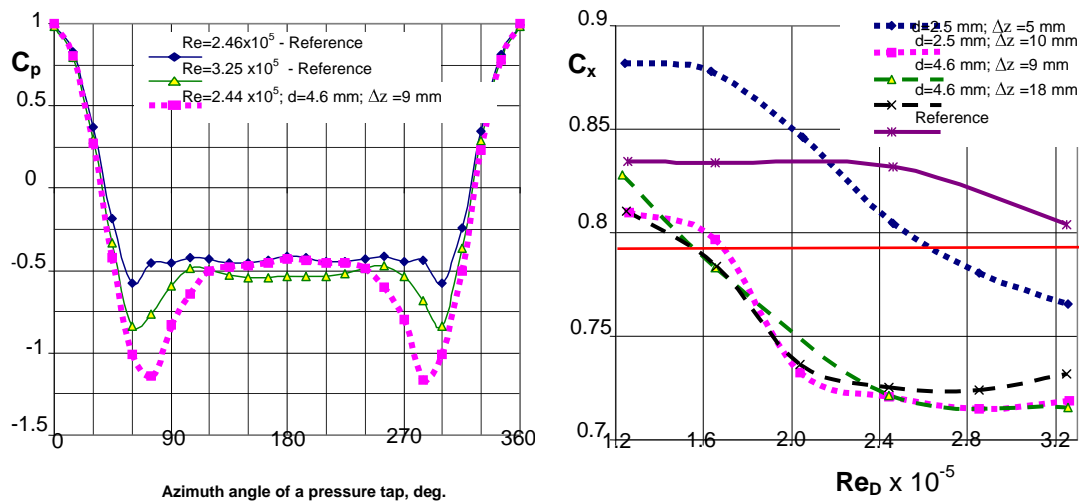


Fig. 2.6. Pressure distributions around a reference and O-ring controlled cylinders,  $D=128$  mm (left) and drag coefficients (right) for different spanwise steps  $\Delta z$  between the neighboring rings depending on Reynolds numbers  $Re_D$

### 3. WIND-TUNNEL EXPERIMENTS IN THE FRAMEWORK OF THE PROTOTYPE PROBLEM (ARRAYS OF MECHANICAL VORTEX-GENERATORS), IHM, Kiev

#### 3.1. Test model and a scope of measurements

A program of comparative experiments (ACIR vs AT-1 wind tunnel of the “Antonov” Design Bureau) was planned so that to pre-calculate a range of free-stream velocities for a given air temperature and barometric pressure in order to get Reynolds numbers equal to those in the “certification tests” in the AT-1.

In the both wind tunnels, the same measurement system was used and the same circular cylinder model. The cylinder of the diameter  $D=106.6$  mm was  $L=200$  mm long. On the both ends of the cylinder, 276 mm in diameter circular endplates are mounted (Fig. 3.1). The model has 24 pressure taps located in the middle section of the model with  $15^\circ$  spacing. From the two models tested earlier in the AT-1 wind tunnel, this model was chosen to reduce a blocking effect and to take it into account using increased free-stream velocities in the ACIR.  $Re_{\max}=3.44 \times 10^5$  for  $D=128$  mm obtained in the AT-1 wind tunnel could be reached now for a smaller diameters. The measurements were carried out at  $Re \approx (1.25, 2.5, \text{ and } 3.5) \times 10^5$ .

In addition to the smooth reference cylinder, four controlled “prototype” models were tested with spherical turbulizers of 4.2 mm in diameter mounted along a cylinder generatrix with a given spanwise step,  $\Delta z = 5, 10, 15, \text{ and } 20$  mm. The summarized test program is given in the Table 1.1.

Table 1.1. Test program summary

Spanwise step of turbulizers, $\Delta z$ , mm	Free-stream velocity $U_0$ , m/s	Reynolds number $Re \times 10^{-5}$	Downstream location - azimuth range $\alpha^\circ$	Downstream location - azimuth step $\Delta\alpha^\circ$
5	17.8	1.26	-15 – +105	7.5
5	35.7	2.51	-15 – +105	7.5
5	48.9	3.42	-15 – +105	7.5
5	48.5	3.39	90 – +120	7.5
10	18.0	1.27	-30 – +120	7.5
10	35.8	2.51	-30 – +120	7.5
10	36.1	2.53	-8 – +2	1.0
10	50.3	3.50	-15 – +135	15
15	18.0	1.26	-15 – +135	7.5
15	36.0	2.50	-15 – +135	7.5
15	51.2	3.54	-15 – +135	7.5
20	18.0	1.26	-15 – +135	7.5
20	36.0	2.49	-15 – +135	7.5

Spanwise step of turbulizers, $\Delta z$ , mm	Free-stream velocity $U_0$ , m/s	Reynolds number $Re \times 10^{-5}$	Downstream location - azimuth range $\alpha^\circ$	Downstream location - azimuth step $\Delta\alpha^\circ$
20	51.5	3.54	-15 – +165	7.5
--	17.6	1.22	-15 – +90	15
--	35.6	2.46	-15 – +135	15
--	51.6	3.56	-15 – +165	15

## 3.2. Test procedure and data reduction

The test procedure followed that developed for previous flow-control measurements. At each angle of attack,  $\alpha$ , or an azimuth of a vortex-generator array, two sets of measurements (“reference” and “controlled” cases) were carried out. Data reduction included denoising of samples and calculation of mean values. In the described tests, both sets of data were averaged to obtain a single value at each azimuth because of identical conditions of measurements in both cases.

## 3.3. Results and discussion

### 3.3.1. Comparison of ACIR and AT-1 results.

Identical measurements in the 2 wind tunnels were planned to verify all further measurement results to be obtained in the ACIR wind tunnel. The certified AT-1 wind tunnel and the same measurement system used in both cycles of experiments enable to indirectly certify the ACIR wind-tunnel facility. This way, it will ensure the quantitative trustworthiness of measurements carried out in the ACIR.

Analyzing the current data, it should be taken into consideration that the chosen model is oversized for the ACIR test section. Its diameter is 18% of the test section height and 13% of the cross-section area that exceeds acceptable values for high-drag bodies. In addition, available endplates reduce the flow field area.

For convenience of perception, the most typical pictures are included into the basic report body while the whole set of plots for analysis is presented in the Appendix 1 with relevant figure captures.

A good agreement is found both for drag coefficients at all Reynolds numbers and for lift coefficients at lower Reynolds numbers, i.e. those before the drag crisis. The best agreement for lift coefficients is found for interjacent steps of vortex generators,  $\Delta z = 10$  mm, and at interjacent  $Re = 2.5 \times 10^5$  (see Figs. 3.1, 3.2 below and the Appendix). In almost all the cases, drag coefficients in ACIR are greater than in AT-1 by the value of 0.1 – 0.2. The most possible explanation of the discrepancy between the measured results is the area of  $Re$  corresponding to the drag crisis which can slightly differ in the compared facilities, e.g. because of different free-stream turbulence levels. Besides, it can be caused by different blockage of test sections and by higher local velocities over the cylinder in the axial test-section part. It is a subject of further detailed flow investigations in the ACIR.

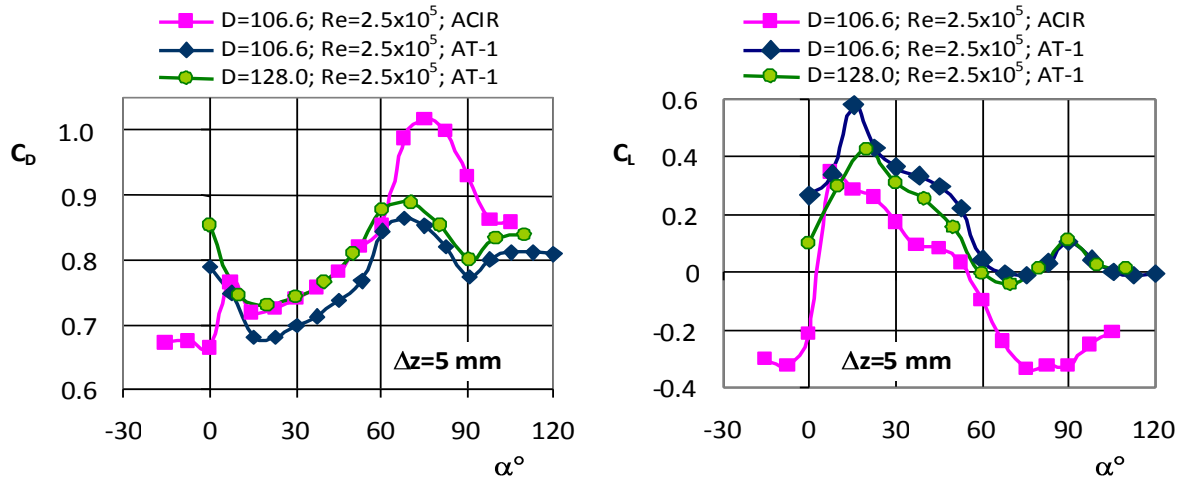


Fig. 3.1. Drag and lift coefficients identically measured in the ACIR and AT-1 wind tunnels: circular cylinder model controlled with spanwise arrays of mechanical vortex-generators with the  $\Delta z = 5$  mm space scale;  $Re=2.5 \times 10^5$

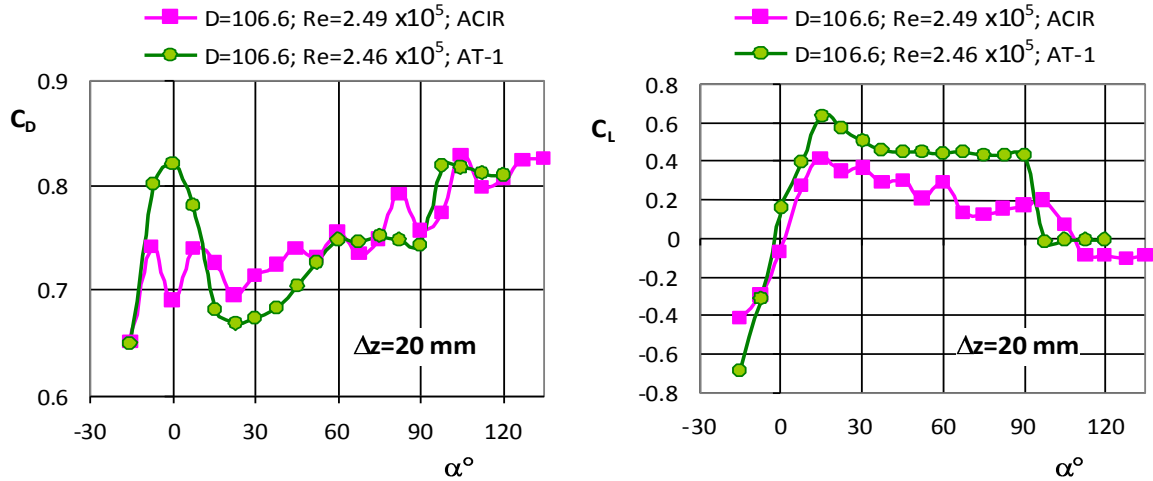


Fig. 3.2. Drag and lift coefficients identically measured in the ACIR and AT-1 wind tunnels: circular cylinder model controlled with spanwise arrays of mechanical vortex-generators with the  $\Delta z = 20$  mm space scale;  $Re=2.5 \times 10^5$

Discrepancy between aerodynamic coefficients in ACIR and AT-1 for  $Re \approx 3.5 \times 10^5$  grows (Figs. 3.3, 3.4) together with the instability of the drag crisis area. In addition, the ACIR must be more sensitive to introduction of the turbulizers contributing to the blocking effect while in the AT-1 wind tunnel, the flow is practically unbounded for the tested models. Lift coefficients differ in the two facilities to a greater extent because the array of turbulizers accelerates the flow in the AT-1 on this side of the model at any Reynolds numbers thus increasing suction here. It is in agreement with pressure distributions.

For now, the found qualitative agreement of the results obtained in ACIR and AT-1 is acceptable for comparative analysis and interpretation of the results as well as for understanding and planning further steps to the indirect ACIR certification.

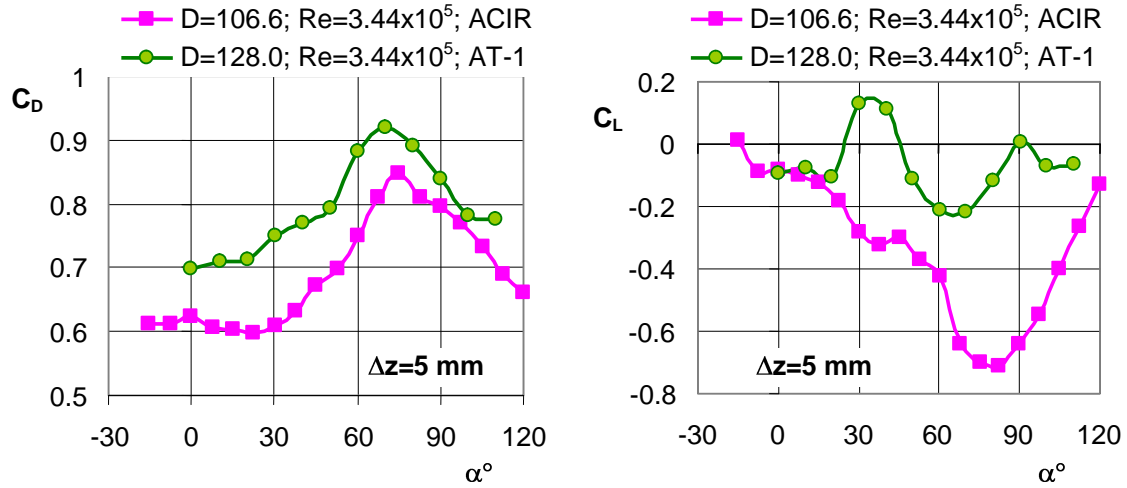


Fig. 3.3. Drag and lift coefficients identically measured in the ACIR and AT-1 wind tunnels: circular cylinder model controlled with spanwise arrays of mechanical vortex-generators with the  $\Delta z = 5$  mm space scale;  $Re=3.5 \times 10^5$

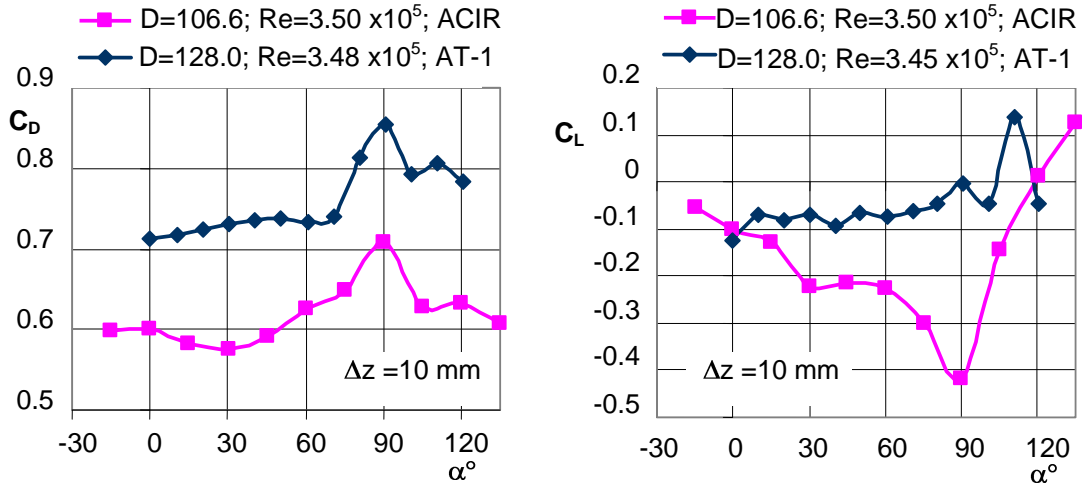
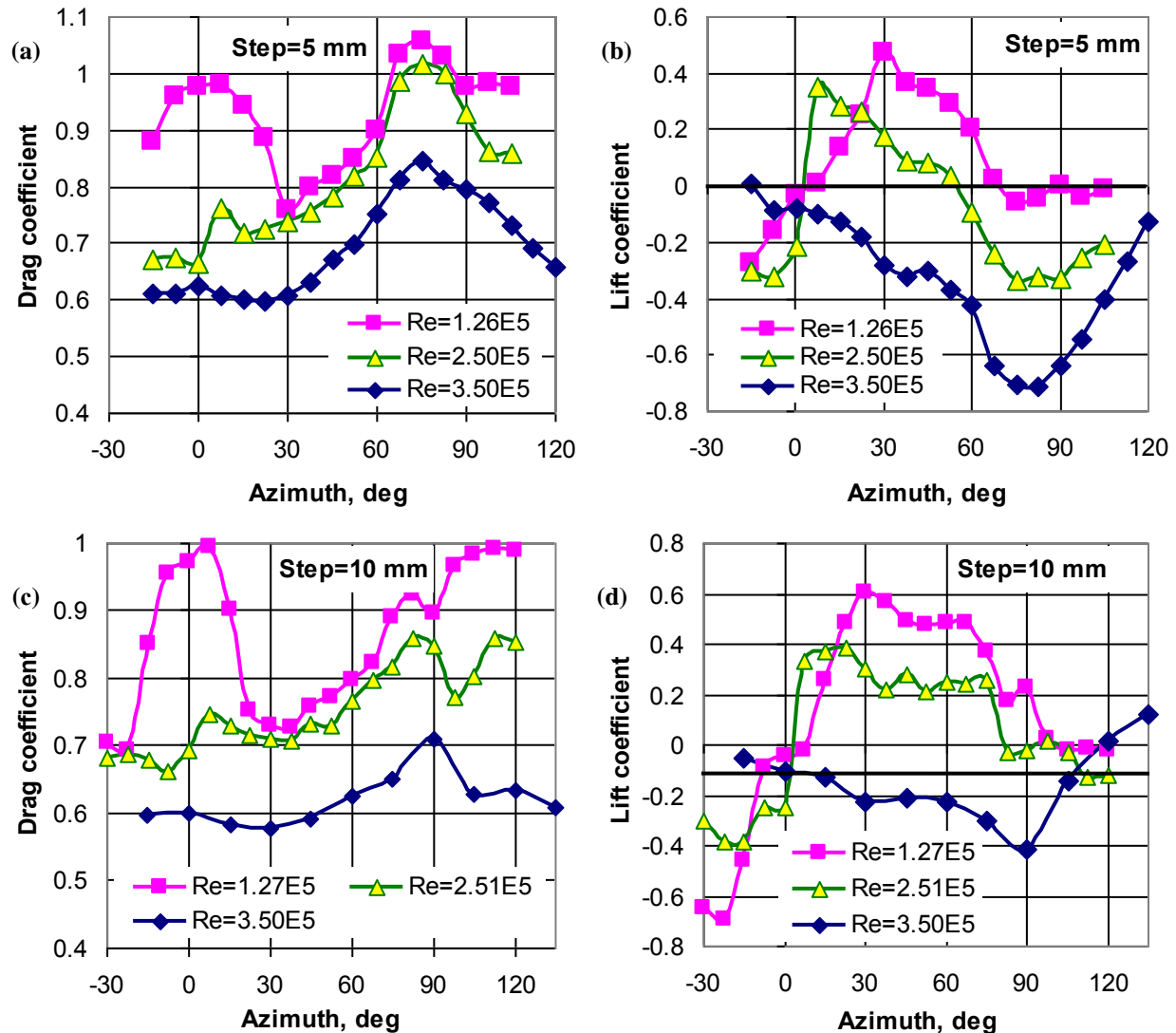


Fig. 3.4. Drag and lift coefficients identically measured in the ACIR and AT-1 wind tunnels: circular cylinder model controlled with spanwise arrays of mechanical vortex-generators with the  $\Delta z = 10$  mm space scale;  $Re=3.5 \times 10^5$

### 3.3.2. Influence of growing Reynolds number

Since the maximum accessible free-stream velocity raised  $\sim 1.5$  times due to the advanced Novenco fan, the new cycle of flow-control measurements aimed at the revealing an impact of higher velocities on aerodynamic characteristics of the controlled model. Figs. 3.4, a-h show drag and lift coefficients measured within  $\alpha = -30^\circ - 120^\circ$  locations of the vortex-generator array relative to the velocity vector. The  $Re$  range,  $(1.25 - 3.5) \times 10^5$ , embraces the pre-crisis and the started drag crisis areas. Under these conditions, 4 space scales of generated vortices are investigated,  $\Delta z = 5, 10, 15, 20$  mm.

The higher Re, the lower lift and drag coefficients under conditions of vortex generation on one side of the cylinder. Moreover for  $Re=(1.26 - 1.27) \times 10^5$ , lift coefficients are positive almost everywhere at  $\alpha = 0^\circ - 90^\circ$ . For  $Re=2.5 \times 10^5$ , this angular region narrows to  $\alpha = 0^\circ - (60-75)^\circ$  for smaller  $\Delta z$ . For  $Re=3.5 \times 10^5$ , lift changes its sign and is negative for all azimuth angles except for the cases of  $\Delta z > 5$  mm, where at  $\alpha > 105^\circ - 120^\circ$  it becomes positive. That is the lift coefficients at  $Re=3.5 \times 10^5$  behave reversely compared to the situations of lower Reynolds numbers.



Drag coefficient dependence on an azimuth angle of vortex-generators weakens both with growing Reynolds number and a spanwise step  $\Delta z$ . It should be noted that at  $Re=2.5 \times 10^5$ , the behavior of drag coefficient vs  $\alpha$  become unstable showing oscillations: the greater a step between the turbulizers, the greater the oscillations. It indicates the transition from subcritical to supercritical flow over the cylinder at this Reynolds number. It requires a more detailed investigation in this region. It can become possible after the general flow investigation in the renewed wind tunnel and relevant adjustments of the fan drive system (including the launch of the fan feedback control).

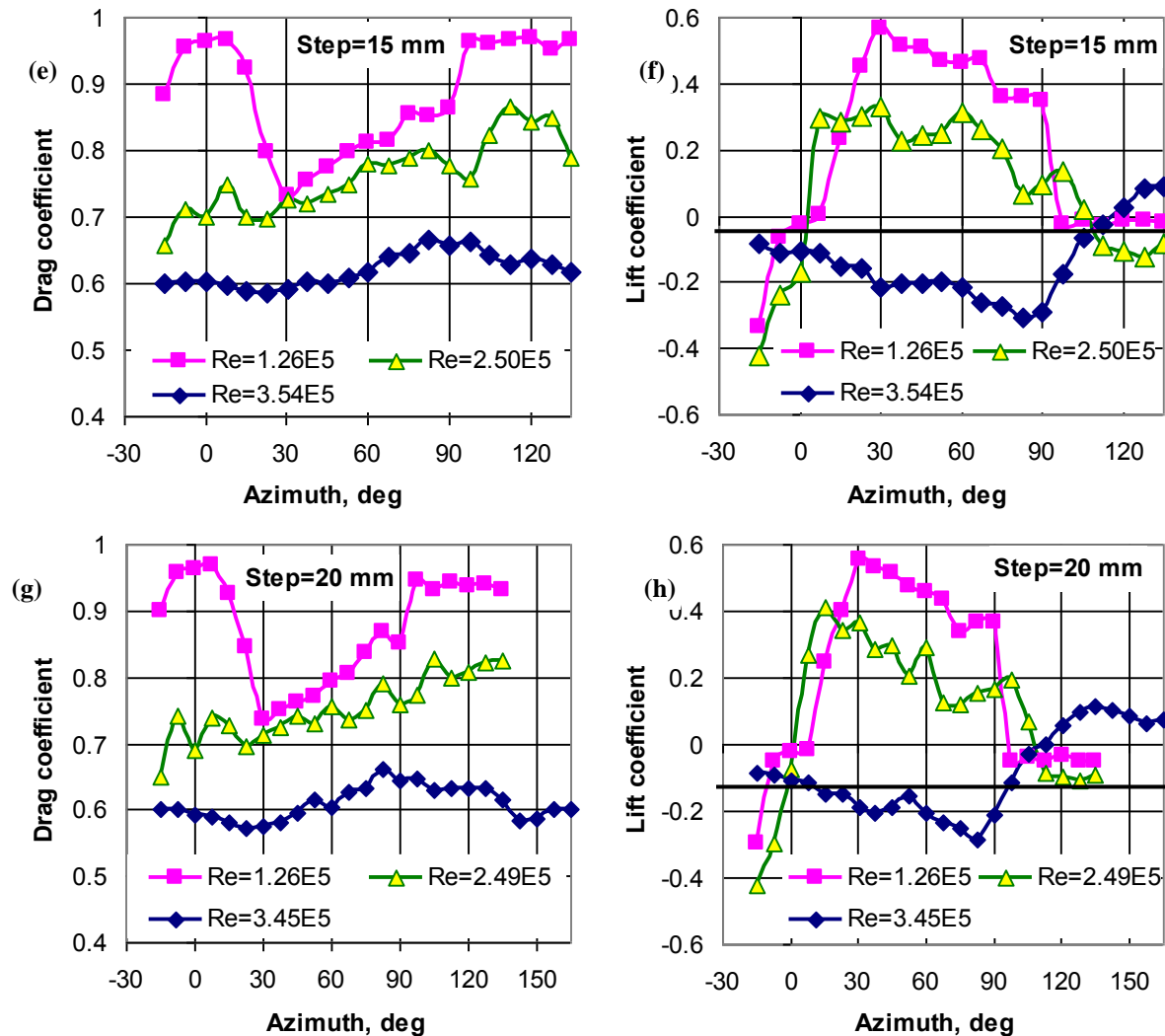


Fig. 3.5. Influence of Reynolds numbers on aerodynamic characteristics of 106.6 mm cylinder

## SUMMARY

Prototype investigations of the circular cylinder model with an array of spherical vortex generators bring to the following conclusions:

- comparative analysis of data obtained in the wind tunnels of ACIR and of AT-1, "Antonov" Design Bureau, shows a good agreement; found discrepancies are a subject of further investigations;
- motion of bluff bodies can be controlled using arrays of simple spherical vortex-generators that was set as a prototype problem for the localized plasma approach; substantial drag reduction together with raised lift was found for supercritical flows,  $Re=3.5 \times 10^5$ . The next stage is to determine an optimal spanwise distance,  $\Delta z$ , between the turbulizers;
- efficiency of flow control with prototype spherical turbulizers was found to be higher at subcritical Reynolds numbers and to drop at supercritical regimes of the flow.